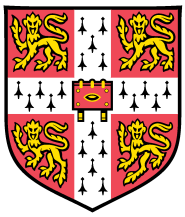

UNIVERSITY OF CAMBRIDGE

Tris-Pyridyl Ligands and Beyond:

Modifications Derived from the Bridgehead and Donor Vector

Jessica Ellen Waters

Selwyn College

University of Cambridge

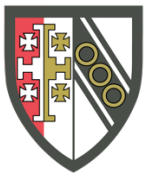

September 2021

This thesis is submitted for the degree of

Doctor of Philosophy.

to my immediate family;

Mum, Dad & Michael

And to Beki, the bubbliest chemist I ever met.

Declaration

This thesis entitled “Tris-pyridyl Ligands and Beyond: Modifications Derived from the Bridgehead and Donor Vector” is submitted to the Degree Committee of Physics and Chemistry at the University of Cambridge in partial fulfilment for the qualification of Doctor of Philosophy. The work in this dissertation was carried out in the Department of Chemistry of the University of Cambridge under the supervision of Prof. Dominic S. Wright between October 2017 and September 2021.

This dissertation is the result of my own work and includes nothing, which is the outcome of work done in collaboration except where it is declared otherwise. This thesis contains no material published or written by another person or presented for any other degree or diploma at a university, except where due reference is given. Furthermore, this dissertation does not exceed the prescribed word limit of 60,000 words including tables, captions and the bibliography.

Jessica Ellen Waters

September 2021, Cambridge

Acknowledgements

There are many people to whom I owe thanks for the opportunity to embark on such an exciting and privileged journey that is a Ph.D. First and foremost, I wish to thank my fantastic supervisor, Prof. Dominic Wright. Dom – thanks so much for your creativity, teaching and most importantly for supporting me throughout my Ph.D. I have learnt so much from you and will certainly miss all the entertaining coffee breaks!

I'd also like to extend my gratitude to those who have provided guidance in a scientific sense throughout my Ph.D.: to the entirety of Lab 301- thank you for your suggestions towards my research and for providing a supportive environment that made failed experiments a lot easier to deal with. Thanks to Dr Andrew Bond for help with X-ray crystallographic data and to Dr Andrew Peel and Dr Alex Plajer for help with refinement and some intellectual conversations; to Dr Schirin Hanf for assistance with DFT studies, and to Dr Jonny Slaughter for proof-reading and general guidance and support throughout the entirety of my Ph.D. studies. Thanks also go to Duncan Howe and Andrew Mason for their help with the quirkier NMR experiments, to technicians Steven Wilkinson, Carlos Davies & Gary Herrington, and to Nigel Howard for microanalysis. Thanks also to Selwyn College and the Walters-Kundert studentship for funding my Ph.D. and to Dr James Keeler for initiating this.

Teaching is something that I've always enjoyed and has always been encouraged in this Department. I am lucky enough to have had the pleasure of supervising and collaborating with three students throughout my Ph.D. who have been a great help to me. Thank you to Georg Berger, Matthew Haynes, and Marina Ricón-Nocíto: for all your hard work and patience with what were at times extremely tricky projects to navigate.

Special thanks go to my friends for their unwavering support: to Nic & Meg, to Sam, Tom, Dave, Becca & Matt, who've provided many entertaining weekends. To Georgina, who's emotional support has always pulled me through even when her physical absence has got in the way. To Beth, Bethan, Dave, Aoife, Helen, Bryna, the Butlers: thank you for your encouragement and many fond memories. In Cambridge, I have been very fortunate in knowing some wonderful people: thank you to Lucie, Amy, Julia, Catherine, Ingrid, Aimée, Jonny & Josh for some wild times. Thank you to Pixie for getting me from A to B in (more or less) one piece. Thank you also to Coco, Lily, and Evan for their support and friendship, and to James, Carlos & Grace - the people with whom I have called 138 Gwydir St Brewery home. George

– thank you for celebrating every single achievement with me and for constantly inspiring me every day; this could not have been done without you. Thanks also go to the Cambridge University Women's Water Polo team for some excellent times both in and out of the water, and to Jo Lockhart, for reigniting my passion for open water swimming with some lovely early morning dips & chilly chats down at the river.

For their encouragement throughout 26 years of education, I would like to extend my sincerest thanks to my family. Michael - nothing I have ever embarked upon would have been a success if it hadn't been for your guidance and advice. Mum - I wholeheartedly thank you for your unfaltering support and advocacy. Your interest in the natural world has always inspired me, Dad, hence the basis of this Ph.D. in the first place. I hope I can continue in that fashion for years to come. I am forever indebted to you all.

Finally, none of this would have been possible without the encouragement and inspiration of the following people. My sincerest thanks go to:

Dr Kylie J. Mitchell, who ignited the idea of undertaking a Ph.D.;

Dr Annie L. Colebatch, who guided and motivated me throughout;

and *Dr Sally R. Boss*, for getting me to the finish line.

Lay Summary

The intention of this lay summary is to facilitate the understanding and public engagement/outreach concerning the work described in this thesis. In other words, it is a take-home message. The hope is that the reader, however familiar with the field, will grasp the purpose of the work as well as its significance within the research area, without the need for specifics and scientific jargon.

Inorganic chemistry is the branch of chemistry that deals with the syntheses, behaviours, and other fundamental aspects of essentially non-carbon compounds across the Periodic Table. This includes, but is not limited to, coordination chemistry, bioinorganic chemistry, organometallic chemistry, solid-state/materials/nanoscale chemistry, photochemistry and energy storage, catalysis, and last but most certainly not least – main group chemistry.[1] The latter is the basis of this project, and concerns those elements found between Groups 1 and 2 (*s*-block) and from Groups 13 to 18 (*p*-block) in the Periodic Table. This project utilises such elements as a means of designing and synthesising compounds that manifest intriguing properties or reactivities. Such behaviours may be of interest because they cater for a well-established application (such as catalysis), or simply because they behave in such a way that is unexpected or unorthodox.

Take the industrial process of catalysis, for example - the process that utilises a chemical that speeds up a reaction's rate (how fast it is) without being consumed in the process. Famously, the 'chemicals' that govern these processes are based around precious metals (platinum, palladium, iridium, rhodium, etc). Whilst these chemicals are 'the best in the business', they're costly and their sources are depleting, rendering them soon to be unsuitable for such processes. In other words, we need to look for cheaper, more abundant alternatives, and one way of doing this is by searching other realms of the Periodic Table. In some cases, main group elements found on the right-hand side of the *p*-block of the Periodic Table have proven to be viable alternatives in some circumstances. However, the use of *p*-block elements to the same extent as their superior transition metal-alternatives is very much in its infancy.

Loosely speaking, this is where this Ph.D. project comes in. We investigate the potential of these *p*-block elements further through ligand design and the studies of their reactivities, followed by any potential application they may cater for.

Whilst designing compounds to suit a particular application is to be praised – and is certainly where the funding is these days! – we should not actively discourage original, more fundamental ideas. In her article on the same topic, Professor Stefanie Dehnen discusses how we should not judge research simply on the nature of its application potential, rather, we should seek to encourage curiosity-driven – and in many cases more diverse – research.[2] She further argues that many of the "*more exciting and often pioneering discoveries (have) been merely coincidental*".

Whilst somewhat lacking an application at present, without a doubt what the research in this thesis caters for is original and innovative contributions towards chemistry. Looking forward, it is hoped that this work could either potentially cater for a well-established application in chemistry - or perhaps a more exciting prospect – it could generate its own niche in the world of science, which could become a future widely-acknowledged application in years to come.

List of Publications

The following publications were published during the period from October 2017 to September 2021, and are directly related to this thesis:

1. *Recent Advances in the Synthesis and Application of Tris(pyridyl) Ligands Containing Metallic and Semimetallic p-Block Bridgeheads*. A. J. Peel, J. E. Waters, A. J. Plajer, R. García-Rodríguez, D. S. Wright, *Recent Advances in Organometallic Chemistry*, **2021**.

2. *Uncovering the Hidden Landscape of Tris(4-pyridyl) Ligands: Topological Complexity Derived from the Bridgehead.* J. E. Waters, G. Berger, A. J. Peel, A. D. Bond, R. García-Rodríguez, D. S. Wright, *Chem. Eur. J.*, 2021, **27**, 12036-12040.

3. *Synthesis and Coordination Behaviour of Aluminate-based Quinolyl Ligands*, J. E. Waters, S. Hanf, A. D. Bond, R. García-Rodríguez, D. S. Wright, A. L. Colebatch, *Dalton Trans.*, 2021, **50**, 14551-14559 - *cover article*.

4. *Synthesis and Coordination Behaviour of Pyridyl-based Stannane and Stibene Ligands*, J. E. Waters, A. D. Bond, A. L. Colebatch & D. S. Wright, *In Preparation*.

The following publications were published during the period from October 2017 to September 2021, and are not directly related to this thesis:

5. *Synthesis of 1,2-Diphospholides using a Main Group 'Superbase'.* L. S. H. Dixon, S. Hanf, J. E. Waters, A. D. Bond, D. S. Wright, *Organometallics*, 2018, **37**, 4465-4472.

6. *Facile Synthesis of a Nickel(0) Phosphine Complex at Ambient Temperature.* S. Hanf, T. Grell, J. E. Waters, R. Garcia-Rodriguez, E. Hey-Hawkins, D. S. Wright, *Chem. Commun.,* 2020, **56**, 7893-7896.

List of Numbered Compounds

The compounds presented in this thesis are listed, below.

Novel Compounds Described in this Thesis

Chapter 3

1 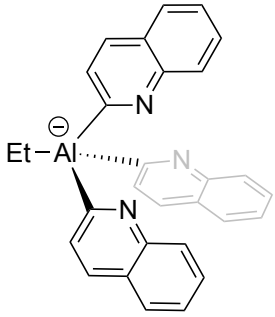	**2a and 2b** 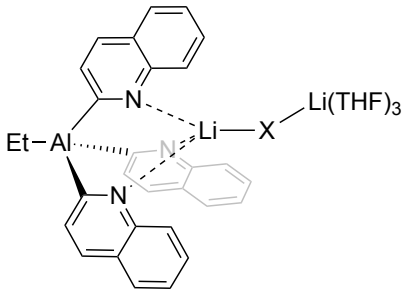 X = Cl, Br 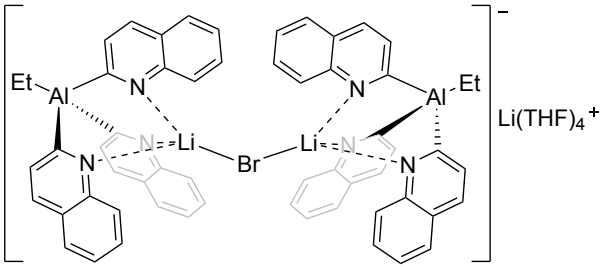
[(3)Li] 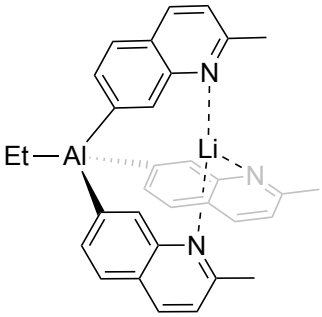	**[(4a)Li(THF)]** 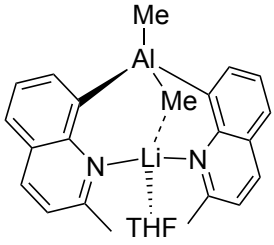
5 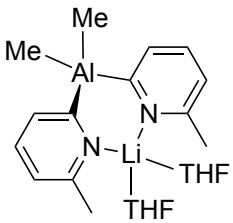	**6** 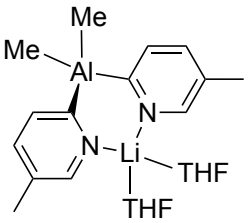

7 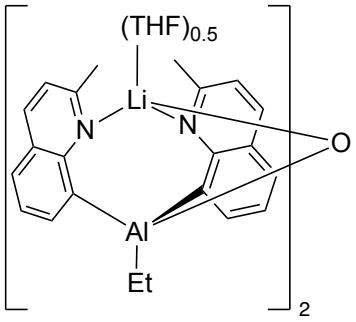	**8** 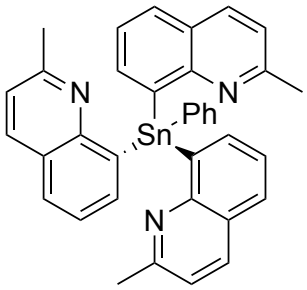
9 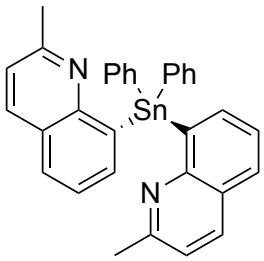	**10** 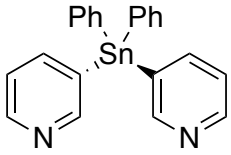
11 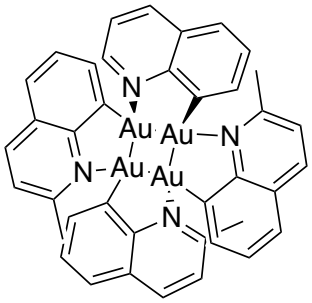	**12** 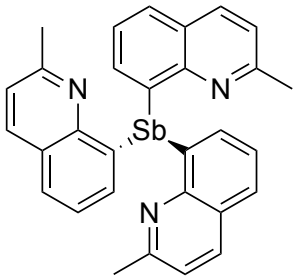
13 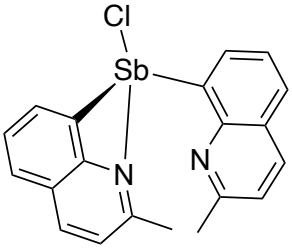	**14** 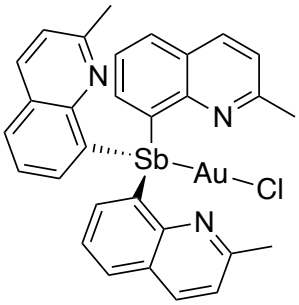

Chapter 4

15 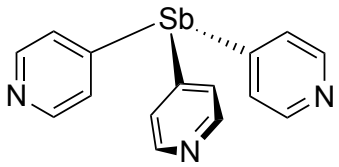	**16** 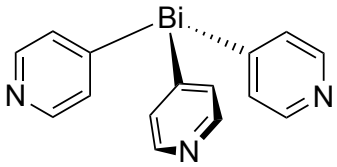
17 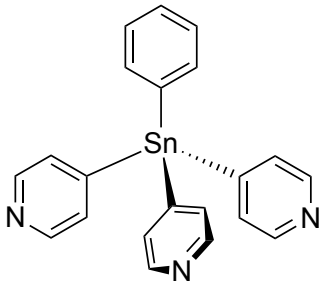	**18** $\{Ag^{I}_{2}(\mathbf{16})_3\}_n(CF_3SO_3)_{2n}$
19 $\{Ag^{I}_{2}(\mathbf{16})_3\}_n(SbF_6)_{2n}$	**20** $\{Ag^{I}_{2}(\mathbf{16})_3\}_n(PF_6)_{2n}$
21 $\{Ag^{I}_{2}(\mathbf{15})\}_n(SbF_6)_n$	**22** $\{Ag^{I}(\mathbf{17})\}_n(CF_3SO_3)_n$
23 $\{Ag^{I}(\mathbf{B})\}_n(CF_3SO_3)$	**24** $\{Cu(\mathbf{16})(MeCN)\}_n(PF_6)_n$
25 $\{Cu(\mathbf{16})_2\}\{Cu(\mathbf{16}\text{-}SiF_5)\}_n(PF_6)_n$	

Chapter 5

26 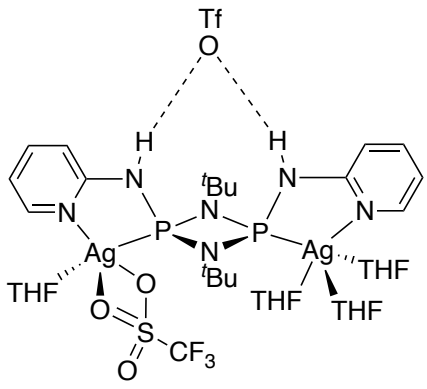	**28** 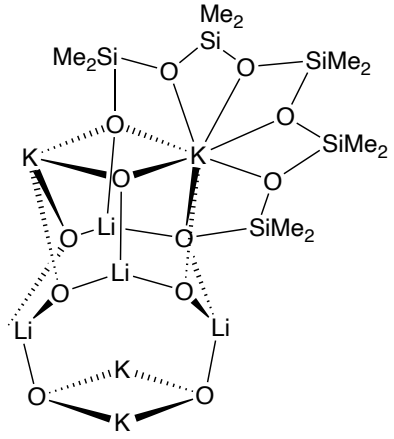

29 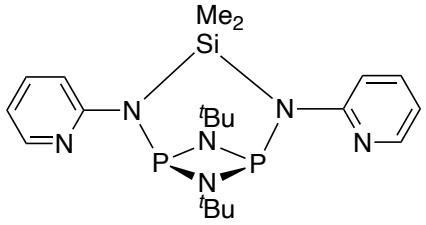 *potential by-product from reaction of **H** with BnK*	**30** 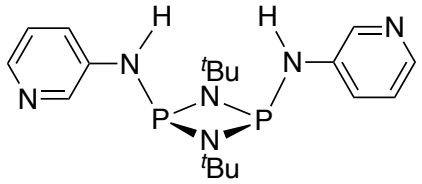
31 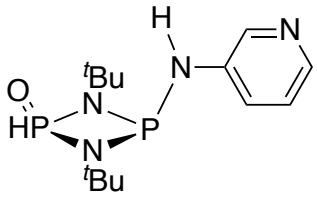	**32** 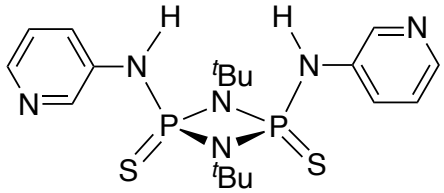
33 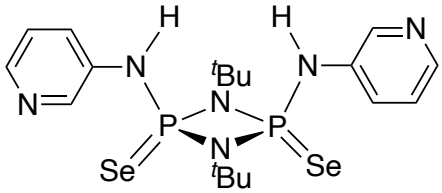	

Published Compounds & Synthesised Starting Materials

A 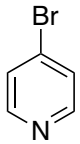	**B** 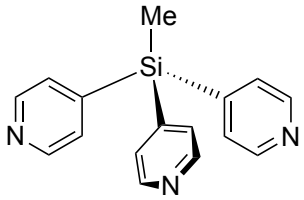
C 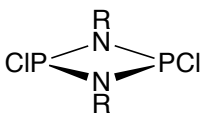	**D** 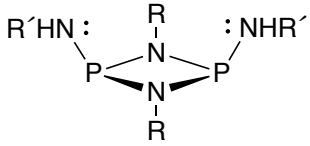

E 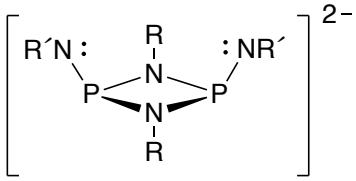	**F** 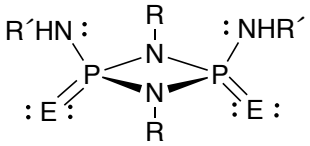
G 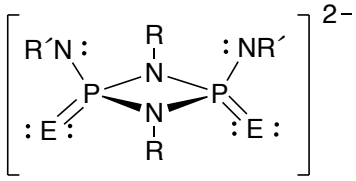	**H** 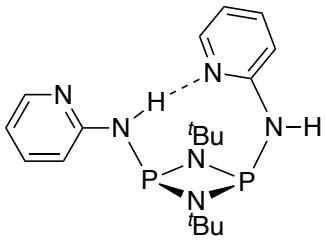
I 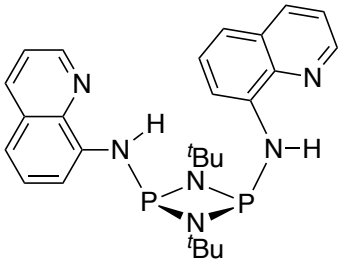	**J** 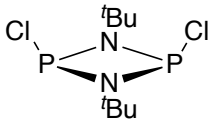
K 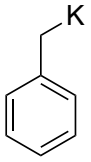	**[27·Li₂]** 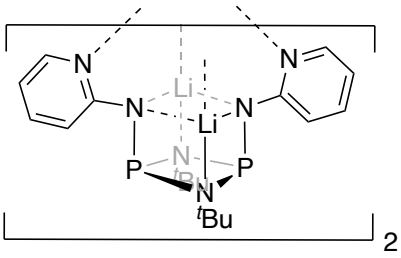 *further use attempted - unsuccessful*

Colour Code for Single-Crystal X-ray Structures

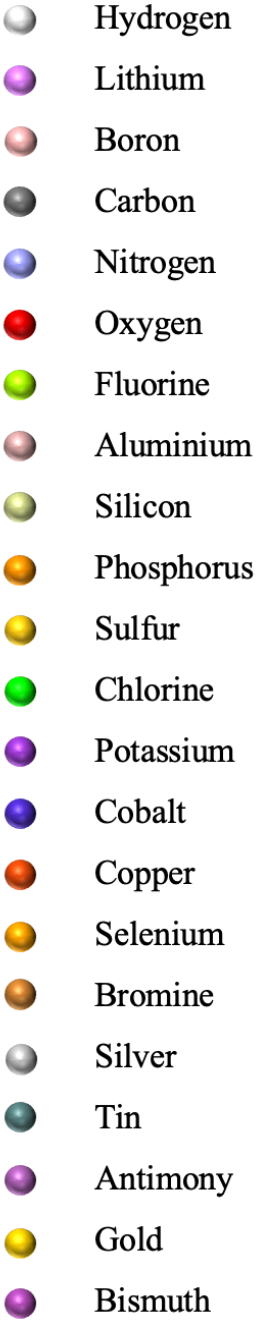

Abbreviations

Ar	Aryl
AIMS	Atoms In Molecules
Bipy/bipy	Bipyridine
b.p.	Boiling point
br	Broad
Bu	Butyl
ca.	*circa*
calcd.	Calculated
cf.	*confer*
COSY	Correlation Spectroscopy
Cp	Cyclopentadienyl
Cp*	1,2,3,4,5-Pentamethylcyclopentadienyl
Cy	Cyclohexyl
d	Doublet
Da	Dalton, unified atomic mass unit
DCM	Dichloromethane
dd	Doublet of doublets
DFT	Density Functional Theory
E	Element
e.g.	*exempli gatia*
EI	Electron Ionisation
ESI	Electrospray Ionisation
Et	Ethyl
Et_2O	Diethyl Ether
eq	Equivalents
GC-MS	Gas Chromatography-Mass Spectrometry
h	Hour(s)
HOESY	Heteronuclear Overhauser Enhanced Spectroscopy
HMBC	Heteronuclear Multiple Bond Correlation

HMQC	Heteronuclear Multiple-Quantum Correlation Spectroscopy
HOMO	Highest Occupied Molecular Orbital
HPLC	High-Performance Liquid Chromatography
HR-MS	High-Resolution Mass Spectrometry
HSQC	Heteronuclear Single Quantum Coherence
i.e.	*id est*
^{i}Pr	isopropyl
IR	Infrared Spectroscopy
J	Coupling constant
LUMO	Lowest Occupied Molecular Orbital
m	Multiplet (NMR), medium (IR)
M	Metal, molecular (HR-MS)
Me	Methyl
MeCN	Acetonitrile
MOF	Metal Organic Framework
m.p.	Melting point
MS	Mass Spectrometry
^{n}BuLi	*n*-Butyllithium
NAO	Natural Atomic Orbitals
NBO	Natural Bond Orbital
NMP	N-Methyl-2-pyrrolidone
NMR	Nuclear Magnetic Resonance
NOESY	Nuclear Overhauser Effect Spectroscopy
OAc	Acetate
OMe	Methoxy
OPh	Phenoxy
OTf	Triflate
Ph	Phenyl
pic	Picolyl
pip	Piperidine
ppm	Parts per million
Pr	Propyl

py	Pyridyl
py′	Substituted pyridyl
pz	Pyrazolyl
qy	Quinolyl
qy′	Substituted quinolyl
rt	Room temperature
s	Singlet (NMR), strong (IR)
t	Triplet
td	Triplet of doublets
TMEDA	Tetramethylethylenediamine
THF	Tetrahydrofuran
THT	Tetrahydrothiophene
tol	Toluene
Tp^{-}	Tris-pyrazolyl (borate)
TPPh	Tri(pyridylmethyl)phosphine
vs.	*versus*
VSEPR	Valence Shell Electron Pair Repulsion
VT	Variable Temperature
w	Weak
δ	Chemical shift
λ	Wavelength
$\tilde{\nu}$	Wavenumber
ν	Frequency

Abstract

Tris-Pyridyl Ligands and Beyond: Modifications Derived from the Bridgehead and Donor Vector – Jessica Ellen Waters

The development of new classes of ligands is a fundamental and ongoing challenge in modern chemistry, and a cornerstone in modern catalysis, supramolecular assembly and biomimetics. The current world of coordination chemistry is dominated by ligands based on organic frameworks. However, there is a developing field of coordination and supramolecular chemistry using inorganic frameworks, and this thesis is focused on fundamental research in the synthesis and design of ligand molecules of this type.

In Chapter 1, a concise account of previous studies of tris 2-, 3- and 4-pyridyl based ligands $E(py)_3$ (where E = a main group bridgehead atom or group, and py = a pyridyl donor arm) is presented. The main conclusion from this survey of the literature is that, despite recent developments in this area, there are some significantly unexplored fields. This is particularly the case for metal-based Group 13, 14 and 15 pyridyl ligands containing 4-pyridyl functionality, which may open new avenues of supramolecular coordination chemistry. In addition, the elaboration of this type of metal-bridgehead by the incorporation of other polycyclic aromatic N-donor groups has been almost completely ignored so far. The aims of the thesis (Chapter 2) are primarily to expand our understanding of the structural effects of moving the donor-N atoms in ligands of this type to different positions in the ring substituents – closer to or further away from the main group bridgehead atoms. Chapter 3 explores one of the primary aims of the program of research, focusing on tris- and bis-8-quinolyl ligand arrangements containing Group 13 (Al), Group 14 (Sn) and Group 15 (Sb) bridgehead atoms, in which the N-donor atoms are more remote from the bridgeheads than in pyridyl counterparts. A highlight in this area is the development of bis-8-quinolyl ligands and the potential interaction of the bridgehead alkyl substituents with coordinated metals – illustrated by the structure of $[\{Me_2Al(2\text{-}Me\text{-}8\text{-}qy)_2\}Li(THF)]$ [(**4a**)Li(THF)]. In Chapter 4, the synthesis of the first examples of heavy Group 14 and 15 4-pyridyl ligands $E(4\text{-}py)_3$ (E = PhSn, Sb, Bi) and their coordination chemistry are reported. It is shown that moving the N-donor atoms within the pyridyl ring to the 4-position results in the ability to build an extensive range of new metal

organic frameworks (MOFs). An important conclusion from this work is that underlying periodic behaviour (*s*-*p* separation and the inert pair effect) has a major effect on the ligand coordination modes, providing the basis for modulation of ligand character (N,N,N- vs N,N,N,E-donor behaviour). Chapter 5 describes more complex research in which, instead of using a bridgehead atom, a bridgehead group is employed (in this case a cyclodiphosphazane ring unit), to separate pyridyl donor functionality and expand the ligand bite.

General conclusions and suggestions for future work are gathered in Chapters 6 and 7. Overall, the research provides new types of main group metal-based ligands which have potential applications in catalysis and in the building of porous networks. As such, it develops new aspects of coordination and supramolecular chemistry which have significant promise for future studies.

Table of Contents

Declaration ..... **iv**

Acknowledgements ..... **vi**

Lay Summary ..... **viii**

List of Publications ..... **x**

List of Numbered Compounds ..... **xii**

Colour Code for Single-Crystal X-ray Structures ..... **xviii**

Abbreviations ..... **xix**

Abstract **1**

1. Introduction **8**

1.1 The Advancement of Main Group Chemistry **8**

1.2 Tripodal Ligands **8**

1.3 Tripodal Ligands Containing Pyridine Rings **11**

1.3.1 Tris-2-Pyridyl Ligands 11

1.3.2 Tris-3-Pyridyl Ligands 37

1.3.3 Tris-4-Pyridyl Ligands 46

1.4 Tris-4-Pyridyl and Beyond: New Directions Towards Tripodal Ligand Design **47**

2. Project Aims **50**

3. Synthesis & Coordination Behaviour of Tris- and Bis-Quinolyl Ligands **53**

3.1 Preface **53**

3.2 Results & Discussion **55**

3.2.1 Tris- and Bis-Quinolyl-Aluminates: Synthesis and Solid-State Structures 55

3.2.2 Quinolyl Ligands Based on Group 14 and 15: Sn and Sb 71

3.3 Conclusions **84**

4. Synthesis of Tris-4-Pyridyl Ligands: Topological Complexity Derived from the Bridgehead **87**

4.1 Preface **87**

4.2 Ligand Design and Synthesis of Sb-, Bi- and PhSn-Bridged Tris-4-Pyridyl Ligands 90

4.3 Coordination Behaviour of 15, 16 and 17 95

4.3.1 Silver Complexes of 15, 16 and 17 96

4.3.2 Copper Complexes of 16 106

4.4 Conclusions 108

5. Structure and Reactivity of Pyridyl Donor cis-disubstituted Cyclodiphosphazanes 111

5.1 Preface 111

5.2 Results & Discussion 115

5.2.1 Synthesis of [(2-py)P(μ-N^{t}Bu)]$_2$ (H) and [(8-qy)P(μ-N^{t}Bu)]$_2$ (I) 115

5.2.2 Coordination Behaviour of H 116

5.2.3 Synthesis of [(3-py)P(μ-N^{t}Bu)]$_2$ (30) 125

5.2.4 Coordination Behaviour and Reactivity of 30 128

5.3 Conclusions 139

6. Conclusions 143

7. Future Work 146

7.1 Studies Following on Directly From the Ph.D. Work 146

7.2 Further Studies and Developments of Main Group N-donor-based Ligands 147

7.2.1 Tris-Diazyl Ligands 147

7.2.2 Tris-Bipyridyl-Ligands 148

8. Experimental 152

8.1 General Laboratory & Inert Atmosphere Techniques 152

8.2 Solvents and Starting Materials 152

8.3 Analytical Techniques 153

8.3.1 Nuclear Magnetic Resonance Spectroscopy 153

8.3.2 Elemental Analysis 154

8.3.3 Infrared Spectroscopy 154

8.3.4 Single-crystal X-ray Diffraction 154

8.3.5 Powder X-ray Diffraction 155
8.3.6 Computational Studies 155
8.3.7 Mass Spectrometry 155

8.4 Synthetic Protocols 156
8.4.1 Synthesis of 4-bromopyridine (A) 156
8.4.2 Synthesis of $MeSi(4\text{-}py)_3$ (B) 156
8.4.3 Synthesis of $[(2\text{-}py)P(\mu\text{-}N^tBu)]_2$ (H) 157
8.4.4 Synthesis of $[ClP(\mu\text{-}N^tBu)_2]$ (J) 157
8.4.5 Synthesis of benzyl potassium (K) 158
8.4.6 Synthesis of $[(1)Li(\mu\text{-}Cl)Li(THF)_3]$, (2a) and $[\{1\}_2(\mu\text{-}Br)]^-Li(THF)_4^+$, (2b) 158
8.4.7 Synthesis of $[\{EtAl(2\text{-}Me\text{-}8\text{-}qy)_3\}Li]$ (1Li), [(3a)THF] 159
8.4.8 Synthesis of $[\{Me_2Al(2\text{-}Me\text{-}8\text{-}qy)_2\}Li(THF)]$, [(4a)Li(THF)] 160
8.4.9 Synthesis of $[\{Me_2Al(6\text{-}Me\text{-}2\text{-}py)_2\}Li(THF)_2]$, $[(5)Li(THF)_2]$ 160
8.4.10 Synthesis of $[\{Me_2Al(5\text{-}Me\text{-}2\text{-}py)_2\}Li(THF)_2]$, $[(6)Li(THF)_2]$ 161
8.4.11 Synthesis of $[\{EtAl(2\text{-}Me\text{-}8\text{-}qy)_2\}_2O\}\cdot(Li_2THF)]$ (7) 161
8.4.12 Synthesis of $PhSn(2\text{-}Me\text{-}8\text{-}qy)_3$ (8) 162
8.4.13 Synthesis of $Ph_2Sn(2\text{-}Me\text{-}8\text{-}qy)_2$ (9) 163
8.4.14 Synthesis of $Ph_2Sn(3\text{-}py)_2$ (10) 163
8.4.15 Synthesis of $Au_4(2\text{-}Me\text{-}8\text{-}qy)_4$ (11) 164
8.4.16 Synthesis of $Sb(2\text{-}Me\text{-}8\text{-}qy)_3$ (12) 164
8.4.17 Synthesis of $Sb(2\text{-}Me\text{-}8\text{-}qy)_2Cl$ (13) 165
8.4.18 Synthesis of $Sb(2\text{-}Me\text{-}8\text{-}qy)_3AuCl$ (14) 165
8.4.19 Synthesis of $Sb(4\text{-}py)_3$ (15) 165
8.4.20 Synthesis of $Bi(4\text{-}py)_3$ (16) 166
8.4.21 Synthesis of $PhSn(4\text{-}py)_3$ (17) 167
8.4.22 Synthesis of $\{Ag^I_2(16)_3\}_n(CF_3SO_3)_{2n}$ (18) 167
8.4.23 Synthesis of $\{Ag^I_2(16)_3\}_n(SbF_6)_{2n}$ (19) 167
8.4.24 Synthesis of $\{Ag^I_2(16)_3\}_n(PF_6)_{2n}$ (20) 168
8.4.25 Synthesis of $\{Ag^I(15)\}_n(SbF_6)_n$ (21) 168
8.4.26 Synthesis of $\{Ag^I(17)\}_n(CF_3SO_3)_n$ (22) 168
8.4.27 Synthesis of $\{Ag^I(B)\}_n(CF_3SO_3)_n$ (23) 169
8.4.28 Synthesis of $\{Cu(16)(MeCN)\}_n(PF_6)_n$ (24) 169
8.4.29 Synthesis of $(\{Cu(16)_2\}\{Cu(16\text{-}SiF_5)\})_n(PF_6)_n$ (25) 169

8.4.30 Synthesis of [TfO.S.{AgOTf(THF)}{Ag(THF)$_3$}] (26) 170
8.4.31 Reaction of H with benzyl potassium (28) 170
8.4.32 Synthesis of [(3-py)P(μ-N^{t}Bu)]$_2$ (30) 170
8.4.33 Synthesis of [(3-py)(S)P^V(μ-N^{t}Bu)]$_2$ (32) 171
8.4.34 Attempted Oxidation of 30 with selenium (33) 171
8.4.35 Synthesis of [(3-py)(Se)P^V(μ-N^{t}Bu)]$_2$ (34) 172
8.4.36 Reaction of 30 with n-butyllithium 172
8.4.37 Reaction of 30 with benzyl potassium 173
8.4.38 Reaction of 30 with methyl iodide 173
8.4.39 Reaction of 30 with [(p-cymene)RuCl$_2$]$_2$ 173
8.4.40 Reaction of 30 with hydrogen peroxide 173

8.5 Infrared Spectroscopy (Chapter 4) 174

8.6 Crystal Data and Refinements for Single-Crystal X-ray Structures 177

9. References 183

1

1. Introduction

1.1 The Advancement of Main Group Chemistry

Over the past half a century, the field of main group chemistry has flourished, a phenomenon that can be largely ascribed to the increasing demand for cheaper, more Earth-abundant (and in some cases more benign) alternatives to transition metals. Power's seminal review in *Science* highlighted inherent differences between lighter and heavier main group elements, and indicated how low oxidation state heavier main group metals bear distinct similarities to transition metals (possessing vacant acceptor and filled donor metal orbitals which can function in synergic bonding).[3] This observation has opened up a new field of main group activation and catalysis which now promises to parallel that of classical organo-transition metal chemistry. Over a decade on, the renaissance in main group chemistry has continued, from the pioneering work of Stephan in Frustrated Lewis Pair chemistry (FLPs)[4] and Hill's calcium-mediated nucleophilic addition reactions of benzene,[5] to Hevia, Mulvey and co-workers' work on organolithiums[6,7] and trans-metal trapping.[8] Harder's very recent "dinitrogen-catching" calcium complex has the potential to move this area forward to a new dimension of small-molecule activation using main group elements.[9] Such landmark discoveries prove that the area is still advancing and thriving, painting a brighter future than could ever have been anticipated for main group chemistry and its applications in today's society. Despite such success, multiple areas of this field are still largely unexplored and unfamiliar, and one of these areas (which is the focus of much of this thesis) is the behaviour of main group-based ligand systems and their supramolecular chemistry.

1.2 Tripodal Ligands

The development of new classes of ligands is an important and ongoing challenge in modern chemistry, and a cornerstone in advances in catalysis, supramolecular assembly, and biomimetic chemistry. Of the many new classes of ligands that have been introduced, C_3-symmetric tripodal ligands have emerged over the past few decades, particularly as one of the most important classes in catalysis.[10–16] A myriad of examples of these ligands exist in the literature, with applications in homogeneous catalysis, coordination chemistry and chiral recognition. By definition, tripodal ligands are polydentate (most commonly tridentate), facially-coordinating C_3-symmetric ligands, which are known to possess remarkable potential in coordination, organometallic and bioinorganic chemistry, catalysis, and also as chiral reporter reagents.[17] In terms of their structural characteristics, tridentate C_3-symmetric ligands

comprise a central non-donor atom attached to three side groups, each of which contains at least one donor atom (Figure 1.1). Tetradentate C_3-symmetric ligands can also exist, possessing an additional donor atom at the bridgehead position. Specifically, tripodal ligands enforce a facial binding to an octahedral or tetrahedral transition metal centre, providing a high degree of stereochemical control and highly stable complexes due to the chelate effect. Such ligands are also less conformationally flexible than many others - namely acyclic/macrocyclic ligands - and typically possess a single bonding mode to metals, rendering them much more rigid.

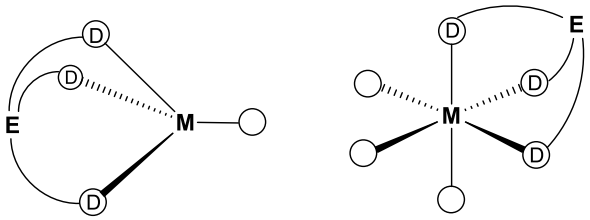

Figure 1.1: Facial coordination of a tripodal ligand to tetrahedral and octahedral transition metal centres, E = non-donor bridging unit, D = donor site.

The incorporation of substituents into the donor arms of tripodal ligands means that the steric and electronic character of the ligands can be easily modulated to a specific function or to promote, for example, a particular catalytic site.[18] The ability to modify the coordination environment in this way has made tripodal ligands one of the most widely studied classes of ligands, and is a characteristic which is far less common with other classes of ligands, such as macrocycles. The rigidity and tunability of tripodal ligands provide a high degree of spatial, electronic and even stereochemical control over the coordination site and has been used extensively to stabilise metal ions in a variety of oxidation states and geometries. A large number of these ligands contain a range of main group element-based mixed donor sets, such as N, S, O and P donor atoms, each with established donor (hard/soft) functionalities,[19] which have been used to form heterobimetallic complexes (Scheme 1.1).[20,21]

A notable milestone in the development of this field, established by S. Trofimenko in the 1970s, explored a breadth of applications using tris-pyrazolyl- and tris-oxazolinyl-borate "scorpionate" ligands (Figure 1.2a and Figure 1.2b, respectively), from their use as ancillary ligands in homogeneous catalysis, to biomimetic models for enzymatic active sites.[22–25]

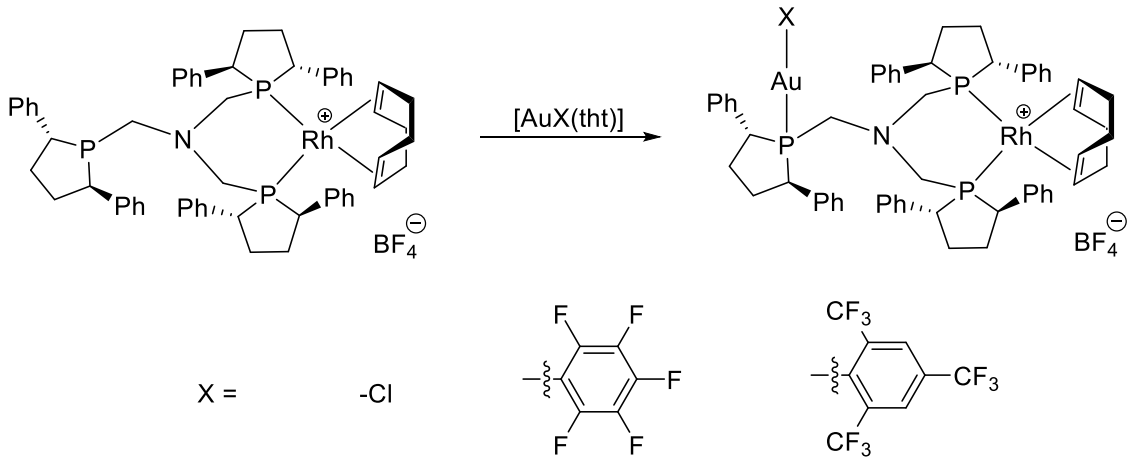

Scheme 1.1: Synthesis of heterodinuclear Rh-Au complexes, known to function as enantioselective hydrogenation catalysts. Coordination of the bulky Au-X led to a significant enhancement of catalytic performance.

The eponymous tris-pyrazolyl-borates provide an exemplary illustration of some of the aforementioned advantages of tripodal ligands. The popularity of these frameworks in modern chemistry can be attributed in large part to their facile synthesis (from pyrazoles and borohydride BH_4^-) and strong donor ability, which is found to be similar to that of cyclopentadienyl, Cp^-.[23]

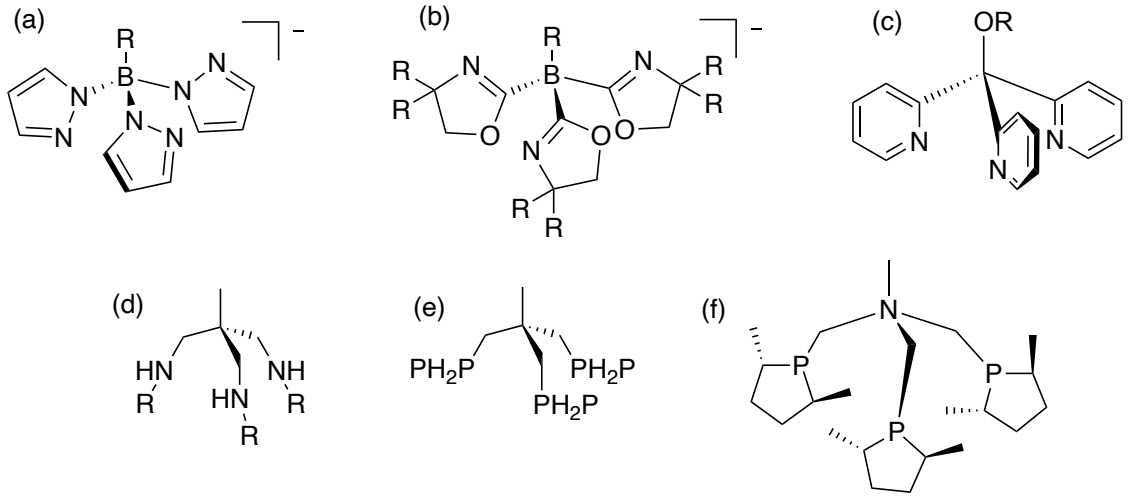

Figure 1.2: Notable examples of tripodal ligands featuring a range of bridgeheads and donor groups; (a) tris-pyrazolyl-borate, (b) tris-oxazolinyl-borate, (c) tris-2-pyridyl-alkoxymethane, (d) aliphatic triamine, (e) triphos and (f) N-bridged-phospholane ligands.

A further important class of tripodal ligands that has been introduced are tris-2-pyridyl ligands, such as the tris-2-pyridyl-alkoxymethane ligand framework (Figure 1.2c). The shear breadth of donor functionality of contemporary tripodal ligands is also illustrated by the remaining examples of Figure 1.2, such as the aliphatic triamine ligand framework (Figure 1.2d) with acyclic and cyclic topologies.[26,27] In addition to amine-based ligands, a variety of C_3-symmetric tripodal phosphine frameworks have also been synthesised, with studies showing that triphos ligands (Figure 1.2e) are particularly useful for a variety of bridgehead atoms (C, N, P)[28,29] with regards to their application as auxiliary ligands in single-site catalysis. Tripodal, tetradentate phosphine ligand complexes with base metals such as Fe and Co have revealed outstanding activity in (among others reactions) dehydrogenation/hydrogenation of CO_2-based fuels and reduction of N_2.[30–33] In addition to this research, M. J. Burk and co-workers have successfully synthesised metal complexes of enantiomerically-pure tripodal phosphines (Figure 1.2f), which are known to exhibit high activity in asymmetric catalytic hydrogenation reactions, providing access to a variety of diverse chiral compounds.[34–37]

This thesis largely concerns synthetic and structural studies of tris- and bis-pyridyl ligands and in the next section the state-of-the-art in the area will be discussed in detail.

1.3 Tripodal Ligands Containing Pyridine Rings

1.3.1 Tris-2-Pyridyl Ligands

Pyridyl donor sets have attracted significant attention over recent years as a basis for novel tripodal ligands. Tris-2-pyridyl ligands containing non-metallic bridgeheads, $E(2\text{-py})_3$, (2-py = 2-pyridyl, E = bridgehead atom/group such as CX (X = H, OR, NH_2), N, P, P=O, (Figure 1.3)) are an important family of tripodal ligands that have been studied extensively over the past three decades. They are closely-related to tris-pyrazolyl-borates $[RB(1\text{-pz})_3]^-$ (1-pz = pyrazolyl, R = H, alkyl, aryl, NR_2, Sar) and tris-oxazolinyl-borates, although all of these earlier examples are neutral rather than anionic.[38,13]

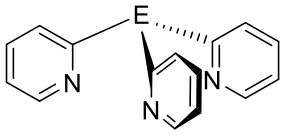

Figure 1.3: General framework of neutral tris-2-pyridyl tripodal ligand family E(2-py)$_3$, containing either non-metallic or metallic main group bridgehead atoms/groups, E.

The primary difference between these tris-2-pyridyl ligands and tris-pyrazolyl/oxazolinyl-borates is the charge of the systems: while the majority of tris-pyridyl frameworks are neutral (with a few metallic and semi-metallic pyridyl ligands providing rare exceptions), tris-pyrazolyl-borates are all monoanionic. Further to this, it has been reported that 2-pyridyl-based systems act as better π-acidic ligands than pyrazole-containing ligands,[39] as well as being better σ-donors (p*K*a values of conjugate acids, BH^+ of pyrazole is 2.48, while that of pyridine is 5.25).[26]

Though not the first Group 13 pyridyl 'ate systems to be reported, the neutral, benchtop-stable species 4-^{t}Bu(C$_6$H$_4$)B(2-py)$_2$(H-2-py) (Scheme 1.2), a tris-2-pyridyl-borate precursor, was first synthesised in 2012 by Jäkle and co-workers who reacted an arylboron dibromide with pre-isolated 2-pyridyl Grignard reagent [Mg$_2$(2-py)$_2$Cl$_2$(THF)$_3$].[40] Access to this ligand enabled coordination studies with transition metal ions (Mg^{2+}, Fe^{2+}, Mn^{2+}, Co^{2+}, Cu^{2+}, Ru^{2+}), with ^{t}Bu(C$_6$H$_4$)B(2-py)$_3^-$ acting as a facially coordinating tridentate ligand in sandwich complexes.

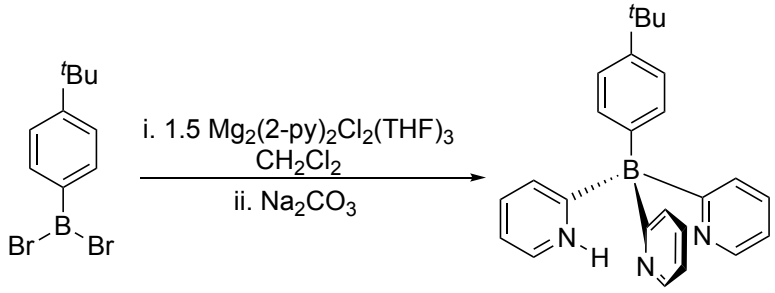

Scheme 1.2: Synthesis of the tris-2-pyridyl-borate ligand, 4-^{t}Bu(C$_6$H$_4$)B(2-py)$_2$(H-2-py).

For the case of [Fe{(^{t}Bu(C$_6$H$_4$))B(2-py)$_3$}$_2$] (Figure 1.4), bond length analysis and spectroscopic measurements indicated Fe(II) to be low spin, suggesting that the borate anion 4-^{t}Bu(C$_6$H$_4$)B(2-py)$_3^-$ possesses strong σ-donor characteristics. Other functionalised borates with alternative substituents to *tert*-butyl (I, Me$_3$Si-) have also been explored.[41]

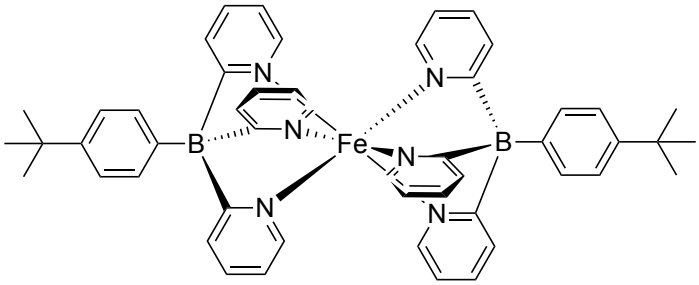

Figure 1.4: Structure of Fe(II) complex [Fe{(^{t}Bu(C$_6$H$_4$))B(2-py)$_3$}$_2$], from the reaction of the tris-2-pyridyl-borate ligand with $FeCl_2$ in a THF/MeOH mixture in the presence of NEt_3.

Closely related tris-2-pyridyl-aluminium(III) ligands have been the subject of intensive study since their inception in 2004.[42] The lower electronegativity of aluminium compared to boron imparts greater ionic character to Al–C bonds, which in turn has a marked impact on the reactivity of these aluminates. Wright and co-workers have successfully prepared the series of tris-2-pyridyl-aluminates [RAl(2-py)$_3$]$^-$ (R = Me, Et, ^{n}Bu, *sec*-Bu, Figure 1.5) via the reaction of the *in situ* generated 2-lithiopyridine with $RAlCl_2$.[43–49]

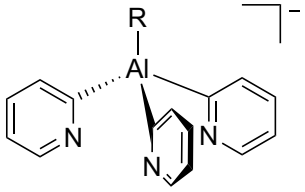

Figure 1.5: The anionic tris-2-pyridyl-aluminate ligand [RAl(2-py)$_3$]$^-$ (R = Me, Et, ^{t}Bu, *sec*-Bu).

The anionic nature and chemical robustness of both the tris-2-pyridyl-borate and -aluminate ligands paved way to extensive coordination chemistry. A notable example in the tris-2-pyridyl-aluminate field comprises the formation of the Fe- and Mn-heterobimetallic compounds, shown in Scheme 1.3a. Combination of [Li(THF){MeAl(2-py)$_3$}] with either $FeCl_2$ or $MnCp_2$ resulted in intact transfer of the aluminate ligand to form the sandwich complexes [M{MeAl(2-py)$_3$}$_2$], (M = Fe, Mn). The paramagnetic nature of these complexes is confirmed by ^{1}H NMR spectroscopic and magnetic measurements, as well as bond length analysis in their crystal structures which indicate both are high-spin.[47] Interestingly, Fe complexes with the aforementioned tris-2-pyridyl-borate ligand (Figure 1.4) were shown to be low-spin.[40] The catalytic activity of the complex [Fe{MeAl(2-py)$_3$}$_2$] has been examined in the

epoxidation of styrene, and it proved to be a selective epoxidation catalyst at modest reaction temperatures, producing 96.5% of the epoxide. Most uniquely, this reaction can be accomplished in dry air without the addition of an oxidising agent – a major environmental and cost-saving advantage (Scheme 1.3b).[47]

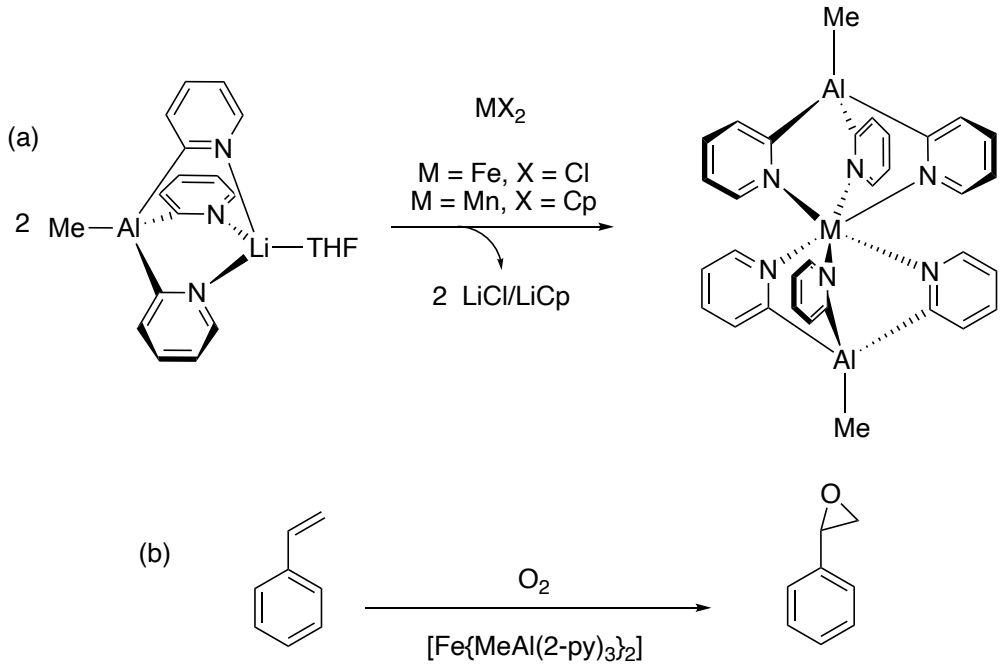

Scheme 1.3: a) Reaction of [Li(THF){MeAl(2-py)$_3$}] with $FeCl_2$ or $MnCp_2$ (1:1 or 1:2 equivalents) forming heterobimetallic compounds [Fe{MeAl(2-py)$_3$}$_2$] and [Mn{MeAl(2-py)$_3$}$_2$], and (b) use of [Fe{MeAl(2-py)$_3$}$_2$] as a catalyst in the epoxidation of styrene.

Further reactions of [Li(THF){MeAl(2-py)$_3$}] with other *s*- and *d*-block metals were met with variable success.[50] Reactions with CaI_2 or $ZnCl_2$ resulted in the formation of sandwich and half-sandwich complexes, giving [Ca{MeAl(2-py)$_3$}$_2$] and [MeAl(2-py)$_3$ZnCl], respectively, with the latter being obtained in lower yield, ostensibly due to its higher solubility. The reaction of the same aluminate ligand with Mo(C_7H_8)(CO)$_3$ yielded the trimetallic complex [(THF)$_3$Li(μ-CO)Mo(CO)$_2${MeAl(2-py)$_3$}] with a Mo(CO)$_3$ moiety capped by an N,N,N-chelating [MeAl(2-py)$_3$]$^-$ ligand and terminated by a Li(THF)$_3^+$ fragment (Scheme 1.4).

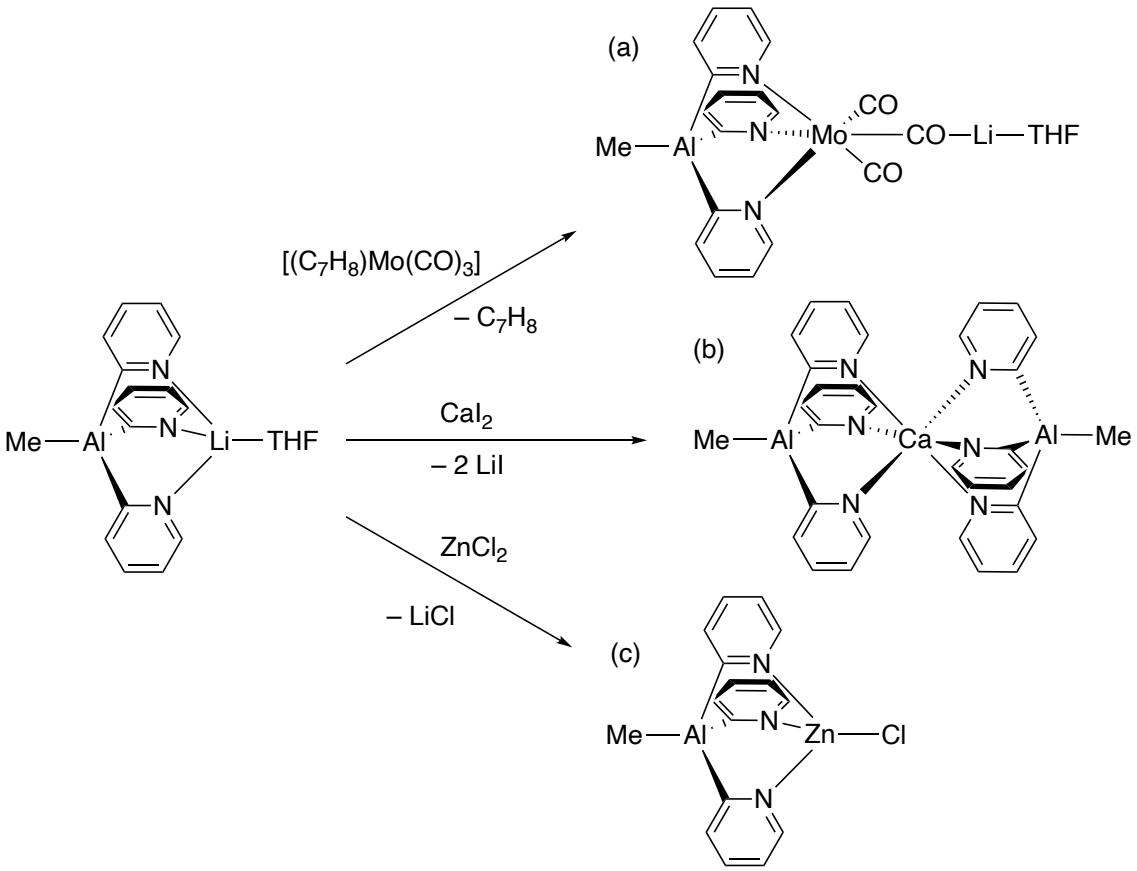

Scheme 1.4: Reactions of [Li(THF)MeAl(2-py)$_3$] with (a) Mo(C_7H_8)$(CO)_3$, (b) CaI_2 and (c) $ZnCl_2$.

The success of producing heavier homologues of tris-2-pyridyl Group 13 ligands has been varied. Comproportionation of $InCl_3$ and Me_3In to $MeInCl_2$, proceeded by reaction with 2-Li-py resulted in decomposition, whereas the one-pot reaction of ^{n}BuLi and $InCl_3$ followed by reaction of 2-Li-py yielded the indate complex [Li(THF){^{n}BuIn(2-py)$_3$}] (Scheme 1.5a and b). X-ray crystallography reveals that the complex is isostructural with [Li(THF){MeAl(2-py)$_3$}]$^–$. A similar route was found not to produce the corresponding gallate compound, due to reductive decomposition depositing elemental gallium (gallium complexes have since been accessed by alternative routes). Further to this, decomposition also occurred when indate [Li(THF){^{n}BuIn(2-py)$_3$}] was reacted with $FeBr_2$ or $MnCp_2$. Further analysis of both aluminate and indate Mo complexes by IR spectroscopy indicated that the bridgehead atom has little effect on the donor/acceptor properties of the pyridyl ligands. Moreover, the difference in bond lengths between the Al–C and In–C (ca. 0.2 Å) is the cause of the increase in ligand bite moving from [MeAl(2-py)$_3$]$^–$ to [^{n}BuIn(2-py)$_3$]$^–$.[50]

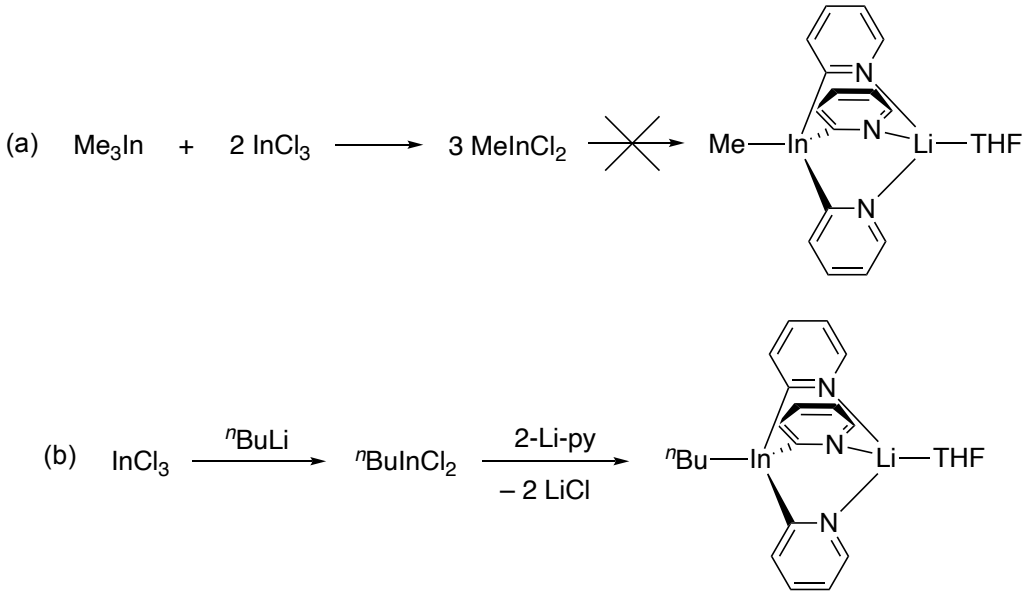

Scheme 1.5: (a) Unsuccessful *in situ* preparation of $MeInCl_2$ followed by reaction with 2-Li-py due to instability of products, and (b) sequential reaction of $InCl_3$ with ^{n}BuLi and 2-Li-py, proving to be successful.

In order to access a more extensive range of ligands $[RAl(2\text{-py}')]^{-}$ (R = alkyl, 2-py′ = substituted 2-pyridyl) that permit variation of the R-group and the substitution pattern of the 2-pyridyl moiety, a more general route to pyridyl-aluminates was adopted since many of the precursors $RAlCl_2$ are not commercially available (Scheme 1.6).[51]

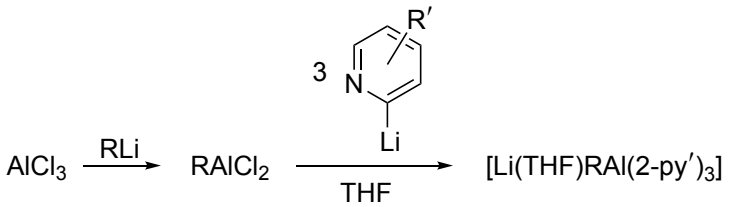

Scheme 1.6: A general route to lithium tris-2-pyridyl-aluminates.

This enabled R = Et, ^{n}Bu, ^{s}Bu and ^{t}Bu bridgehead substituents to be introduced into pyridyl-aluminates, which seemingly do not cause major structural distortions in the resulting lithium complexes. On the contrary, it was found that substitution of the 2-pyridyl groups has a far more marked influence of bite angle, as seen in the structurally characterised complexes

[Li(THF)$_3$(μ-X)Li{MeAl(3-Me-2-py)$_3$}] (X = Cl, Br), [Li(THF){MeAl(5-Me-2-py)$_3$}] and [Li(THF){MeAl(6-Me-2-py)$_3$}]. In particular, Me-substitution at the 3-position of the pyridyl ring units results in reduced ligand bite angle due to steric interaction with the bridgehead Me-Al group, whilst the bite angle of the aluminate in [Li(THF){MeAl(5-Me-2-py)$_3$}] is largely similar to that of the un-substituted aluminate anion in [Li(THF){MeAl(2-py)$_3$}]. However, in the case of [Li(THF){MeAl(6-Me-2-py)$_3$}] a distorted tetrahedral coordination environment for the Li-centre results from the steric congestion of the Me-groups at the coordination site of the aluminate which produces a twist of one of the pyridyl moieties by ca. 24º away from the sterically crowded site.[51]

Consequently, more extensive studies of 2-pyridyl-aluminate complexes containing Ca^{2+}, Fe^{2+} and Mn^{2+} have been explored, with variation of both the bridgehead atom and substitution patterns of the 2-pyridyl ring units. Evaluation of the Fe–N bond lengths in sandwich complexes [Fe{(MeAl(2-py′)$_3$}$_2$] suggested spin-crossover between 180 K and 298 K for Fe(II).[45] Reaction of [Li(THF){EtAl(6-Me-2-py)}$_3$] with $MnCl_2$ gives [{EtAl(6-Me-2-py)$_3$}Mn(μ-Cl)Li{(6-Me-2-py)$_3$AlEt}] (Scheme 1.7). as opposed to a sandwich complex, presumably due to the avoidance of unfavourable steric interactions between the pyridyl 6-Me substituents of the aluminate ligand, which is tolerated in the corresponding sandwich complex with Ca, owing to its larger ionic radius (Ca^{2+} 1.14 Å, Mn^{2+} 0.97 Å) (hence, Ca^{2+} forms a sandwich complex). Isolation of the aforementioned Mn complex [{EtAl(6-Me-2-py)$_3$}Mn(μ-Cl)Li{(6-Me-2-py)$_3$AlEt}] further suggests that halide-bridged (M–X–Li) bimetallic complexes of this type could be transmetallation intermediates, along the way to sandwich complexes.

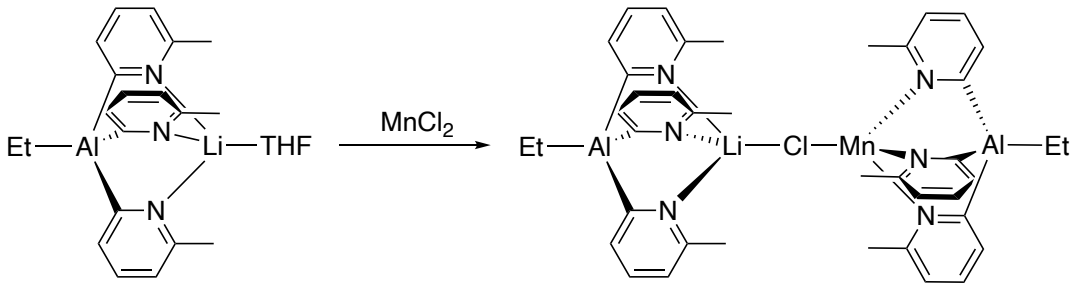

Scheme 1.7: Synthesis of [{EtAl(6-Me-2-py)$_3$}Mn(μ-Cl)Li{(6-Me-2-py)$_3$AlEt}], showing an exception to the formation of sandwich complexes as seen previously with tris-2-pyridyl-aluminate ligands.

Apart from their ability to function as ligands, it has also been shown that tris-2-pyridyl-aluminates can act as soft 2-pyridyl transfer reagents. This was first observed in the reaction of the lithiated [Li(THF){MeAl(2-py)$_3$}] with CuCl which gave the trimeric Cu(I) complex [{Cu(2-py)}$_3$]$_\infty$, the trimeric unit of which is shown in Figure 1.6.[42]

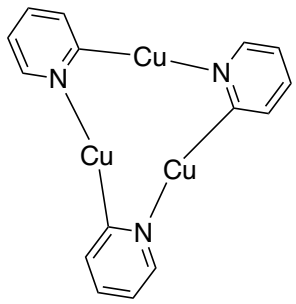

Figure 1.6: Trimeric ring monomer unit from [{Cu(2-py)}$_3$]$_\infty$.

Association of the trimeric macrocyclic units via Cu···Cu interactions form stacks to yield [{Cu(2-py)}$_3$]$_\infty$. A related result has also been found in the case of the reaction of [Li(THF){EtAl(2-py)$_3$}] with $SnCl_2$,[52] which gives the Janus head ligand [(6-Me-2-py)$_3$Sn]$_2$, featuring an Sn–Sn bond (Scheme 1.8a), the structure of which was confirmed by X-ray crystallography.

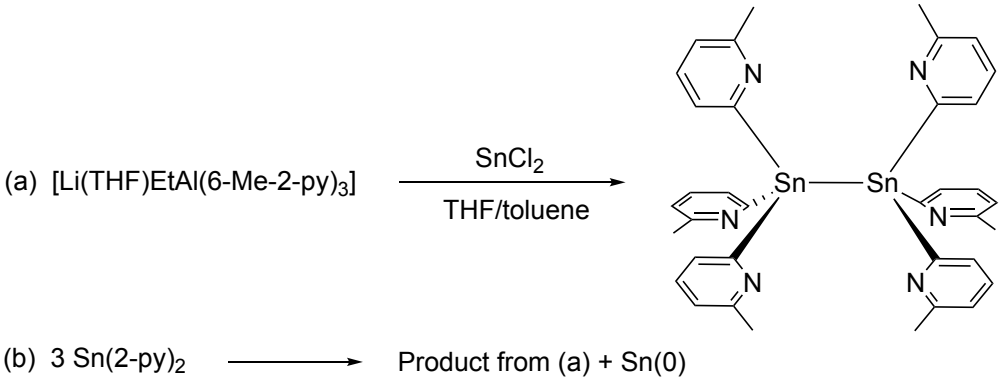

Scheme 1.8: (a) Synthesis of [(6-Me-2-py)$_3$Sn]$_2$ and (b) likely disproportionation pathway leading to its formation.

Further information regarding the mechanism by which ligand $[Sn(6\text{-}Me\text{-}2\text{-}py)_3]_2$ was formed was provided by *in situ* NMR spectroscopy: reaction of $[Li(THF)\{EtAl(2\text{-}py)_3\}]$ with $SnCl_2$ at room temperature revealed rapid formation of the Janus head Sn ligand, and concomitant production of $[AlCl_4]^-$ (alongside other species) but crucially *not* including bipyridine [(6-Me-2-py)$_2$]. Taking into further consideration the observation from a larger scale reaction of the formation of a black metallic precipitate, disproportionation of Sn(II) to Sn(0) and Sn(IV) is the most likely scenario (see Scheme 1.8b). From the reaction of $[Li(THF)\{MeAl(2\text{-}py)\}_3]$ with $SnCl_2$, the intermediate $[\{Cl_2(2\text{-}py)_2Sn\}Al\{Sn(2\text{-}py)_3\}]$ (Figure 1.7) can be isolated, containing an Al(III) centre coordinated by two Sn(II)-centred anions, $[SnCl_2(2\text{-}py)]^{2-}$ and $[Sn(2\text{-}py)_3]^-$.

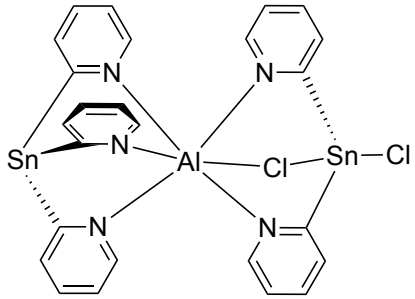

Figure 1.7: Structure of $[\{Cl_2(2\text{-}py)_2Sn\}Al\{Sn(2\text{-}py)_3\}]$.

Evidence of the strong steric influence of substitution at the 6-position of the pyridyl ring units on the donor properties of aluminate ligands is apparent from structural and reactivity studies of lithium aluminates $[Li(THF)\{EtAl(6\text{-}R\text{-}2\text{-}py)_3\}]^-$ (R = Me, Br, CF_3).[44] In contrast to the unsubstituted $[Li(THF)\{MeAl(2\text{-}py)_3\}]$, $[Li(THF)\{EtAl(6\text{-}Me\text{-}2\text{-}py)_3\}]$ loses THF when heated under vacuum, forming the monomer $[Li\{EtAl(6\text{-}Me\text{-}2\text{-}py)_3\}]$ in which the Li^+ cation has a (trigonal) pyramidal geometry. Alternatively, $[Li(THF)\{MeAl(2\text{-}py)_3\}]$ dimerises upon loss of THF to form $[Li\{MeAl(2\text{-}py)_3\}]_2$ (Scheme 1.9). Furthermore, both $[Li\{EtAl(6\text{-}Br\text{-}2\text{-}py)_3\}]$ and $[Li\{EtAl(6\text{-}CF_3\text{-}2\text{-}py)_3\}]$ crystallize as unsolvated monomers, even when etherate solvent was used.

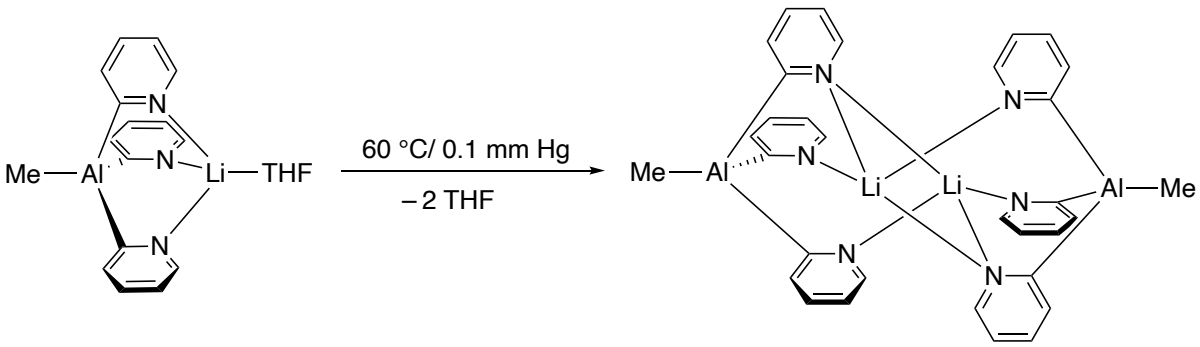

Scheme 1.9: Desolvation of [Li(THF){MeAl(2-py)$_3$}], producing the dimer [Li{MeAl(2-py)$_3$}]$_2$.

All of the ligands [EtAl(6-R-2-py)$_3$]$^-$ (R = Me, Br, CF$_3$) did not form sandwich compounds with Fe(II). This again can be rationalised by the steric effect of the 6-Me groups, which would be brought together in a sandwich structure. Nonetheless they are useful as precursors in controlled hydrolysis (alcoholysis) reactions, in which novel functionalised aluminates were produced (Scheme 1.10).[53–55] Such selective alcoholysis proved to be even more interesting if a chiral alcohol was used. The reaction of [Li{EtAl(6-Me-2-py)$_3$}], with chiral alcohols generates diastereotopic dimers. The magnetic inequivalence of the 6-Me groups of these dimers allows detection and measurement of the relative amount of *R* and *S* enantiomers in racemic mixtures (allowing measurement of the enantiomeric excess). The replacement of one or more of the 2-py groups in these aluminates with alkoxide groups (in anions of the type [RAl(2-py)$_2$(OR´)]$^-$ and [RAl(2-py)(OR´)$_2$]$^-$) can also result in interesting supramolecular chemistry.[54]

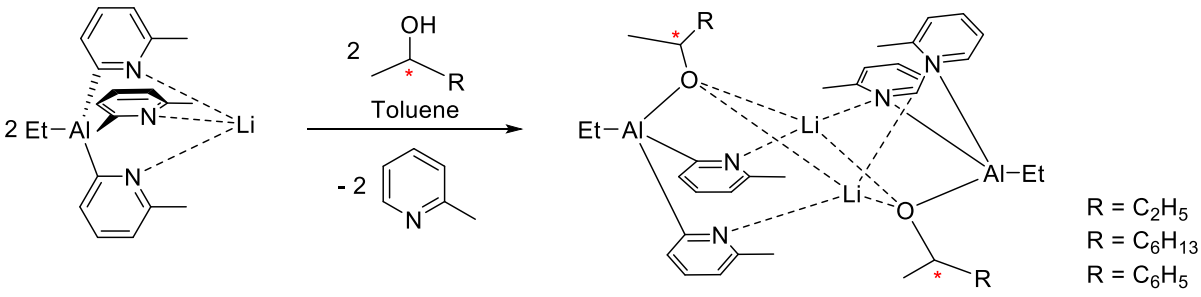

Scheme 1.10: Reactivity of [Li{EtAl(6-Me-2-py)$_3$}] towards chiral alcohols.

Tris-2-pyridyl-aluminate ligands can also stabilise lanthanide(II) ions, particularly where 6-susbstitution of the pyridyl groups is present (since this provides steric encasement of the metal environment).[46] The sandwich complexes with both $[EtAl(6\text{-}Me\text{-}2\text{-}py)_3]^-$ and $[EtAl(6\text{-}Br\text{-}2\text{-}py)_3]^-$ as the ligands can be obtained from the reactions of the lithium complexes with EuI_2 and YbI_2 (Scheme 1.11). Interestingly, using $[EtAl(6\text{-}CF_3\text{-}2\text{-}py)_3]^-$ no coordination of the lanthanides was observed, as it is too weak a donor. The observed weaker coordinative properties of both $[EtAl(6\text{-}Br\text{-}2\text{-}py)_3]^-$ and $[EtAl(6\text{-}CF_3\text{-}2\text{-}py)_3]^-$ towards lanthanoid ions compared to the 6-Me anion is likely due to the steric bulk and electron-withdrawing properties of Br and CF_3 substituents.

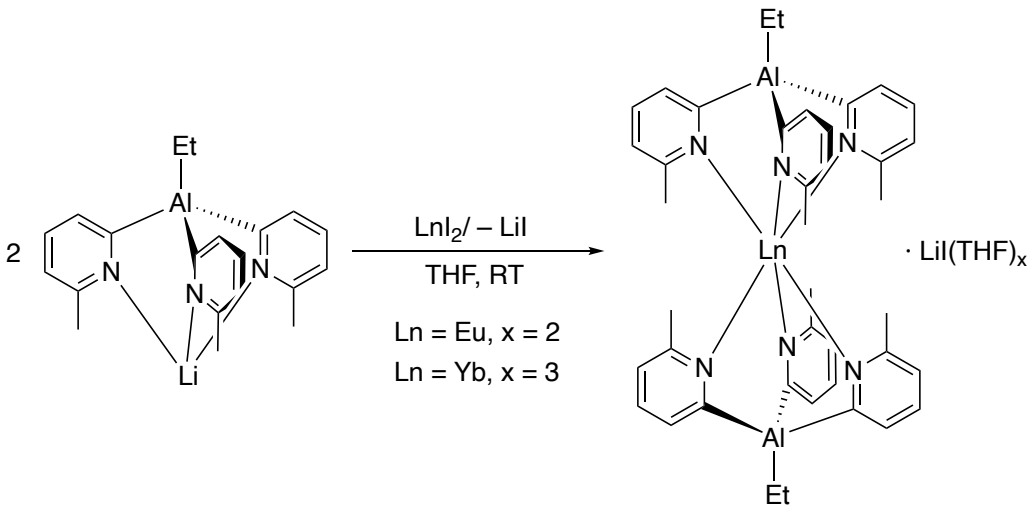

Scheme 1.11: Preparation of tris-2-pyridyl-aluminate lanthanide sandwich complexes as $LiI(THF)_x$ co-complexes.

In the case of the Yb(II) complexes, which are f^{14} diamagnetic species, the solution dynamics could be followed by NMR spectroscopy. $[Yb\{EtAl(6\text{-}Me\text{-}2\text{-}py)_3\}_2]$ was unaffected by the addition of LiI in THF solvent, whilst the bromo-substituted $[Yb\{EtAl(6\text{-}Br\text{-}2\text{-}py)_3\}_2]$ showed dynamic behaviour upon addition of LiI. These observations pointed towards ligand exchange to give putative half-sandwich complex $[YbI(THF)_2\{EtAl(6\text{-}Br\text{-}2\text{-}py)_3\}]$ and $[Li\{EtAl(6\text{-}Br\text{-}2\text{-}py)_3\}]$ upon complete addition of one equivalent of LiI (Scheme 1.12). Further to this, treatment of $[Yb\{EtAl(6\text{-}Me\text{-}2\text{-}py)_3\}_2]$ with $[Li\{EtAl(6\text{-}Me\text{-}2\text{-}py)_3\}]$ did not lead to detectable ligand exchange by 2D NMR spectroscopy, whereas a mixture of $[Yb\{EtAl(6\text{-}Br\text{-}2\text{-}py)_3\}_2]$ and $[Li\{EtAl(6\text{-}Br\text{-}2\text{-}py)_3\}]$ was shown to exchange components, and when LiI was added to the mixture, $[YbI\{EtAl(6\text{-}Br\text{-}2\text{-}py)_3\}]$ was observed. In addition, a 1:1 mixture of $[Yb\{EtAl(6\text{-}Br\text{-}2\text{-}py)_3\}_2]$ and $[Yb\{EtAl(6\text{-}Me\text{-}2\text{-}py)_3\}_2]$ led to ligand exchange of $[EtAl(6\text{-}Me\text{-}2\text{-}py)_3]^-$ and

$[EtAl\{(6\text{-}Br\text{-}2\text{-}py)_3\}]^-$ and when $[Yb\{EtAl(6\text{-}Br\text{-}2\text{-}py)_3\}_2]$ was combined with $[Li\{EtAl(6\text{-}Me\text{-}2\text{-}py)_3\}]$, ligand exchange produced the heteroleptic complex $[Yb\{EtAl(6\text{-}Me\text{-}2\text{-}py)_3\}\{EtAl(6\text{-}Br\text{-}2\text{-}py)_3\}]$. These results show how the electron-withdrawing character of the group at the 6-position can have a large effect on the donor character.[46]

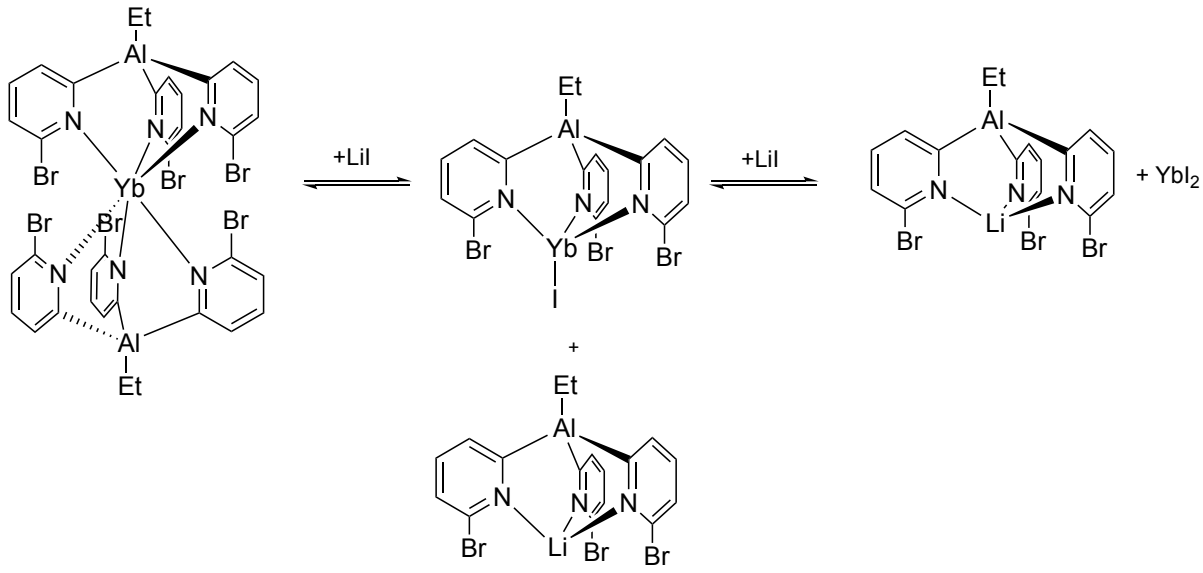

Scheme 1.12: Series of equilibria involved in Yb/Li exchange.

As noted previously, tris-2-pyridyl ligands containing indium have also been reported. However, the major synthetic difficulty in preparing these is instability of the (+III) oxidation state metals in the presence of strongly reducing 2-lithiopyridines. Zeckert showed that, like the transfer of 2-pyridyl groups from an aluminate to $SnCl_2$ noted previously for the Janus head compound $[Sn(6\text{-}Me\text{-}2\text{-}py)_3]_2$[52], tris-2-pyridyl-stannates and -plumbates are useful transfer reagents in this area. Decomposition of tris-2-pyridyl-stannate–MEt_3 adducts in the presence of $SmCp^*_2(OEt_2)$ gave $[SmCp_2(5\text{-}Me\text{-}2\text{-}py)_2MEt_2]$(M = Ga, In) containing the bis-2-pyridyl anions $[MEt_2(5\text{-}Me\text{-}2\text{-}py)_2]^-$ (Scheme 1.13).[56]

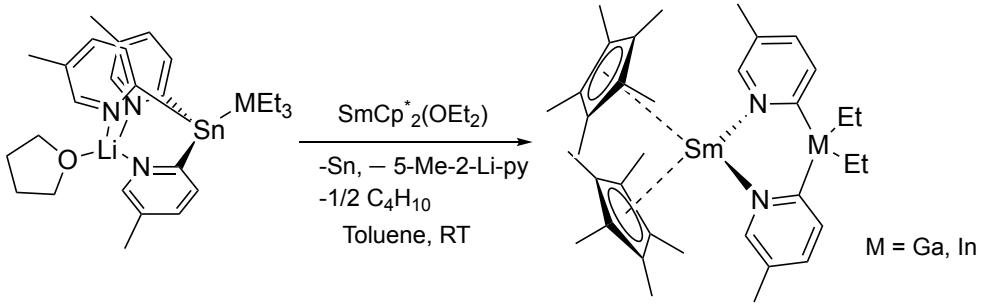

Scheme 1.13: Production of $[SmCp_2(5\text{-Me-2-py})_2MEt_2]$, (M = Ga, In) accompanied by elimination of Sn.

This Group 14-to-Group 13 2-pyridyl transfer process has been extended to a range of other Ga and In species, using reactions based on the facile degradation of a lithium plumbate $[LiPb\{(6\text{-}^tBuO\text{-}2\text{-}py)_3\}]$.[57] Scheme 1.14 shows the reaction of the aforementioned complex with GaR_3 to form dimeric $[LiR_2Ga(6\text{-}^tBuO\text{-}2\text{-}py)_2]_2$ (R = Et) and monomeric $[Li(THF)R_2Ga\{(6\text{-}^tBuO\text{-}2\text{-}py)_2\}]$, (R = ^{i}Pr and ^{t}Bu).

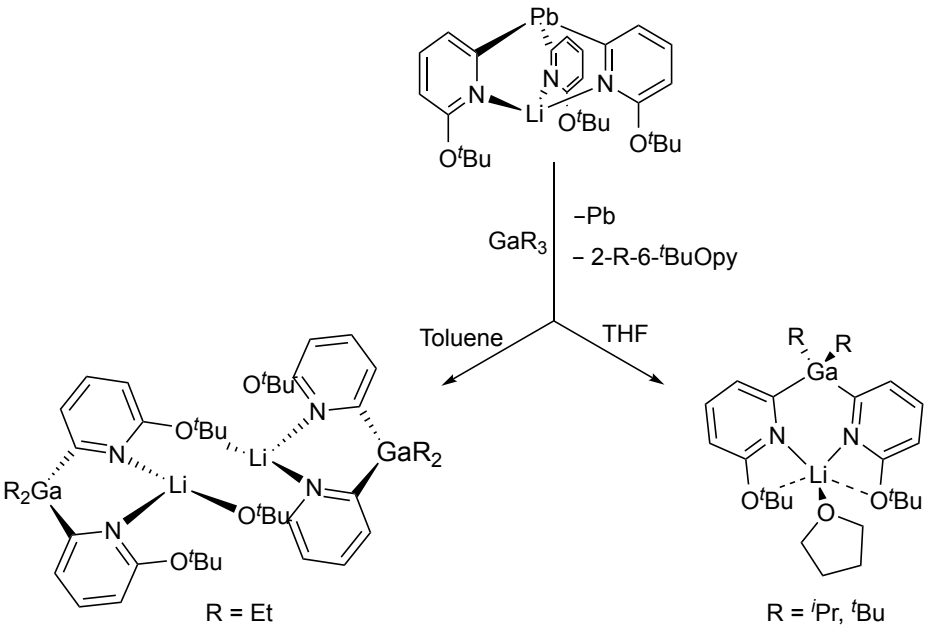

Scheme 1.14: Synthesis of the gallate complexes $[LiR_2Ga(6\text{-}^tBuO\text{-}2\text{-}py)_2]_2$ (R = Et) and $[Li(THF)R_2Ga(6\text{-}^tBuO\text{-}2\text{-}py)_2]$, (R = ^{i}Pr and ^{t}Bu).

Similar reactions with InR_3 (R = Me, Et) afforded the tris-2-pyridyl-indates (Scheme 1.15a). This study highlighted the importance of both the steric properties of the bridgehead substituent in directing the outcome of 2-pyridyl transfer to Ga or In and the involvement of redox processes.[57]

Further to this, the reaction of InI with the previously mentioned lithium plumbate [LiPb(6-^{t}BuO-2-py)$_3$] yielded the tris-2-pyridyl-indate [Li(THF)(I)In(6-^{t}BuO-2-py)$_3$] (Scheme 1.15b).

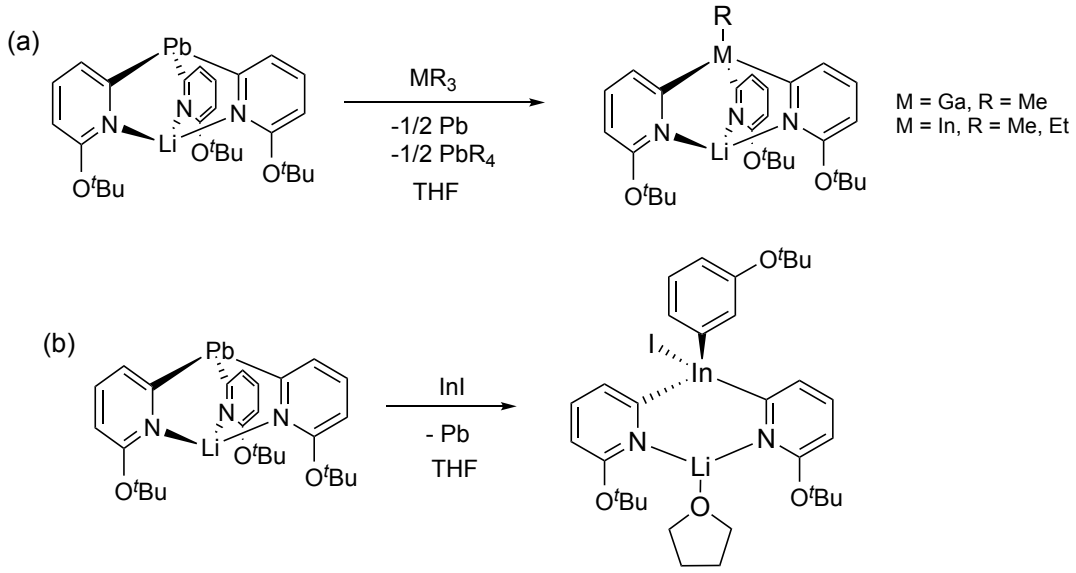

Scheme 1.15: (a) Formation of tris-pyridyl-gallates and -indates and (b) formation of a lithium tris-2-pyridyl-indate.

Turning to Group 14, the first carbon-bridged tris-2-pyridyl ligand, (OH)C(2-py)$_3$, was developed by J. P. Wibaut and co-workers in 1951, using the reaction between a dipyridyl ketone and 2-lithiopyridine (Scheme 1.16).[58]

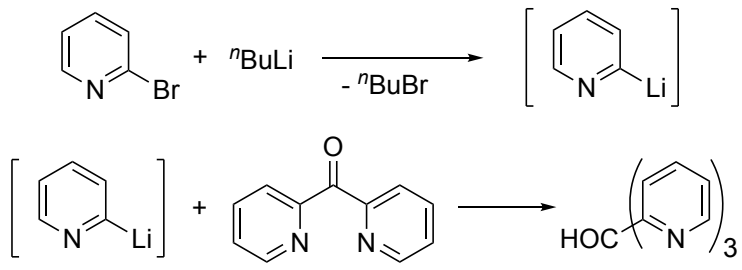

Scheme 1.16: Synthesis of tris-2-pyridyl-methanol.

Since then, D. L. White and J. W. Faller successfully prepared a variety of tris-2-pyridyl-methanol derivatives, namely tris-2-pyridyl-methane (H)C(2-py)$_3$, tris-2-pyridyl-chloromethane (Cl)C(2-py)$_3$ and tris-2-pyridyl-ethoxymethane (OEt)C(2-py)$_3$.[59] In addition, it was realised that changing substituents on the bridgehead carbon led to variation in properties such as solubility, coordination modes and overall charge. A chiral analogue of the tris-2-pyridyl-methanol ligand was prepared in 1992 by H. Adolfsson et al., by incorporating a chiral substituent at the 6-position of the pyridine.[60]

In contrast to the extensive studies of the carbon bridgehead, the chemistry of tris-2-pyridyl ligands containing heavier Group 14 congeners as the bridgeheads is explored to a much lesser extent. The incorporation of metallic or semi-metallic Group 14 bridgehead atoms, Si to Pb (and other main group elements such as Al (discussed previously) and Bi) has been employed as a strategy for the synthesis of a range of heterometallic complexes,[42,61] which are generated simply by the coordination of another metal ion. Tris-2-pyridyl ligands based on the heavier Group 14 elements in the +IV oxidation state are shown in Figure 1.8.

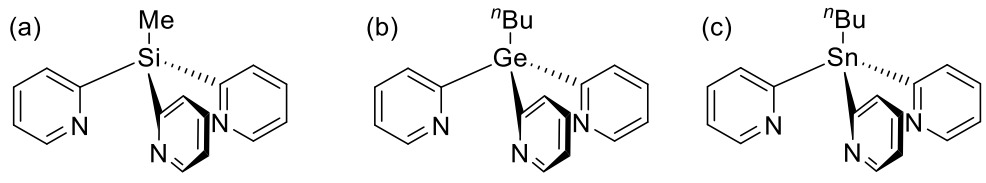

Figure 1.8: Group 14 tris-2-pyridyl ligands in which the bridgehead is in the +IV oxidation state, (a) MeSi(2-py)$_3$, (b) ^{n}BuGe(2-py)$_3$, (c) ^{n}BuSn(2-py)$_3$.

Like the previously discussed Group 13 tris-2-pyridyl ligands, the neutral Group 14 ligands are facially bonding, tridentate ligands, which commonly form sandwich and half-sandwich complexes with transition metals.[43,62,63,64] Their general preparation involves the *in-situ* generation of 2-lithiopyridine, followed by reactions with chloro-precursors such as $^{n}BuSnCl_3$ and $MeSiCl_3$. The first structurally-characterised tris-2-pyridyl-silane, $MeSi(2\text{-py})_3$ (Figure 1.8a), was reported by Wright and Hopkins using the reaction of 2-Li-py (generated through Br/Li exchange) with $MeSiCl_3$ at low temperature (Scheme 1.17).[65]

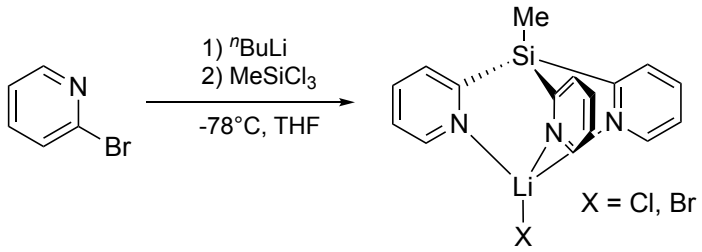

Scheme 1.17: Synthesis of tris-pyridyl-silane ligand, $MeSi(2\text{-py})_3$.

Compared to the heavier Sn analogues (discussed later) the silane ligand $MeSi(2\text{-py})_3$ is more compact, primarily on account of the shorter bridgehead C–Si bonds. Whilst NMR spectroscopy confirmed the formation of $MeSi(2\text{-py})_3$ in the reaction, X-ray crystallography revealed that it complexes the lithium salt by-products (LiCl/LiBr). The lithium halides proved difficult to remove and this limited the applications of the ligand in coordination studies, which were complicated by the incorporation of Li^+ into products. An alternative route to other Group 14 tris-2-pyridyl ligands involves the one-pot reaction of $SiCl_4$ or $GeCl_4$ sequentially with $^{n}BuLi$ and then 2-Li-py (producing $^{n}BuSi(2\text{-py})_3$ and $^{n}BuGe(2\text{-py})_3$, respectively).[43] However, the yields of the tris-2-pyridyl ligands can be greatly improved by the introduction of a methyl substituent in the 6-position of the pyridyl ring (primarily as a result of the stability of the 2-lithio- intermediate).[66] One such example is $PhSi(6\text{-Me-2-py})_3$, whose coordination chemistry towards metals has been studied extensively (Scheme 1.18).[67] Further advantages of the 6-Me substitution are the increased air-stability of the ligands, and the absence of lithium halide coordination.

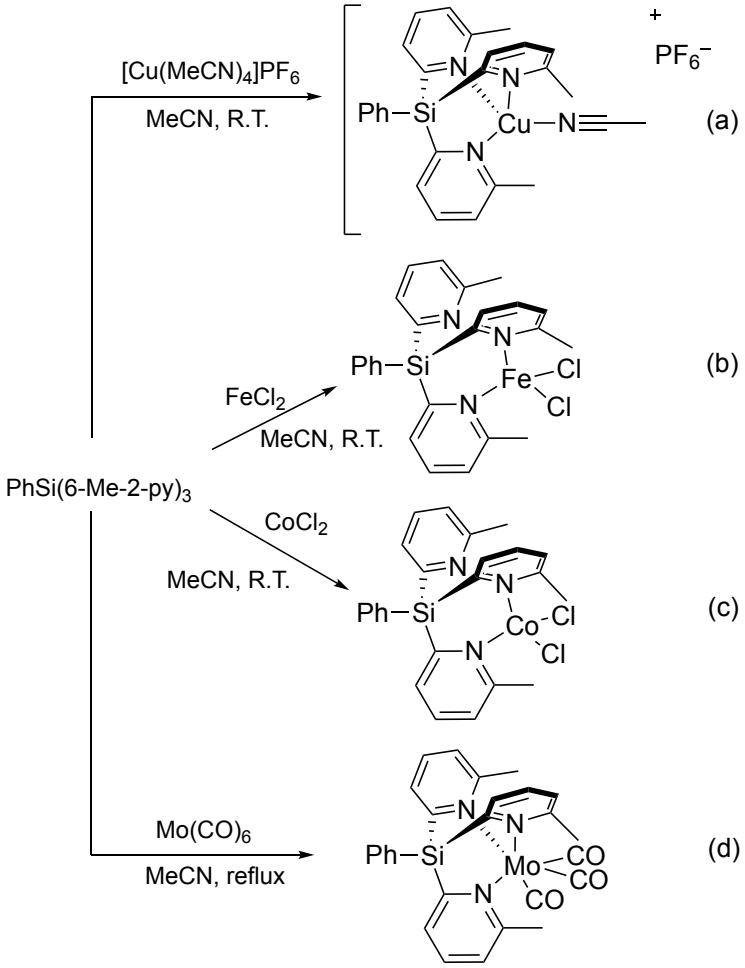

Scheme 1.18: Synthesis of tris-pyridyl-silane-metal complexes with various transition metals.

Upon complexation with transition metals PhSi(6-Me-2-py)$_3$ can behave as a bi- or tridentate ligand. In the case of the complexes [$FeCl_2${PhSi(6-Me-2-py)$_3$}] and [$CoCl_2${PhSn(6-Me-2-py)$_2$}$_3$] (Scheme 1.18b and c) bis-coordination is observed in the solid state and dynamic behaviour is observed by NMR spectroscopy in solution, involving an intramolecular process in which the bis-coordination of the ligand switches between the N-atoms (Scheme 1.19). The adoption of a bis-coordination mode in complexes [$FeCl_2${PhSi(2-py)$_3$}] and [$CoCl_2${PhSn(2-py)$_2$}$_3$] can be partially ascribed to the steric effect of the 6-Me ring substituents combined with the small cation sizes of Fe^{2+} and Co^{2+}.

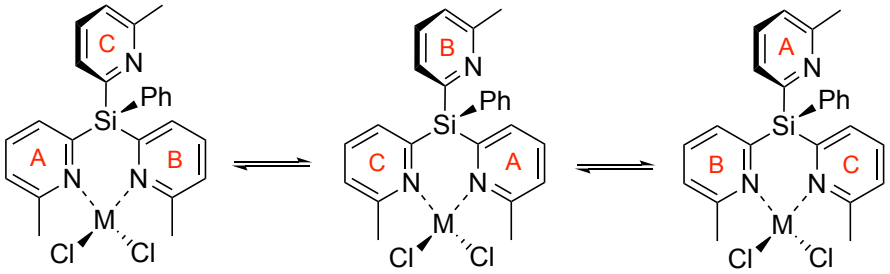

Scheme 1.19: Precession of the pyridyl groups for $[MCl_2\{PhSi(6\text{-}Me\text{-}2\text{-}py)_3\}]$, M = Co, Fe.

The chemistry of the tris-pyridyl Sn and Pb ligands is further enriched by the possibility of adopting the +II or +IV oxidation states of the bridgehead atoms. Specifically in the case of lead, the inert pair effect leads to the large propensity for the +II oxidation state. Although the reaction of $SnCp_2$ with 2-Li-py produces the Sn(IV) ligand $[^nBuSn(2\text{-}py)_3]$, as a result of nucleophilic substitution of the Cp ligands followed by oxidative addition of ^{n}BuBr (which is generated in the initial metal-halogen exchange reaction of ^{n}BuLi with 2-Br-py) (Scheme 1.20a),[62] the corresponding reaction of $PbCp_2$ in THF generates the Pb(II) complex $[Li(THF)\{Pb(2\text{-}py)\}_3]$, containing a $Pb(2\text{-}py)_3^-$ anion (Scheme 1.20b). Whereas $[^nBuSn(2\text{-}py)_3]$ acts as a robust ligand, as is seen in its coordination to a $Mo(CO)_3$ fragment in Scheme 1.21,[64] +II oxidation state ligands like the $Pb(2\text{-}py)_3^-$ anion commonly act as pyridyl transfer reagents.

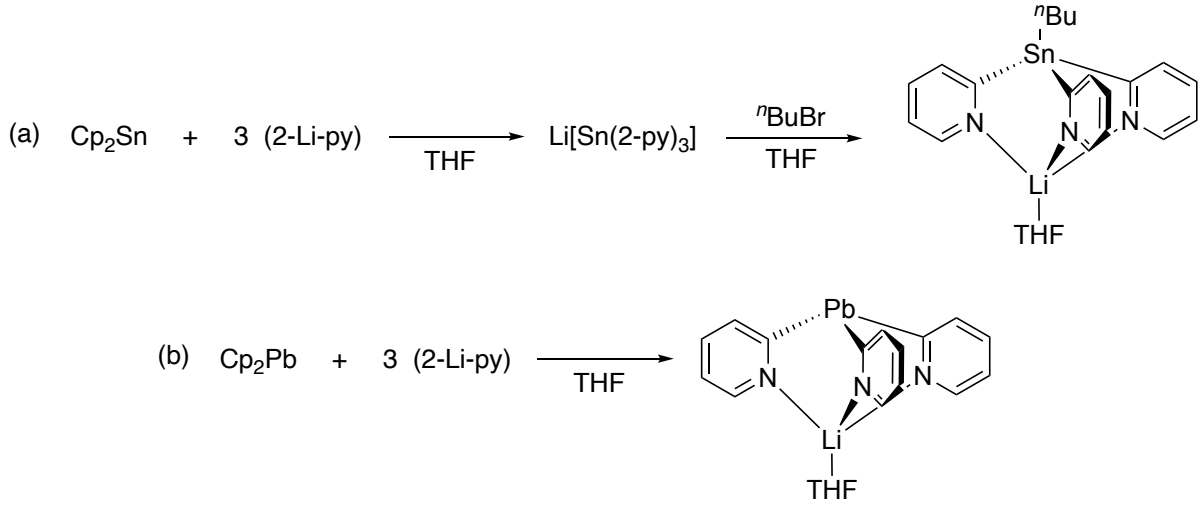

Scheme 1.20: (a) Formation of $[^nBuSn(2\text{-}py)_3LiBr]\cdot 0.5(THF)$, and (b) plumbate $[Li(THF)\{Pb(2\text{-}py)_3\}]^-$

.

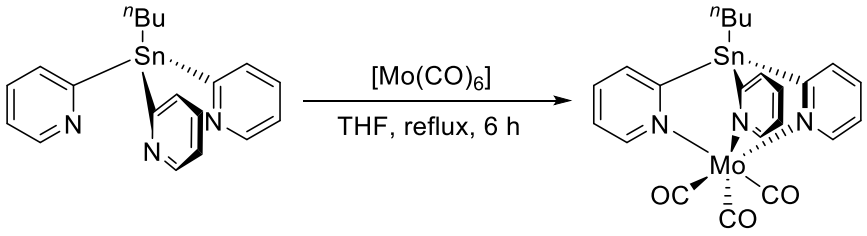

Scheme 1.21: Synthesis of $[Mo(CO)_3\{^nBuSn(2\text{-}py)_3\}]$.

Unlike the Pb(II) anion $[Pb(2\text{-}py)_3]^-$, Zeckert and co-workers showed that the lithium tris-2-pyridyl-stannate $[Li(THF)Sn(5\text{-}Me\text{-}2\text{-}py)_3]$ can be transferred intact onto lanthanide(III) cations.[68] The synthesis of these Sn ligands involves the reaction of 2-bromo-5-methylpyridine with phenyllithium to generate the lithiated intermediate, followed by reaction with $Sn\{N(SiMe_3)_2\}_2$ in THF at –70 °C. Purification of the lithium stannate was possible through recrystallisation from THF after workup, affording crystals sufficient for X-ray analysis.

The reaction of $[Li(THF)\{Sn(5\text{-}Me\text{-}2\text{-}py)\}_3]$ with various trivalent $LnCp_3$ (Ln = La, Yb) (Scheme 1.22a)[69] produced complexes in which the framework of the original lithium stannate is retained and, instead of elimination of LiCp, the product contains a Sn–Ln as a result of a donor interaction of the Sn(II) lone pair with the La^{3+} cation. Interestingly, the further reaction of the Sn(II)/La(III) complex with $YbCp^*_2(OEt_2)$ now leads to the elimination of Cp*Li and the coordination of Yb(II) by the N-atoms of two $[Cp_3La\{Sn(5\text{-}Me\text{-}2\text{-}py)\}_3]^-$ anion units (Scheme 1.22b).[70]

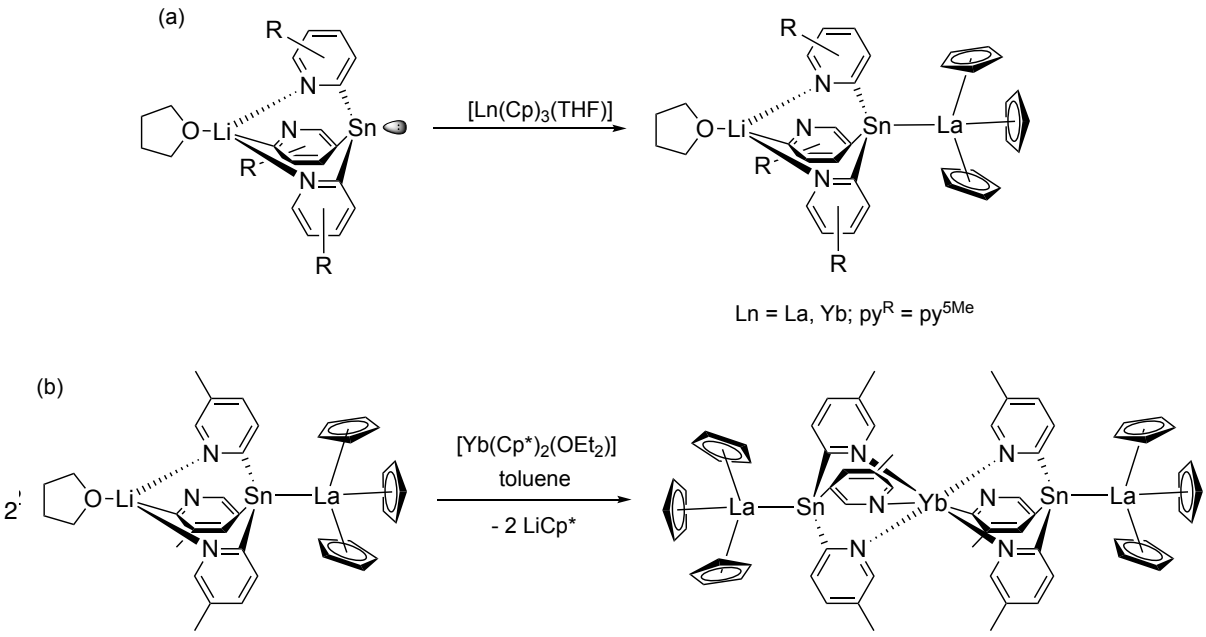

Scheme 1.22: (a) Reactivity of [Li(THF){Sn(5-Me-2-py)$_3$}] towards tris-cyclopentadienyl organolanthanide compounds, and (b) treatment of [Yb(Cp*)$_2$(OEt$_2$)] with 2 eq. of [La(Cp)$_3${Sn(2-py$_5$Me)$_3$Li(THF)}], resulting in LiCp* elimination and the formation of [Yb{Sn(5-Me-2-py)$_3$La(Cp)$_3$}$_2$].

[Li{Sn(5-Me-2-py)$_3$}] also forms Ga–Sn and In–Sn bonded adducts with organo-gallium(III) and indium(III) compounds, using the Sn lone pair (Scheme 1.23).[56] The Ga–Sn and In–Sn bonds are retained in solution but the long metal-metal bonds observed in the solid-state structures suggest that the bonding is weak. Reaction of the sandwich compound [Yb{Sn(5-Me-2-py)$_3$}$_2$] with AlMe$_3$ also yields the Al–Sn bonded adduct [Yb{Sn(5-Me-2-py)$_3$AlMe$_3$}$_2$].[52]

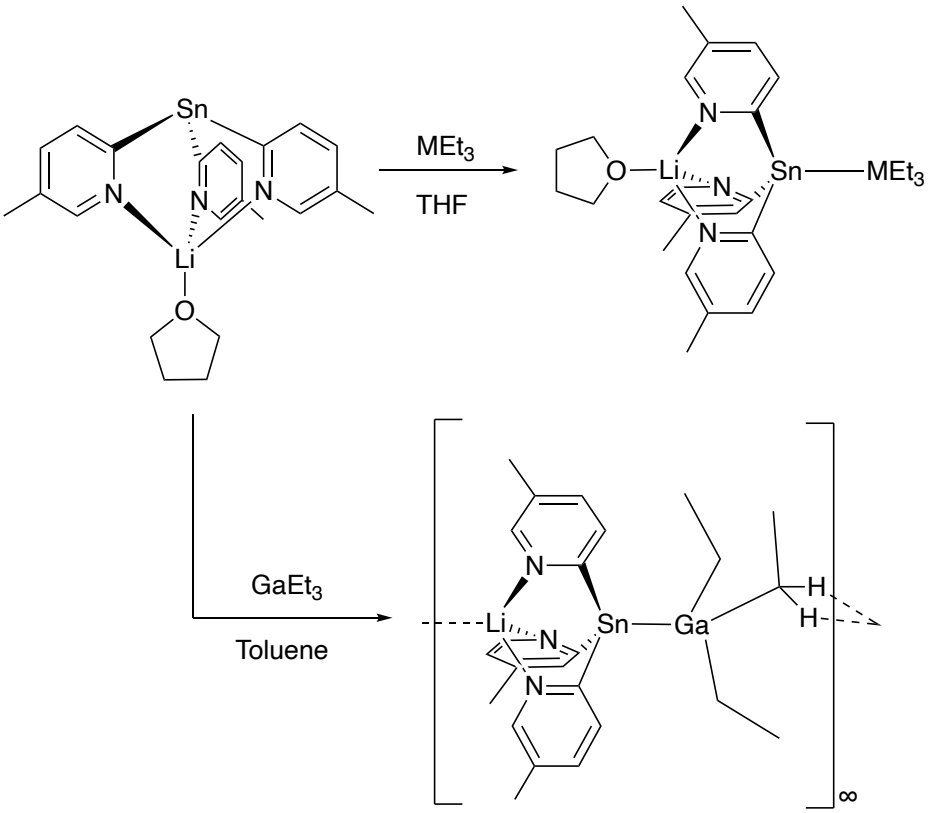

Scheme 1.23: Solvent-dependent synthesis of Sn–Ga/In-bonded adducts. Dashed lines indicate (C–H···Li) interactions, M = Ga, In.

The most intensively studied and widely applied of the tris-2-pyridyl ligand family are those of Group 15. The first of these to be reported was the nitrogen-bridged compound, $N(2\text{-py})_3$, prepared by J. P. Wibaut and G. L. C. la Bastide in 1933. The synthesis involves the sequential condensation of 2-halopyridine with 2-aminopyridine, resulting in a 50% yield (Scheme 1.24).[71]

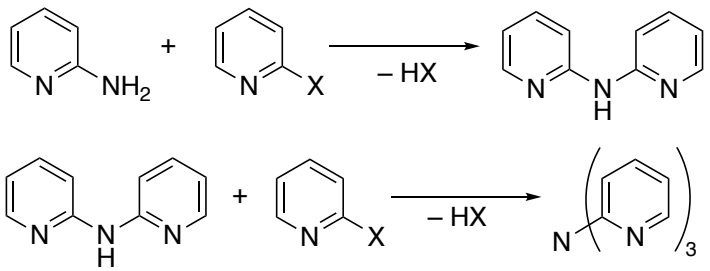

Scheme 1.24: Two-step synthesis of tris-2-pyridyl-amine.

This initial work then led on to the synthesis of the phosphorus-bridged tris-2-pyridyl ligand tris-2-pyridyl-phosphine, $P(2\text{-py})_3$ (along with the phosphine oxide counterpart, $O{=}P(2\text{-py})_3$).[72–75] First synthesised by W. C. Davies and F. G. Mann in 1944, tris-2-pyridyl-phosphine is arguably one of the most well-established of the tris-pyridyl ligands. Part of the interest in this ligand stems from its ability not only to act as a tris-N-donor ligand but also as a P-donor.[76] A large number of bonding modes have been observed for this ligand involving combinations of the available N- and P-donor atoms (e.g., N,N′,N′′-, N,N′,P-). Initial synthetic procedures used in its formation involved the reaction of phosphorus trichloride with the Grignard reagent 2-pyridyl magnesium bromide in benzene, or the reaction of 2-bromo- or 2-iodopyridine derivatives with *n*-butyllithium, affording the 2-lithiated pyridine species, which is then reacted *in situ* with PCl_3 (Scheme 1.25). The tris-2-pyridyl-arsine counterpart can be accessed in a similar manner, through reaction of the 2-lithiopyridine intermediate with arsenic trichloride.

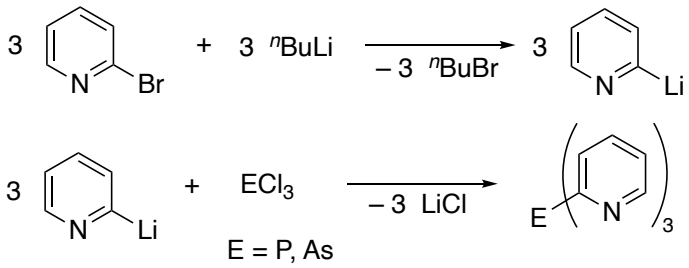

Scheme 1.25: Synthesis of tris-2-pyridyl-phosphine and tris-2-pyridyl-arsine.

A newer approach to $P(2\text{-py})_3$ involves the reaction of 2-bromopyridine with elemental phosphorus (both red and white) in a super-basic $KOH/DMSO(H_2O)$ suspension.[77] The easy access to this ligand which this approach furnishes has now meant that $P(2\text{-py})_3$ is commercially available. Oxidation of $P(2\text{-py})_3$ by H_2O_2 or ^{t}BuOOH affords the oxide, $O{=}P(2\text{-py})_3$.[78,79]

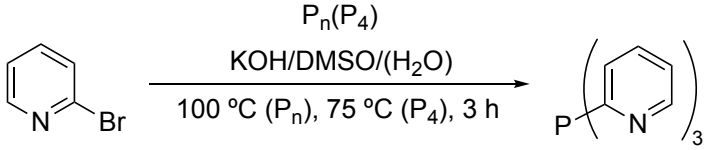

Scheme 1.26: The recent synthesis of the tris-2-pyridyl-phosphine ligand via elemental phosphorus.

The copper complexes of both the As- and P(2-py)$_3$ ligands have been studied for their luminescent properties and for the construction of photoluminescent materials. In the case of the former, [CuI{As(2-py)$_3$}] exhibits tetrahedral geometry at copper with packing effects causing a slight deviation at the halide from the bridgehead···Cu vector. The arsenic ligand also comprises a slightly larger bridgehead bite angle when compared to the phosphorus analogue.[79]

Whilst tris-2-pyridyl ligands of the lighter Group 15 elements have been studied most extensively,[14,63,82–91,72,92–101,73,102–106,74,75,77,79–81] there has been an emerging interest in tris-2-pyridyl ligands which contain heavier (more metallic) Group 15 bridgehead atoms (Sb and Bi, in particular). These advances have been motivated primarily by the potential for new reactivity and ligand behaviour. Until recently, there have been few examples with Sb or Bi as the bridgehead. This is largely because of the tendency for these heavier ligands to reductively eliminate bipyridine, resulting in the generation of elemental Sb or Bi. This was shown in an example by S. Condon and co-workers, which found that the Bi(2-py)$_3$ could not be obtained even from the reaction of BiCl$_3$ with the more stable 2-(ZnBr)-pyridine reagent.[104] However, a recent study by Wright and co-workers presented the successful synthesis of the first examples of this type in the series of ligands E(6-Me-2-py)$_3$ (E = As, Sb, Bi), which were obtained in good yields (64-69%) from the reactions shown in Scheme 1.27.[102] The stability of these ligands can be ascribed to the electron-donating effect of the 6-methyl group, which suppresses reductive elimination. A further factor is that the lithiated 6-Me-2-Li-py is more stable during metathesis than the unsubstituted lithiated 2-Li-py.

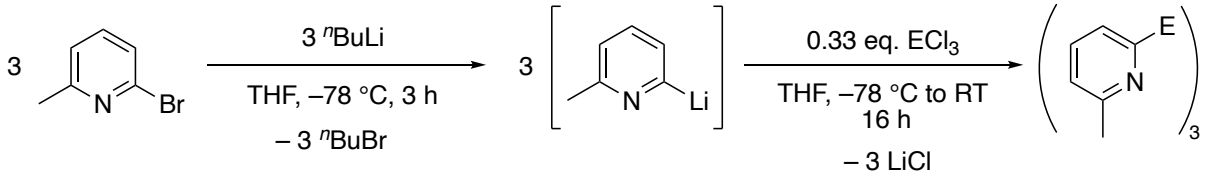

Scheme 1.27: Synthesis of the tris-6-methyl-2-pyridyl Group 15 ligand frameworks E(6-Me-2-py)3, E = As, Sb, Bi.

In the solid state, all of the ligands exhibit a propeller type conformation, with the Me-groups orientated towards the main group bridgehead atom.[63] Upon complexation to Cu(I) (Scheme

1.28) it was found that an increase in the size of the bridgehead as Group 15 is descended only had a minor effect on the Cu(I) geometry, and consequentially the steric environments of the coordination sites of the ligands are similar.

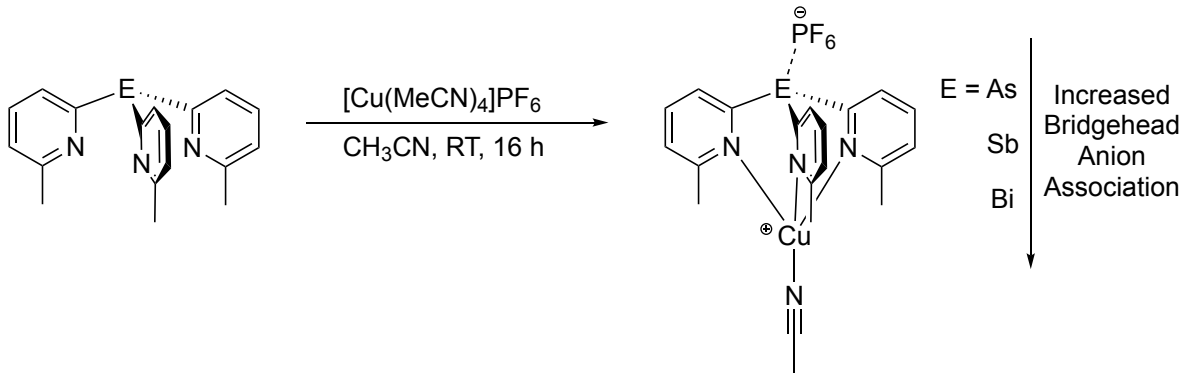

Scheme 1.28: Synthesis and structural trend observed in the solid-state structures of E(6-Me-2-py)$_3$, (E = As, Sb, Bi).

In the solid state structure of the Cu(I) complex with As(6-Me-2py)$_3$ there are no close As···F contacts between the As(III) bridgehead and the PF_6^- counter-anion. However, the Sb and Bi complexes show increasing interactions between the [E(6-Me-2-py)$_3$Cu(MeCN)]$^+$ cation and PF_6^- anion as Group 15 is descended. These bridgehead···anion interactions can have a major effect on structure, as is seen in a further study of the coordination of CuCl using these ligands (Scheme 1.29). As expected, As(6-Me-2-py)$_3$ and Sb(6-Me-2-py)$_3$ form C_3-symmetric arrangements with Cu(I), in the ion-paired complexes [{E(6-Me-2-py)$_3$}CuCl] in which the E(6-Me-2-py)$_3$ ligands have a chelating N,N,N-coordination mode. However, an unprecedented dimeric arrangement is observed for Bi(6-Me-2-py)$_3$, where one of the intramolecular N-Cu bonds to the ligand is broken and replaced by an intermolecular Cu-Cl···Bi interaction (Scheme 1.29, right). Addition of an excess of chloride ions (tetrabutylammonium chloride, TBACl) in MeCN demonstrates the anion-mediated switching of the coordination mode of the Bi(6-Me-2-py)$_3$ ligand from tris-N-donor in the $CuPF_6$ complex to bis-N-donor/Bi-acceptor in the dimer (Scheme 1.29).

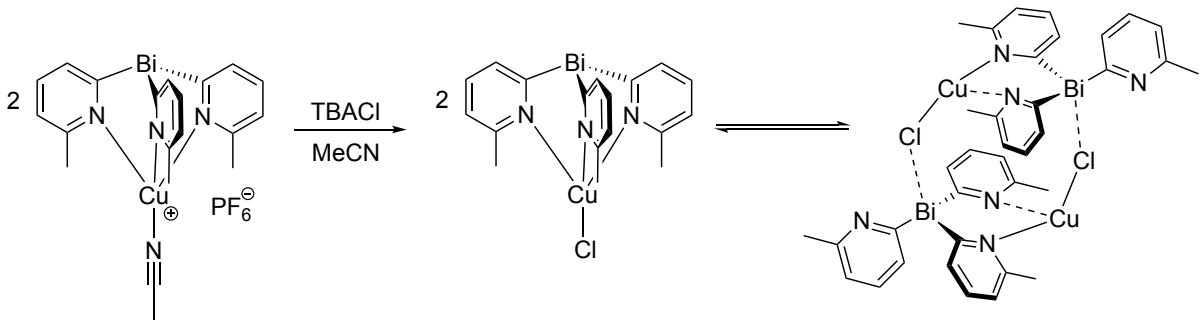

Scheme 1.29: Anion-mediated switching of the coordination mode from [CuCl{Bi(6-Me-2-py)$_3$}] to [CuCl(6-Me-2-py)Bi(6-Me-2-py)$_2$]$_2$ upon addition of Cl^- ions.

The effect of the electronegativity of the bridgehead atom not only has an impact on the Lewis acidity of the bridgehead but also the σ-donor character of the ligands. This is shown by cyclic voltammetry studies of the Cu(I) complexes [E(6-Me-2-py)$_3$Cu(MeCN)]$^+$ PF_6^-, which reveal that there is an increase in the σ-donor character as Group 15 is descended (in line with the greater development of negative charge on the ligands as the electronegativity of the bridgehead decreases). This modulation of σ-donor character can be used to modify the behaviour of catalytic centres.

A more recent study by García-Rodríguez and co-workers has shown that the unsubstituted Bi(2-py)$_3$ ligand can be made using the standard lithiation route, albeit in low yield. Spectroscopic measurements indicated that, where previous ligands containing 6-R-2-py groups do not coordinate LiCl, ligands in which the N-donor atoms are not sterically shielded (3-Me-2-py, 5-Me-2-py or no substituent) are generally better donors and coordinate lithium halides (Scheme 1.30).[103]

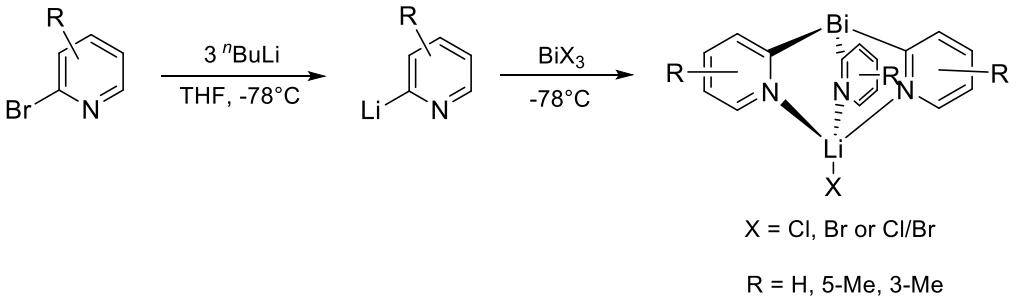

Scheme 1.30: Synthesis of tripodal bismuth ligands, isolated as lithium halide complexes, [Bi(2-py′)$_3$LiX] (X = Cl, Br).

Studies on the coordination of silver salts indicated that 6-Me- and 6-Ph-substituted Bi(2-py′)$_3$ were competent ligands for Ag(I), whereas the presence of more electron-withdrawing groups within the 2-pyridyl rings (Br or CF_3) suppresses coordination as a result of the poor donor properties. Simple complexes containing tripodal coordination of Ag(I) are formed (from $AgPF_6$), as opposed to aggregates, which occurs with P(2-py)$_3$.[81] However, differing stabilities were observed depending on the coinage metal coordinated, with Cu(I) complexes being less thermally stable that those of Ag(I). The prolonged reaction of Bi(6-Me-2-py)$_3$ with [Cu(MeCN)$_4$]BF_4 yielded a mixture of [Cu(Me-bpy)$_2$]BF_4 and [{Bi(6-Me-2-py)$_3$}(MeCN)Cu(Me-bpy)](BF$_4$)$_2$, (Me-bpy = 6,6′-dimethyl-2,2′-bipyridine). This is due to reductive coupling of the 6-Me-2-py substituents and the formation of elemental Bi(0) and/or Cu(0). Replacing $CuBF_4$ with CuCl resulted in much faster coupling to the bipyridine products, suggesting that such coupling reactions are highly dependent upon the anion present. This observation points towards an anion-triggered mechanism involving hypervalent Bi intermediates and is supported by the observation that reactions of $CuCl_2$ with Bi(6-R-2-py)$_3$ (R = Me, CF_3) in MeCN gives Cu(I) complexes containing hypervalent [Bi(6-Me-2-py)$_2$Cl$_2$]$^-$ anions, and the bipyridine coupling products (Scheme 1.31).[107]

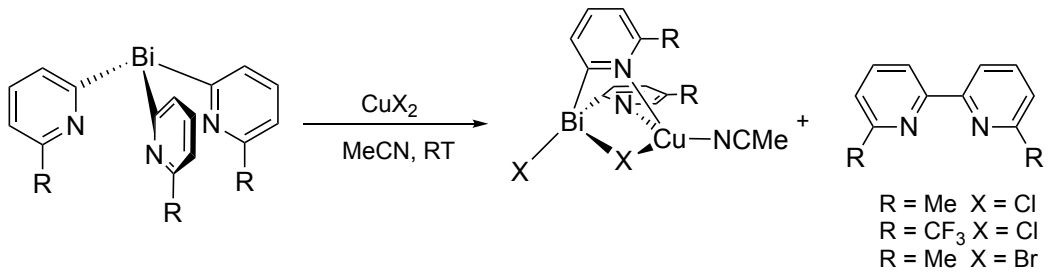

Scheme 1.31: Formation of hypervalent bismuthines and substituted bipyridines.

1.3.2 Tris-3-Pyridyl Ligands

Another way in which the coordination properties of tris-pyridyl ligands can be changed is by varying the position of the N-donor in the pyridyl ring units, and hence the coordination vector. This alteration would be expected to encourage coordination to more than one metal centre. Unlike their tris-2-pyridyl relatives, the facial coordination to a single metal ion is precluded in related tris-3-pyridyl ligands, $E(3\text{-py})_3$, and they are instead expected to behave as tridentate metal-bridging ligands (Figure 1.9).

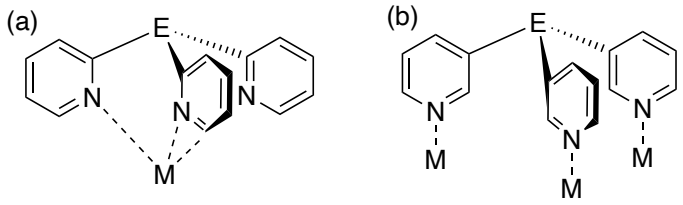

Figure 1.9: Figure showing different coordination behaviour for (a) tris-2-pyridyl ligands (facial) and (b) tris-3-pyridyl ligands (bridging).

In contrast to the tris-2-pyridyl frameworks, reports on the tris-3-pyridyl ligands are significantly less-common, and so far these have seen limited applications. Examples are shown in Figure 1.10.[104,15,108]

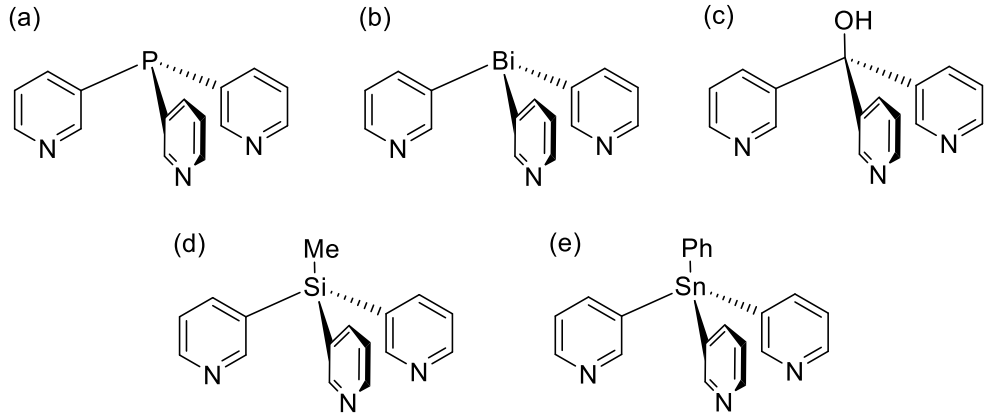

Figure 1.10: Examples of previously-reported tris-3-pyridyl ligands, (a) P(3-py)$_3$, (b) Bi(3-py)$_3$, (c) (OH)C(3-py)$_3$, (d) MeSi(2-py)$_3$ and (e) PhSn(3-py)$_3$.

While there are currently no examples of tris-3-pyridyl ligands of Group 13 elements, García-Rodríguez and co-workers introduced 2-, 3- and 4-(CH_2O)-py groups into the aluminate ligand framework by reactions of [Li(THF){EtAl(6-Me-2-py)}$_3$] as the base with the corresponding alcohols, producing the dimers shown in Scheme 1.32.[54]

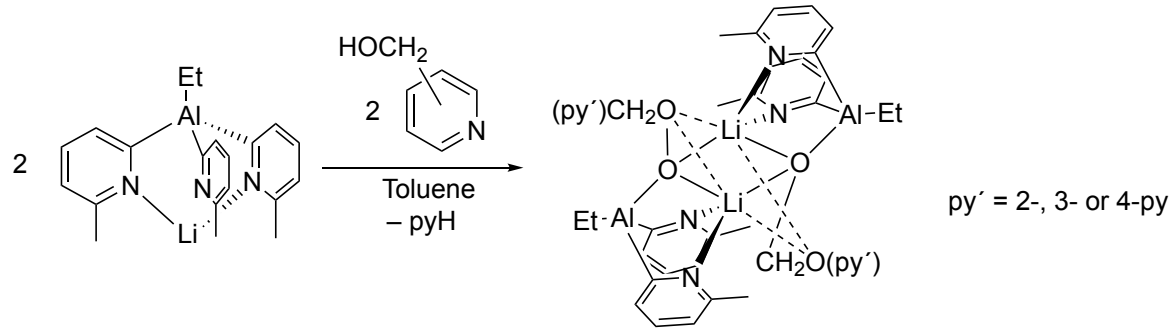

Scheme 1.32: Acid-base reaction of pyridyl alcohols with the aluminate [Li{EtAl(6-Me-2-py)$_3$}].

In the case of the OCH_2(2-py) substitution, the dimer formed is augmented by intramolecular Al···N interactions between the OCH_2(2-py) N-atom and the bridgehead Al centres, giving rise to a distorted trigonal bipyramidal coordination environment for Al(III). Such secondary interactions are not present, however, for neither the 3- nor 4-pyridyl structure analogues. Interestingly, the 2:1 reaction of $HOCH_2$-4-py with [Li(THF){EtAl(6-Me-2-py)$_3$}] resulted in

the polymer $[EtAl(6\text{-}Me\text{-}2\text{-}py)(py\text{-}2\text{-}CH_2O)_2Li]_\infty$. in which the dimer units are associated via intermolecular Al···N interactions.

Tris-3-pyridyl ligands have been explored to a greater extent in Group 14. The first examples of carbon-based tris-3-pyridyl ligands were reported by J. P. Wibaut and co-workers in the 1950s.[58,109] Tris-3-pyridyl-methanol, $(OH)C(3\text{-}py)_3$, (Figure 1.11) was synthesised in a manner identical to that of its 2-pyridyl analogue, in a reaction between a dipyridyl ketone and the corresponding (3)-lithiopyridine (see Scheme 1.16, previously).

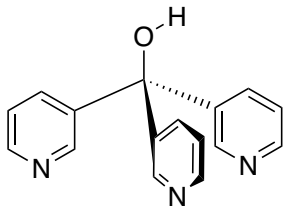

Figure 1.11: Structure of tris-3-pyridyl-methanol.

Tris-3-pyridyl-silane ligands have gained attention in recent years in the field of supramolecular chemistry, with applications found in the production of luminescent materials and construction of supramolecular clusters. R. Boomishankar and co-workers reported the synthesis of $MeSi(3\text{-}py)_3$ and its quinolyl analogue $MeSi(3\text{-}qy)_3$ (qy = quinolyl) and their reactions with CuI to give MOF structures containing stoichiometry-dependent $[CuI]_n$ nodes.[15] The syntheses of these ligands involves the lithiation of the relevant 3-Br-py/qy, followed by the addition of $MeSiCl_3$ and purification using column chromatography. The 3:1 reaction of CuI and $MeSi(3\text{-}py)_3$ produced a 2D MOF, with the tris-3-pyridyl ligands bridging between Cu_6I_6 clusters (Scheme 1.33). Crystallography reveals 2D topologies best described as hexagonal sheets containing Cu_6I_6 clusters linked by the silane ligands and showing inter-sheet π-interactions. Interestingly, other silane:CuI ratios gave 1D MOFs, containing Cu_2I_2 or CuI motifs and conversion between the 2D and 1D-type MOFs could be achieved by addition of ligand or CuI under appropriate conditions.

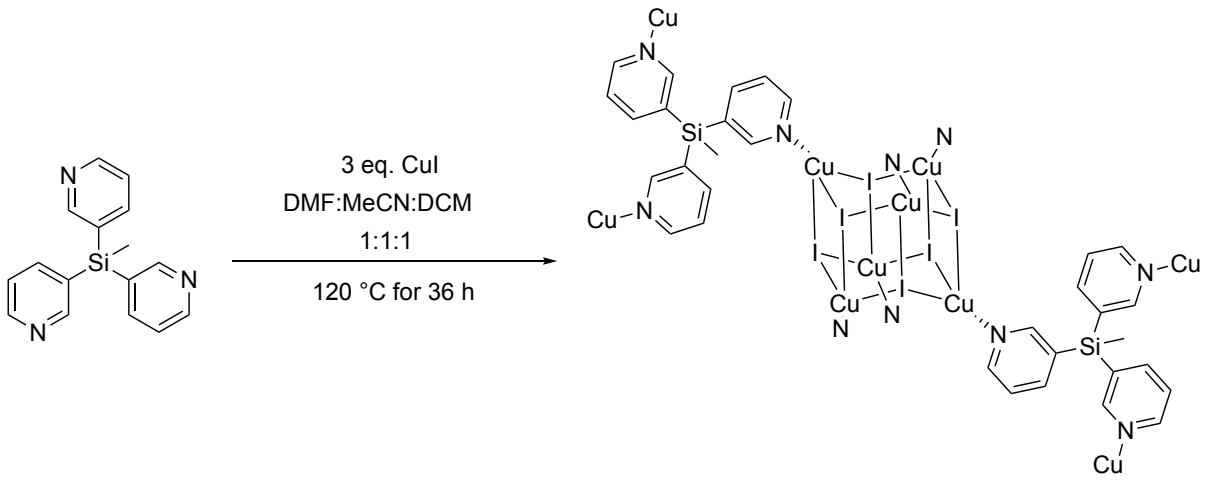

Scheme 1.33: Reaction scheme showing the formation of a 2D MOF with CuI and $MeSi(3\text{-py})_3$.

Further to this, tris-3-pyridyl-silane $MeSi(3\text{-py})_3$ forms a discrete octahedral supramolecular coordination cage with $CoCl_2$, lending itself to applications as a photocatalyst for water splitting and further demonstrating the utility of tris-3-pyridyl ligands in supramolecular coordination chemistry (Scheme 1.34).[110]

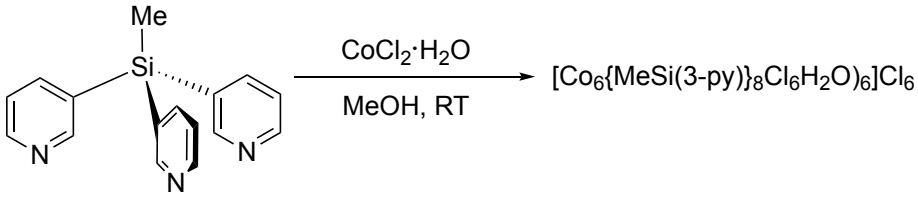

Scheme 1.34: Synthesis of the M_6L_8 cage $[Co_6\{MeSi(3\text{-py})\}_8Cl_6H_2O)_6]Cl_6$.

The solid-state structure of the Co complex $[Co_6\{MeSi(3\text{-py})\}_8Cl_6H_2O)_6]Cl_6$ revealed a cage of six Co(II) ions arranged in an octahedron (Figure 1.12). Each ion is coordinated by four N-donor atoms of tris-3-pyridyl ligands and by internally and externally coordinating Cl and H_2O ligands. Crucially, the nanocage structure of metal ions obtained make it impenetrable to guest molecules, further ensuring the cage's integrity in aqueous media, all owing to the rigidity of the tris-3-pyridyl-silane linkers.

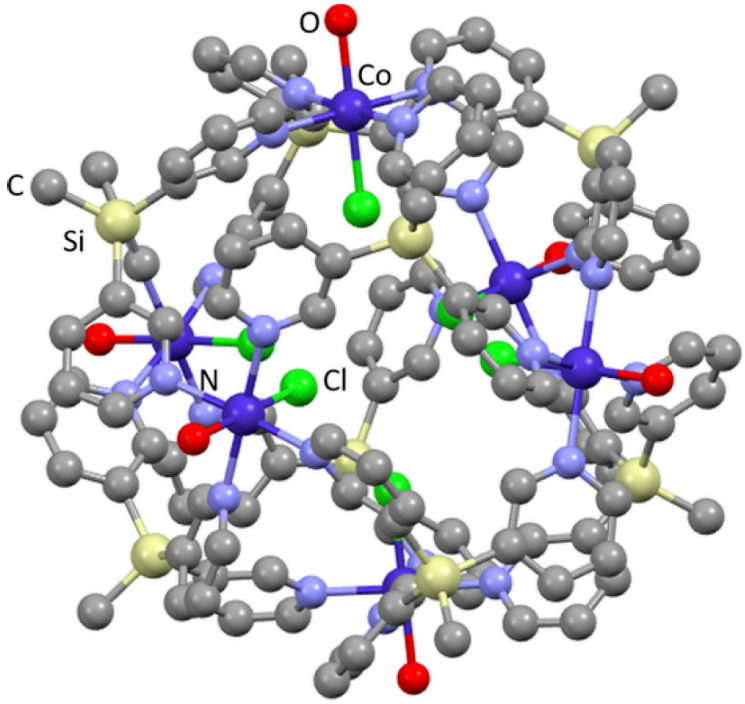

Figure 1.12: Solid-state structure of Co complex from Scheme 1.34.

Replacing Co(II) with Ni(II) gave a similar cage structure containing a Ni_6L_8 unit.[111] Whilst the core structure largely resembles that of the Co cage, the overall structure consists of $[Ni_6\{MeSi(3\text{-}py)_8\}Cl_9(H_2O)_2]^{3+}$ cages connected by bridging chloride ligands, forming a 1D coordination network. Cyclic voltammetry was run for both cage complexes: the data for the Co complex revealed a region of pH dependence for the Co^{II}/Co^{I} redox couple, but pH independence for the Co^{III}/Co^{II} redox couple, suggesting a proton-coupled electron transfer process is supposedly important in the electrochemical proton reduction pathway of water. In the case of the Ni complex, two quasi-reversible redox couples which exhibited pH dependent behaviour were revealed, again pointing towards proton-coupled electron transfer. A plausible mechanism of H_2 production using the Ni cage complex involves reduction of Ni(II) to Ni(I), proceeded by protonation to afford a Ni(III) hydride species; reduction to Ni(II) and reaction with another proton completes the formation of hydrogen. Photocatalytic activity in the presence of $[Ru(bipy)_3]Cl_2$ as a photosensitiser was also studied, with ascorbic acid as a sacrificial electron donor: this revealed turnover numbers of 43 over 2 h and 2824 over 69 h for Co and Ni cages, respectively.

Whilst they are obtained in high yields and have shown great potential in terms of their applications, both the P- and MeSi-bridgehead tris-3-pyridyl ligands $P(3\text{-}py)_3$ and $MeSi(3\text{-}py)_3$

are either air sensitive and/or require chromatographic purification, making them time-consuming or difficult to handle.[15,110] To date, there is only one report on the synthesis and application of a heavy Group 14 element tris-3-pyridyl ligand. In recent work published by Wright et al., the tin-bridged tris-3-pyridyl-phenylstannane $PhSn(3\text{-py})_3$ (Scheme 1.35) was shown to form both coordination polymers and discrete cationic cages with various transition metals.[16]

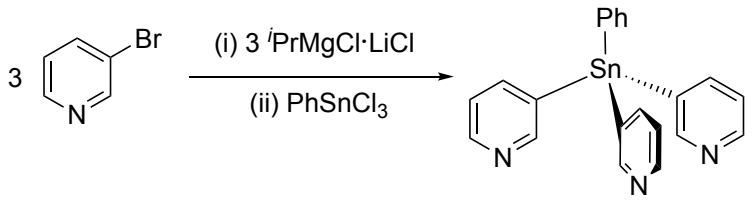

Scheme 1.35: Synthesis of $PhSn(3\text{-py})_3$ ligand.

In contrast to the previously reported silicon ligands by R. Boomishankar et al., this tin ligand is bench stable and is a readily obtained crystalline solid, making it a far more easily prepared and handled ligand. For its preparation, a Turbo-Grignard (an ^{i}PrMgCl·LiCl) was selected as a metalating reagent as opposed to ^{n}butyllithium, owing to the higher selectivity of Br/Mg exchange at the 3-position, as previously reported by A. Krasovskiy and co-workers.[112] In terms of its coordination behaviour, $PhSn(3\text{-py})_3$ provides straightforward access to a range of new heterobimetallic supramolecular arrangements: the structures of the resulting coordination complexes depend on the transition metal coordinated, and also on the nature of the counterion, both factors providing a means of controlling the nature of the supramolecular structure formed. Like $MeSi(3\text{-py})_3$, reactions between $PhSn(3\text{-py})_3$ and first-row transition metals with strongly coordinating anions such as CuI and $CoCl_2$ formed 1D coordination polymers. However, reactions of $PhSn(3\text{-py})_3$ with salts containing weakly-coordinating anions tend to form discrete anion-encapsulating cages, as is demonstrated by the reaction with $[Cu(NCMe)_4]PF_6$ or $Co(BF_4)_2$ which results in the cage complexes shown in Scheme 1.36.

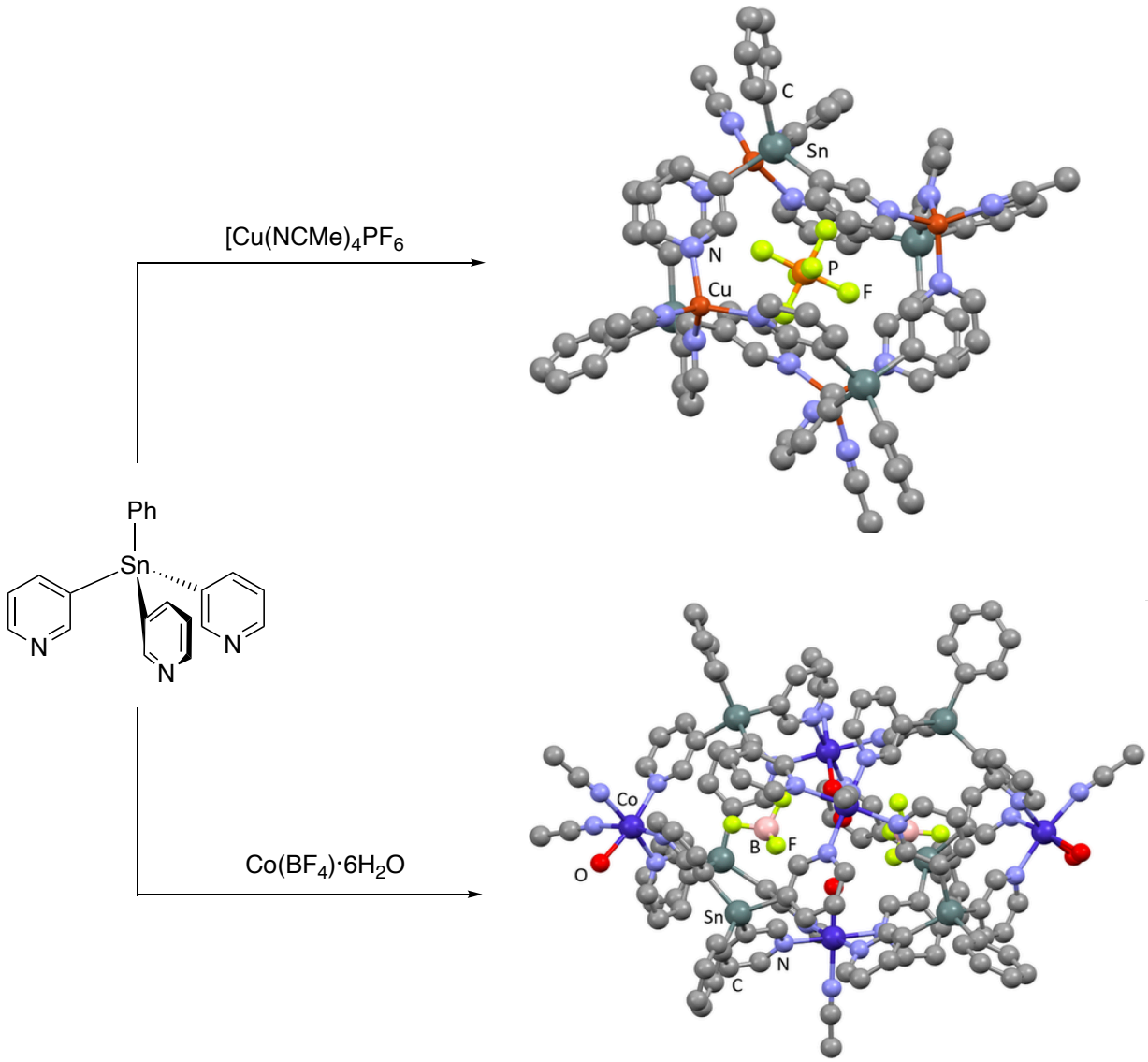

Scheme 1.36: Scheme showing the formation of cages complexes: $[Cu\{PhSn(3\text{-}py)_3\}(NCMe)]_4[PF_6]_4$ and $[Co_5\{PhSn(3\text{-}py)_3\}_6(H_2O)_6(NCMe)]_6[BF_4]_{10}$ with $PhSn(3\text{-}py)_3$.

First prepared by S. Condon and co-workers in 2012, the synthesis of $Bi(3\text{-}py)_3$ involves the addition of $BiCl_3$ to 3-bromopyridine and ^{n}BuLi in the presence of $ZnCl_2$, followed by flash chromatography on silica gel.[104] It can be noted that the tris-2- and tris-4-pyridyl ligands could not be successfully obtained by this route. Ligand $Bi(3\text{-}py)_3$ has since been used in the Pd-catalysed chemoselective cross-coupling reactions with 3,6-dihalopyridazines.[105] There have also been no other recent reports of heavier Group 15 tris-3-pyridyl compounds to date.

Of the previously reported tris-3-pyridyl ligands, the phosphine $P(3\text{-py})_3$ has certainly been studied the most extensively, the most efficient laboratory synthesis of which is shown in Scheme 1.37.

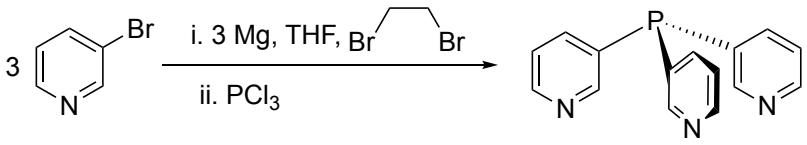

Scheme 1.37: Synthesis of the tris-3-pyridyl-phosphine via a Grignard reaction.

$P(3\text{-py})_3$ was found to act as a template for Rh hydroformylation catalysts, consisting of three porphyrin-encapsulated Zn(II) centres bound to the pyridyl N-atoms of the phosphine. This provides a sterically congested environment for a phosphine-coordinated Rh-centre that enables highly selective hydroformylation catalysis of internal olefins (Figure 1.13).[113] This study also demonstrates how the bridgehead of a tris-pyridyl ligand can be used to introduce further functionality into a supramolecular coordination complex, in this case by binding to a reactive catalytic species.

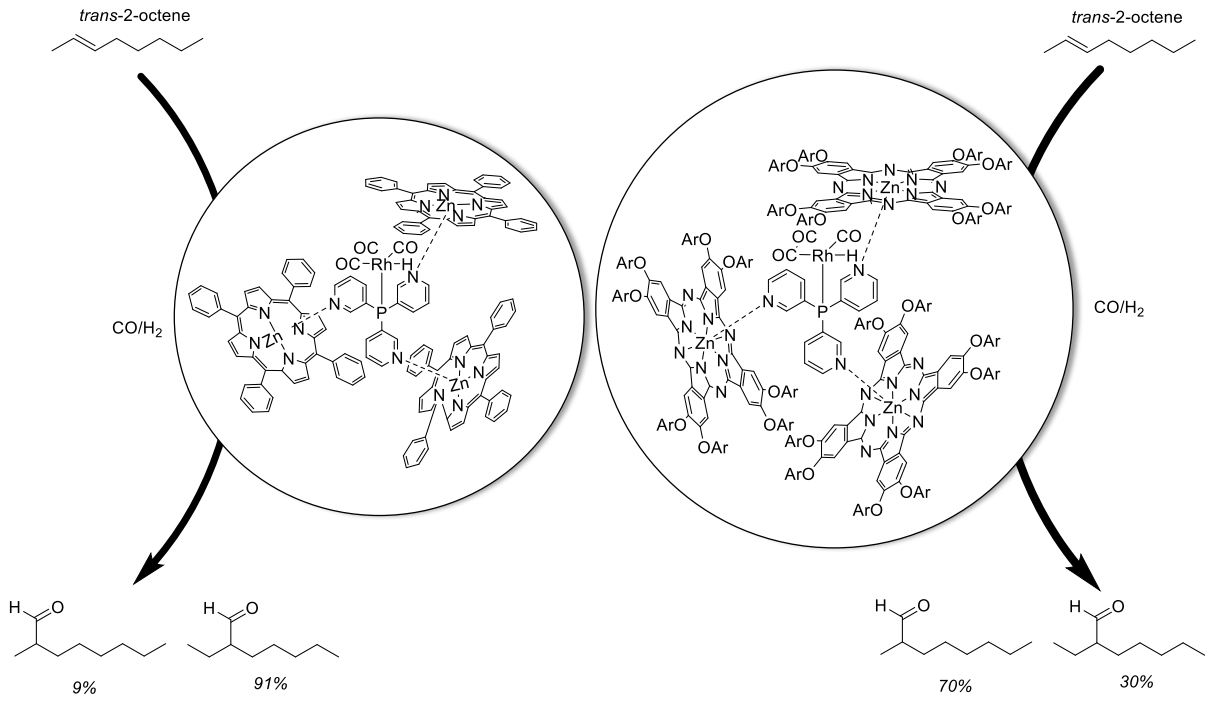

Figure 1.13: Hydroformylation catalysts with capsule-controlled selectivity using a tris-3-pyridyl-phosphine ligand. Reproduced from reference 113.

Additional work conducted by J. N. H. Reek, J. R. Nitschke and co-workers used a similar strategy, which will be discussed later in more detail, to create another hydroformylation catalyst encapsulated in a supramolecular coordination cage.[114] More recently, Reek and co-workers have found countless applications for the tris-3-pyridyl-phosphine ligand in supramolecular chemistry, such as the ability to act as a proton relay in hydrogenase mimics for proton reduction catalysis, as well as further use as a template to form a Rh-based catalyst for hydroformylation reactions.[93,115] The latter is of particular interest, as a catalytic system was designed that only forms an efficient supramolecular complex when a small cofactor molecule is added, proving that catalyst encapsulation can be manipulated by the addition of a cofactor, which in turn affects crucial catalyst properties, such as activity and selectivity.

Further studies by the same groups show that it is also possible to perform enantioselective hydroformylation by encapsulating $P(3\text{-py})_3$ as an achiral ligand template with chiral "capsule building blocks" (Figure 1.14).[98]

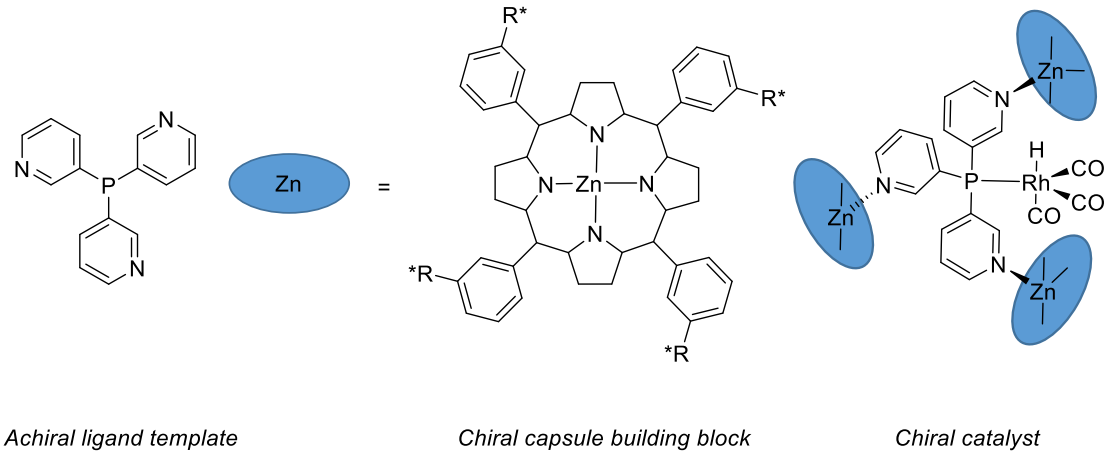

Figure 1.14: Tris-3-pyridyl-phosphine as an achiral template, encapsulated with chiral capsule building blocks, explored as asymmetric catalysts in hydroformylation in work by J. N. H. Reek and co-workers.

1.3.3 Tris-4-Pyridyl Ligands

As previously discussed, there are already several well-established tris-2- and tris-3-pyridyl ligands (although less work has been reported on the latter). The switch from facial coordination to bridging of metal centres is the most obvious outcome of changing the position of the N-atom within the pyridyl ring units. However, clearly the most dramatic effect would be seen in tris-4-pyridyl ligands. Despite this prospect, there are very few studies of the coordination chemistry of tris-4-pyridyl ligand systems, and all of these have so far involved only the lighter P and N bridgeheads, using the ligands $P(4\text{-py})_3$ and $N(4\text{-py})_3$. These studies have, however, illustrated the large potential of this area for new supramolecular chemistry,[88,114,116–120] an example being the work by J. N. H. Reek and co-workers, which shows that $P(4\text{-py})_3$ can coordinate to Zn porphyrins, resulting in an unusual 2:5 phosphine : Zn-porphyrin structure (Scheme 1.38).[119] This area will be one of the major focuses of this thesis, especially in regard to ligands containing the heavier main group elements.

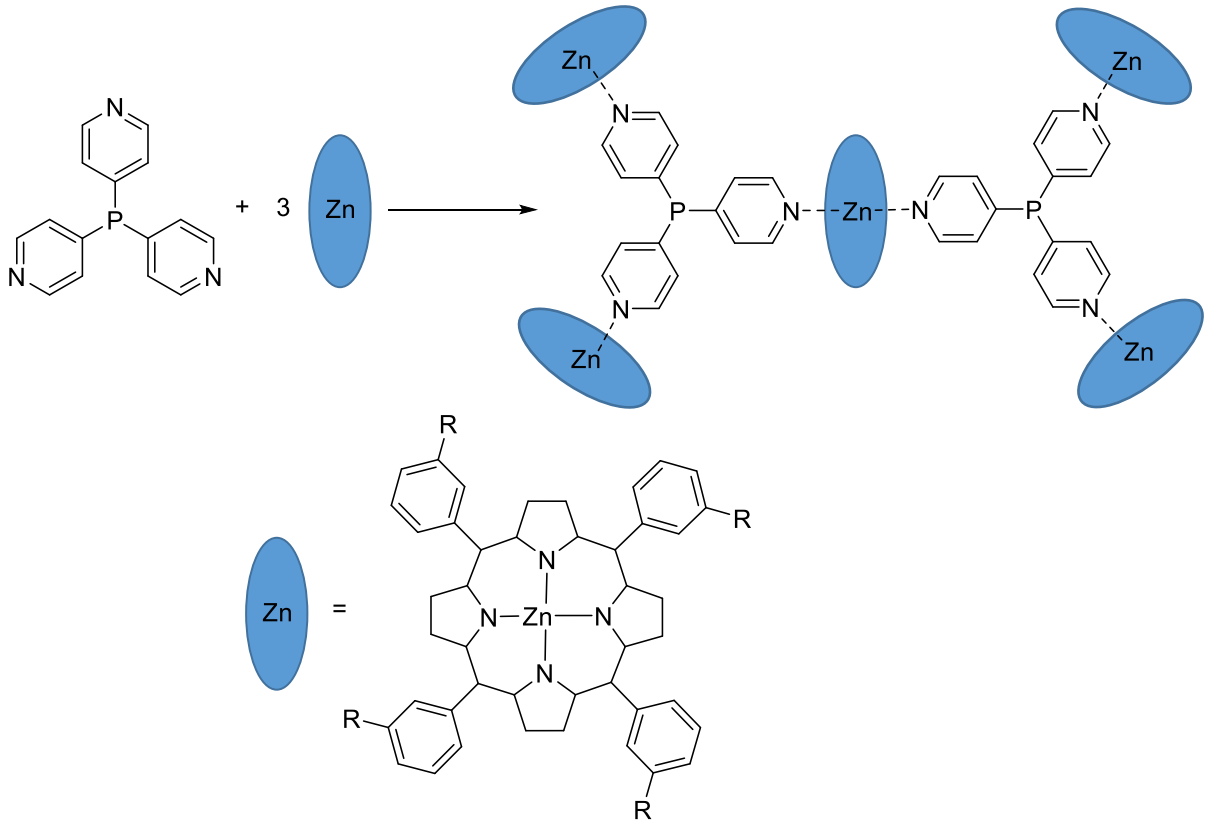

Scheme 1.38: Formation of supramolecular phosphine ligands via Zn(II)-N-pyridyl interactions using various Zn(II)porphyrin building blocks.

1.4 Tris-4-Pyridyl and Beyond: New Directions Towards Tripodal Ligand Design

Despite numerous advances in the area of main group ligand design, it remains true that literature involving more drastic deviations from the classical "tripodal" ligand is somewhat lacking. Further studies could be extended not only to bridgehead modification, but moreover to diversify the format in which the N-donor atom is present (i.e., away from tris-2- and tris-3-pyridyl systems). The immaturity of this particular area means that great progress can be made in terms of generating novel main group-based systems based on tris-pyridyl systems and the study of their reactivities and/or coordination behaviour. By advancing work in this area, it is hoped that a deeper understanding of the reactivity of tris-pyridyl and related ligands is gained, allowing for further optimisation of current systems, as well as discovery of novel ones.

2

2. Project Aims

With the previous perspective in mind, this thesis aims to investigate a range of new *p*-block metal bis- and tris-pyridyl and related ligand systems using the following design strategies:

1. *Synthesis of novel bis-pyridyl ligand derivatives with various bridgeheads (Chapter 3)*

The synthesis of bis-pyridyl ligands will significantly alter the steric properties of the systems, providing two coordination sites with metals as opposed to three and in turn affecting the coordination behaviour, therefore providing a direct comparison to tris-pyridyl ligand systems and their reactivities towards metals.

2. *Investigation of ligands' reactivity with increasing remoteness of the N-donor from central bridgehead atom (Chapter 3)*

Given that changing the donor atom from the 2- to the 3-position significantly alters the coordination behaviour, it is hypothesised that incorporating more extended polyaromatic systems (e.g. quinolyl) will permit control over the remoteness of the N-donor atom with respect to its central bridgehead, and this may drastically alter the ligand characteristics.

3. *Tris-4-pyridyl ligand systems containing heavier elements (Chapter 4)*

So far, many studies have investigated the coordination behaviour of tris-2- and tris-3-pyridyl ligand systems, but none have explored heavier main group-based tris-4-pyridyl ligands. This area will be a major target of the research.

4. *Extending the concepts to alternative established ligand systems (Chapter 5)*

By incorporating 2-, 3- or 4-pyridyl fragments into more complicated molecular arrangements such as cyclodiphosphazanes it may be possible to build multifunctional ligand arrangements

which have a larger ligand bite than the simpler pyridyl ligands based on a single bridgehead atom.

3

3. Synthesis & Coordination Behaviour of Tris- and Bis-Quinolyl Ligands

3.1 Preface

As mentioned in Chapter 1, changing the position of the N-donor atoms within the pyridyl ring units from the 2- to 3-position is known to significantly alter the coordination characteristics of the ligands, allowing the coordination of more than one metal centre. This has been seen in studies of the Group 14 ligands $MeSi(3\text{-py})_3$[15,110] and (air-stable) $PhSn(3\text{-py})_3$,[16] which are known to form a range of extended and supramolecular cage arrangements with various metal ions. In these reports, Boomishankar and co-workers have shown that both the $MeSi(3\text{-py})_3$ and its quinolyl analogue $MeSi(3\text{-qy})_3$ (qy = quinolyl) form metal-organic frameworks (MOFs) when reacted with CuI in various stoichiometries, acting as bridging ligands between CuI clusters.[15] For example, the 3:1 reaction of $MeSi(3\text{-py})_3$ gives rise to a 2D MOF with tris-3-pyridyl ligands bridging between the Cu_6I_6 clusters (Scheme 3.1). However, slightly different coordination chemistry was observed in the reactions of CuI and $MeSi(3\text{-qy})_3$, which produced a 1D MOF containing Cu_2I_2 dimers at room temperature, or a MOF composed of monomeric CuI units under solvothermal conditions, indicating that both stoichiometric and thermal control of the product structure are at work in the coordination chemistry of the quinolyl ligand. The 3:1 reaction gave the analogous 2D $[Cu_6I_6L_6]_n$ MOF to the pyridyl ligand system. Further to this, altering the thermal conditions and stoichiometries permits reversible interchanging between the three architectures.

So far, however, the functionalisation of tris-pyridyl ligands with polyaromatic N-donor groups has been largely ignored as a means of modifying the coordination site, and to our knowledge the only example of this type is the aforementioned ligand $MeSi(3\text{-qy})_3$. This is despite earlier studies on the impact of replacing pyridyl with quinolyl groups in tripodal ligands of this type, which indicated that sequentially replacing 2-pyridyl groups with 2-quinolyl substituents in the $HC(2\text{-py})_3$ framework can lead to large changes in the geometries of coordinated metal centres.[121]

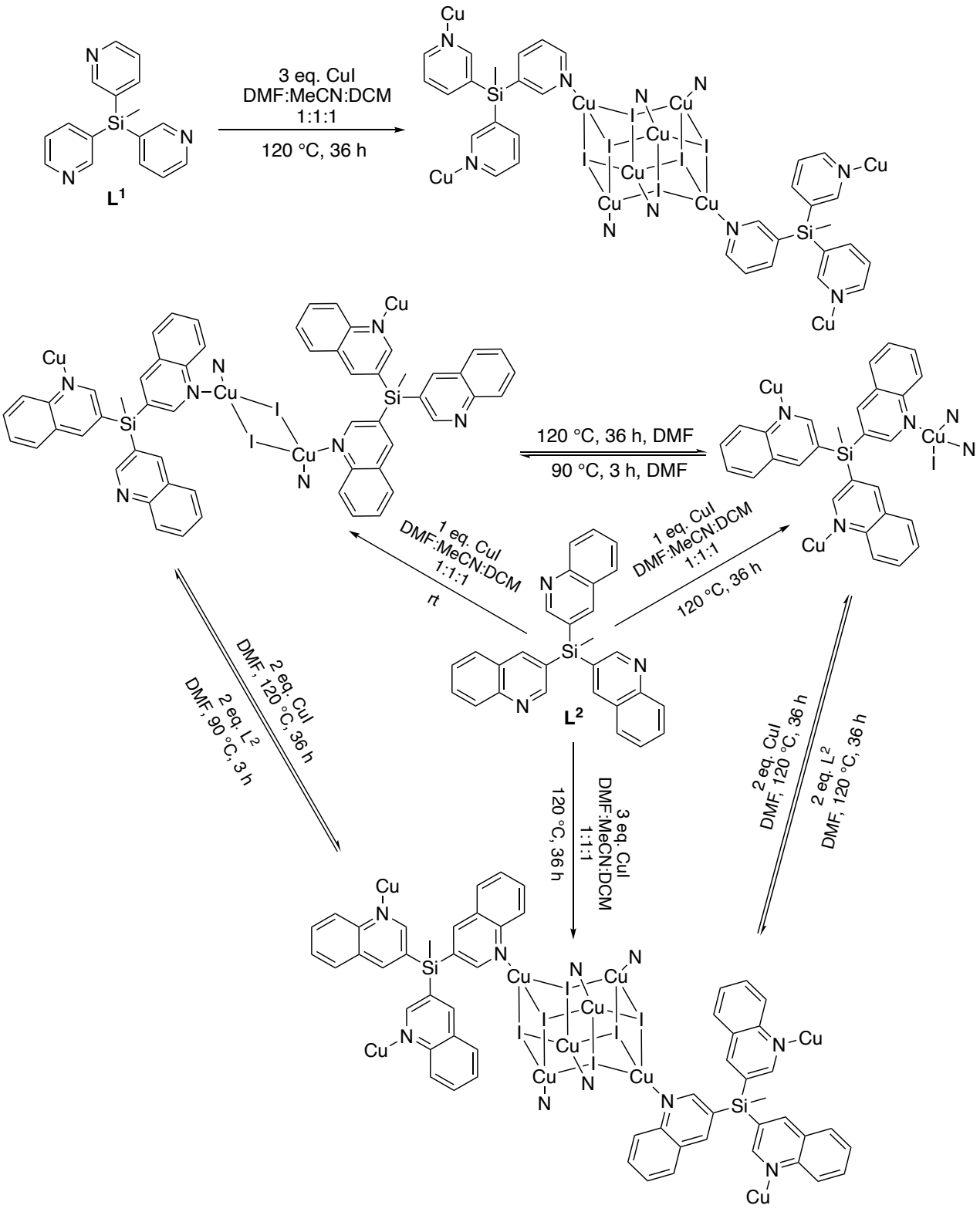

Scheme 3.1: Reaction scheme showing the formation of 1D and 2D MOFs with CuI and $MeSi(3\text{-}py)_3$ (**L**[1]) or $MeSi(3\text{-}qy)_3$ (**L**[2]), reproduced from reference 15.

The quinolyl substituent is a particularly interesting candidate for ligand modification since the position of the donor N-atom relative to the bridgehead atom can be changed readily, making the coordinated metal centre closer (i.e., 2-qy) or further away (i.e., 8-qy) from the bridgehead (Figure 3.1).

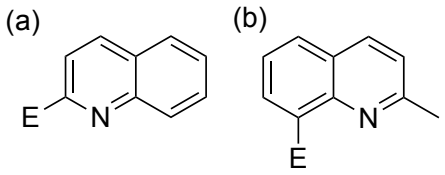

Figure 3.1: (a) 2-quinolyl (2-qy) and (b) 2-Me-8-qy variants presented in this study.

Some of the following sections were published in: J. E. Waters, S. Hanf, A. D. Bond, R. García-Rodríguez, D. S. Wright, A. L. Colebatch, *Dalton Trans.*, 2021, **50**, 14551-14559.

3.2 Results & Discussion

3.2.1 Tris- and Bis-Quinolyl-Aluminates: Synthesis and Solid-State Structures

In this study the synthesis and coordination properties of a series of tris- and bis-quinolyl ligands containing 2-qy and 8-qy substituents were investigated. With the previous background in mind, the aim was to obtain a range of bis- and tris-quinolyl ligands containing various main group bridgehead atoms from Groups 13, 14 and 15. It was thought that the Group 13-derived Al bridgehead quinolyl ligands would provide a good starting point, because there are a relatively large number of studies of the tris-pyridyl-aluminates (outlined in Chapter 1 of this thesis) on which the synthesis of new quinolyl ligands could be based and the structures of the resulting complexes compared. The novel aluminium compounds synthesised in the current study are shown in Figure 3.2, which also shows the numbering scheme used throughout the discussion and experimental sections.

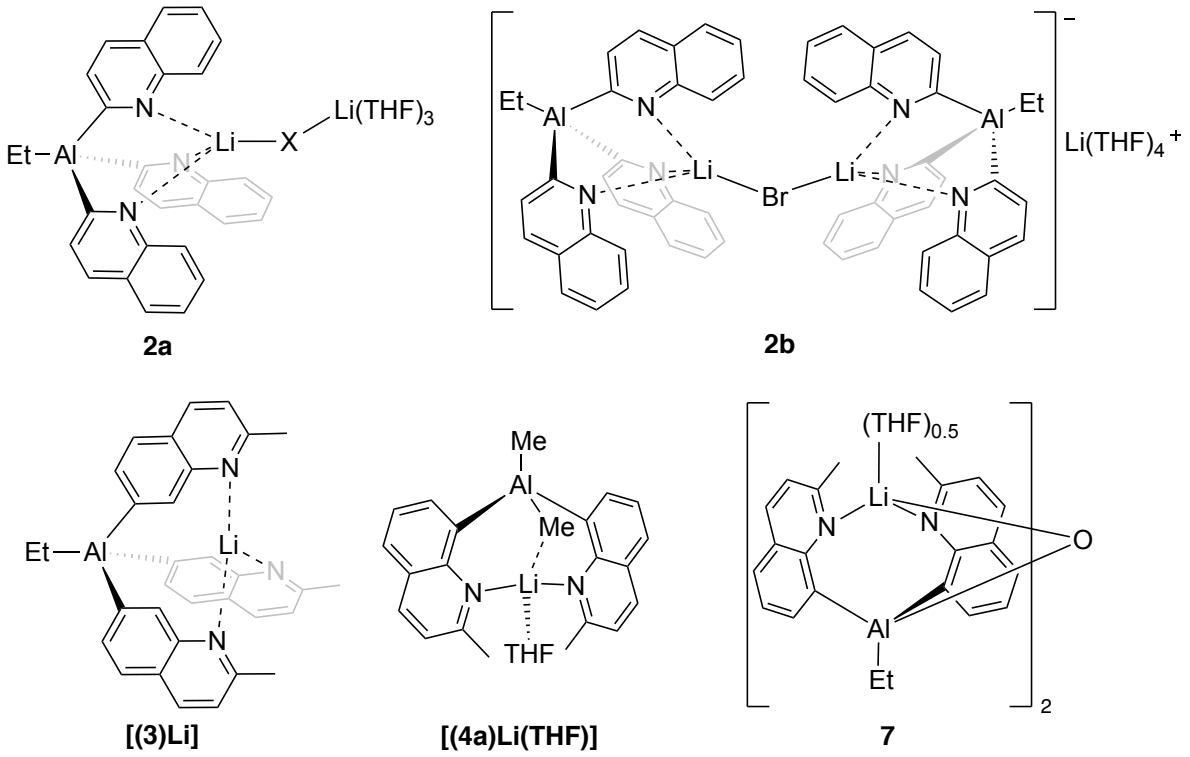

Figure 3.2: Bis- and tris-quinolyl-based aluminate ligands and complexes explored in this Chapter: [{EtAl(2-qy)}Li(μ-X)Li(THF)$_3$] (X = Cl/Br 62:38) [(**1**)Li(μ-X)Li(THF)$_3$] (**2a**), [{(EtAl(2-qy)$_3$)Li}$_2$(μ-Br)]$^-$Li(THF)$_4^+$ [{(**1**)Li}$_2$(μ-Br)]$^-$Li(THF)$_4^+$, (**2b**), [{EtAl(2-Me-8-qy)$_3$}Li] [(**3**)Li], [{Me$_2$Al(2-Me-8-qy)$_2$}Li(THF)] [(**4a**)Li(THF)], and [{{EtAl(2-Me-8-qy)$_2$}$_2$O}(Li$_2$THF)] (**7**). *Note: compounds **4b**, **5** and **6** exist within this study, but were deemed more appropriate to discuss in later paragraphs.*

Studies began by exploring the synthesis of the aluminate anion [EtAl(2-qy)$_3$]$^-$ (**1**), in which the N-donor functionality is in close proximity to the Al(III) bridgehead, providing a potentially similar coordination for metal coordination to the previously explored aluminates [RAl(2-py)$_3$]$^-$. However, lithiation of 2-bromoquinoline with ^{n}BuLi at –78 °C in THF followed by *in situ* reaction of the intermediate 2-lithioquinoline in with EtAlCl$_2$ (3:1 equiv.) only afforded a small crop of crystalline material, which contained a mixture of the ion-paired complex [(**1**)Li(μ-X)Li(THF)$_3$], (**2a**) (X = Cl/Br in a ratio of 62:38, respectively) and ion-separated complex [{**1**}$_2$(μ-Br)]$^-$Li(THF)$_4^+$ (**2b**), (as shown by single-crystal X-ray diffraction studies, Scheme 3.2).

The reason for the low yield in the case of 2-bromoquinoline appears to be the instability of anion [EtAl(2-qy)$_3$]$^-$ (**1**) towards reductive elimination of 2,2′-biquinoline, which was detected in the ^{1}H NMR spectroscopy of the crude reaction mixture. High-Resolution Mass

Spectrometry (HR-MS, +ve ion) of this crude mixture was also used to confirm the formation of 2,2′-biquinoline (Figure 3.3). The mass spectrum of the crude product mixture displays a molecular ion m/z peak of 257.1083 which indicates the presence of 2,2′-biquinoline with the predicted m/z peak value of 257.1079 predicted for (2,2′-biquinoline)H^+. Similar reductive elimination processes have been observed with tris-2-pyridyl systems involving various other main group element bridgeheads.[43,102,122]

Scheme 3.2: Synthesis of [(**1**)Li(μ-X)Li(THF)$_3$], (**2a**), (X = Cl/Br 62:38) and ion-separated complex [{(**1**)Li}$_2$(μ-Br)]$^-$Li(THF)$_4^+$, (**2b**).

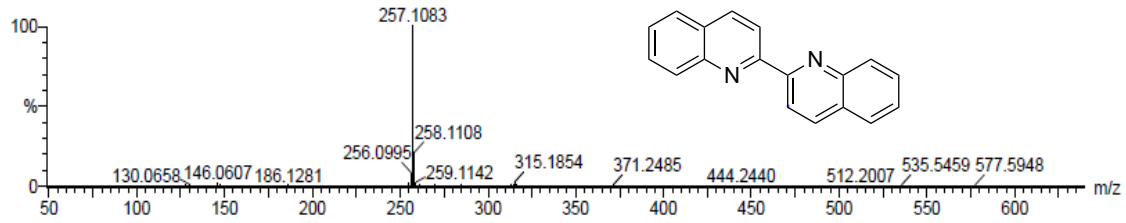

Minimum:				-1.5				
Maximum:		5.0	5.0	50.0				
Mass	Calc. Mass	mDa	PPM	DBE	i-FIT	Norm	Conf(%)	Formula
257.1083	257.1079	0.4	1.6	13.5	1063.7	n/a	n/a	C18 H13 N2

Figure 3.3: Mass spectrum (+ve ion), indicating the formation of 2,2'-biquinoline from reductive elimination from the anion **1**.

The solid-state structures of **2a** and of the **2b** anion are shown in Figure 3.4. Both have conceptually similar arrangements, in which one of the Li^+ cations is coordinated by the three N-atoms of the aluminate **1** and with the pseudo-tetrahedral geometry being completed by a halide (Cl^- or Br^-) anion. The halide ions bridge the two Li^+ cations together. The structures are similar to those observed previously for the tris-2-pyridyl-aluminate complexes [MeAl(3-Me-2-py)$_3$Li(μ-Br)Li(THF)$_3$,[123] and [{MeAl(2-py)$_3$}$_2$Li(μ-Cl)]$^-$.[124] The similarity of the new 2-qy complexes to these previous examples is perhaps unsurprising, bearing in mind the similar

position of the N-donor atoms, and indicates that the presence of the fused-benzene substituent has little effect on the coordination environment compared to the parent 2-pyridyl-aluminates.

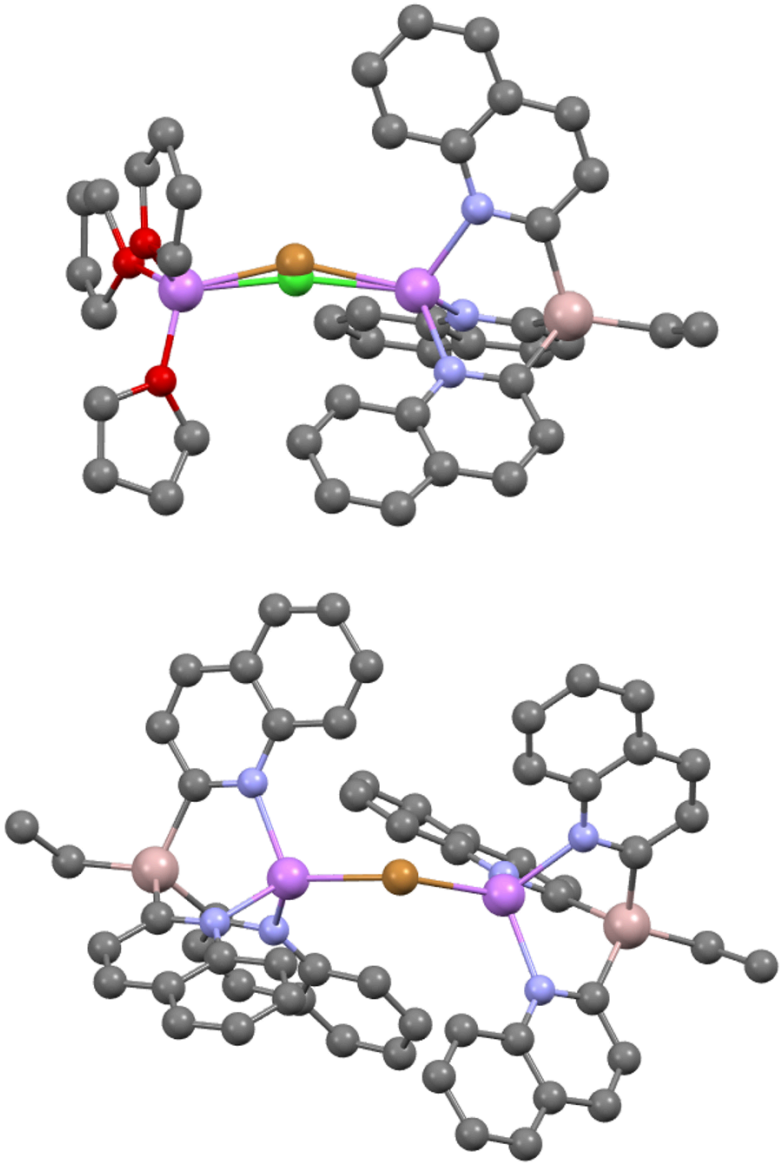

Figure 3.4: Top: Structure of **2a** (X = Cl/Br 62:38). Bottom: Anion **2b**. H-atoms and lattice solvation have been omitted for clarity. Selected bond lengths (Å) and angles (°): **2a**: C_{Et}-Al 1.987(7), C_{qy}-Al range 2.007(6)-2.021(6), N-Li range 2.164(10)-2.191(10), Al···Li 3.060(9), Li-O range 1.880(12)-1.902(11), Li-X range 2.32(2)-2.511(15), C_{qy}-Al-C_{qy} range 104.4(2)-106.1(2), N-Li-N range 100.9(4)-104.8(4), Li-Cl-Li 164.6(9), Li-Br-Li 153.2(8). **2b**: C_{Et}-Al range 1.978(7)-1.980(7), C_{qy}-Al range 2.009(7)-2.022(7), N-Li range 2.145(11)-2.198(12), Al···Li range 3.054(11)-3.058(10), Li-Br range

2.558(11)-2.568(10), C_{qy}-Al-C_{qy} range 101.9(3)-107.6(3), N-Li-N range 97.2(4)-108.8(5), N-Li-Br range 111.0(4)-118.8(5), Li-Br-Li range 126.0(5)-129.0(5).

In light of this initial work on the 2-qy aluminates, it was decided to direct the investigation to aluminates incorporating 2-Me-8-qy substituents. In previous work on tris-2-pyridyl ligand systems, it had been shown that the presence of a Me-substituent adjacent to the donor N-atom increases the stability by supressing the elimination of bipyridines. At the same time, it was reasoned that the greater separation of the N-donor atoms from the bridgehead would result in a significantly different coordination environment. Lithium-halogen exchange of 8-bromo-2-methylquinoline with ^{n}BuLi was accomplished at –78 °C in THF, followed by (3:1) reaction with $EtAlCl_2$ (Scheme 3.3).

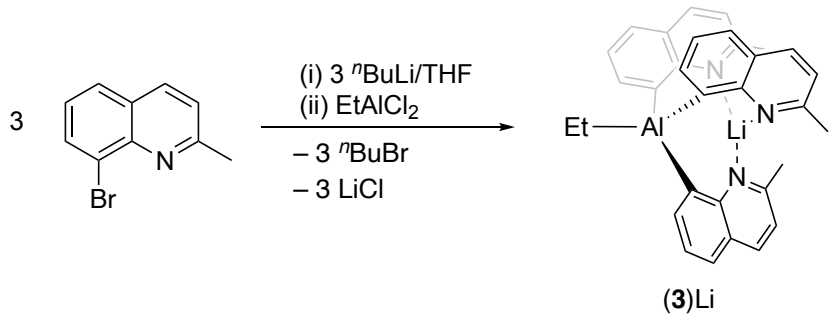

Scheme 3.3: Synthesis of (**3**)Li.

Crystals of the new complex [EtAl(2-Me-8-qy)$_3$Li], (**3**)Li, were isolated in 42% yield after workup. The room-temperature ^{1}H NMR spectrum in D_8-THF shows the expected 1:3 ratio of the Et(-Al) and 2-Me-8-qy groups (Figure 3.5, top). The single-crystal X-ray structure of (**3**)Li (Figure 3.5, bottom) is that of a monomeric arrangement in which the Li^+ cation has a trigonal planar geometry (N-Li-N range 118.97(3)-120.45(3)°). This appears to result from a combination of the geometric disposition of the quinolyl N-donor atoms and the steric shielding of the Li-centre (which is therefore not able to attain a tetrahedral geometry by the coordination of a THF molecule). It can be noted in this regard that (albeit weak) coordination of the Li^+ cation by a THF ligand *does* occur in the analogous lithium tris-2-pyridyl-aluminate complex [{EtAl(6-Me-2-py)$_3$}Li(THF)],[45] also containing Me-groups adjacent to the N-donor atoms (i.e., in a similar position to those present in (**3**)Li). The trigonal planar geometry observed in

(**3**)Li is in marked contrast to the three-coordinate, pyramidal geometry of the Li^+ cation found in the unsolvated complex [{EtAl(6-Me-2-py)$_3$}Li],[44] resulting from the loss of THF from [{EtAl(6-Me-2-py)$_3$}Li(THF)].

Unexpectedly, despite apparently greater remoteness of the Li^+ coordinated cation in (**3**)Li from the bridgehead Al centre compared to 2-pyridyl aluminates, the Al···Li separation (2.736(5) Å) is significantly shorter than that in tris-2-pyridyl aluminate complexes (e.g., mean in 2.84 Å in [{EtAl(2-py)$_3$Li]). The accommodation of the trigonal planar Li^+ cation within the coordination site of the aluminate anion **3** results in noticeable misalignment of the sp^2 lone pairs of the N-atoms, with the planes of the quinolyl groups being tilted by ~ 30 ° with respect to the N-Li bond axes (Figure 3.5b, space-filling diagram of (**3**)Li).

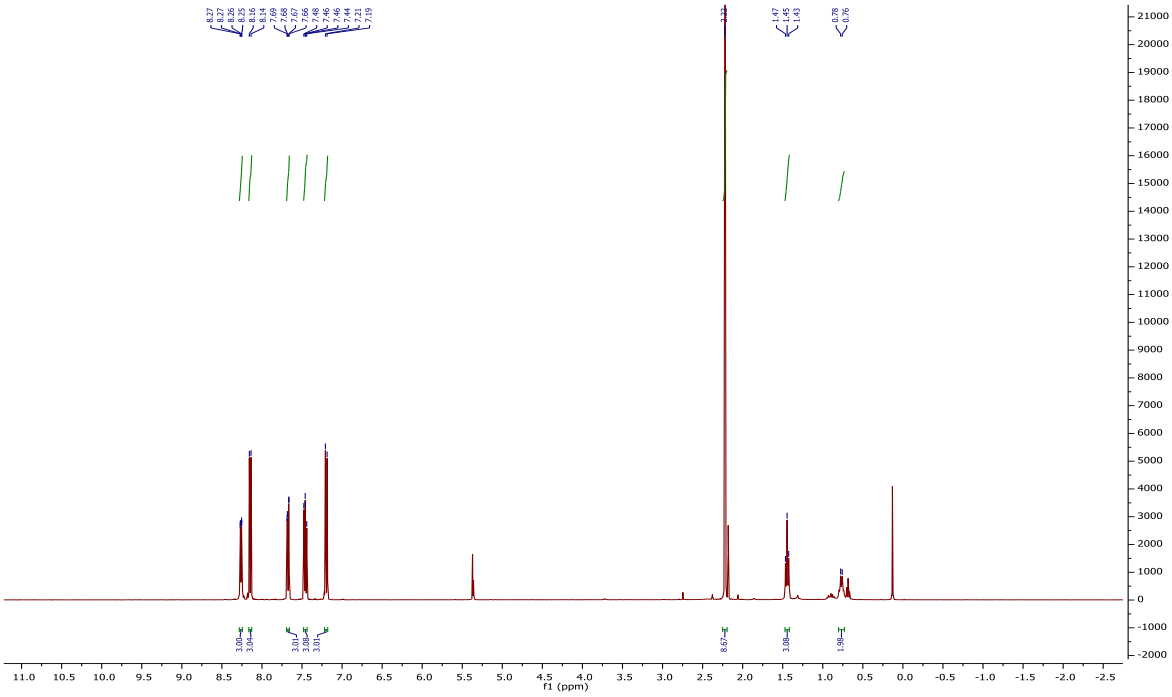

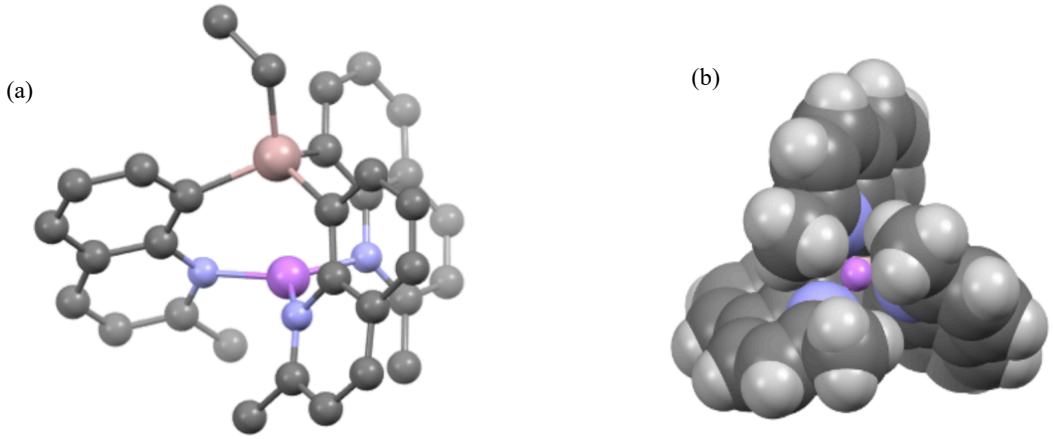

Figure 3.5: Top: ^{1}H NMR spectrum of (**3**)Li. Bottom: (a) Ball-and-stick structure of (**3**)Li, (b) Space-filling model of (**3**)Li. H-atoms and THF lattice solvent have been omitted for clarity. Selected bond lengths (Å) and angles (°): C_{Et}-Al 2.000(3), C_{qy}-Al range 2.043(3)-2.052(3), N-Li range 1.952(5)-1.971(5), Al···Li 2.736(5), C_{qy}-Al-C_{qy} range 109.27(11)-113.97(12), N-Li-N range 118.9(2)-120.6(3). (b) View of the molecules down the approximate Al···Li C_3-axis of the molecules, showing the sterically shielded Li^+ cation and the distorted arrangement of the three 2-Me-8-qy substituents.

A similar synthetic procedure involving lithiation of 8-bromo-2-methylquinoline in THF and *in situ* reaction of the intermediate lithioquinoline in 2:1 stoichiometric ratio with Me_2AlCl_2 gave the bis-8-quinolyl aluminate complex [(**4a**)Li(THF)] (Scheme 3.4). This was isolated in 50% yield after crystallisation from toluene.

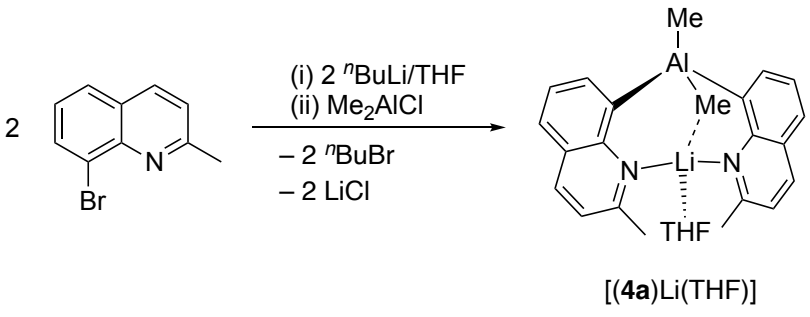

Scheme 3.4: Synthesis of [(**4a**)Li(THF)].

The solid-state structure was determined by single-crystal X-ray analysis, the H-atoms being located in the Fourier map but fixed with idealised C-H bond lengths and angles during refinement (Figure 3.6). The structure is that of a monomer in which the $[Me_2Al(2\text{-}Me\text{-}8\text{-}qy)_2]^-$ anion (**4a**) coordinates the Li^+ cation using the two qy-N atoms (Li-N range 2.046(5)-2.075(5) Å), with the Al···Li contact (2.808(4) Å) being slightly longer than that seen in (**3**)Li. Further coordination by a THF molecule, and the presence of an additional Al-Me···Li interaction with one of the Me groups of the Al bridgehead, results in a very distorted pseudo tetrahedral geometry at the Li centre (in which the N and O atoms are approximately coplanar). The most significant Me···Li interaction in the complex (C(6)···Li 2.449(5) Å; H(8)···Li 1.84 Å) compares to mean C···Li and H···Li distances 2.285 and 2.07 Å, respectively, found in previously reported lithium aluminate containing similar interactions.[125,126] In addition, there are two longer-range C–H···Li with the 2-Me groups of the quinolyl ligands (2.61 Å). It is worthwhile noting that the type of bridgehead alkyl···Li interaction found in [(**4a**)Li(THF)] has not been observed in the few previously reported bis-2-pyridyl Group 13 complexes of Ga and In[70] - [(**4a**)Li(THF)] being the first bis-aluminate of this class.

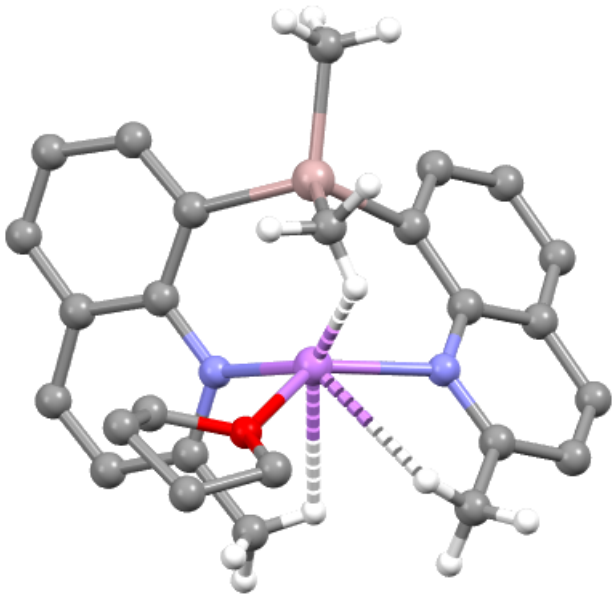

Figure 3.6: Solid-state structure of [(**4a**)Li(THF)] (in the toluene mono-solvate). H-atoms on the qy groups and the lattice toluene molecule have been omitted for clarity. Selected bond lengths (Å) and angles (°): C_{Me}-Al (terminal) 1.998(2), C_{Me}-Al (bridging) 2.024(3), C_{qy}-Al range 2.019(2)-2.025(3), N-Li range 2.046(5)-2.075(5), C···Li 2.449(5) (C-H···Li 1.84), Li-O 2.002(5), Al···Li 2.808(4), C_{qy}-Al-C_{qy} 109.03(10), N-Li-N 113.6(2), O-Li-N range 97.50(19)-135.3(2), Al-C···Li 77.1(1).

The room-temperature ^{1}H NMR spectrum shows that some of the THF has been removed during isolation under vacuum (Figure 3.7), which can be shown by integration (numbering scheme denoted in Experimental, Section 8.3.1). This is consistent with elemental analysis of the complex when placed under vacuum for prolonged periods (which shows complete removal of the THF ligand). The spectrum also shows only one Me resonance (at δ –0.34 ppm in D_8-THF), even though the Me-groups of the bridgehead are inequivalent in the solid-state structure, suggesting fluxionality. However, variable-temperature ^{1}H NMR spectroscopy revealed no splitting of this peak, even at substantially lower temperatures (ca. 238 K), suggesting that the activation energy for this process is very low. Confirmation of the persistence of the C–(H)···Li interactions in solution and the maintenance of its molecular structure is seen in the ^{7}Li-^{1}H HOESY NMR spectrum, which shows two (albeit weak) correlations to the Li^{+} cation – one to the Al-CH_3 peak at δ –0.34 ppm and another to the 2-Me substituents of the quinolyl group at δ 2.58 ppm (Figure 3.8).

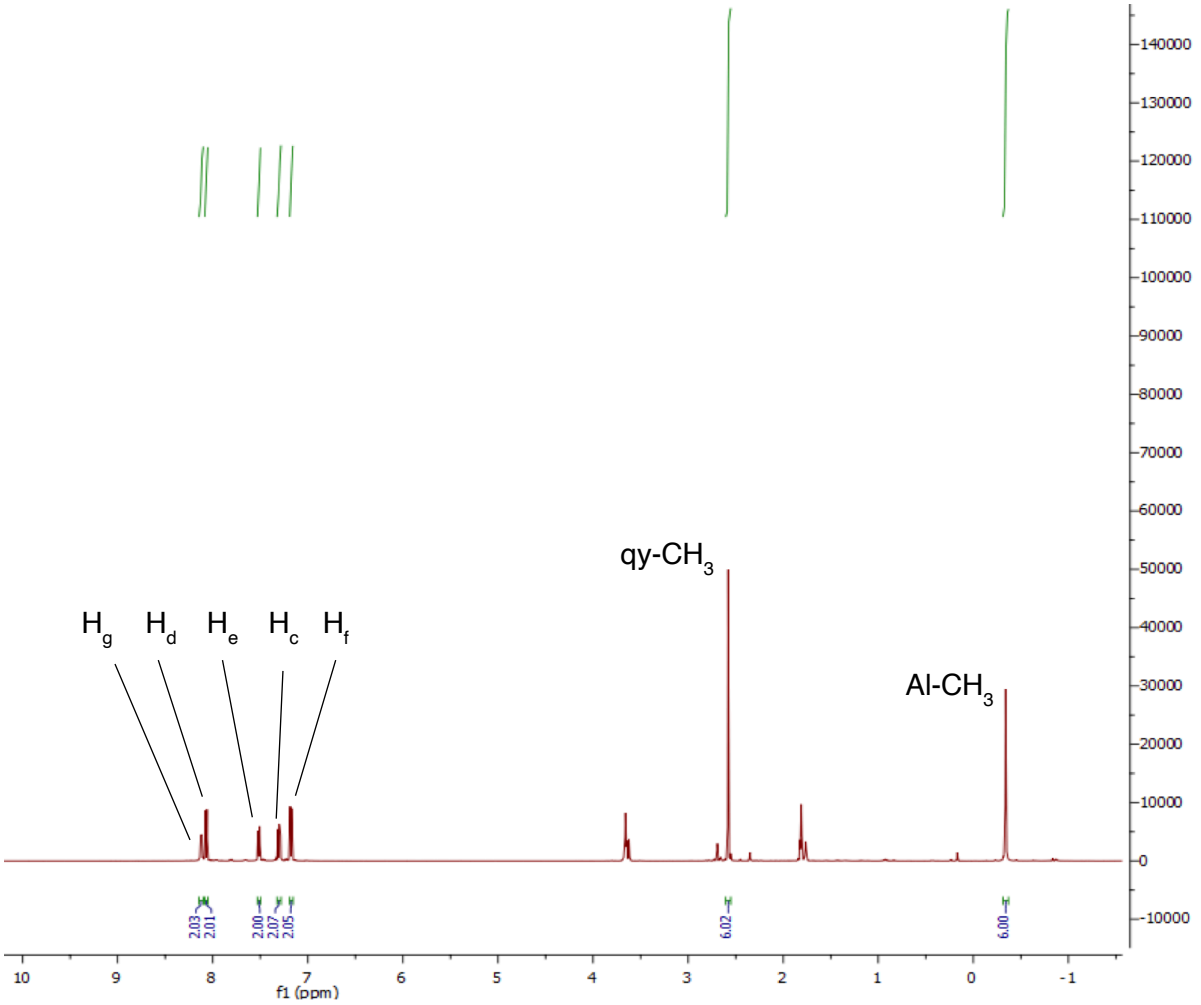

Figure 3.7: ^{1}H NMR spectrum (25 °C, 400 MHz, D_8-THF) of [{Me_2Al(2-Me-8-qy)$_2$}Li(THF)], [(**4a**)Li(THF)]. THF resonances have a lower integration than the expected 2:1 qy, as THF is found within the structure.

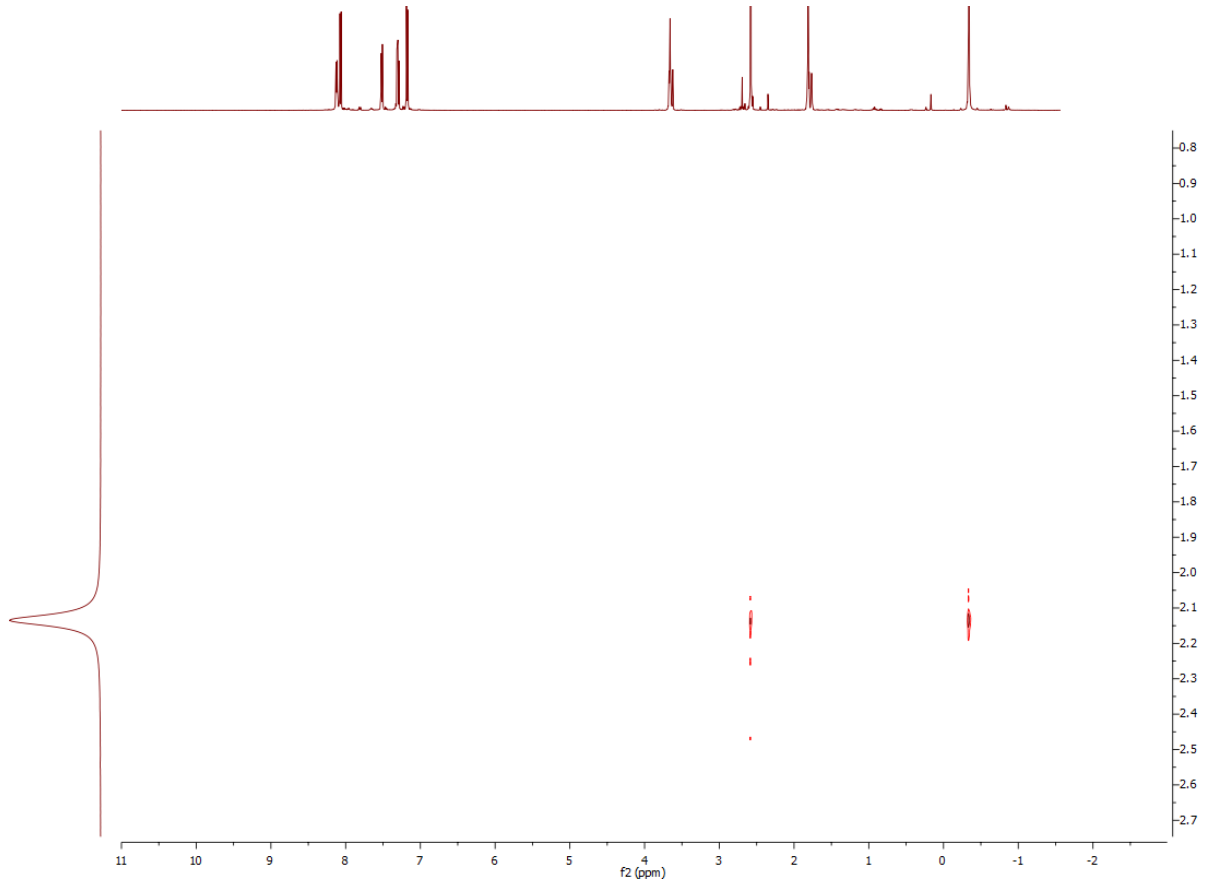

Figure 3.8: ^{7}Li-^{1}H HOESY NMR spectrum (25 °C, D_8-THF) of [{Me_2Al(2-Me-8-qy)$_2$}Li(THF)], [(**4a**)Li(THF)].

In a background study, the 6-methyl-2-pyridyl analogue of **4a** [{Me_2Al(6-Me-2-py)$_2$}Li(THF)$_2$] (**5**), along with another variant [{Me_2Al(5-Me-2-py)$_2$}Li(THF)$_2$] (**6**) - in which the pattern of the pyridyl substitution is varied - were also prepared and structurally characterised. Reacting 2-bromo-6-methylpyridine with ^{n}BuLi (1:1 equivalents), followed by reaction with Me_2AlCl (2:1 equivalents) at –78 °C in THF gave an orange solution, which was recrystallised from toluene/THF at –14 °C. Storage of the solution for a week produced colourless crystals which were identified as [{Me_2Al(6-Me-2-py)$_2$}Li(THF)$_2$] (**5**, Figure 3.9). Whilst the compound could also be further analysed by NMR spectroscopy, it is worth mentioning that isolation of the crystals was extremely difficult due to the presence of an orange oil, which resulted in poor elemental analysis.

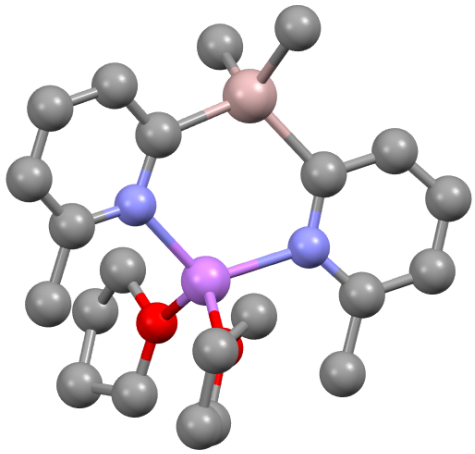

Figure 3.9: Solid-state structure of **5**. H-atoms omitted for clarity. Selected bond lengths (Å) and angles (°): C_{Me}–Al range 1.996(2)-2.000(2), C_{py}–Al range 2.028(2)-2.030(2), N–Li range 2.052(3)-2.068(3), Li–O range 1.971(3)-1.978(3), C_{py}–Al–C_{py} 113.70(8), C_{Me}–Al–C_{Me} 112.91(12), N–Li–N 118.36(15), O–Li–O 115.86(15).

The solid-state structure comprises an aluminium bridgehead atom in a slightly distorted tetrahedral structure (range 106.98(11)-113.70(8)°), which is coordinated to two methyl groups and two methyl-substituted pyridyl ligands. In addition, the structure of **5** is isolated as the bis-THF adduct [(**5**)Li(THF)$_2$], whereas its related tris-2-pyridyl analogue, MeAl(2-py)$_3$, just coordinates the one THF molecule. Not unexpectedly, bis-THF solvation of the Li^+ cation in this case is preferred to the monosolvation and accompanying Al-Me···Li interaction that is observed for the tris-pyridyl and quinolyl systems. It can therefore be concluded that the unusual arrangement in [(**4a**)Li(THF)] arises primarily from the steric effects of the 2-Me-8-qy groups on the coordination site of the aluminate anion, as well as the change in geometry required to accommodate the additional distance between the N-donor atom and the Al bridgehead. As previously seen with tris-pyridyl compounds, the influence of the coordination behaviour of such ligands to Li^+ was further examined by varying the position of the methyl groups on the pyridyl ring. Changing the 2-bromo-6-methylpyridine for 2-bromo-5-methylpyridine, and repeating the same procedure as for [Me_2Al(6-Me-2-py)$_2$Li·2THF] (**5**) (reacting the bromopyridine with ^{n}BuLi at –78 °C and later with Me_2AlCl) gave [Me_2Al(5-Me-2-py)$_2$Li·2THF], **6**. Unsurprisingly, the solid-state structures shows that compound **6** is also solvated by two THF molecules that are coordinated to the Li^+ cation through both N-atoms from each of the pyridyl ring units (Figure 3.10).

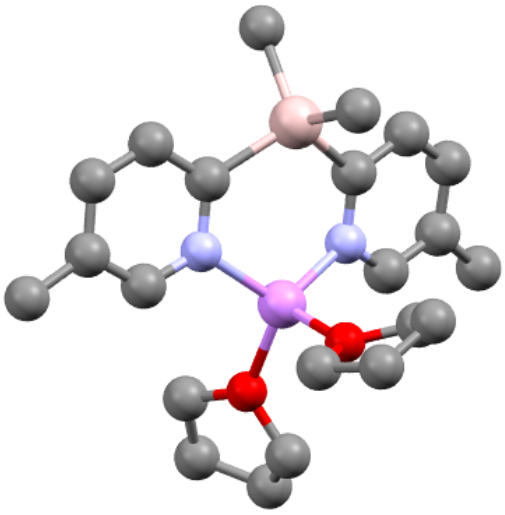

Figure 3.10: Solid-state structure of **6**. H-atoms omitted for clarity. Selected bond lengths (Å) and angles (°): C_{Me}–Al range 1.992(4)-2.003(3), C_{py}–Al range 2.026(3)-2.027(3), N–Li range 2.025(5)-2.025(5), Li–O range 1.958(6)-1.071(6), C_{py}–Al–C_{py} 111.75(13), C_{Me}–Al–C_{Me} 111.77(19), N–Li–N 115.4(2), O–Li–O 102.5(2).

Direct comparison of **6** to **5** reveals that the steric constrain is decreased as the methyl groups previously located in the 6-position, which are the cause for the steric hindrance around the Li^+ cation, are now in the 5-position. This can be observed when comparing the lengths and angles of the two species. The C_{py}–Al range for **6** is 2.026(3)-2.027(3) Å, in comparison with the one from **5**, which is 2.028(2)-2.030(2) Å. This suggests that the position of the Me group does not affect the C-Al distances.

DFT calculations were carried out on [(**4a**)LiTHF] by Dr. Schirin Hanf in order to explore the nature of the bonding within the Al-Me···Li bridge of [(**4a**)LiTHF]. The data presented here was geometry optimised at the TPSS[27]/def2-TVZP[127,128] level of theory, which produced Li–H and Li–C bond lengths that were most consistent with the X-ray structure. However, the results were also confirmed using BP86[129–131] and B3LYP[132,133] functionals. A single point calculation of the optimised structure was used for the population and NBO analyses.[134,135] From these calculations (Figure 3.11 and Figure 3.12), it can be seen that the formation of the Al-Me···Li interaction results in weakening of the Al-C bond compared to the terminal Al-C bond and a net increase in the total negative charge of the Me group (from – 1.20e for the terminal CH_3 group to –1.21e for the bridging CH_3 : – 0.59e to -0.61e for the C atoms of the bridging Me).

From the Wiberg bond order and second-order perturbation theory, the presence of a very weak interaction largely involving one of the H-atoms and the C-atom of the bridging Me-group can be assumed. A σ(C(6)-H(8))···Li delocalisation energy of 3.72 kcal mol^{-1} was computed.

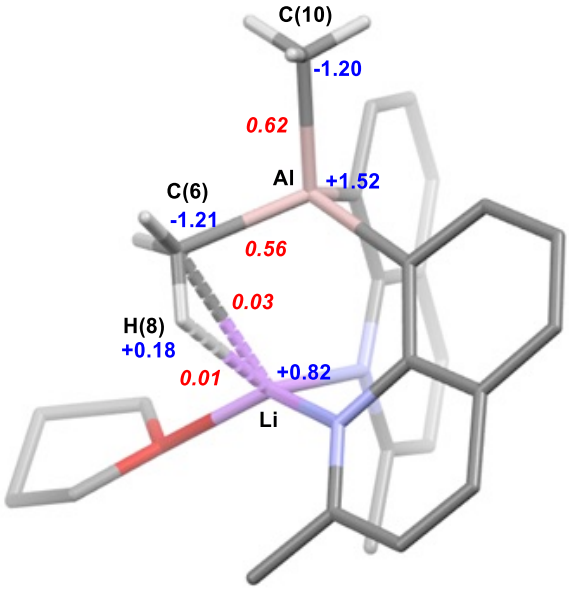

Figure 3.11: Selected natural charges (in blue) and NBO bond orders (in red) from the TPSS27/def2-TVZP28,29 optimised structure of [(**4a**)Li(THF)].

To verify the nature of this CH···Li interaction further and to classify it either as a hydrogen bond or agostic interaction, an Atoms in Molecules (AIMS) analysis was carried out (see Figure 3.12 – top).[136] From this, a bond critical point between the bridging carbon atom C(6) and the lithium was identified. The electron density at the bond critical point of the C···Li interaction is –0.402 eV, from which the bond energy for this interaction can be estimated to be 2.55 kcal mol^{-1} (in line with the NBO analysis, with the delocalisation energy of 3.72 kcal mol^{-1}).[137] However, no bond critical point could be found between the H and Li atoms using the AIMS approach. Based on the NBO results and the AIMS analysis, the distinction between a weak hydrogen bond or agostic interaction is not trivial and can lead to misassignment of the type of interaction involved.[138] However, despite the reduced charge on H(8), which is typical for agostic interactions, the geometric parameters of the Al-Me···Li bridge, such as the large Li-H···C bond angle of 117 ° and the presence of different Li···H and Li···C distances, point more towards the existence of a weak hydrogen bond rather than an agostic interaction.[139] This conclusion is in line with a recent combined experimental and theoretical study that suggested

that an NBO based σ(C-H)···M delocalisation energy of >5.0 kcal mol^{-1} is characteristic of an agostic interaction (i.e., well above the 2.55 kcal mol^{-1} calculated for the interaction in [(**4a**)LiTHF]).[140]

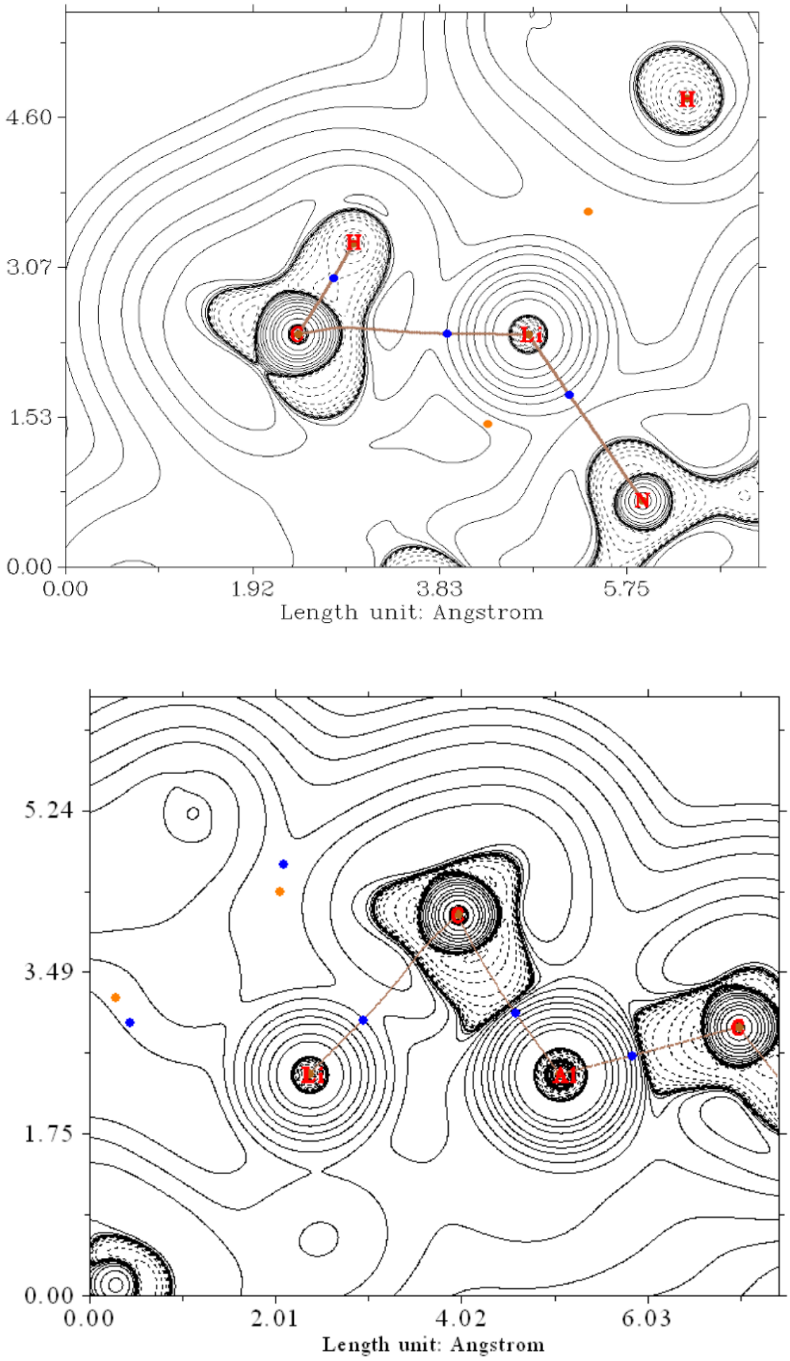

Figure 3.12: Top: Graph of the Laplacian of the electron density of compound [(**4a**)Li(THF)]. The red lines represent bond critical paths and the blue points are bond critical points within the Li(2)–C(6)–H(8) plane. Bottom: Graph of the Laplacian of the electron density of [(**4a**)Li(THF)]. Bond critical points and bond critical paths within the Al(1)-Li(2)···C(6) plane. The numbering scheme refers to that applied in the DFT calculations.

Repeated attempts to prepare the analogue of [(**4a**)Li(THF)] containing an Et_2Al bridgehead, [{Et_2Al(2-Me-8-qy)$_2$}Li(THF)] [(**4b**)Li(THF)], using the same synthetic procedure but with Et_2AlCl in place of the Me_2AlCl, unexpectedly produced the crystalline aluminate complex [{EtAl(2-Me-8-qy)$_2$}$_2$O}·(Li_2THF)] (**7**) in up to 23% yield (Scheme 3.5), with respect to Et_2AlCl supplied. The yields were found to be highly variable in this case. The complex contains an [{EtAl(2-Me-8-qy)$_2$}$_2$O}]$^{2-}$ dianion in which two Al centres are bridged together by an oxo-ligand. This arrangement apparently results from reaction of the desired product [(**4b**)Li(THF)], with adventitious H_2O during crystallisation at –20 °C or present in the solvent used. This reaction pathway was supported by the observation of ethane formation as one of the by-products, which was observed during *in situ* ^{1}H NMR spectroscopy studies. However, attempts to obtain the complex by the deliberate addition of a stoichiometric amount of H_2O after *in situ* formation of [(**4b**)Li(THF)] led only to a mixture of products (including free quinoline). Compound **7** proved to be highly moisture sensitive and was characterised only by single-crystal X-ray analysis and elemental analysis. The formation of the complex is of interest in respect to previously reported studies of the hydrolysis and alcoholysis of lithium tris-2-pyridyl-aluminate complexes, which showed that the Al-C bonds to the 2-pyridyl groups are considerably more reactive than the Al-bonded alkyl groups of the bridgehead;[53,44] the opposite to the reactivity pattern observed for the putative intermediate [(**4b**)Li(THF)]. A potential explanation for this is provided by the previously discussed DFT calculations of [(**4a**)Li(THF)], which showed that bridging of the Me-group between the Al and Li atoms results in significant weakening of the Al-C bond compared to the terminal Me-Al bond (as seen in the reduction in NBO bond order from 0.62 to 0.56).

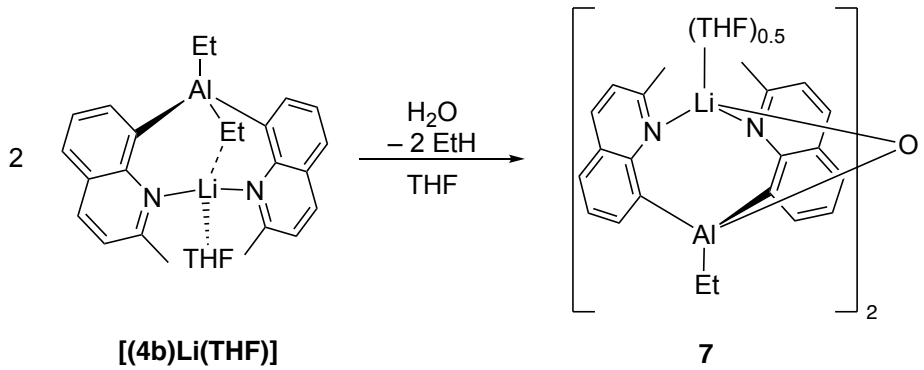

[(4b)Li(THF)] **7**

Scheme 3.5: The partial hydrolysis of [(**4b**)Li(THF)] with adventitious H_2O to form the dianion [{EtAl(2-Me-8-qy)$_2$}$_2$O}]$^{2-}$, **7**.

The molecular structure of **7** consists of a $[\{EtAl(2\text{-}Me\text{-}8\text{-}qy)_2\}_2O\}]^{2-}$ dianion in which two $[EtAl(2\text{-}Me\text{-}8\text{-}qy)_2]$ subunits are joined together by a bridged O-atom (Figure 3.13). There are two chemically distinct Li environments in this arrangement, with both Li^+ cations being coordinated by the two quinolyl-N atoms from each $[EtAl(2\text{-}Me\text{-}8\text{-}qy)_2]$ subunit (range 2.088(5)-2.175(5) Å), but with one being THF solvated while in the other the THF solvation is replaced by a long-range μ-N···Li interaction with a quinolyl-N atom of the other $[EtAl(2\text{-}Me\text{-}8\text{-}qy)_2]$ subunit (2.467(5) Å). As a result, both Li^+ cations have distorted tetrahedral geometries.

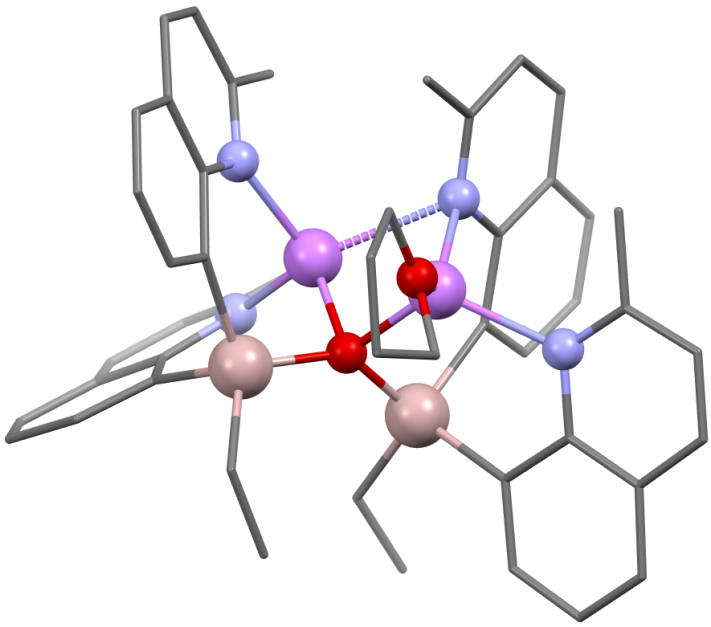

Figure 3.13: Solid-state structure of **7**. H-atoms and the lattice THF molecule have been omitted for clarity. Selected bond lengths (Å) and angles (°): C_{Et}-Al 1.995(3)-2.003(3), C_{qy}-Al range 2.015(3)-2.042(3), Al-O range 1.7693(17)-1.7720(17), N-Li range 2.088(5)-2.175(5) (the longest of these bonds is to the μ-N-quinolyl group), μ-N_{qy}···Li 2.467(5), Li-O_{oxo} range 1.926(5)-1.947(4), C_{qy}-Al-C_{qy} range 105.10(10)-106.90(10), Al-O-Al 135.47(10), N_{qy}-Li-N_{qy} 100.49(19)-107.0(2) (within each subunit), Li-(μ-N_{qy})···Li 76.52(16).

3.2.2 Quinolyl Ligands Based on Group 14 and 15: Sn and Sb

Moving from Group 13, the syntheses of neutral Group 14 and 15 tris- and bis-quinolyl ligands was also explored. To date, the only known example of tris- or bis- quinolyl ligand based on a bridgehead from Group 14 is the aforementioned $MeSi(3\text{-}qy)_3$, with no examples of heavier *p*-block-based bridgeheads having been investigated. Moreover, there have been no such

examples of any Group 15-based quinolyl ligands reported in the literature thus far, making this a rather promising area of study.

The synthesis of the tris- and bis-quinolyl Sn(IV) derivatives is similar to the Al(III) counterparts: lithium-halogen exchange of 8-bromo-2-methylquinoline with ^{n}BuLi at –78 °C in THF, followed by either a 3:1 reaction with $PhSnCl_3$ (Scheme 3.6a) or a 2:1 reaction with Ph_2SnCl_2 (Scheme 3.6b). The methyl-substituted quinoline precursor was chosen in all cases, so as to prevent decomposition of the ligands through reductive elimination.

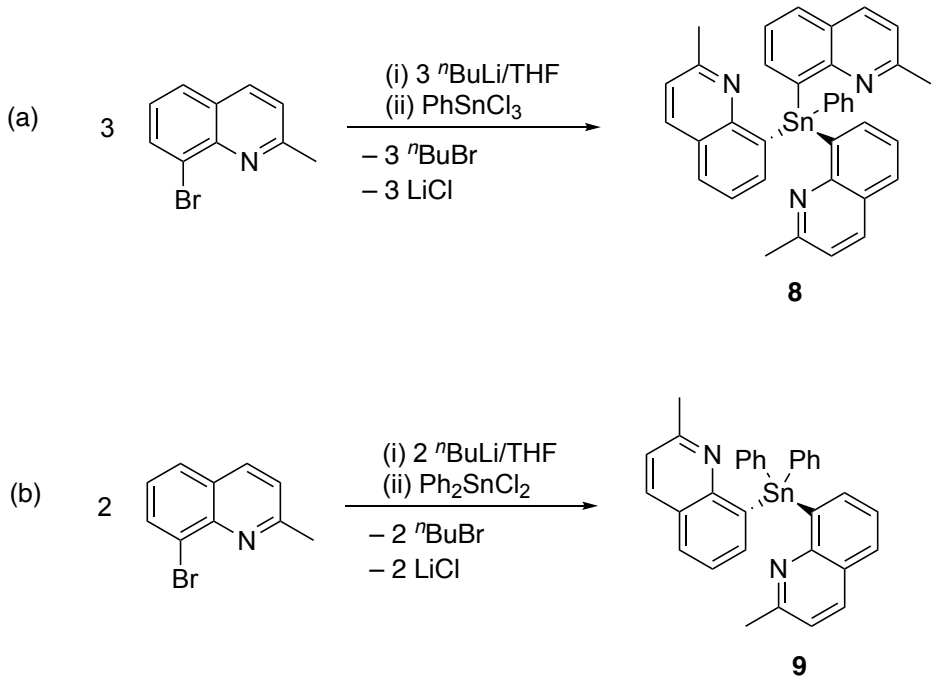

Scheme 3.6: Synthesis of (a) $PhSn(2\text{-Me-8-qy})_3$ (**8**) and its bis- counterpart $Ph_2Sn(2\text{-Me-8-qy})_2$ (**9**).

Unlike their aluminate counterparts, both $PhSn(2\text{-Me-8-qy})_3$ (**8**) and $Ph_2Sn(2\text{-Me-8-qy})_2$ (**9**) are seemingly indefinitely air- and moisture-stable. Both are readily isolated as colourless needle-like crystals after crystallisation from dichloromethane/hexane (in 57% and 45% yields for **8** and **9**, respectively), without the need for further purification. The room-temperature ^{1}H NMR spectrum for **8** in D_8-THF shows the expected 1:3 ratio of the Ph(-Sn) and 2-Me-8-qy groups, with the spectrum of **9** in the same solvent displaying the corresponding Ph_2(-Sn) and 2-Me-8-qy ratio of 1:2.

The solid-state structures of both compounds (Figure 3.14) have a monomeric arrangement and, unlike their Al counterparts, are not seen to coordinate any Li^+ cations (despite the presence of LiBr and LiCl in the reaction mixtures). This situation is similar to that seen previously for the $MeSi(6\text{-}Me\text{-}2\text{-}py)_3$ ligand which can also be isolated without lithium halide coordination,[141] but unlike that of $MeSi(2\text{-}py)_3$ which forms $MeSi(2\text{-}py)_3LiX$ (X = Cl/Br). Clearly this is a steric consequence of the Me-substituents on the quinolyl rings, which are adjacent to the N-donor atoms.

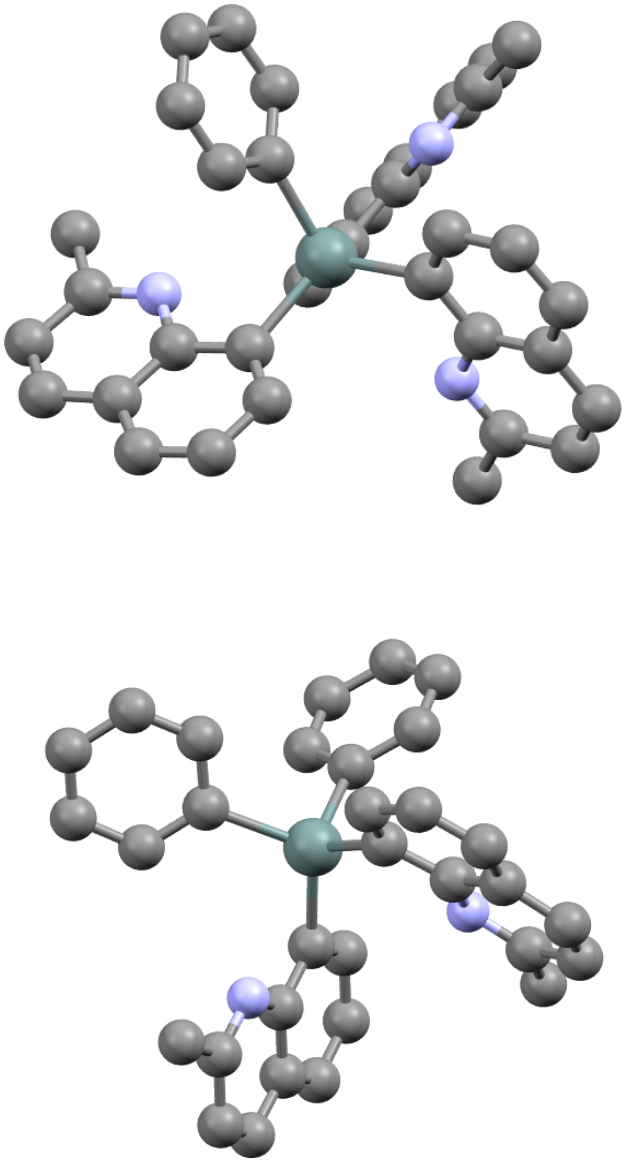

Figure 3.14: Top: Solid-state structure of $PhSn(2\text{-}Me\text{-}8\text{-}qy)_3$ (**8**). Selected bond lengths (Å) and angles (°) Sn–C_{qy} 2.150(3), Sn–C_{py} 2.151(3), C_{qy} –Sn–C_{qy} 104.3(4), C_{qy} –Sn–C_{py} 102.5(7). Bottom: Solid-state structure of the bis- counterpart $Ph_2Sn(2\text{-}Me\text{-}8\text{-}qy)_2$ (**9**). Selected bond lengths (Å) and angles (°) Sn–

C_{py} 2.149(2), Sn–C_{qy} 2.129(2), C_{qy} –Sn–C_{qy} 104.3(4), C_{qy} –Sn–C_{py} 102.5(7). H-atoms have been omitted for clarity.

The structures demonstrate the tetrahedral structure around Sn in each case, and are comparable to the tris-3-pyridyl-stannane in that the pyridyl-N atoms are orientated towards the Sn(IV) bridgehead. The only noticeable interactions between molecules of **8** in the crystal lattice are weak π - π interactions between quinolyl rings of neighbouring molecules (ca. 3.32 Å). However, the ring units involved are not parallel to each other, and although the distance involved in this interaction is consistent with a graphitic interaction, it is unclear at this point whether this is significant.

As part of another background study, the novel bis-pyridyl ligand $Ph_2Sn(3\text{-py})_2$, **10**, was synthesised, in order to provide a direct comparison to its tris-counterpart $PhSn(3\text{-py})_3$,[16] but also to the bis-quinolyl compound **9**. The synthesis and workup of **10** are akin to that of $PhSn(3\text{-py})_3$, and is obtained through the one-pot reaction of 3-bromopyridine and the Turbo-Grignard $^{i}PrMgCl{\cdot}LiCl$ at –15 °C,[112] followed by addition of Ph_2SnCl_2 (Scheme 3.7). The solid-state structure of **10** is shown in Figure 3.15.

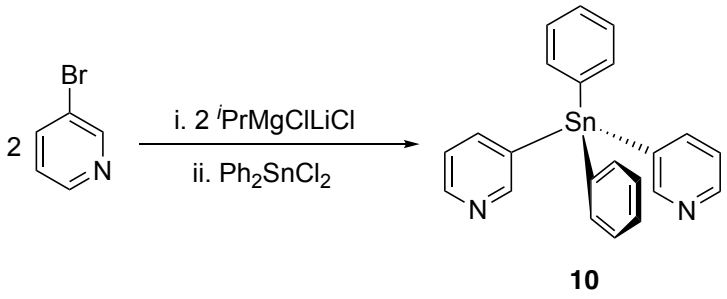

10

Scheme 3.7: Synthesis of bis-pyridyl ligand $Ph_2Sn(3\text{-py})_2$.

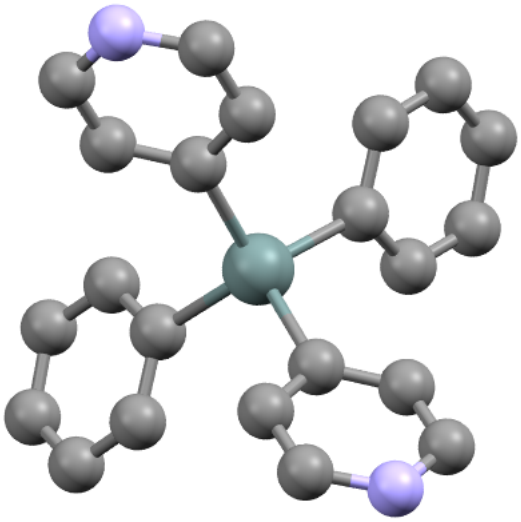

Figure 3.15: Solid-state structure of **10**. Selected bond lengths (Å) and angles (°): Sn(1)-C_{py} 2.141(3), C_{py}-Sn(1)-C_{py} 109.4(8).

As with the quinolyl ligand set, the crystal structure of **10** demonstrates the tetrahedral environment of Sn, with both the bond lengths and angles all within the ranges expected (when compared to the aforementioned tris-pyridyl stannane ligand, $PhSn(3\text{-}py)_2$).

The coordination behaviour of **8** was briefly examined. The reaction between AuCl(THT) (THT = tetrahydrothiophene) and **8** (1:1 equiv.) in THF yielded $[Au(2\text{-}Me\text{-}8\text{-}qy)]_4$ (**11**, Scheme 3.8).

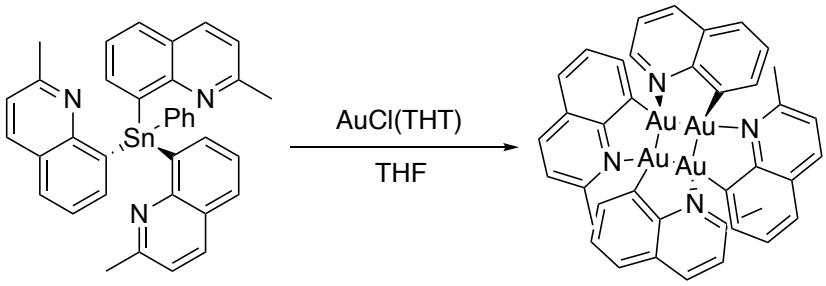

8 **11**

Scheme 3.8: Formation of the Au quinolyl complex $[Au(2\text{-}Me\text{-}8\text{-}qy)]_4$, (**11**).

Characterisation of this compound (other than single-crystal X-ray crystallography) was not straightforward since only approximately 1 mg of crystalline material was isolated, with the ^1H

NMR in CD_2Cl_2 indicating the presence of both the desired compound **11** (major peaks) along with a minor compound consisting of six resonances in the aromatic region (Figure 3.16).

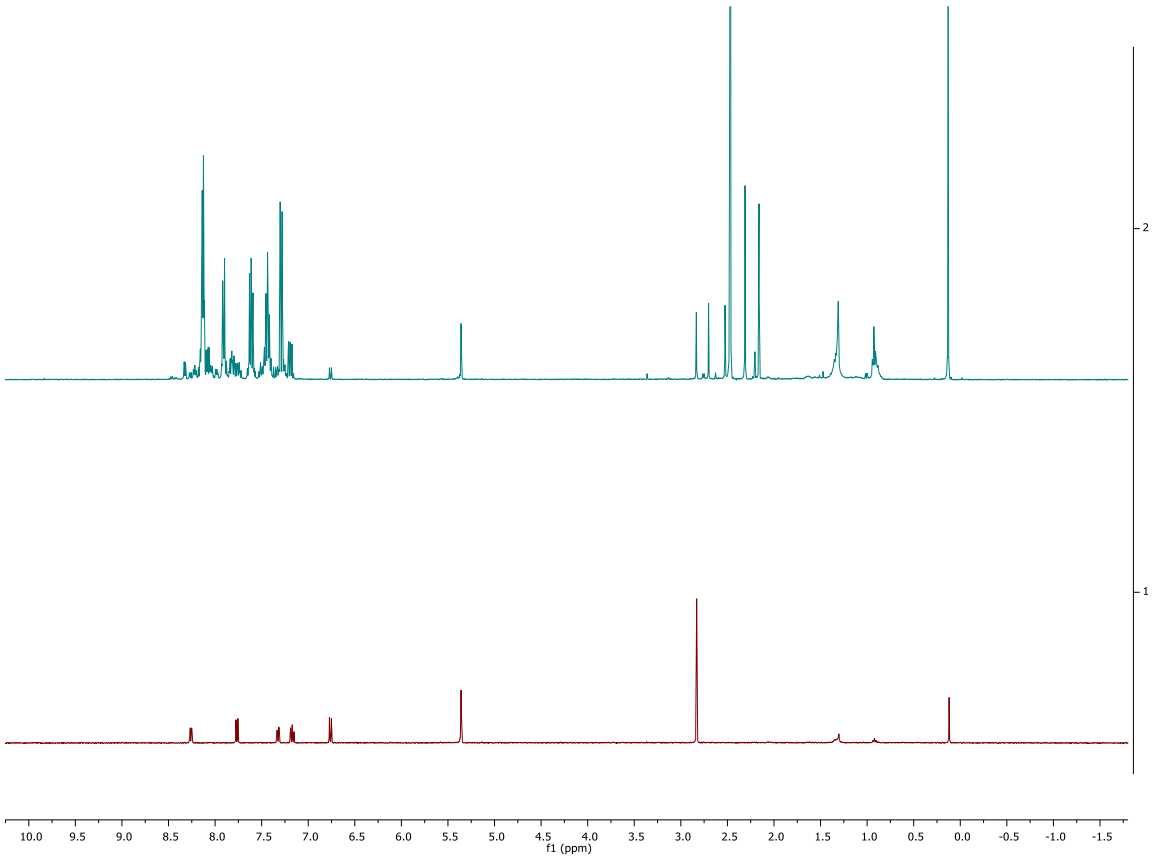

Figure 3.16: ^{1}H NMR spectra of **11** (both in CD_2Cl_2). Red: ^{1}H NMR of the crystalline product of **11**; Blue: ^{1}H NMR of filtrate (from the solution of which crystals were grown).

The ^{1}H NMR spectroscopy of the reaction filtrate showed one major product along with approximately six other components. The major product is evidently not the crystalline material. These (aromatic) peaks most likely belong to 2-methylquinoline (6-Me-Hqy), which is presumably formed by protonation at the Sn-C_{qy} bonds of **8** due to trace water present in the solvent, and are similar to those seen previously for 6-Me-Hqy in $CDCl_3$.[142] Ligand decomposition such as this may not be surprising, given the reactivity of Sn-aryl compounds.[143]

The solid-state structure of **11** comprises a 4-membered ring consisting of four Au(I) atoms, each bound to either a C or N atom from flanking quinolyl groups. Due to the crystallography data being of a relatively low quality, it will not be appropriate to discuss bond lengths/angles

in great detail. Nonetheless, the structure has been unambiguously characterised in the solid state (Figure 3.17).

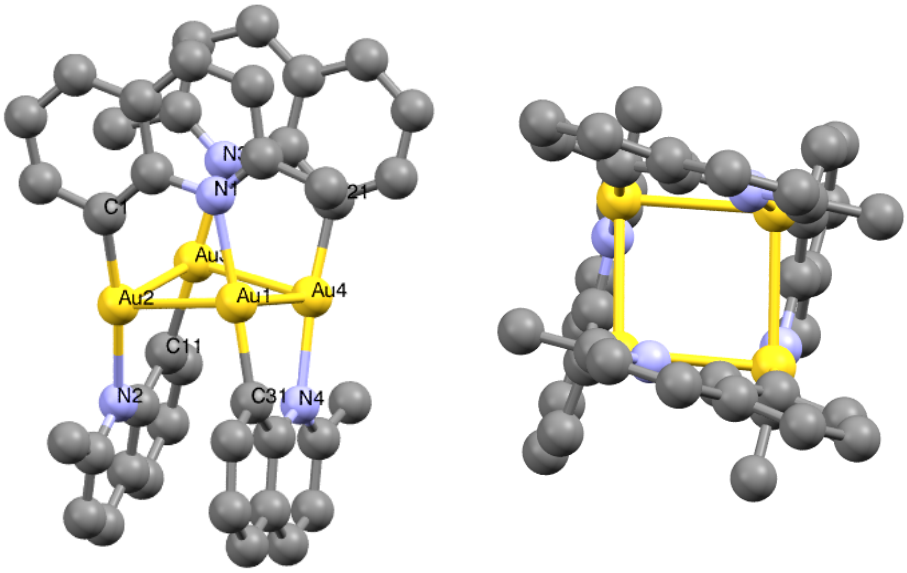

Figure 3.17: Solid-state structure of $[Au(2\text{-Me-8-qy})]_4$, (**11**). View of molecule approximately in the Au_4 plane (left), and perpendicular to this plane (right). Selected bond lengths (Å) and angles (°) Au(1)-C(31) 2.004(15), Au(2)-N(1) 2.178(11), Au(1)-Au(2) 2.8813(9), Au(2)-Au(3) 2.8532(8), Au(3)-Au(4) 2.8526(8), Au(4)-Au(1) 2.8505(8) Au(1)-Au(2)-Au(3) 85.12(2). H-atoms omitted for clarity.

The four Au-Au bonds vary from 2.8505(8) to 2.8813(9) Å in length, which are similar to closed-shell interactions observed in a number of structurally characterised compounds, a related example being the dication $[Ag_4L_2]^+(PF_6)_2^-$, (L = 3,5-bis((*N*-methylimidazoliumyl(methyl)pyrazolyl), with metal···metal distances of 3.276(1) and 3.292(1) Å.[144]

As part of a broader study, the synthesis of heavy Group 15-bridged quinolyl ligands was also investigated. A similar synthetic procedure involving lithiation of 8-bromo-2-methylquinoline in THF and *in situ* reaction of the intermediate lithioquinoline in a 3:1 stoichiometric ratio yielded the stibine compound $Sb(2\text{-Me-8-qy})_3$ (**12**) (Scheme 3.9). The decomposition of **12** was also examined and was evident upon formation of a white precipitate during its attempted synthesis, suggesting that it is rather unstable towards moisture and/or oxygen.

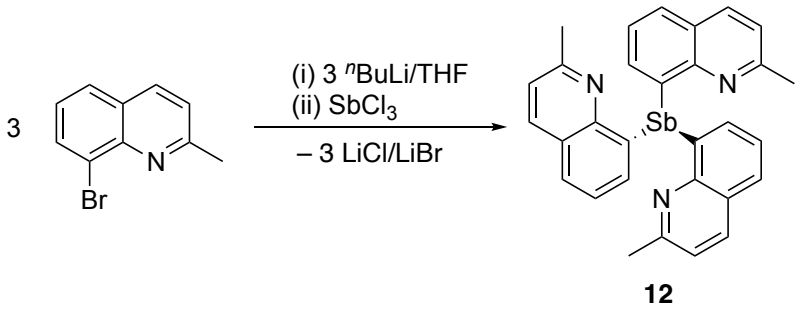

Scheme 3.9: Synthesis of Sb(2-Me-8-qy)$_3$, (**12**).

Ligand **12** was isolated in 49% yield after crystallisation from layering hexane onto a solution of the ligand in dichloromethane at room temperature, which afforded crystals suitable for X-ray diffraction. **12** was further characterised by ^{1}H NMR spectroscopy and elemental analysis, with the latter indicating only trace amounts of lithium halide impurities in crystalline samples of **12**, which was further confirmed by the single-crystal data. The solid-state structure of **12** (Figure 3.18a) is that of a monomer, and is comparable to the pyridyl counterpart, Sb(6-Me-2-py)$_3$, in which the 2-Me groups and N-atoms of the quinolyl ring are orientated "upwards", towards the lone pair on Sb (Figure 3.18b).[102] Interestingly, in the lattice of **12** the quinolyl ring units of two neighbouring molecules interdigitate (Figure 3.18c), forming a sixfold 'sextuplet embrace'- a bonding interaction first recognised by Dance and co-workers in 2002.[145] This differs from the behaviour seen in compound **16**, later introduced in Chapter 4, in which the Bi···N interactions are found.

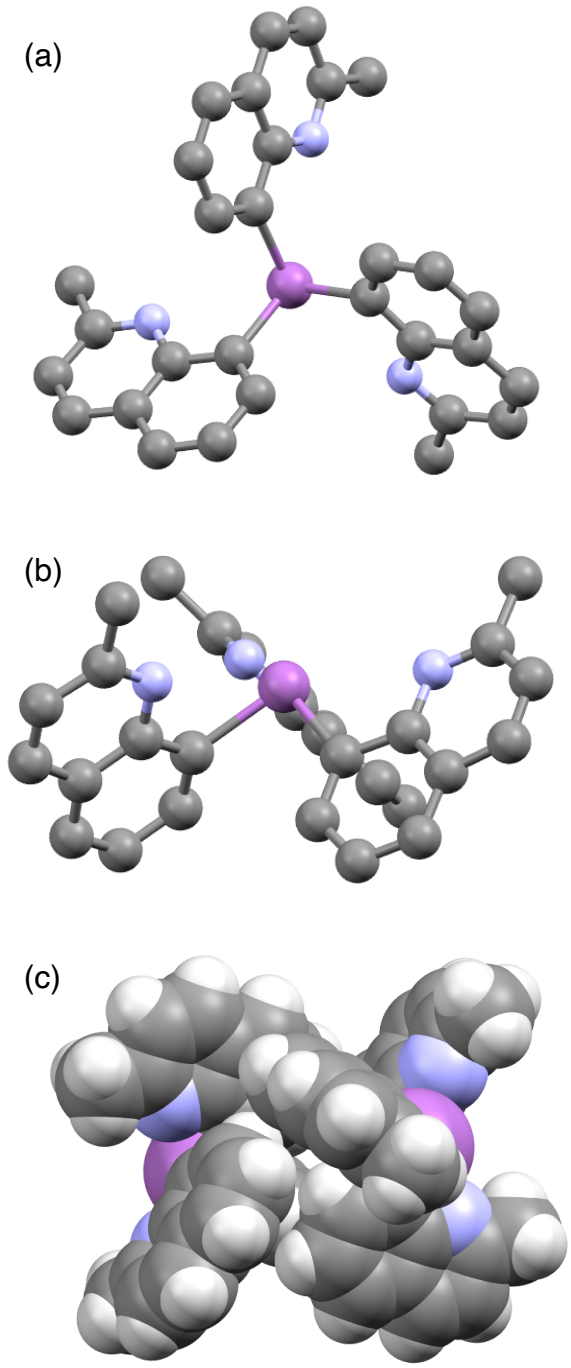

Figure 3.18: Top: Solid-state structure of **12**. Selected bond lengths (Å) and angles (°) Sb–C_{qy} 2.165(3), C_{qy}–Sb–C_{qy1} 94.08(12). Middle: H-atoms omitted for clarity. Orientation of 2-Me groups and N-atoms of the quinolyl ring units towards the lone pair on Sb. Bottom: Space-filling model of **12**, indicating the sextuplet embrace of two neighbouring molecules. (bottom).

Like the aforementioned Sn(IV) counterparts, the absence of LiCl/LiBr coordination in **12** presents a technical advantage as there is no requirement to separate LiCl/LiBr from reaction

products after transfer of the ligand to metal centres - owing to the presence of the qy-Me group as previously stated.

The coordination behaviour of **12** was explored with several transition metal salts and organometallic precursors. In most cases, decomposition resulted in the formation of intractable mixtures and Sb metal. However, the 2:1 reaction of **12** with $[RuCl_2(p\text{-cymene})]_2$ (cymene = 1-Methyl-4-(propan-2-yl)benzene) refluxed in MeCN under nitrogen produced $Sb(2\text{-Me-8-qy})_2Cl$, **13** in 64% yield (Scheme 3.10). A similar reaction has been seen previously in the literature between tri(pyridylmethyl)phosphine (TPPh) and ruthenium(II), which resulted in the complexation of the Ru centre with the P-bridgehead and two of the N-donor atoms.[146]

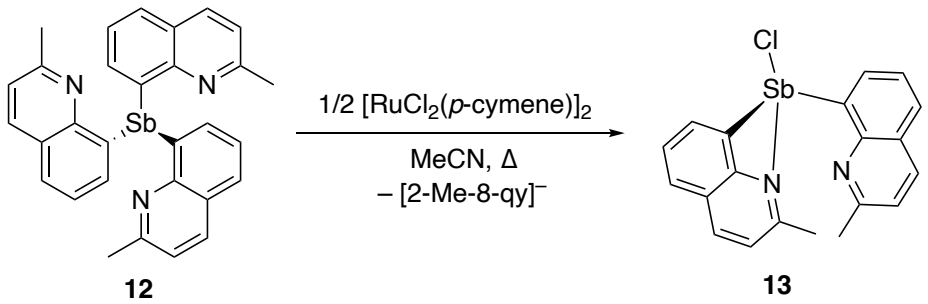

12 **13**

Scheme 3.10: Reaction of **12** with $[RuCl_2(p\text{-cymene})]_2$, leading to the formation of Sb(2-Me-8-qy)Cl, (**13**).

The solid-state structure of **13** is shown in Figure 3.19. The structure is that of a monomer, in which one of the 2-Me-8-qy substituents of **12** has been substituted for a Cl atom. This suggests that **12** simply acts as a source of the $[2\text{-Me-8-qy}]^-$ anion in a ligand-exchange reaction with $[RuCl_2(p\text{-cymene})]_2$, with the quinolyl-N donor atom coordinating to the Ru(II) centre. This behaviour is not surprising, due to the strongly-coordinating nature of acetonitrile as the solvent and the strong affinity of nitrogen to Ru(II) centres. However, attempts to identify other products of the reaction using ^1H NMR spectroscopy were unsuccessful, showing a range of other unidentified products were formed. In addition to the Cl atom, the Sb(III) centre of **13** is also bonded to two 2-Me-8-qy ligands. One of these is bonded only by its 8-C atom to the Sb(III) atom (2.154(2) Å), while the other is bonded in a chelating mode, using both the 8-C atom (2.161(2) Å) and the donor N-atom of the quinolyl group (2.708(2)Å). The Sb-N bond in **13** has a similar bond length to that seen previously in donor-type Sb-N bonds, e.g. in the

organoantimony(III) sulfide $(LSbS)_2$, (L = chelating ligand C_6H_3-2,6-$(CH_2NMe_2)_2$) with an Sb-N bond length of 2.58 Å (average).[147]

In terms of the packing of compound **13**, there are long-range π-π interactions involving the chelating quinolyl groups of neighbouring molecules (ca. 3.08 Å).

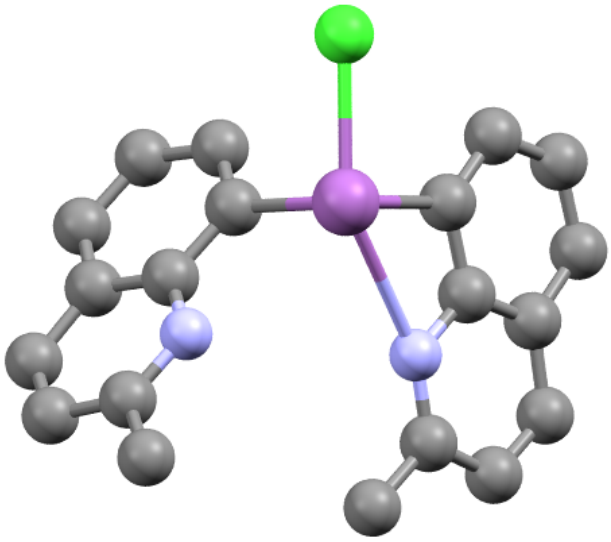

Figure 3.19: Solid-state structure of **13**. Selected bond lengths (Å) and angles (°): Sb–C_{qy1} 2.154(2), Sb–C_{qy2} 2.161(2), Sb–Cl 2.4594(6), Sb–N_{qy} 2.703(3), C_{qy}–Sb–C_{qy1} 93.83(8).

Despite the fact that the Sb–N interaction in **13** is only present between the Sb(III) bridgehead and one of the quinolyl ring units in the solid-state structure, the room-temperature ^{1}H NMR spectrum shows only one set of quinolyl resonances, suggesting fluxional interchange between the two ligand bonding modes (Scheme 3.11).

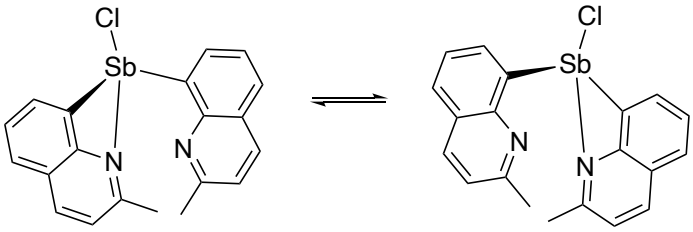

Scheme 3.11: Scheme showing fluxional interchange between two bonding modes in **13**.

However, variable-temperature ^{1}H NMR spectroscopy revealed no splitting of the quinolyl resonances down to 213 K (Figure 3.20) in increments of ca. 6 K, indicating that this fluxional process is too fast on the NMR timescale to be observed.

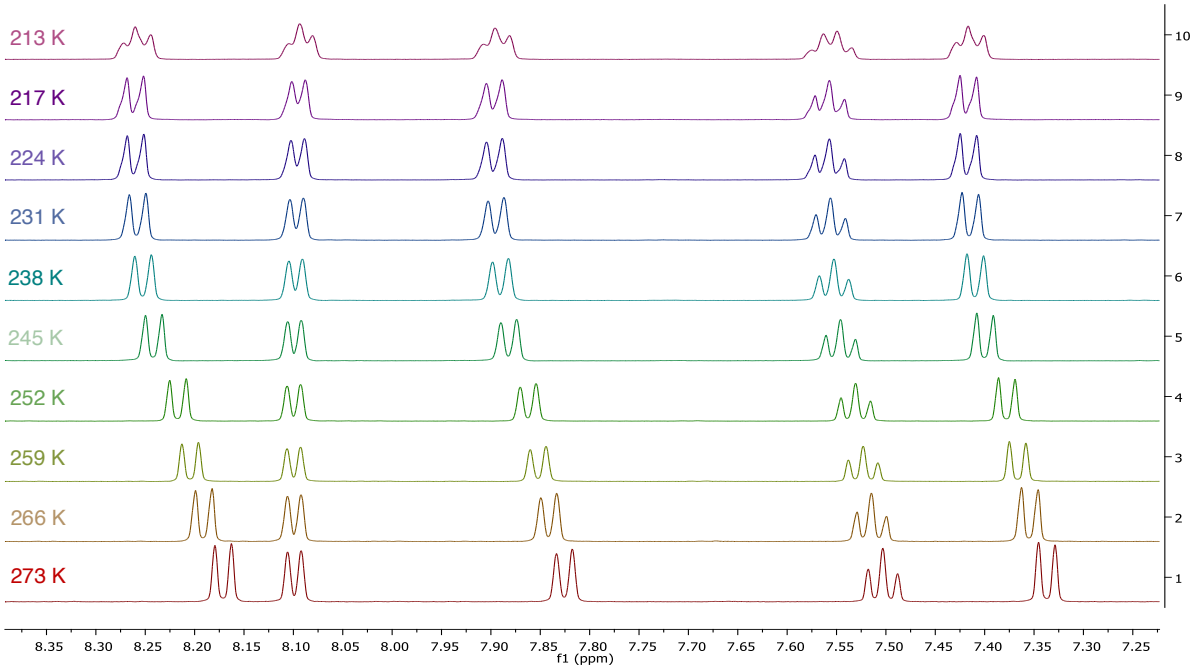

Figure 3.20: Variable-temperature ^{1}H NMR spectrum of **13** in D_8-THF, showing the aromatic region.

The coordination behaviour of **12** was further explored in its reaction with AuCl(THT) in 1:1 THF:DCM, yielding Sb(2-Me-8-qy)$_3$AuCl, (**14**) (Scheme 3.12). The solid-state structure is shown in Figure 3.21. The complex consists of monomers in which the Sb(III) lone pair of the bridgehead forms a donor interaction to Au(I) (2.843 Å), which is in line with similar Sb-Au examples form the literature, [Mes$_3$SbAuCl] = 2.510 Å.[148] The observation of ligand **12** acting as an Sb(III) donor to Au(I) in **14** contrasts with the behaviour of the Sn(IV) ligand **8** for which quinolyl transfer was observed in the formation of **11** (Figure 3.17). The reasons for this difference are currently unclear. However, one potential reason is the higher Pauling electronegativity of Sb (2.05) compared to Sn (1.95) which leads to greater ionic character in the Sn-C bonds of **8** than in **11** (hence, greater development of negative charge on the 8-C atom of the quinolyl groups of **8**).

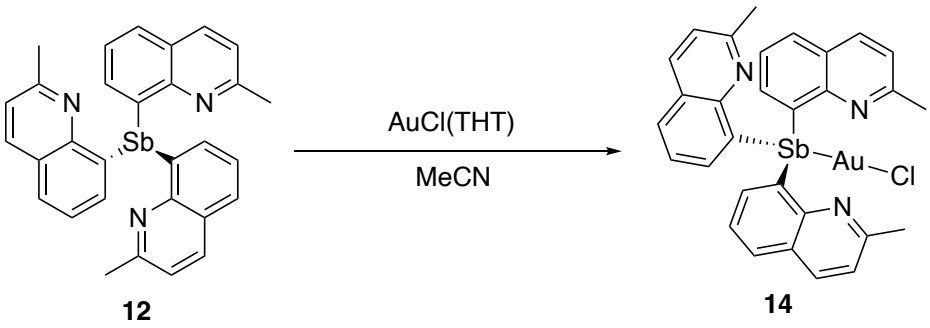

Scheme 3.12: Reaction of **12** with AuCl(THT) in 1:1 THF:DCM, leading to the formation of Sb(2-Me-8-qy)$_3$AuCl, **14**.

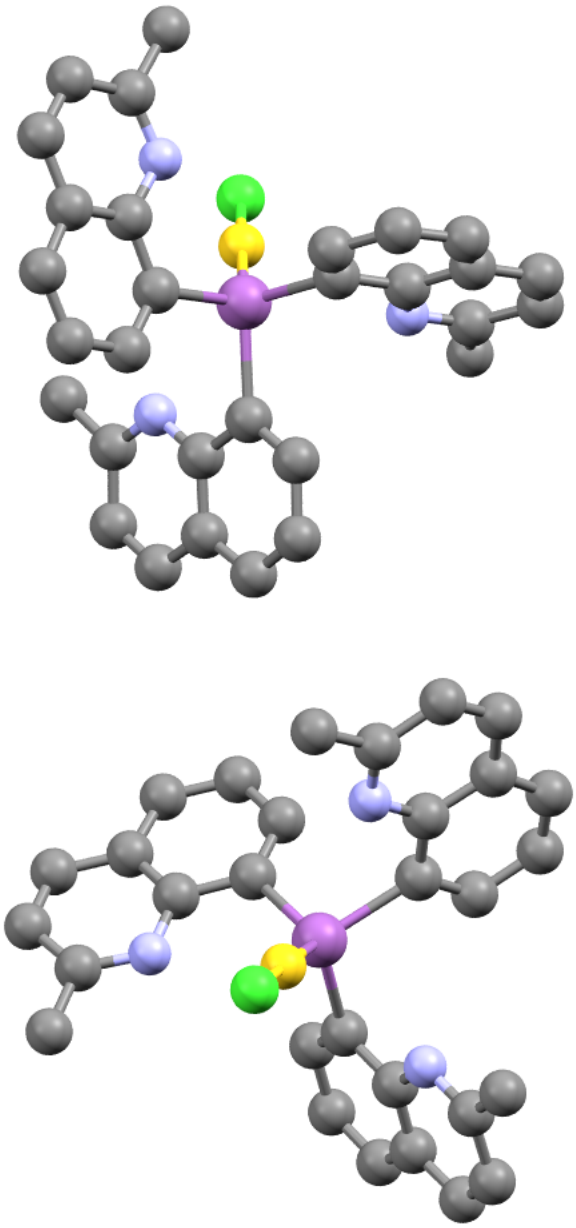

Figure 3.21: Solid-state structure of **14**. Selected bond lengths (Å) and angles (°): Sb–C_{qy} 2.129(8), Sb–Au 2.4834(6), Au–Cl 2.284(2), C_{qy}–Sb–C_{qy1} 98.1(3). H-atoms omitted for clarity.

3.3 Conclusions

The results of this investigation show that moving the donor N-atom from the 2-position of 2-quinolyl groups to the more remote position in 8-quinolyl substituents can have a large effect on the coordination of Li^+ cations in the corresponding aluminate complexes. This is seen perhaps most dramatically in the structure of [{EtAl(2-Me-8-qy)$_3$}Li] (**3**Li), in which the Li^+ cation has an unusual three-coordinate, trigonal planar arrangement stemming from a combination of steric effects and the geometric constraints of the donor-N atoms. The bis-

quinolyl aluminate complex [{Me_2Al(2-Me-8-qy)$_2$}Li(THF)] (**4a**Li) is of particular interest, in which N-donor bonding in the tris(2-Me-8-qy) aluminate is replaced by a bridging agostic interaction. The *in situ* reaction of closely related complex [{Et_2Al(2-Me-8-qy)$_2$}Li(THF)] (**4b**Li) with H_2O occurs selectively with one of the Et groups, giving the novel, O-bridged [{EtAl(2-Me-8-qy)$_2$}$_2$O}]$^{2-}$ dianion. This reactivity is the opposite of that seen in the case of tris-2-pyridyl-aluminates [RAl(2-py)$_3$]$^-$, in which the 2-py groups are more basic than the R-group.

Further studies of Sn(IV) and Sb(III) tris- and bis-quinolyl complexes containing the 2-methyl-8-quinolyl ligands were successful in obtaining representative ligand arrangements (which, unlike the aluminates, are neutral). These ligands exhibit two types of reactivity with transition metals – quinolyl ligand transfer and (where lone pairs on the bridgehead are available) lone pair donation.

Overall, it can be concluded that the replacement of 2-pyridyl functionality with 8-quinolyl groups can result in some major differences in coordination behaviour, especially in respect to aluminate chemistry.

4

4. Synthesis of Tris-4-Pyridyl Ligands: Topological Complexity Derived from the Bridgehead

4.1 Preface

In comparison to all other classes of tris-pyridyl ligands, the number of tris-4-pyridyl ligands studied has been significantly more limited, as mentioned in Chapter 1. This is thought to be due to the fundamental problem of the unreliability of the metal-halogen exchange reactions that generate the 4-lithiopyridine intermediates from the corresponding 4-halogeno-pyridines. This was also identified as a fundamental problem in the synthesis of any of the 3-pyridyl ligand systems.[149,150] Whilst a straightforward route to accessing heavier Group 14-based tris-3-pyridyl ligands has since been developed using a Turbo-Grignard reagent in the metal-halogen exchange reaction,[16] in comparison very few studies have explored the efficient synthesis of 4-pyridyl counterparts.

Upon the incorporation of a N-donor functionality at the 4-position of the pyridyl ring units, a fundamental change in the character of the ligand is expected: from intramolecular for 2-pyridyl substituents to intermolecular for 3- and 4-pyridyl groups (Figure 4.1, see also Chapter 1 Sections 1.3 and 1.4). Such structural changes introduce the prospect of forming supramolecular assemblies as a result of bridging ligands between metal centres.

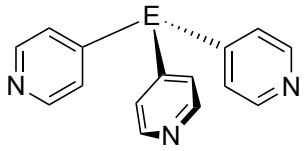

Figure 4.1: General framework of neutral tris-4-pyridyl ligands E(4-py)$_3$ (E = CR (R = alkyl or H), N, P, As), containing non-metallic main group bridgehead atoms/groups.

A rare example of a structurally characterised complex containing this type of ligand set is the carbon bridgehead tetra-4-pyridyl ligand C(4-py)$_4$, which functions as a tetrahedral node in the diamondoid lattice arrangement of [AgBF$_4${C(4-py)$_4$}] (Scheme 4.1).[151] Furthermore, carbon-bridgehead systems have been successfully used as scaffolds in a small number of Pd/Pt-based supramolecular cages,[152–154] and, in one instance, a Zn coordination polymer.[155]

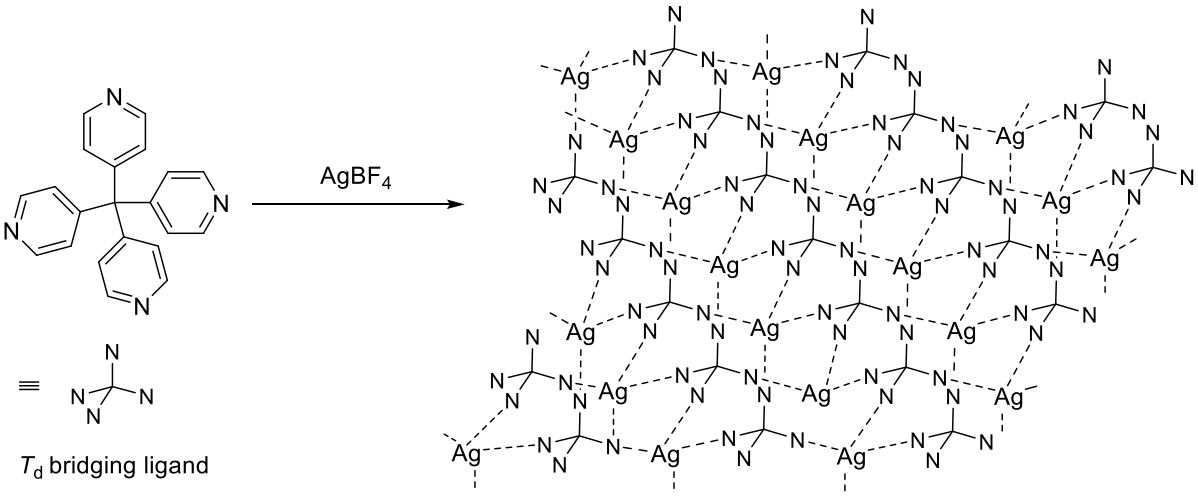

Scheme 4.1: Schematic diagram of three-dimensional diamondoid coordination network of silver(I) tetrafluoroborate complex of C(4-py)$_4$. Dotted lines show coordination bonds between silver and nitrogen. The BF_4^- anions are located in the pores within this network.

A novel supramolecular arrangement was reported by P. J. Stang and co-workers involving the 1:3 reaction of the Group 14 bridgehead ligand MeSi(4-py)$_3$ with strongly Lewis acidic [$Rh_2(O_2CCF_3)_4$], yielding a discrete pyramid-shaped hexanuclear complex, terminated by η^2-bonded benzene ligands.[120] Switching the bridgehead atom for a Group 15 element is of particular interest and the nitrogen bridgehead ligand N(4-py)$_3$ was first prepared by N. S. Al Zayed and co-workers (Scheme 4.2).[156] The tunability of these molecules and the ability to modify their specific properties can be seen with their HOMO-LUMO gap, which can be fine-tuned by attaching or removing electron-withdrawing substituents on the 4-pyridyl rings and by quaternization of the N-atoms (pyridine vs. pyridinium acceptors).[156]

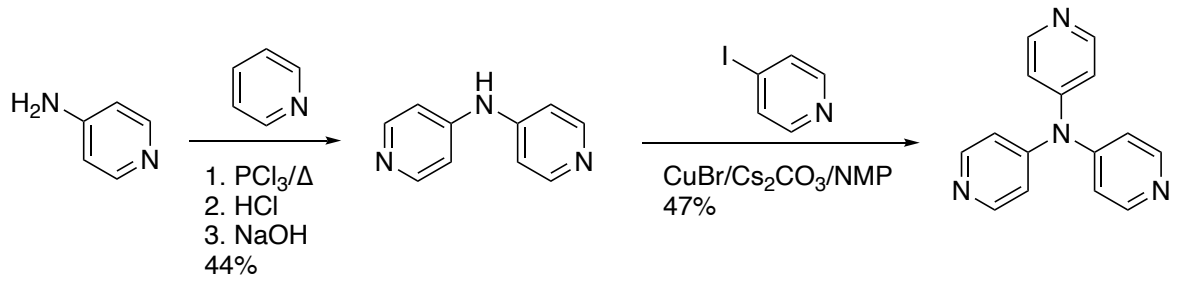

Scheme 4.2: Synthetic methodology towards N(4-py)$_3$ ligand, NMP = N-Methyl-2-pyrrolidone. Numbers indicate yields.

The only recent structural report on heavier tris-4-pyridyl compounds was the synthesis of a range of perfluorinated derivatives of the type $E(C_5F_4N)_3$ (E = As, Sb, Bi) which were prepared via an unusual route involving the elemental pnictogens (Scheme 4.3). Only the electron-poor arsenic derivative, $As(4\text{-}C_5F_4N)_3$, could be characterised in the solid state, where a π···π stacking motif was observed between the heterocyclic rings.[106] Despite the fact that Sb and Bi homologues could not be crystallised, NMR spectroscopy and mass spectrometry confirmed that the corresponding moisture-sensitive Sb and Bi compounds were indeed prepared.

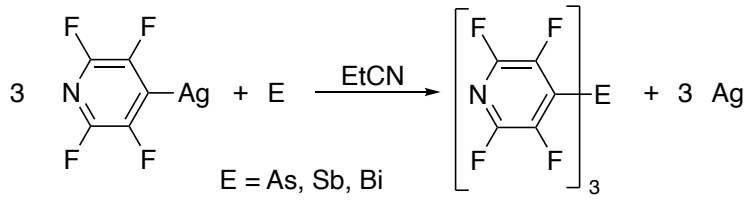

Scheme 4.3: Redox transmetallations of AgC_5F_4N and As, Sb and Bi.

Studies of the coordination behaviour of tris-3- and 4-pyridyl ligands have so far been limited to only a few $E(3\text{-py})_3$ (E = P, MeSi, PhSn)[149,15,16] as mentioned in Chapter 1, and $E(4\text{-py})_3$ (E = CR, N, P, MeSi)[151,88,114,116–120] ligands, as mentioned here and later in this Chapter. More significantly, the coordination chemistry of tris-4-pyridyl ligands containing the heavier, more metallic *p*-block bridgeheads is a totally unexplored area.

The work in this Chapter focuses on the heavier Group 14 and 15 tris-4-pyridyl ligands $E(4\text{-py})_3$ (E = Sb, Bi and PhSn), not just because of the scarcity of fundamental structural knowledge for the heavier congeners, but also because of their obvious potential to act as building blocks for supramolecular, three-connected polyhedral (Figure 4.2a), and tetrahedral nodes in MOFs (MOFs), (Figure 4.2b). In addition to this, a distinct feature of the heavier homologues of tris-4-pyridyl ligands is the far greater Lewis acidity of the bridgehead atoms, resulting in the prospect of these atoms to act not only as donors but also as acceptors to counterions and Lewis base donors (Figure 4.2c).

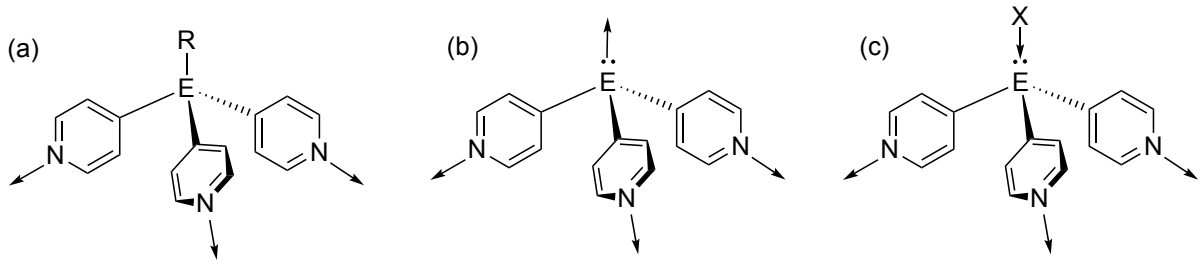

Figure 4.2: (a) An N,N,N-coordination mode, (b) an N,N,N/E-coordination mode and (c) an N,N,N-coordination with the bridgehead acting as an acceptor to an anion or Lewis base donor (E = main group-based bridgehead atom/group).

Relevant to the idea of using tris-4-pyridyl main group ligands to build metal organic frameworks is the use of organic N-donors,[157] as well as main group elements as structure-directing units in crystal engineering and supramolecular chemistry.[158] However, the potential to build new MOFs using main group metal-based ligands has not been explored systematically in tris-pyridyl systems, even for the phosphorus counterpart, $P(4\text{-py})_3$, which has been known for a number of years.[83] All of these considerations suggest that the metal-based Group 15 ligands should have a rich and multifaceted coordination chemistry.

Some of the following sections were published in: J. E. Waters & G. Berger, A. J. Peel, R. García-Rodríguez, A. D. Bond and D. S. Wright, *Chem. Eur. J.*, 2021, **27**, 12036-12040. This work was carried out in collaboration with ERASMUS student and supervisee Georg Berger.

4.2 Ligand Design and Synthesis of Sb-, Bi- and PhSn-Bridged Tris-4-Pyridyl Ligands

The initial hurdle in the development of this area proved, as initially anticipated, to be finding a reliable method to generate the 4-lithiopyridine intermediate (4-Li-py) used in the synthesis of the tris-4-pyridyl ligands. Previous syntheses of $P(4\text{-py})_3$ have predominantly used 4-iodopyridine as a precursor, which can be lithiated under various conditions.[83] These include the use of *n*-butyllithium as the metalating source under various conditions, including activation with TMEDA (TMEDA = tetramethylethylenediamine). It is clear from these previous studies that the temperature used in the formation of 4-lithiopyridine, the choice of solvent and the reaction time are all critical to the successful formation of this key intermediate. However, one major drawback is that 4-iodopyridine is thermally- and photolytically-unstable,

and commercially supplied material proved to be highly impure. Direct experience of this was obtained from initial work on this area as part of the current study in which commercially supplied 4-iodopyridine was received as a dark brown/black impure material (Aldrich), containing what appeared to be a large percentage of insoluble polymeric residue. Attempts to purify this by crystallisation or high-vacuum low-temperature sublimation (in the dark) were unsuccessful.

In order to circumvent this issue, 4-bromopyridine hydrochloride was adopted as the precursor, which is stable indefinitely under ambient conditions and is much cheaper than the iodide. Free 4-bromopyridine is readily obtained from the hydrochloride by reaction with $NaHCO_3$ in H_2O and this can be stored for a week at –14 °C in the dark without significant decomposition occurring.[114] Using D_2O quenching experiments, the metalation procedure was optimised using a range of conditions, solvents and reaction times under dry nitrogen atmosphere. Table 4.1 shows the various metalation reagents and conditions that were investigated. After metalation, the reaction mixtures were quenched with D_2O (Scheme 4.4), and the product mixtures were analysed by ^1H NMR spectroscopy to quantify the amount of deuterated pyridine produced. Deuterated pyridine indicated a successful metalation, undeuterated pyridine is probably formed by the presence of H_2O in the D_2O and/or by unknown side-reactions. Figure 4.4 shows the ^1H NMR spectra of the various D_2O-quenched reactions described in Table 4.1. The labels A, B, C, and D correspond to the proton environments indicated in Figure 4.3. On the basis of these data, the use of *n*-butyllithium as the metalation reagent was preferred over magnesiation with a Turbo-Grignard reagent (in terms of reaction time and cost). This is different to the previous observations for metalation of 3-bromopyridine, which only works effectively using the Turbo-Grignard.[112]

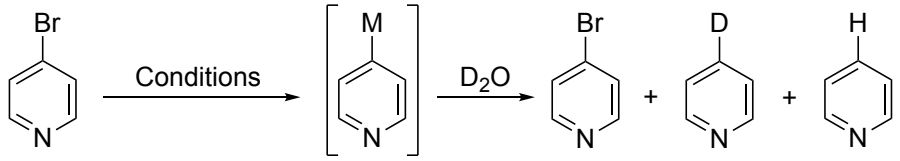

Scheme 4.4: Quenching of the metalated intermediate using deuterium oxide.

Table 4.1: Results of the optimisation experiment of the halogen/metal exchange. Results are relative concentrations determined by ^{1}H NMR spectroscopy.

	Metalation Reagent	T, t	Solvent	4-Br-pyridine	4-D-pyridine	4-H-pyridine
1	1.0 eq. ^{i}PrMgCl·LiCl	–78 to –30 °C, 16 h	THF	97	3	
2	1.0 eq. ^{i}PrMgCl·LiCl	–78 to –30 °C, 16 h	Et_2O	55	45	
3	1.0 eq. ^{i}PrMgCl·LiCl	rt, 10 min	THF	42	50	8
4	1.2 eq. ^{i}PrMgCl·LiCl	rt, 24 min	THF	18	70	12
5	1.2 eq. ^{i}PrMgCl·LiCl	rt, 40 min	THF	9	81	10
6	1.0 eq. ^{n}BuLi	–78 °C, 4 min	THF	3	89	8

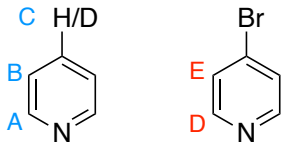

Figure 4.3: Indication of proton environments corresponding to peaks in Figure 4.4.

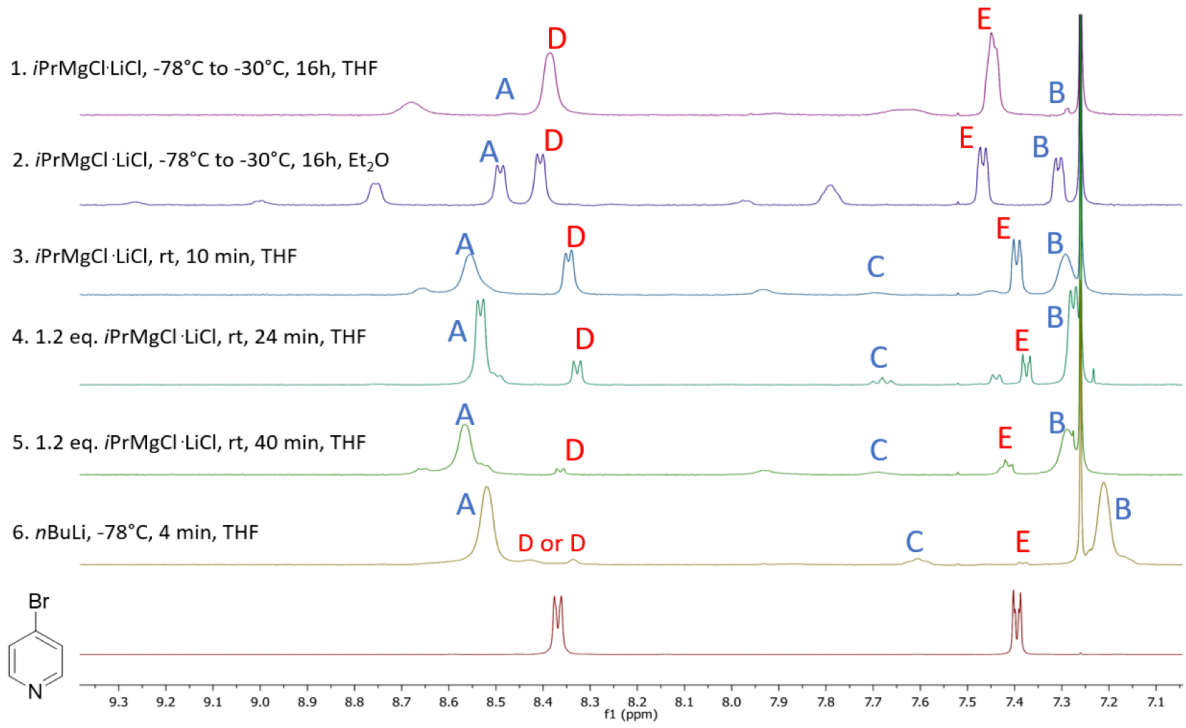

Figure 4.4: ^{1}H NMR spectra (300 MHz, $CDCl_3$) of the intermediate 4-metallopyridine quenched with deuterium oxide. The ^{1}H NMR spectrum corresponding to 4-bromopyridine is shown for comparison (red). Conditions and results in Table 4.1.

For preparative purposes through a long process of trial and error, it was found that the best conditions for the preparation of heavier main group-based tris-4-pyridyl ligands involved the lithiation of 4-bromopyridine in THF at –115 °C for 15 mins, followed by addition of $SbCl_3$ (**15**), $BiCl_3$ (**16**) and prolonged reaction at –115 °C (5 h) then at –78 °C (40 h) before aqueous workup. Compound **17** was prepared similarly, but using ^{n}BuLi as the metalation reagent in Et_2O alone as the solvent and through addition of $PhSnCl_3$ (Scheme 4.5). The isolated yields of **15**, **16** and **17** were 20%, 55% and 11%, respectively.

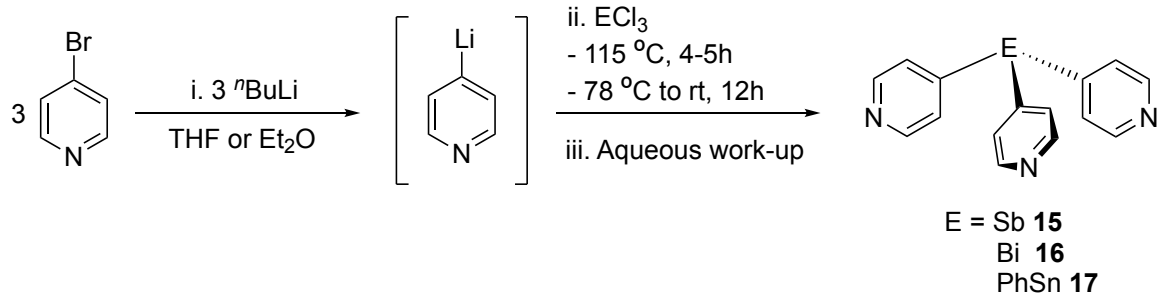

Scheme 4.5: Synthesis of heavier Group 14 and 15 E(4-py)$_3$ ligands (E = Sb (**15**), Bi (**16**), PhSn (**17**)).

Furthermore, the workup and purification techniques differ slightly in that compounds **15** and **16** require slow warming to room temperature over 40 h and may be recrystallised from DCM, whereas the workup of **17** may be undertaken after 5 h, and recrystallisation possible through layering hexane on top of a DCM solution of ligand **17**. The identities of all three ligands were confirmed by ^{1}H NMR spectroscopy and elemental analysis, with X-ray crystal structures also being obtained for **16** and **17**, which are shown in Figure 4.5 and Figure 4.6, respectively. Both compounds are monomeric in the solid state. A significant observation is the larger C–Sn–C angle in **17** (110.7(0) °) compared to the C–Bi–C angle in **16** (91.1(6) °). This is a consequence of relativistic contraction of the 6*s* (lone-pair) orbital on Bi(III) and the resulting resistance to mix with the 5*p* orbitals, so that the Bi–C bonds involve primarily *p*-character (thus the C_{py}–Bi–C_{py} angle is close to 90 °). Reflecting the Lewis acidity of the Bi(III) atom, molecules of ligand **16** are associated in the crystal lattice via intermolecular N···Bi and π-arene···Bi interactions (unlike the discrete arrangement found in P(4-py)$_3$).[83] Overall, the Bi(III) centres have a highly distorted octahedral geometry, forming two long-range N···Bi interactions (3.071(5) and 3.306(5) Å)[159,160] and one (η^6)π-arene interaction ($py_{centroid}$···Bi 3.74 Å) with neighbouring molecules, resulting in significant distortion of the Bi(4-py)$_3$ molecular units. While there are no previous precedents for π-pyridyl-Bi^{III} interactions, this bonding in **16** is within the sum of the van der Waals radii of Bi and C (ca. 3.79 Å).[161] In contrast, molecules of **17** are discrete.

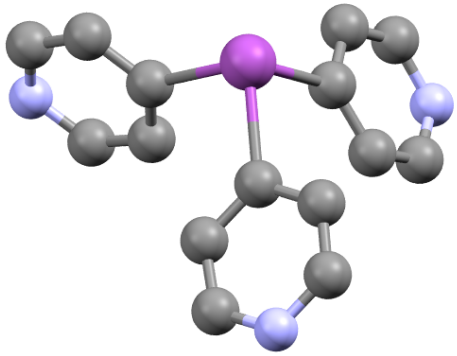

Figure 4.5: Solid-state structure of Bi(4-py)$_3$ (**16**). Selected bond lengths (Å) and angles (°): Bi–C 2.262(5), C_{py}–Bi–C_{py} 91.14(19).

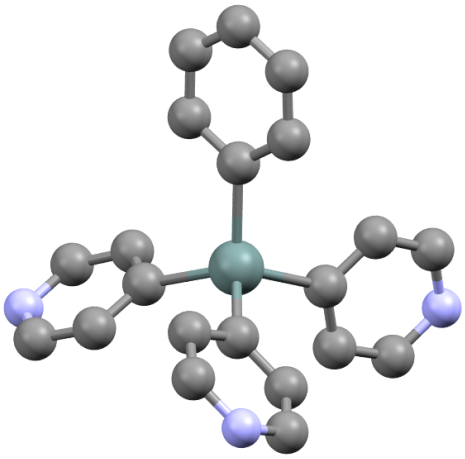

Figure 4.6: Solid-state structure of **17**, PhSn(4-py)$_3$. Selected bond lengths (Å) and angles (°): Sn–C_{py} 2.149(3), Sn–C_{Ph} 2.149(3), C_{py}–Sn–C_{py} 110.71(17).

4.3 Coordination Behaviour of 15, 16 and 17

Complexes of ligands **15**, **16** and **17** with Cu^I and Ag^I salts were obtained in crystalline form by layering MeCN solutions of the appropriate Ag^I salt onto DCM solutions of **15** or **16**, after prolonged storage at room temperature in the dark. Satisfactory elemental analyses were obtained on most of the complexes, but only after repeated attempts. This was complicated partly as a result of loss of lattice solvent when they were dried under vacuum during isolation prior to analysis, and because they proved to be highly unstable to light in the solid state, especially. It therefore proved necessary to perform any analysis immediately after isolation. For completeness, solid-state IR spectra of the complexes were also recorded, although these

were largely uninformative. Owing to the polymeric nature of the complexes, they are all insoluble in organic solvents and ^{1}H NMR spectroscopy in D_6-DMSO indicated only de-coordination of the ligands. The only definitive characterisation possible under the circumstances was single-crystal X-ray crystallography. Table 4.2 shows the new Cu^I and Ag^I complexes that were obtained in this study, the method of crystallisation and the yields of each.

Table 4.2: Table shows the compounds that were produced in this study, their compound numbers used in the following discussion, the methods used in their crystallisation and the yields.

Compound Formula	Compound Number	Method of Crystallisation	Yield %
$\{Ag^I_2(\mathbf{16})_3\}_n(CF_3SO_3)_{2n}$	**18**	Layering MeCN/DCM	74
$Ag^I_2(\mathbf{16})_3\}_n(SbF_6)_{2n}$	**19**	Layering MeCN/DCM	59
$\{Ag^I_2(\mathbf{16})_3\}_n(PF_6)_{2n}$	**20**	Layering MeCN/DCM	80
$Ag^I(\mathbf{15})\}_n(SbF_6)$	**21**	Layering MeCN/DCM	45
$\{Ag^I(\mathbf{17})\}_n(CF_3SO_3)_n$	**22**	Layering MeCN/DCM	30
$\{Ag^I(\mathbf{B})\}_n(CF_3SO_3)_n$	**23**	Layering MeCN/DCM	60
$\{Cu(\mathbf{16})(MeCN)\}_n(PF_6)_n$	**24**	Layering MeCN/DCM	63
$(\{Cu(\mathbf{16})_2\}\{Cu(\mathbf{16}\text{-}SiF_5))_n(PF_6)_n$	**25**	Layering MeCN/DCM	30

4.3.1 Silver Complexes of 15, 16 and 17

In order to explore the coordination landscape of ligands **15** and **16**, Ag^I salts containing a range of weakly-coordinating anions (AgX, X = $CF_3SO_3^-$, PF_6^-, SbF_6^-) were initially selected. It was further reasoned that the softness of Ag^I would encourage the N,N,N/E coordination mode (Figure 4.2b) and lead to condensed MOF arrangements. At the same time, the presence of weakly-coordinating anions should limit competing anion-bridgehead (E) interactions.

For comparison to the structures of the complexes described in this work, Ag^I networks containing the nitrogen homologue N(4-py)$_3$ have been described recently,[116] with both trifluoroacetate (CF_3COO^-) and PF_6^- anions. In both, the pyridyl-N atoms of the ligand adopt an approximately planar geometry and the Ag^I atoms also act as three-coordinate nodes, producing simple planar 2D honeycomb nets (topology descriptor **hcb**). By contrast, the

networks $\{Ag^{I}_{2}(\mathbf{16})_3\}_n(CF_3SO_3)_{2n}$ (**18**) and $\{Ag^{I}_{2}(\mathbf{16})_3\}_n(SbF_6)_{2n}$ (**19**), show a more complex arrangement on account of the approximately orthogonal coordination vectors within ligand **16**.

The structures of **18** and **19** consist of identical (although not fully isostructural) 2D nets (Figure 4.7) in which the Ag^{I} centres have ("see-saw") four- and (square-pyramidal) five-coordinate environments. The Ag^{I} cations are coordinated by pyridyl-N atoms of the ligand **16** only, which adopts the N,N,N-coordination mode. The result is a complicated, undulating sheet network, consisting of interlocked Bi_3Ag_3 and Bi_2Ag_2 ring units. The $CF_3SO_3^-$ or SbF_6^- anions (and some DCM solvent) are also present in the structures, but they do not form any clear interactions with Ag^{I}. Like the crystal structure of **16**, the overall Bi coordination environment can be viewed as pseudo-octahedral, with two sites being capped by long-range, face-on pyridyl rings, and one site being capped by either a F atom of SbF_6^- or an O atom from $CF_3SO_3^-$, in addition to the three bonds made with the 4-py groups.

The network topology of **18** and **19** can be rationalised by referring to an idealised NaCl-type structure, comprising Bi and Ag atoms, with an Ag–Bi distance of 7.6 Å (lattice dimension = 15.2 Å, Figure 4.8a). Since the $Bi(4\text{-py})_3$ ligands act as three-coordinate nodes, three edges must be removed from the NaCl lattice around each Bi atom. Appropriate removal of edges produces both five-coordinate (square-pyramidal, after removal of one edge) and four-coordinate ("see-saw", after removal of two adjacent edges) environments for Ag^{I}, as seen in the network structures. The overlay of the observed Ag/Bi positions in the 2D network in **18** and **19** and the hypothetical net derived from the NaCl lattice is almost exact (Figure 4.8b). The topology of the resulting network is based on the **hcb** net, but with every other row of hexagons capped by a further tripodal $Bi(4\text{-py})_3$ ligand, to produce rows with rhombus tiling. In this way, the net can be viewed as a hybrid of the **hcb** and kagome dual (**kgd**) nets.

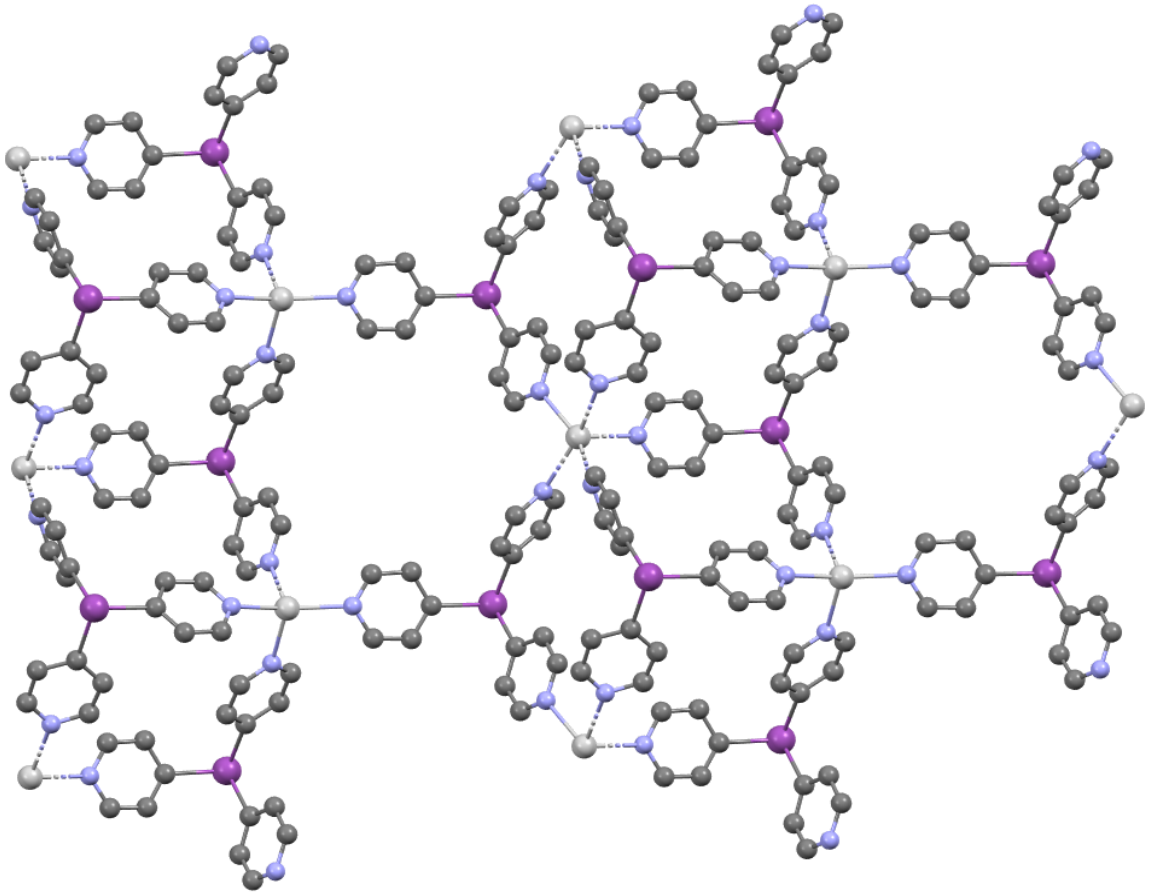

Figure 4.7: The 2D network structure of $\{Ag^{I}_{2}(\mathbf{16})_3\}_n(CF_3SO_3)_{2n}$ (**18**) (the network formed in $\{Ag^{I}_{2}(\mathbf{16})_3\}_n(SbF_6)_{2n}$ (**19**) has the same connectivity). CF_3SO^{-} anions and CH_2Cl_2 solvent molecules are omitted for clarity.

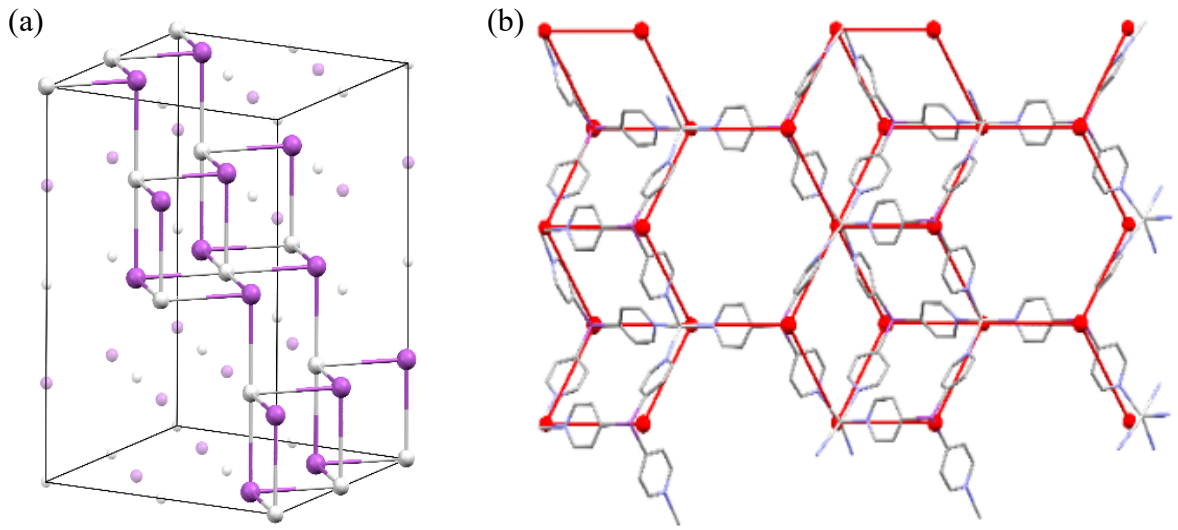

Figure 4.8: (a) A model of the lattice of **18** and **19** as an extended segment of the NaCl lattice, and (b) overlay of the lattices of **18** and **19** with an idealised NaCl lattice (with Ag-Bi 7.6 Å, red).

As noted in at the beginning of this section, drying of the crystalline materials resulted in loss of lattice solvent and in all cases the formation of powders. Attempts to employ X-ray powder diffraction were generally unsuccessful as a further analytical aid to verify that the bulk materials were the same as that observed by single-crystal diffraction studies. This, it was assumed, was the result of the formation of amorphous material after drying under vacuum (a potential consequence of the collapse of the MOF structure). However, in the case of **19** it was shown that the lattice clearly survives isolation and drying of the crystals. Figure 4.9 shows the powder X-ray data from **19** and the simulated pattern from the single-crystal structure data. Minor differences in the positions of the peaks between the experimental and simulated powder patterns reflect the temperature difference between the measured and simulated data, and the measured intensities are almost certainly affected by preferred orientation. The isolated sample quantity was limited, and the resulting signal-to-background ratio is accordingly low. Nonetheless, the principal peaks in the measured pattern (particularly at low angle) indicate that the bulk crystalline product is consistent with the single-crystal structure of **19**.

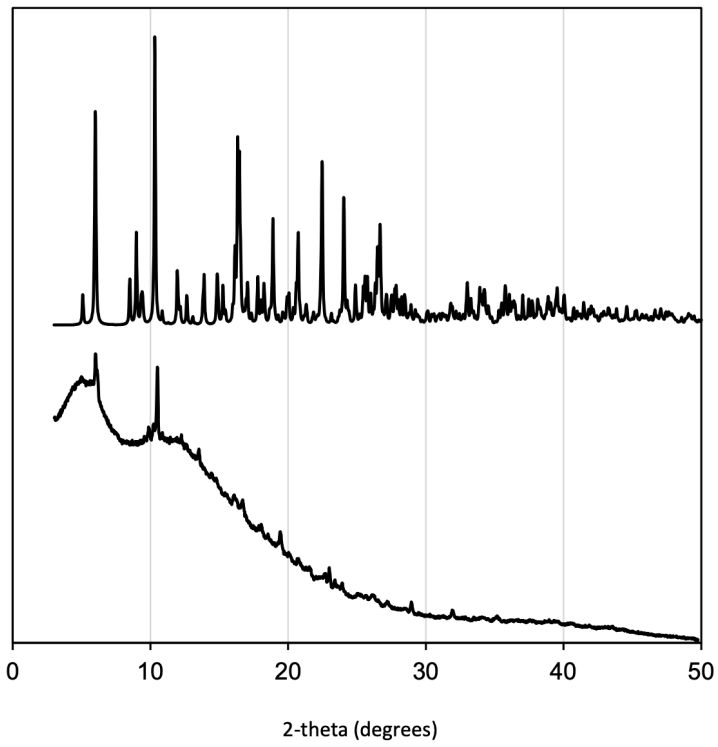

Figure 4.9: Measured PXRD pattern for collected crystals of **19** under ambient conditions (bottom), compared to the pattern simulated from the single-crystal structure at 180 K (top).

Employing the same chemistry with $AgPF_6$ and compound **16** produces the coordination compound $\{Ag^{I}_2(\mathbf{16})_3\}_n(PF_6)_{2n}$, (**20**), which shows a remarkable 3D network structure (Figure 4.10).

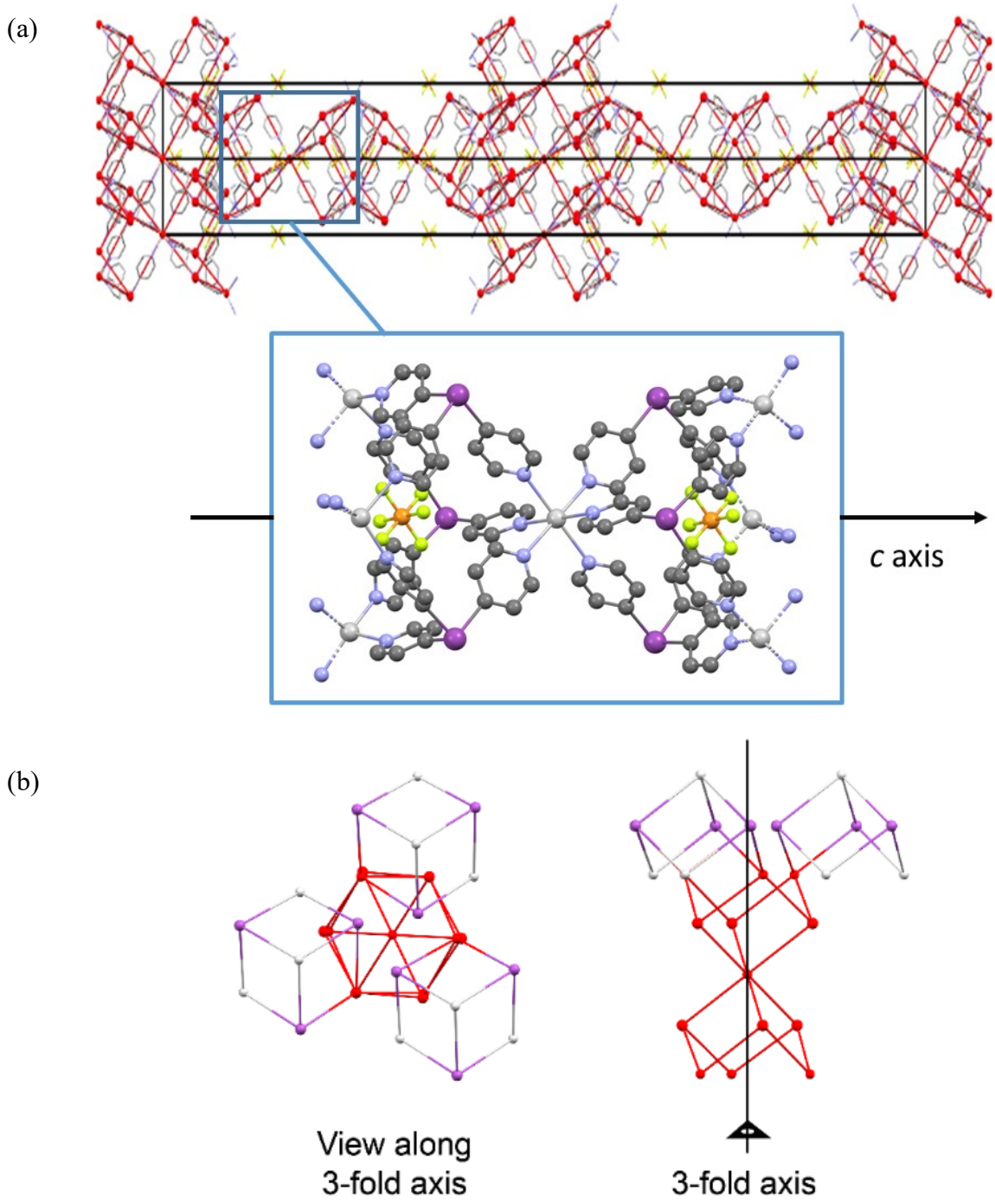

Figure 4.10: (a) The complicated 3D network of **20**, and (b) built up from cube fragments, which aggregate into the lattice along the 3-fold, *c*-axis.

This structure is based on building units of corner-sharing cubes extracted from the parent NaCl lattice, in which the shared corner comprises a six-coordinate Ag^{I} atom and the exposed Ag^{I} are all four-coordinate (inset to Figure 4.10a). In a regular NaCl lattice of Ag and Bi atoms, the cube corners opposite to six-coordinate Ag would each comprise a six-coordinate Bi. Since ligand **16** acts as a three-coordinate (N,N,N-coordination) node, however, the structure diverges from the parent lattice of NaCl in this region. The body diagonals of the cube units are aligned with the long *c*-axis (i.e. the three-fold axis) of the R-centred unit cell. Looking down the *c*-axis (Figure 4.10b), the three connected corner-sharing cubes within the next layer along the *c*-axis are offset and rotated by ca. 30 °. The next layer along *c* induces a further rotation of 30 °, which brings the corner-sharing cubes back to a translational relationship.

The large change in the lattice compared to that of **18** and **19** can be traced to the structure-directing effect of the PF_6^- anion in **20**. As shown in Figure 4.10, some of the PF_6^- anions are encapsulated within the cubane units and potentially act as templates. Similar templating using PF_6^- anions has recently been observed for discrete molecular cages formed from the PhSn(3-py)$_3$ ligand,[16] and the influence of counter anions in supramolecular chemistry and crystal engineering is a well-documented field.[162]

A glimpse at the effect of changing the bridgehead atom is provided by the structure of the complex of the Sb(III) ligand **15** with $Ag(SbF_6)$, $\{Ag^{I}(\mathbf{15})\}_n(SbF_6)_n$, (**21**). The result is a completely different lattice to that of complex **16** with $Ag(SbF_6)$ (complex **20**). Complex **21** forms a 3D network structure in which the ligand **15** adopts the N,N,N/E coordination mode, which is unprecedented for any Group 15 E(4-py)$_3$ complex.[81] The adoption of this mode stems from the greater Lewis basicity of Sb(III) compared to Bi(III), and provides the key reason for the difference in structure between these complexes of **15** and **16**. The structure of **21** is composed of honeycomb layers of interlocked Sb_3Ag_3 puckered ring units (Figure 4.11), which stack vertically into a porous network solely by Sb-Ag bonds, involving all of the Sb and Ag atoms within the layers (Sb–Ag 2.6029(9) Å).[163] For comparison, the donor-acceptor Sb–Ag bond length in $[(Ph_3Sb)_4Ag]^+ClO_4^-$ falls between 2.7200(6) and 2.7297(6) Å.[164] Both Ag and Sb form four-coordinate tetrahedral nodes, and the resulting network is topologically identical to the zinc imidazolate framework, ZIF-64 (CSD:GITTEJ).[165]

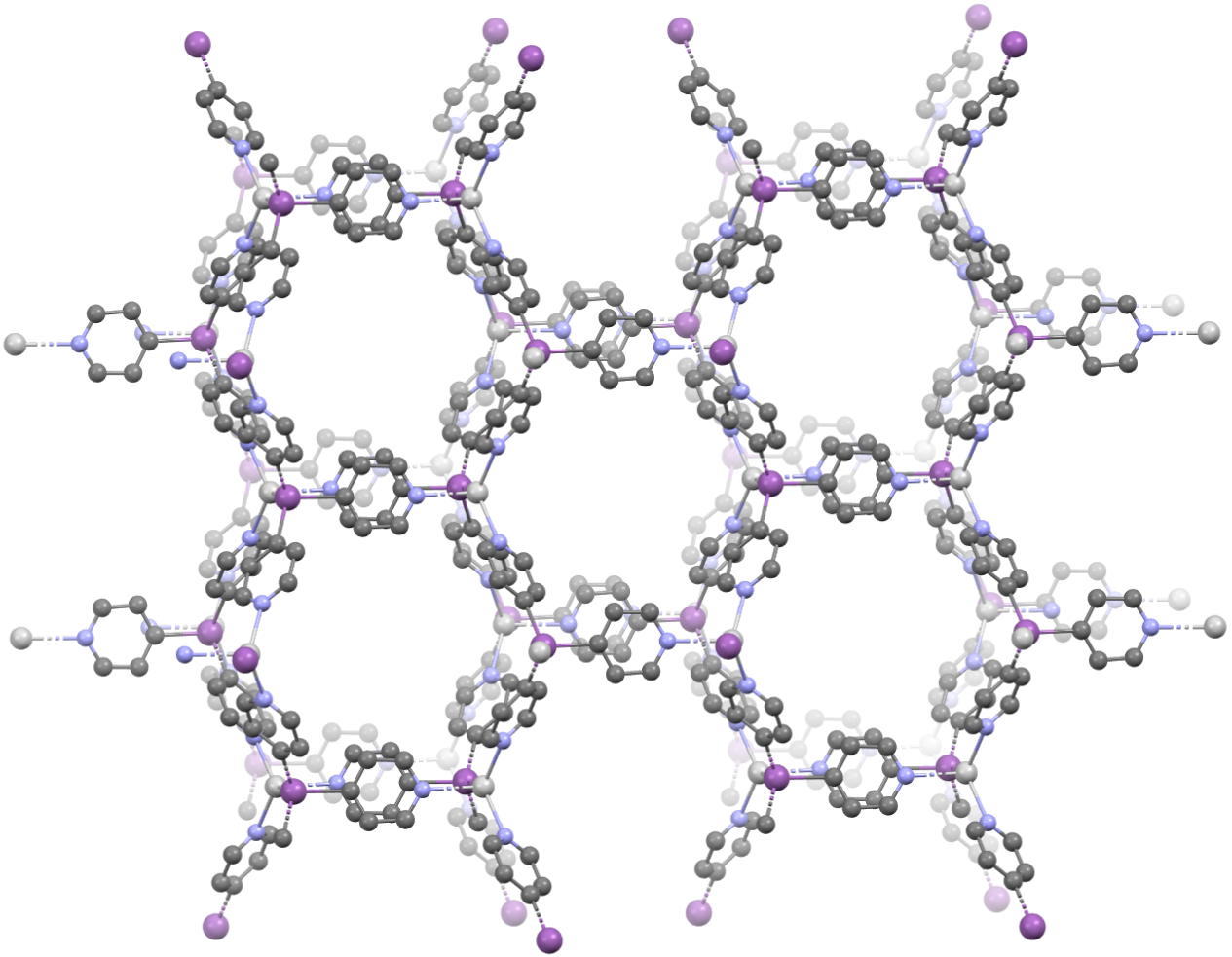

Figure 4.11: The honeycomb layers of **21**, formed from Sb_3Ag_3 ring units (viewed approximately along crystallographic *a*-axis). The pores created are occupied by SbF_6^- anions, which are omitted for clarity. The pores measure ca. 11.1 Å in diameter.

An interesting comparison can be made between the structure of **21** and the $Ag(CF_3SO_3)$ complex of the ligand $PhSn(4\text{-py})_3$ (**17**), which was also prepared as part of the current work. The blocking of the metal-donor site by the Ph group in **17** (which adopts an N,N,N-coordination mode) and the replacement of interlayer interactions by $CF_3SO_3^-$ coordination of the Ag^I cations in the resulting complex $\{Ag^I(\mathbf{17})\}_n(CF_3SO_3)_n$ (**22**) leads to the formation of a lattice consisting of discrete honeycomb layers composed of fused chair-shaped $Ag_3(\mathbf{17})_3$ ring units, with an AB packing arrangement which is similar to graphite (Figure 4.12). The layers interdigitate, with the Ph-substituents from ligands of **17** in each layer occupying the macrocyclic void of a $Ag_3(\mathbf{17})_3$ ring in the layers above and below each layer.

A further comparison can be made with the AgOTf complex of the known ligand $MeSi(4\text{-py})_3$ (**B**),[120] $\{Ag^I(\mathbf{B})\}_n(CF_3SO_3)_n$ (**23**), which was prepared as part of this study for comparison. Remarkably, the structure now consists of similar honeycomb layers to those seen in **22**, but which form an interlocked lattice in which the layers penetrate each other in an infinite catenane-like lattice arrangement (Figure 4.13). The reason for the difference between the two arrangements probably stems from the lower steric demands of the bridgehead Me-group in this case (compared to the bulkier Ph group in the Sn ligand **17**), which allows the Me–Si fragment of the ligands in **23** to be accommodated (side-on) at the centre of the Si_3Ag_3 ring units.

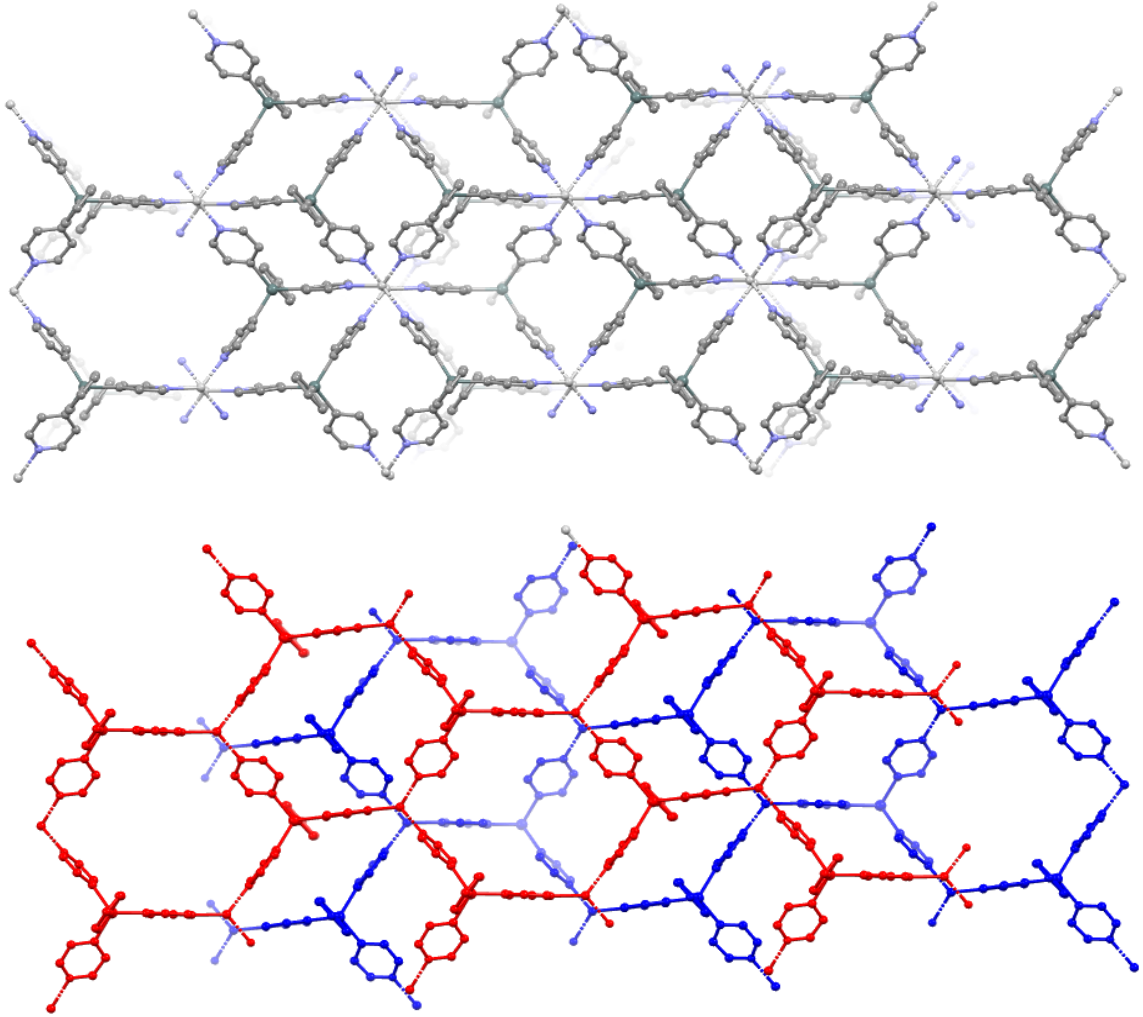

Figure 4.12: Top: Lattice structure of complex **22** (viewed approximately along the *a*-axis). The OTf^- anions are bonded to the Ag^I atoms by O-Ag bonds but are not shown. Bottom: Showing the relationship between the top layer (in red) and a layer beneath (in blue).

(a)

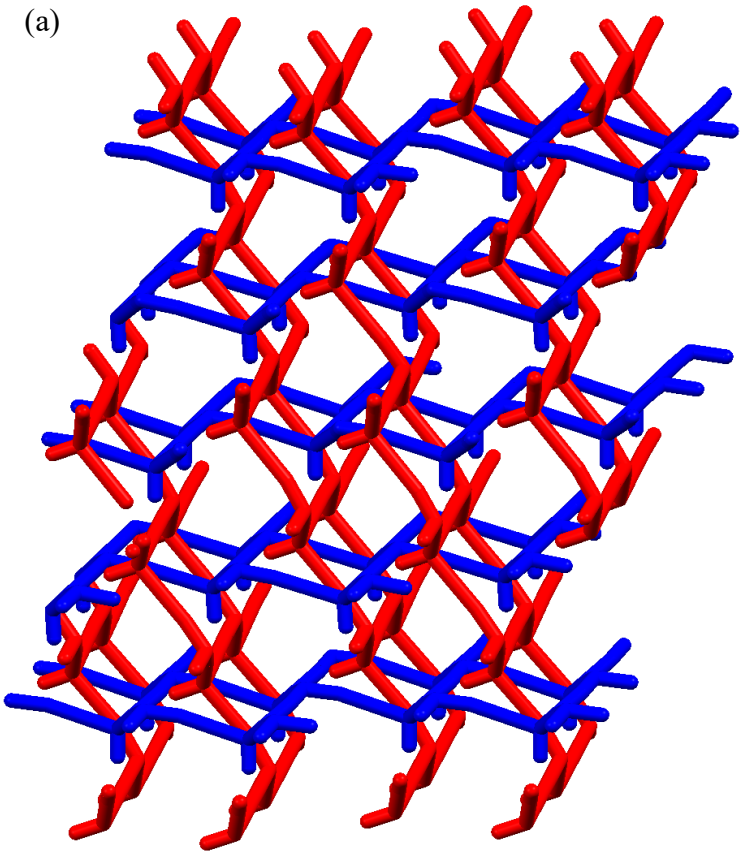

Figure 4.13: Lattice arrangement of complex **23**, showing the formation of the extended catenane-like lattice of interlocked layers.

4.3.2 Copper Complexes of 16

Moving to Cu^{I} salts was expected to result in some changes in the structures of the complexes formed. As it turned out, however, very few of the complexes of **15**, **16** or **17** could be produced with sufficient crystallinity to obtain their single-crystal X-ray structures. The coordination of $[MeCN]Cu^{+}PF_6^{-}$ by Bi(4py)$_3$ (**16**) gives the complex $\{Cu(\mathbf{16})(MeCN)\}_n(PF_6)_n$ (**24**). Unlike the Ag^{I} complex (**20**) to which its structure can be compared, the Cu^{I} ions of **24** are coordinated by the N atom of MeCN ligand. This donor was used in the crystallisation of **20**, but presumably because of the softer character of Ag^{I}, **20** does not coordinate the metal atoms. Thus, although the Cu^{I} and Ag^{I} ions in both complexes are either four-coordinate (and tetrahedral) or six-coordinate, a completely different arrangement is seen in **24** (Figure 4.14) to that of **20** (Figure 4.10), in which the Cu^{I} ions are coordinated to three pyridyl N-atoms and the MeCN ligand rather than to four pyridyl-N atoms (as in **20**). The MOF structure of **24** can be regarded as

being composed of helical left-hand and right-hand polymer sub-units propagated along the crystallographic *c*-axis (Figure 4.14a), in which two of the pyridyl-N atoms of **16** join the $Cu(MeCN)^+$ units together, which are then further associated into a layer network by pyridyl–N–Cu bonds to the remaining N atoms of each of the ligands **16** along the *a*-axis (Figure 4.14b).

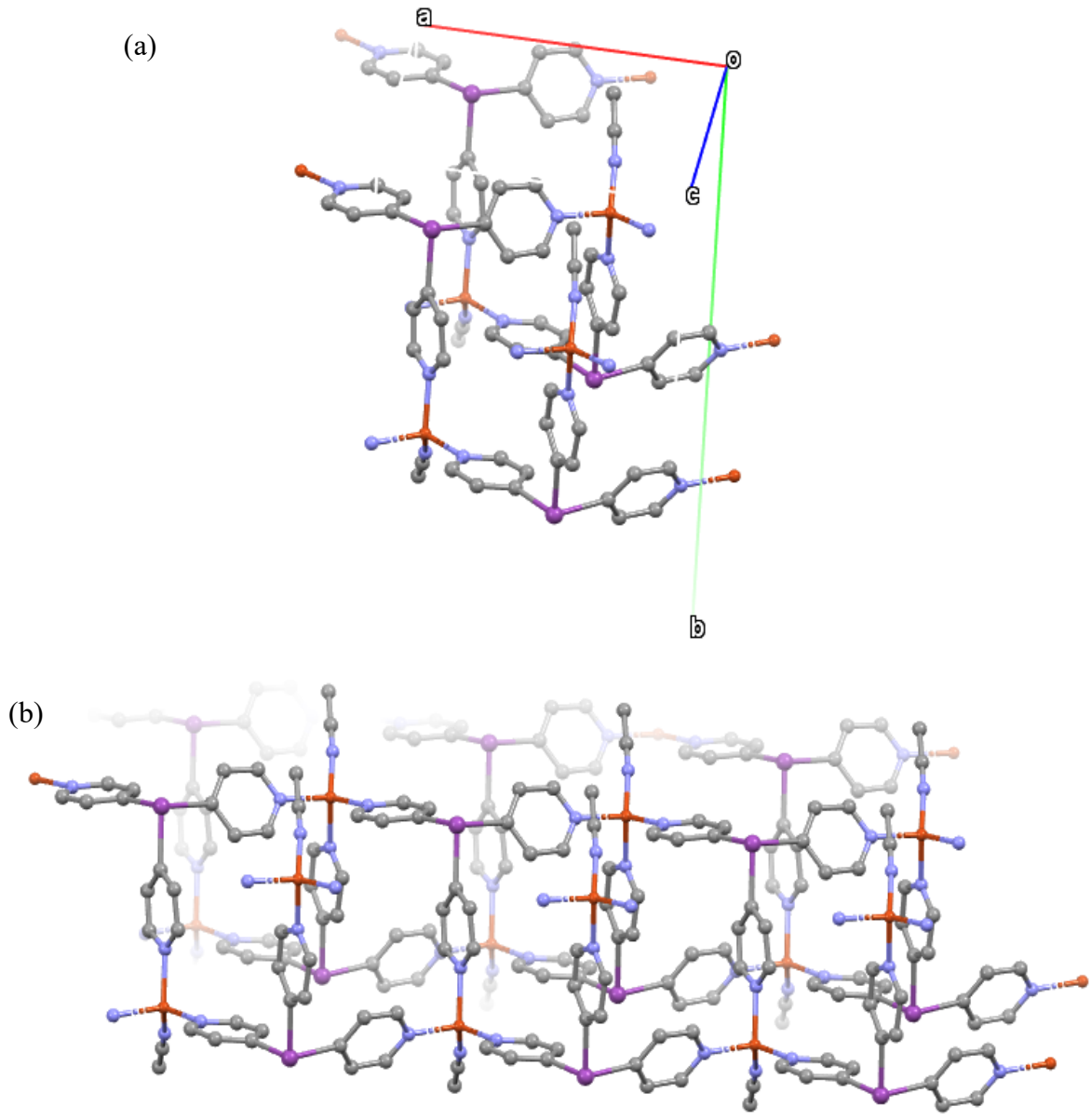

Figure 4.14: (a) Right-hand helical fragment of the lattice of **24**, showing the association of the (**16**)Cu(MeCN) units using two of the pyridyl-N atoms of the ligands, (b) Bottom: the association of these helices into layers using the 'dangling' pyridyl groups within the helical units. The PF_6^- anions are found within and between the layers.

On one occasion while attempting to grow crystals of **24** in order to obtain improved crystallographic data, an apparent reaction involving the silicon in the glassware was observed which generated a complex containing SiF_5 units which are coordinated to one of the pyridyl-N atoms in every three of the molecules of **16** present in the lattice. This outcome presumably arose from the hydrolysis of the PF_6^- anion in the presence of moisture, which is known to generate HF. The structure of the complex formed $(\{Cu(\mathbf{16})_2\}\{Cu(\mathbf{16}\text{-}SiF_5)\})_n(PF_6)_n$ (**25**) is included here for completeness (Figure 4.15).

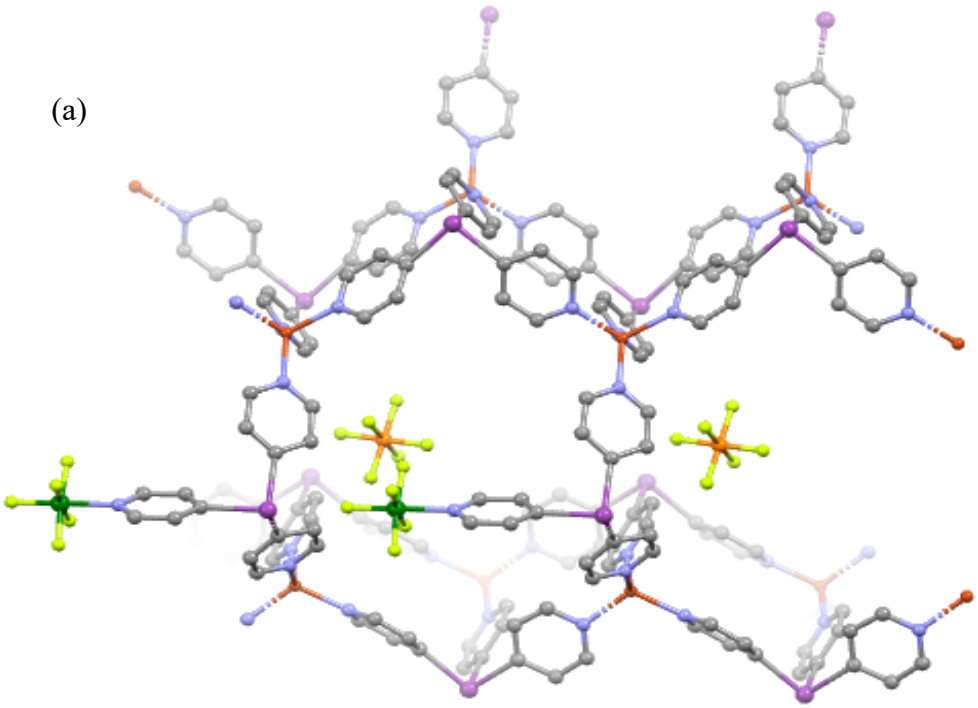

Figure 4.15: (a) Lattice arrangement of **25**, showing the presence of N-donor-coordinated SiF_5^- in the structure, as well as PF_6^- incorporated within the network's pores.

4.4 Conclusions

In conclusion, the first examples of tris-4-pyridyl ligands of heavier *p*-block elements of Groups 14 and 15 have been reported, permitting systematic exploration of the structure-directing effects of the bridgehead and anion on the formation of MOFs. Both the Ag^I and Cu^I frameworks show rich topological complexity, ranging from 2D to 3D networks, which, in the cases of **18**, **19** and **20** can be neatly related to a parent NaCl-type structure based on the Group 15 and Ag atoms. Perhaps the most important conclusion on the basis of this work and previous studies of the $N(4\text{-py})_3$ ligand is that the coordination mode can be modulated by descending

Group 15 (planar N,N,N-, to tetrahedral N,N,N/E-, to pyramidal N,N,N-) as a result of the dual periodic effects of the decrease in *s*/*p* mixing and Lewis basicity. This is represented in Figure 4.16 for Group 15. At nitrogen sp^2 hybridisation results in a planar arrangement of the N(4-py)$_3$ ligand which will therefore form planar coordination networks. As the group is descended the decrease in *s*/*p*-separation leads to decrease *s*/*p*-mixing (at P, As and Sb. However, at Bi relativistic stabilisation results in poor availability of the 6*s* orbital as a donor atom. The resulting coordination modes are reflected in the structural data described in this Chapter (i.e., the lack of involvement of the Bi lone pair of **16** in any of the arrangements and the involvement of the lone pair of **15**). This transition provides a potentially important tool in the future targeted assembly of specific molecular and extended lattice arrangements.

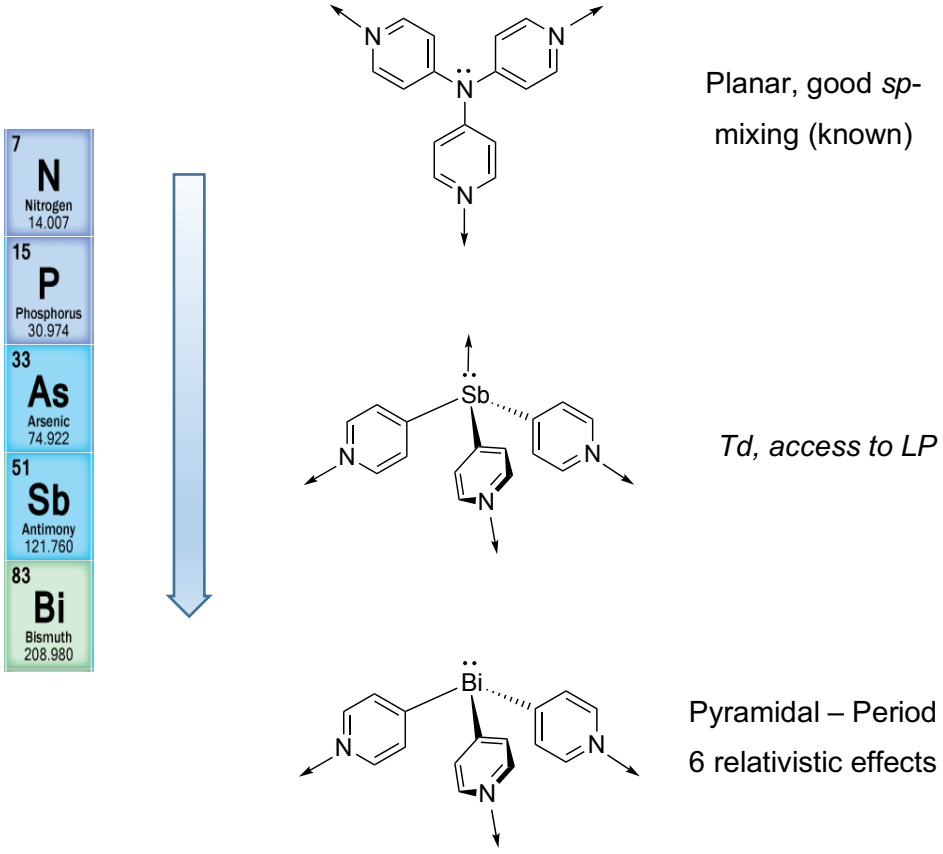

Figure 4.16: The variation of the coordination behaviour of Group 15 tris(4-pyridyl) ligands.

5

5. Structure and Reactivity of Pyridyl Donor *cis*-disubstituted Cyclodiphosphazanes

5.1 Preface

The ability to manipulate the coordination characteristics of main group-based pyridyl ligands by changing the bridgehead atom and N-donor position within the (quinolyl/pyridyl) ring units has been the theme of this thesis so far. However, little research has been done using more complicated molecular main group arrangements as scaffolds for ligand design in this area. There is a developing area of main group supramolecular chemistry based on increasingly complicated main group frameworks which parallel the principles of ligand design found in the conventional area of organic ligands. Whilst this area is too extensive to discuss in detail in this thesis, some salient points are worth noting in respect to the work presented in this Chapter.

Moving beyond carbon, the principal framework atom in any ligand arrangement is complicated by the fact that other main group systems suffer from weaker/less covalent and more polar bonds, making them less thermodynamically stable than organic counterparts and prone to reaction. However, the P-N bond energy is similar to that of a C-C bond (290 kJ mol^{-1} and 350 kJ mol^{-1}, respectively)[166] and is relatively non-polar. As a result, phosphazanes have become important building blocks in the developing area of supramolecular main group chemistry, since they are capable of supporting robust ligand systems. A case in point are the cyclodiphosph(III)azane-based dianions of the type $[(RN)P(\mu\text{-}NR)]_2^{2-}$, **E**, (R = sterically-demanding group, i.e. ^{t}Bu; R´ = alkyl or aryl group), which have been investigated extensively by Stahl and co-workers.[167] Such dianions are robust ligands, and have been shown to have an extensive coordination chemistry. They can be simply prepared from reactions of cyclodiphosph(III)azane precursors of the type $[ClP(\mu\text{-}NR)]_2$, **C**, with primary amines (RNH_2), followed by deprotonation of the intermediates, **D** (Scheme 5.1).

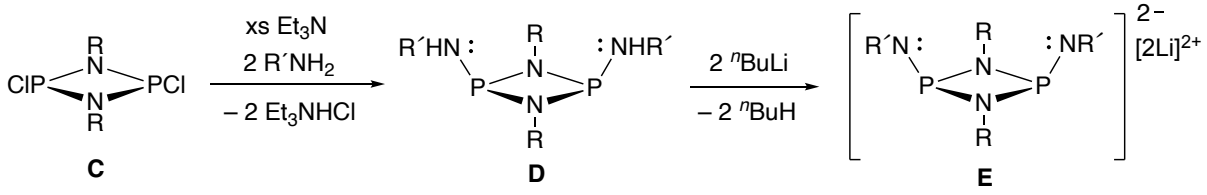

C **D** **E**

Scheme 5.1: The cyclodiphosph(III)azane precursor $[ClP(\mu\text{-}NR)]_2$, **C**. R = normally a sterically-demanding group, e.g. ^{t}Bu. Note that the dichlorides of this type usually have a *cis*- arrangement, as depicted.

In addition, the P atoms of **D** can also be oxidised, incorporating O-atoms (by oxidation with H_2O_2) or S or Se (by direct reactions with the elements). Chivers and Woollins have used this reactivity to obtain P(V) counterparts $[(R'N)(E=)P(\mu\text{-}NR)]_2^{2-}$ (E = O, S, Se) (**G**) of the P(III) ligands, by deprotonation of the oxidised species formed (**F**) (Scheme 5.2).[168]

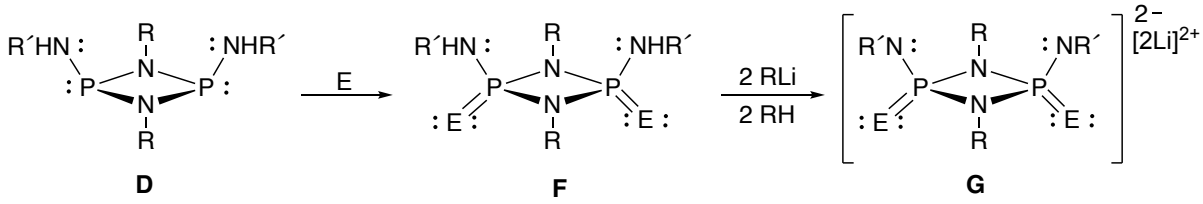

Scheme 5.2: Synthesis of P(V) dianionic ligands **G** via deprotonation of neutral P(V) species, **F**.

Dianionic P(III) and P(V) phosphazanes can adopt a wealth of coordination modes in order to coordinate transition metals, alkali metals and main group elements, some examples of which are shown in Figure 5.1.[166,167,169]

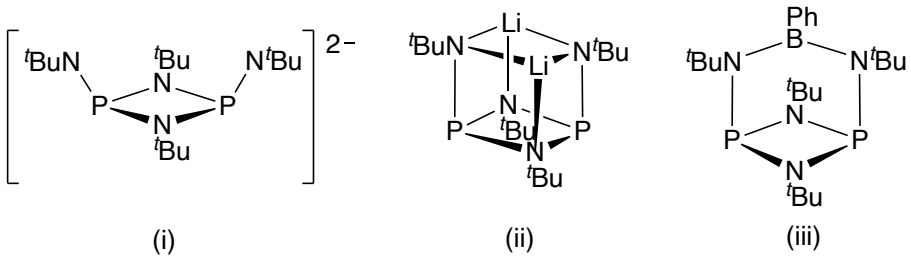

Figure 5.1: Complexes formed from dianionic cyclophosphazanes (i) with Li (ii); and BPh (iii).

The neutral P(III) and P(V) cyclodiphosphazane arrangements **C** and **F** are highly versatile ligands in their own right, whose donor characteristics and steric demands can be radically altered by the installation of different electron-donating or electron-withdrawing organic substituents, R. The specific interest in the use of these neutral ligands is their H-bond donor character, which combined with their ability to coordinate metal ions using the P- or E-atoms means that they are capable of coordinating the cation and anion of metal salts (i.e., they are ambiphilic ligands). An important effect in this area is the way in which either oxidation of the P-atoms or coordination with a metal atom can be used to modulate the H-bond donor character

of the N-H bonds. Both modifications at the P-atoms of the cyclophosphazane units result in increased acidity of the N-H atoms as a result of electron withdrawal (either to the metal or E atoms). Examples of anion coordination by these P(III) and P(V) ligands are shown in Figure 5.2.

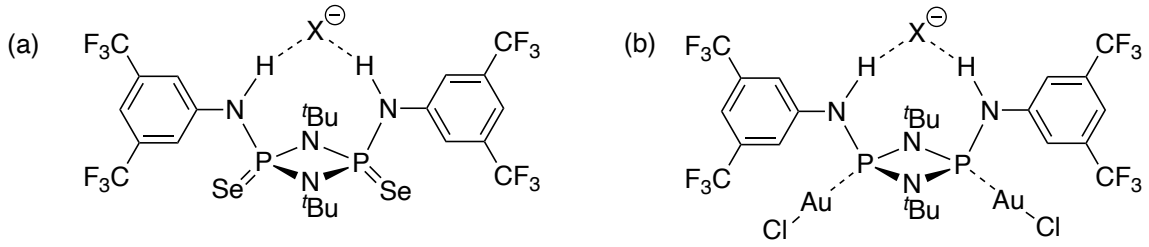

Figure 5.2: *Cis*-disubstituted cyclodiphosph(V)azanes with electron-withdrawing groups on the exocyclic amino nitrogens for their use as anion receptors, with selenuium oxidation in (a), and Au(I) coordination to the P-atoms in (b). X = anion.

The anion coordination ability of P(III) cyclodiphosphazanes can be further enhanced by the *cis*-disubstitution of the P_2N_2 ring with N-donor-containing groups, specifically 2-aminopyridyl and 8-aminoquinolyl groups in [(2-py)P(μ-N^{t}Bu)]$_2$ (**H**) and [(8-qy)P(μ-N^{t}Bu)]$_2$ (**I**) respectively.[170] In both cases the chelation of metal atoms by the P- and N- atoms of the arrangements results in preorganisation of the N-H groups for optimum H-bonding to anions (Scheme 5.3). This effect has a large impact on the anion affinity, with metal-based anion receptors having high anion binding constants.

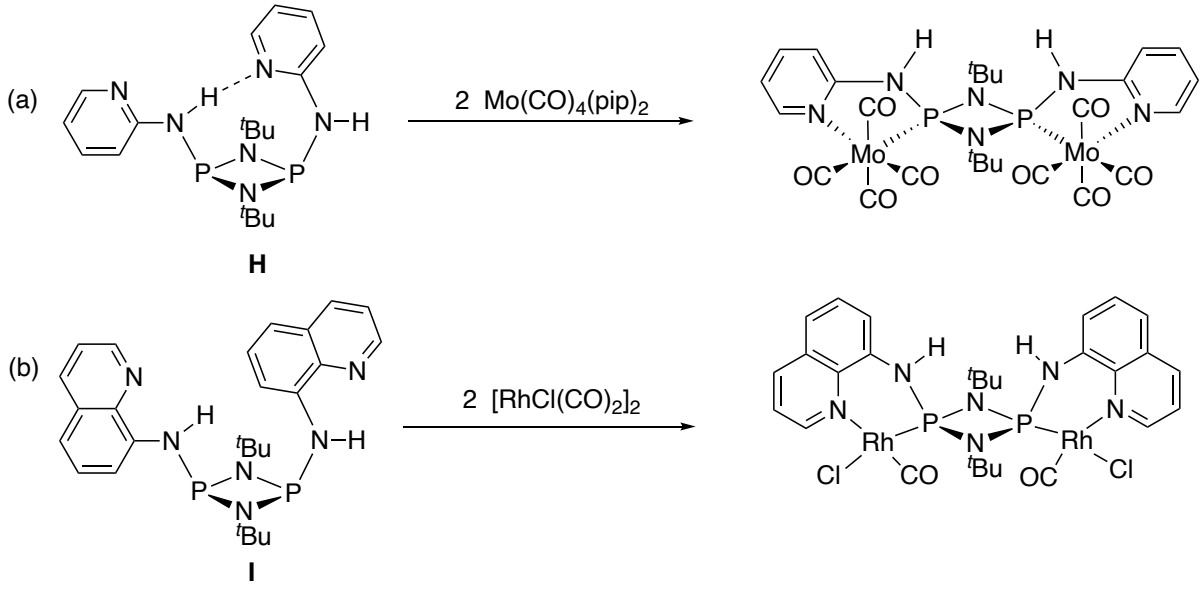

Scheme 5.3: Coordination of *cis*-disubstituted **H** and **I**: (a) Functionalised with 2-aminopyridine ligands and $Mo(CO)_4(pip)_2$ (pip = piperidine), and (b) with 8-aminoquinoline ligand and $[RhCl(CO)_2]_2$. In both cases, the ligands are fixed in an *exo-exo* conformation by metal chelation (optimal for H-bonding). This has the effect of changing the *endo-exo* conformation of the RNH groups in the free ligands.

NMR spectroscopic measurements of binding constants have revealed that metal coordination of P-atoms in this way results in anion binding properties superior to previously-reported organic systems, such as thioureas and squaramides (they can bind chloride anions one to two orders of magnitude stronger).[170–175] This behaviour can be attributed to a number of factors. A major factor is that coordination of a metal centre polarises the N-H donors through σ-donation of electron density from the N-atoms of the pendant RN groups to the P-atoms. DFT calculations have shown that this backdonation of the lone pairs of the exocyclic amino nitrogens occurs into the σ* orbitals of the ring P-N bonds.[171] One of the major advantages of oxidation of the P(III) atoms with Se or metal coordination of the P(III) atoms is that the arrangements are now air- and moisture-stable.

From these studies, it is evident that the incorporation of N-donor substituents onto the well-established cyclodiphosphazane framework has profound effects on the anion binding affinity as well as the anion selectivity, showing the great potential and promise of these in anion transport through membrane and counterion catalysis. This Chapter will focus on the further exploration of the coordination chemistry of **H**, and on incorporating the 3-aminopyridine

donor functionality into these arrangements. The installation of 3-aminopyridine functionality into cyclodiphosphazane units was inspired by earlier work presented in this thesis on the use of 3- (and 4-pyridyl) groups in the design of ligands containing a single main group bridgehead atom. By using a P_2N_2 ring unit in place of this bridgehead it was hoped to develop a new range of 3-pyridyl ligands with, in particular, a larger ligand bite which could be applied as building blocks in molecular and supramolecular chemistry.

Part of this work was carried out in collaboration with a Part III (4th year undergraduate) student, Matthew Haynes, who was supervised by the author over a four-month project.

5.2 Results & Discussion

5.2.1 Synthesis of [(2-py)P(μ-N^{t}Bu)]$_2$ (H) and [(8-qy)P(μ-N^{t}Bu)]$_2$ (I)

The starting material [ClP(μ-N^{t}Bu]$_2$ (**J**) was prepared on a multi-gram scale according to a modified literature procedure,[176] in which ^{t}BuNH$_2$ is reacted in a 3:1 molar ratio with PCl_3. The excess amine is employed as the Brønsted base in this reaction to scavenge the HCl generated (Scheme 5.4).[177]

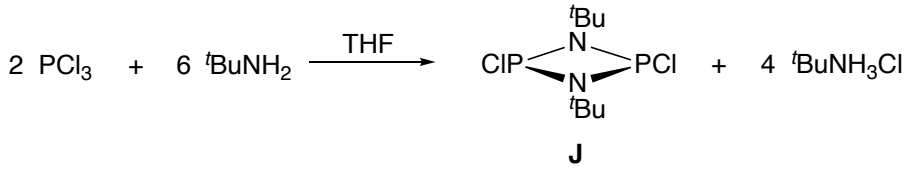

Scheme 5.4: Synthesis of [ClP(μ-N^{t}Bu)]$_2$, **J**.

From this starting material the ligands **H** and **I** were synthesised from an adapted literature procedure, involving the condensation of **J** with two equivalents of the corresponding amine (Scheme 5.5). In this case, Et_3N was used as the Brønsted base.

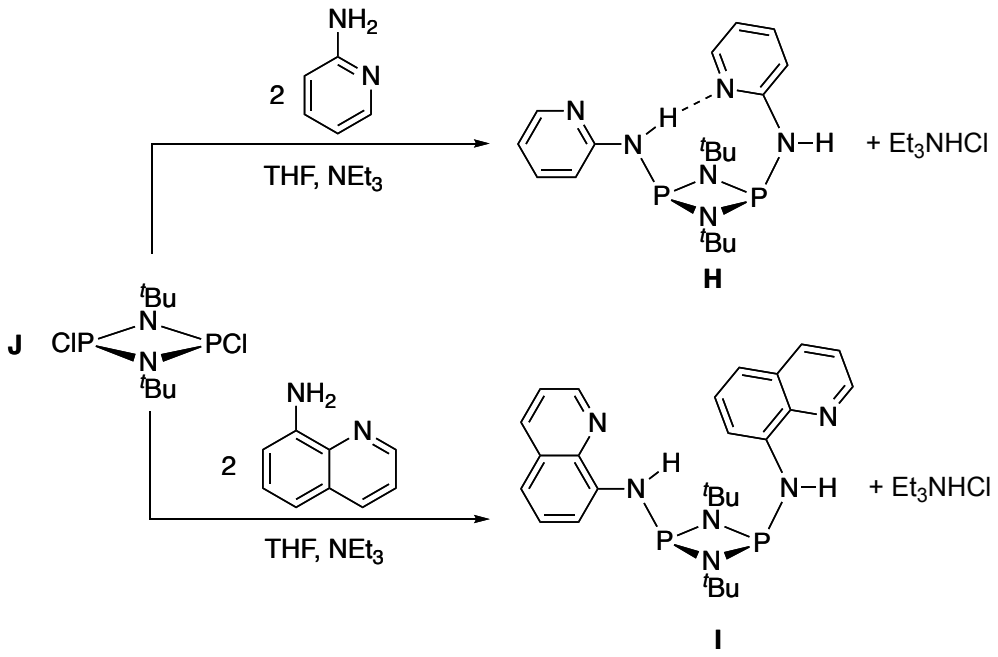

Scheme 5.5: Synthesis of **H** and **I** from the condensation of **J** with two equivalents of the corresponding amine.

The isolation of both **H** and **I** in sufficient yields and purity to allow further studies was difficult, owing to their air- and moisture-sensitive nature which frequently led to the formation of oxidised by-products. Nonetheless, both ligands could be successfully obtained in around 90% purity, as determined by ^{1}H and ^{31}P NMR spectroscopy, and elemental analysis. Compound **H** was obtained in sufficient yield (25%) to facilitate further studies. However, whilst the yield of **I** (17%) is similar, the compound proved to be difficult to purify, rendering it impractical for further investigations.

5.2.2 Coordination Behaviour of H

The coordination chemistry of **H** and **I** has been investigated previously, with some of the most interesting complexes formed mentioned in Section 5.1. Further reactivity studies of **H** were undertaken with silver(I) trifluoromethanesulfonate, silver(I) hexafluorophosphate and copper(I) chloride chosen as candidates, inspired by the previously reported Au(I) complexes [**H**·$(AuCl)_2$] and [**I**·$(AuCl)_2$].[170,171] The reaction of **H** with two equivalents of AgOTf, (OTf = trifluoromethanesulfonate, triflate) in THF resulted in the formation of a pale-grey solution of the complex [**H**·{AgOTf(THF)}{$Ag(THF)_3$}OTf], (**26**), Scheme 5.6. Upon storage of the pale-grey solution of **26** at –17 °C for 72 h, silver-grey crystals were isolated.

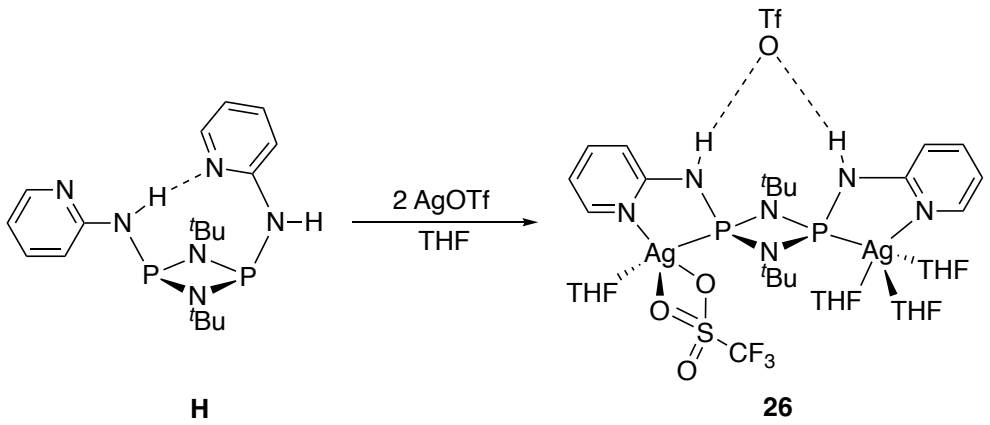

Scheme 5.6: Synthesis of **26** from **H**.

Elemental analysis and recording of the yield of **26** were prevented, owing to the photosensitivity of **26**, which degraded rapidly once isolated in the solid state. Nevertheless, analysis of the compound was made possible through ^{1}H (Figure 5.3) and ^{31}P NMR spectroscopy (Figure 5.4), with the former revealing a downfield shift ($\Delta\delta$ = + 2.76 ppm) of the broad N-H peak (H_e), pointing towards N-H bond polarisation, confirming coordination of Ag(I) to **26** – as expected from previous bimetallic coordination complexes of **H**.[170,171] Further shifts are also observed as evidence of metal coordination: the H_d resonance is shifted ($\Delta\delta$ = + 0.35 ppm), which points towards reduced donation of the amino-N lone pair into the pyridyl ring because of Ag(I) binding. The remaining three pyridyl resonances (H_a, H_b and H_c) are all shifted upfield. In addition, the further splitting of the H_a resonance into a multiplet also points towards coordination as it indicates ^{3}J coupling to ^{109}Ag (I = ½, 48.2%) and ^{107}Ag (I = ½, 51.8%).[178] There are two py environments, each possessing separate H-atoms, which is also shown in the NMR spectra.

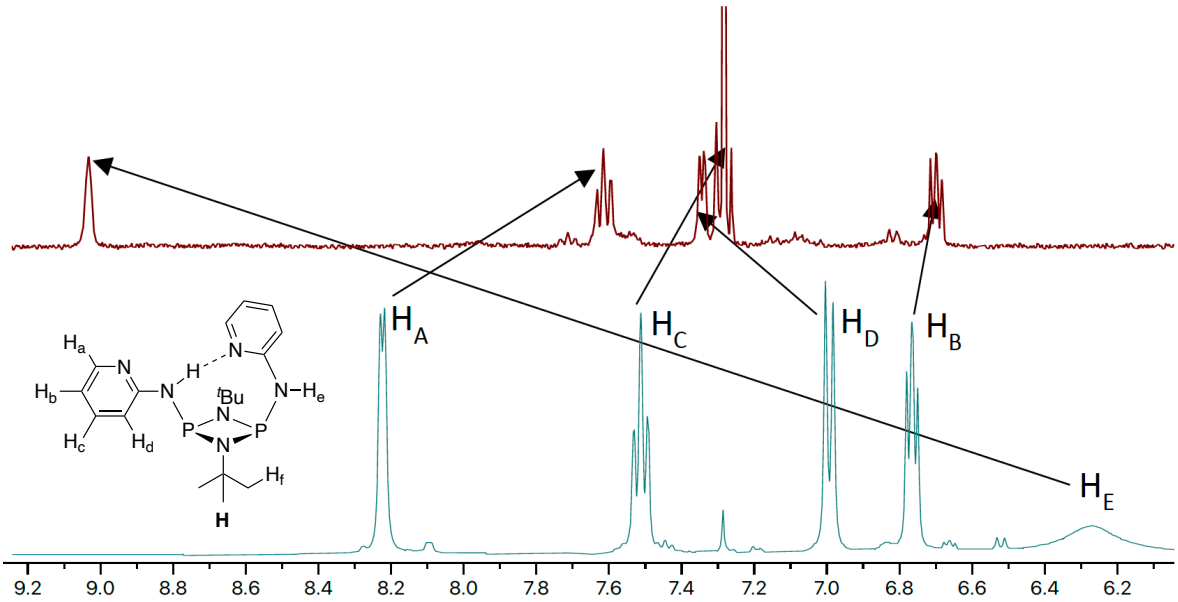

Figure 5.3: Labelled for **H** alongside stacked downfield regions of ^{1}H NMR spectra of **H** (blue) in $CDCl_3$, and **26** (red) in D_8-THF.

At first site, the ^{31}P NMR spectrum consists of two 1:1 phosphorus environments, with each peak split into a doublet by coupling to $^{107/109}$Ag. Assigning the spectrum in this manner, however, gives $^{1}J_{P\text{-}Ag}$ coupling constants an order of magnitude lower than those reported for similar compounds in the literature.[179] A more consistent (and, indeed, the correct) interpretation is that there is a single ^{31}P environment (centred at δ = 86.8(5) ppm) which is split into two doublets by coupling to the two naturally-abundant Ag isotopes ($^{107/109}$Ag, both I = ½). The coupling constants ($^{1}J_{P\text{-}107Ag}$ = 656 Hz and $^{1}J_{P\text{-}109Ag}$ = 570 Hz) are in-line with the literature values and the ratio of the two coupling constants (1:1.15) is the same as the ratio of the gyromagnetic ratios of the two Ag isotopes.[178] This, in tandem with the ^{1}H NMR spectroscopic data, points towards a symmetrical structure for **26** in $CDCl_3$ solution. The chemical shift in the ^{31}P NMR spectrum for **26** (δ = 86.8 ppm) is considerably upfield of that for **H** (δ = 107 ppm, $\Delta\delta$ = – 19.8 ppm). This decrease in chemical shift is potentially associated with the increased $N_{exocyclic}$ lone pair donation into the P-N σ^* antibonding orbital of the cyclodiphosph(III)azane ring, which results from bonding of the Ag(I) ions to the P-atoms of the cyclodiphosphazane ring. This metal bonding may also be responsible for the improved air- and moisture-stability relative to ligand **H**, itself.

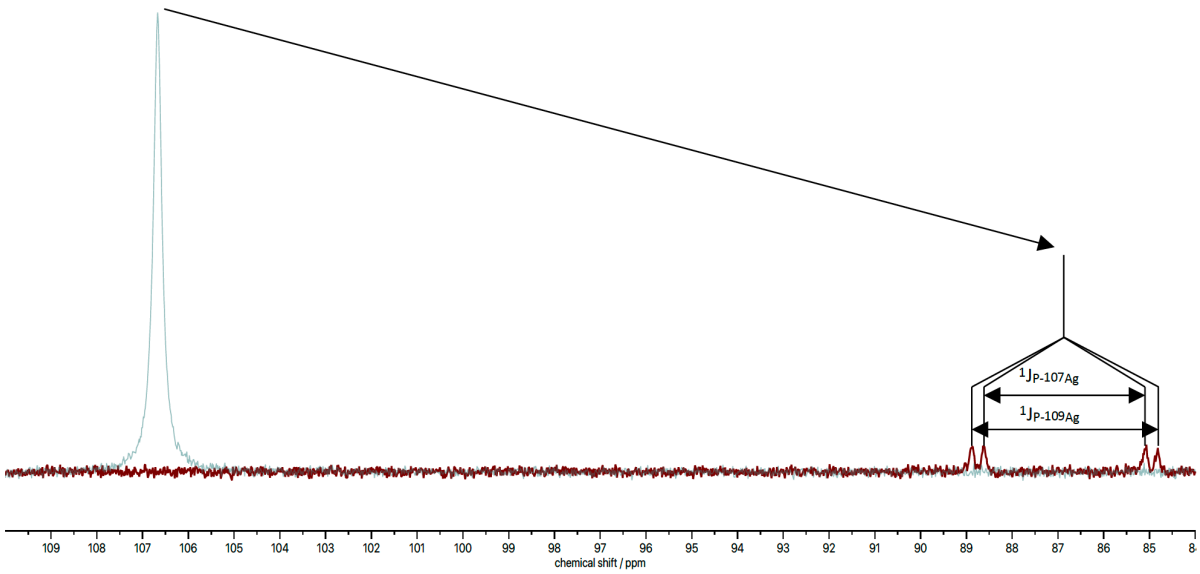

Figure 5.4: Overlaid $^{31}P\{^1H\}$ spectra of **H** (blue) in $CDCl_3$ and **26** (red) in D_8-THF, with the splitting diagram illustrating the two different $^1J_{P\text{-}Ag}$ present in the latter.

The crystals isolated from the reaction mixture were also suitable for an X-ray diffraction study (Figure 5.5 and Figure 5.6). The structure of **26** comprises the coordination of two Ag(I) centres through P,N-chelation to the ligand **H**, and H-bonding of the two exocyclic amino protons (fixed in the *exo-exo* conformation) to a triflate anion. This is in contrast to the aforementioned-literature examples of $[\mathbf{H}\cdot(AuCl)_2]$[171] and $[\mathbf{I}\cdot(AuCl)_2]$[170], where only the phosphorus atoms of the phosphazane units coordinate the two metal centres, with each of Au(I) centres retaining a chloride ligand. The use of the P,N-chelation mode in **26** is similar to that previously seen in complexes of **H** with Mo and Rh (Scheme 5.3).[171] Both of the Ag(I) centres in **26** are five-coordinate. In addition to P,N-chelation by the phosphazane ligand, Ag(1) is coordinated by a THF ligand and chelated by the two O-atoms of a OTf^- anion, while Ag(2) is bonded to three THF ligands. While these coordination numbers are known for Ag(I),[180] they are fairly rare, with two-coordinate linear geometry being the most common for Ag(I).[181] Ag(1) has a particularly distorted geometry in which the pyridyl nitrogen N(1) can be regarded as being in an axial position, with two THF O-atoms and P(1) forming an approximate trigonal plane. However, the strained coordination of the chelating OTf^- with the O(11)-Ag(1)-O(12) angle being 52.3 ° leaves the remaining O-atom of the OTf^- anion significantly displaced from an idealised axial position. Ag(2) adopts a slightly distorted trigonal bipyramidal geometry, with the pyridyl nitrogen N(3) being axial and phosphazane phosphorus P(2) being equatorial. The remaining OTf^- anion is H-bonded to the N-H groups of the phosphazane **H**, in seeming

preference to its bonding to Ag(2). This structure is clearly not retained in solution, as only one phosphorus environment is observed in the ^{31}P NMR spectrum. This is probably the result of a fluxional process, and it is easy to visualise (for example) the interchange of the Ag-bonded OTf^- anion and an Ag-bound THF ligand between the two Ag(I) centres.

The structure of **26** clearly demonstrates the anion binding properties of ligand **H**. The $N_{exocyclic}$-P bond lengths observed in **26** (1.66(2) and 1.67(1) Å) are shorter than those seen in **H** (average 1.71(1) Å), in line with previous calculations which show that metal coordination will result in increased donation of the amido-lone pair to the ring P-N σ*-orbital. This effect enhances the polarisation of the N-H bonds and the ability to H-bond to OTf^- anions. At the same time, Ag chelation also brings the N-H functionality into optimum alignment for anion binding.

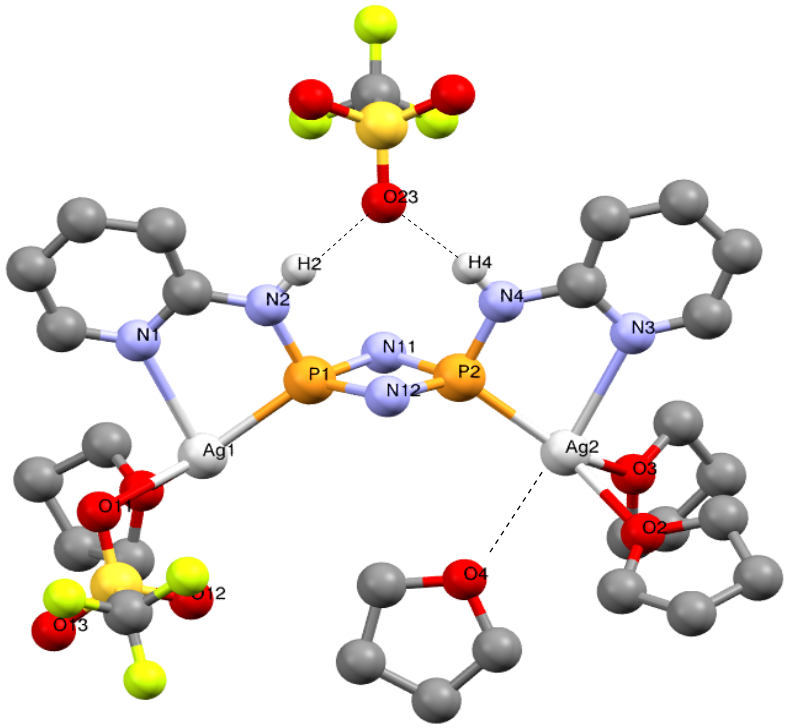

Figure 5.5: Structure of **26**, showing P,N-chelation of two Ag(I) centres and hydrogen bonding of the two $N_{exocyclic}$ amino protons – now fixed in the *exo-exo* position – to a triflate anion.

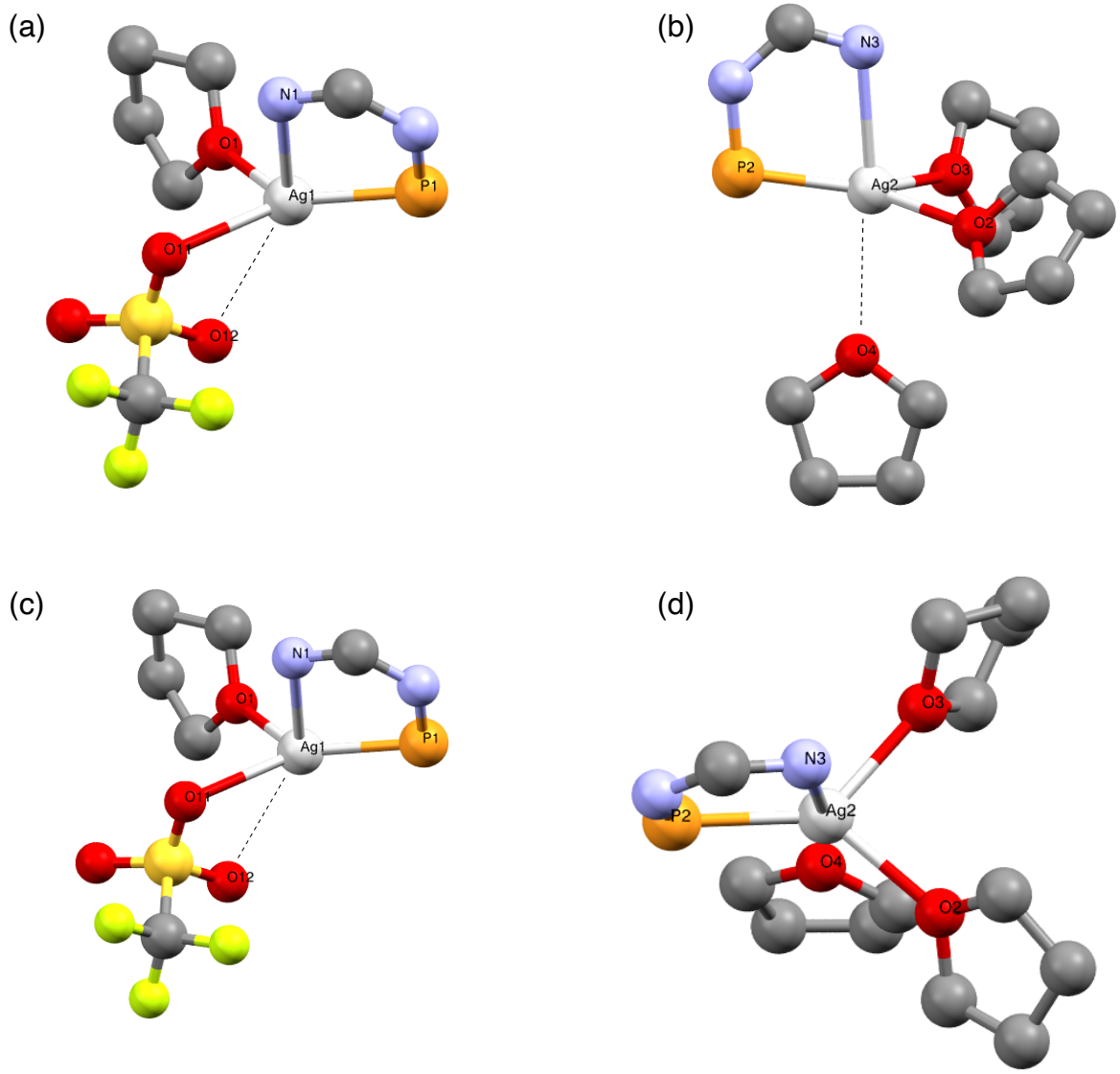

Figure 5.6: X-ray crystals structures of **26**: (a) Cross section through equatorial plane of Ag(I). (b) View along N(1)-Ag(1) axis. Selected bond lengths (Å) and angles (°): P(1)-Ag(1) 2.350(4); N(1)-Ag(1) 2.50(1); O(11)-Ag(1) 2.53(2); O(12)-Ag(1) 2.784; O(1)-Ag(1) 2.25(2); N(2)-P(1) 1.66(2); N(2)-H(2) 0.88; N(1)-Ag(1)-P(1) 77.3; P(1)-Ag(1)-O(12) 124.73; O(11)-Ag(1)-O(12) 52.3; P(1)-Ag(1)-O(1) 134.4; O(1)-Ag(1)-O(11) 92.9; O(11)-Ag(1)-P(1) 132.3. (c) Cross section through equatorial plane of Ag(2) and (d) view along N(3)-Ag(2) axis. Selected bond lengths (Å) and angles (°): P(2)-Ag(2) 2.354(4); N(3)-Ag(2) 2.58(1);O(4)-Ag(2) 3.058; O(2)-Ag(1) 2.29(1); O(3)-Ag(1) 2.33(1); N(4)-P(2) 1.67(1); N(4)-H(4) 0.88;N(3)-Ag(2)-P(2) 76.7; P(2)-Ag(1)-O(4) 95.4; P(2)-Ag(2)-O(2) 135.1; O(2)-Ag(2)-O(3) 91.1; O(3)-Ag(1)-P(2) 133.8.

Further studies of **H** in this work included its metalation by ^{n}BuLi, in order to obtain the dianion $[(2\text{-py})N)P(\mu\text{-}N^{t}Bu)]_2^{2-}$ (**27**). The plan was to use this dianion in further coordination studies

with a range of other metals. This approach has been used previously with the reaction of the dilithiate [**27**.Li_2] with $SbCl_3$, giving the cage compound [{(2-pyN)P(μ-N^{t}Bu)}$_2$SbCl]. Scheme 5.7 shows the formation of the dilithiate [**27**.Li_2]. This reaction was done *in situ* in the current work and was followed by the 1:1 reactions with metal salts MX (CuCl, AgOTf, AuCl(THT)).

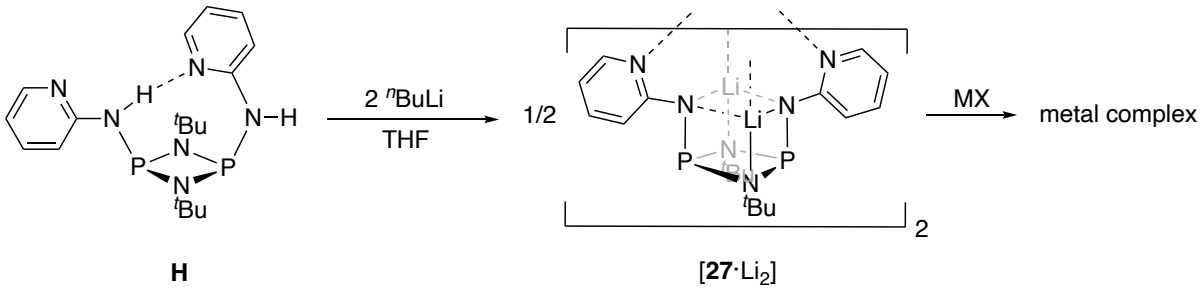

Scheme 5.7: Formation of a dilithiate [**27**·Li_2] from **H**, followed by attempted reactions with Group 11 salts.

However, none of the products of these reactions could be isolated or characterised sufficiently, owing to the formation of insoluble precipitates. In the case of AuCl(THT), the formation of a purple solution with a black precipitate was formed, pointing towards the formation of Au(0) nanoparticles in this case.

In previous work, the dilithiate [**27**·Li_2] has been shown to adopt a highly unusual 'double-cubane' structure in the solid state (as indicated in Scheme 5.7). As part of the studies in this thesis, the synthesis of the potassium complex was also attempted, in order to provide a potentially more effective precursor for transmetallation. Benzyl potassium (BnK, **K**) was synthesised in a manner similar to that published previously (see Chapter 8 Experimental – Synthesis of Starting Materials section, compound **K**),[182] and used in place of ^{n}BuLi as the base in the reaction shown in Scheme 5.7. A colour change from red to yellow was observed upon addition of a THF solution of **H** to a THF solution of benzyl potassium, and removal of all THF solvent *in vacuo* yielded a yellow precipitate. ^{1}H NMR spectroscopy of this solid was inconclusive and suggested that a mixture of products had been formed. Despite this, subsequent storage at –14 °C of the precipitate dissolved in toluene yielded a crop of small yellow crystals, suitable for X-ray diffraction. However, the solid-state structure obtained from these crystals was identified as [KLi{$(SiMe_2)_5O_4$}O_2]$_4$ (**28**), resulting from an apparent side-reaction with silicone grease used to seal the ground glass joints in the Schlenk tube (Scheme

5.8). It can only be speculated what the mechanism of formation of **28** actually is. However, one possibility is outlined in Scheme 5.8. The presence of lithium in the cage arrangement of **28** arises from the method by which benzyl potassium is generated – from reaction of ^{n}BuLi with ^{t}BuOK in toluene. The complicated cage structure of **28** appears to arise from extrusion of a Me_2Si^{2+} fragment from the polymer structure of vacuum grease, with the approximate formula $[Me_2SiO]_{24}$. This would generate the silicon-bridged by-product **29** and the observed product **28**. It should be noted that there is currently no evidence for the formation of the by-product **29**. However, similar species have been observed previously in the reactions of phosph(III)azane dianions with silicon electrophiles.[183] Although reactions of organometallics with silicon grease have been reported previously,[184] normally only one Me_2SiO unit is incorporated into the anionic unit that is formed. The formation of a $[\{(SiMe_2)_5O_4\}O_2]^{2-}$ anion, containing five Si atoms, in **28** is unprecedented.

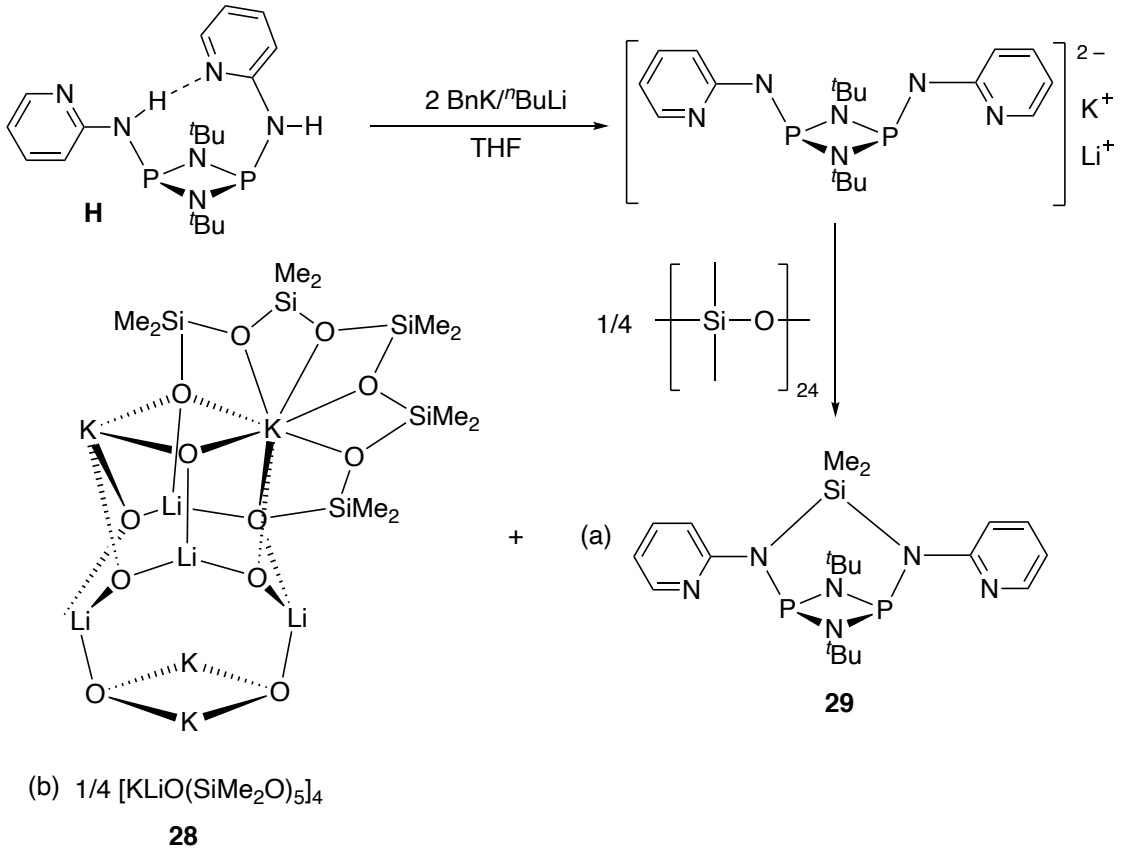

Scheme 5.8: Proposed mechanism of reaction of **H** with benzyl potassium producing (b) cage structure **28**, and (a) **29** – a proposed by-product.

The solid-state structure of **28** (Figure 5.7) is that of a cage consisting of a Li_4K_4 metal core of two interlocked Li_4 and K_4 tetrahedra which are linked together at the periphery by $[\{(SiMe_2)_5O_4\}O_2]^{2-}$ anions (Figure 5.7b). Each potassium cation is eight-coordinate, being chelated by all six oxygens of a $[\{(SiMe_2)_5O_4\}O_2]^{2-}$ anion, in a manner reminiscent of crown ether coordination of an alkali metal, as well as by two terminal (anionic) O-atoms of other $[\{(SiMe_2)_5O_4\}O_2]^{2-}$ anions in the cage. The Li^+ cations are all three-coordinate and coordinated to three of the terminal anionic oxygens from $[\{(SiMe_2)_5O_4\}O_2]^{2-}$ anions.

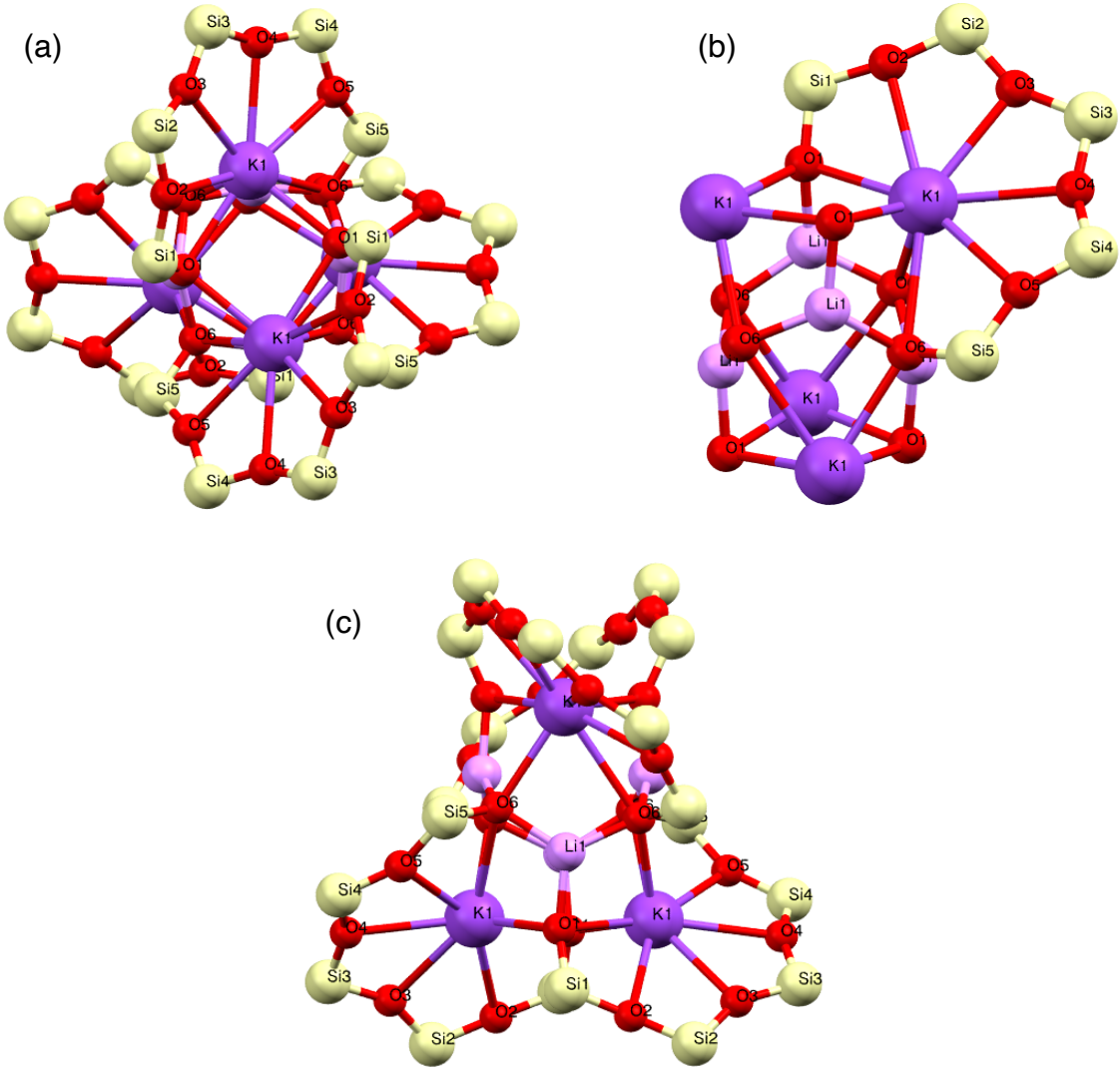

Figure 5.7: Solid-state structure of **28**. Selected bond lengths (Å) and angles (°): K(1)-O(1) 2.677(3); K(1)-O(2) 3.039(3); K(1)-O(3) 2.975(3); K(1)-O(4) 2.996(3); K(1)-O(5) 2.968(3); K(1)-O(6) 3.157(2); Li(1)-O(1) 1.821(6); Li(1)-O(6) 1.893(7), O(1)-Li(1)-O(6) 118.8(4), O(1)-K(1)-O(1) 82.02(8). (a) View down the C_2 axis of the two metal tetrahedra, illustrating the symmetry of the complex, (b) Three $(OSiMe_2)_5O^{2-}$ chains emitted to clearly show the Li_4 and K_4 tetrahedra and terminal oxygens of the

central cage, and (c) View showing the chelation of each of the K^+ cations at the vertices of the cage by one $(OSiMe_2)_5O^{2-}$ chain unit.

Further work is required to uncover the mechanism of formation of **28** and to reproduce its synthesis in reasonable yield. However, bearing in mind the current interest in silicone macrocycles,[185] **28** could represent an interesting precursor to a range of macrocycles of this type (i.e., by closing the chain anion with an electrophile such as Me_2SiCl_2). At this time, studies of **28** are included here because of the potential for future interest in this area.

5.2.3 Synthesis of [(3-py)P(μ-N^{t}Bu)]$_2$ (30)

As mentioned previously in Section 5.1, a central interest in the current Chapter is the incorporation of 3-aminopyridine groups into phosphazane scaffolds. With experience of the 2-pyridyl phosphazane ligand **H** gained from the previous studies, research moved on to the attempted preparation of [(3-py)P(μ-N^{t}Bu)]$_2$ (**30**). The synthetic route is exactly the same as that used previously for **H** and **I**, through the condensation of [ClP(μ-N^{t}Bu)]$_2$ (**J**) with 3-aminopyridine in the presence of Et_3N (Scheme 5.9). However, initial attempts to obtain **30** using the same solvent extraction procedure as that employed for **H** and **I** failed to produce **30** in good reasonable yield.

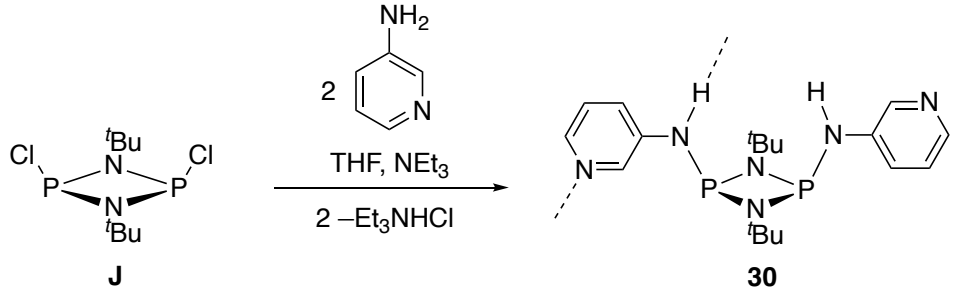

Scheme 5.9: Synthesis of **30** from **J** and 3-aminopyridine.

Subsequently the procedure was modified, with the product being extracted in hot acetonitrile as opposed to hot hexane. After being left to stand for 72 h at room temperature, **30** was isolated as a pale-yellow crystalline product (57% yield). Samples were shown to be highly pure by

elemental analysis. ^{1}H and ^{31}P NMR spectra also confirmed the purity and unambiguously assigned ligand **30**.

The solid-state structure of **30** is shown in Figure 5.8. As anticipated, the structure of **30** shows the same type of cyclodiphosphazane arrangement as that seen for **H** and **I**. Also expected is the *cis*- conformation of the amido groups with respect to the P_2N_2 ring unit. However, unlike **H** and **I**, which adopt *endo-exo* conformations of the organic substituents in the solid state, an *exo-exo* conformation is adopted in **30**. This is the result of the disposition of the pyridyl-N atom which, now being in the 3-position, cannot form an intramolecular H-bond across the centre of the P_2N_2 ring unit. Instead, the N-atom within the 3-pyridyl groups in **30** is involved in an H-bonded network formed between molecules of **30**, which may be observed in the extended solid-state structure in Figure 5.9. The formation of an H-bonded network in the lattice of **30** points towards potential applications in supramolecular coordination chemistry.

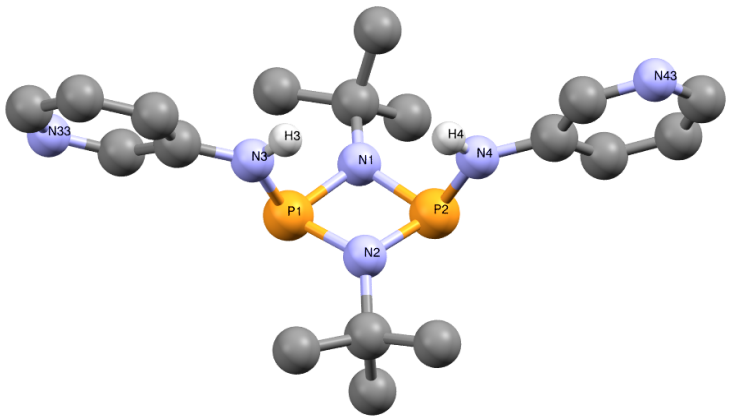

Figure 5.8: Solid-state structure of **30**. H-atoms omitted for clarity. Selected bond lengths (Å) and angles (°): P(1)-N(3) 1.694(2), P(2)-N(4) 1.701(2), P(1)-N(2) 1.731(2), P(1)-N(1) 1.711(2), P(2)-N(2) 1.718(2), P(2)-N(1) 1.701(2); N(1)-P(1)-N(3) 101.95, N(2)-P(2)-N(4) 102.81, N(1)-P(2)-N(4) 106.52, N(1)-P(1)-N(3) 106.11.

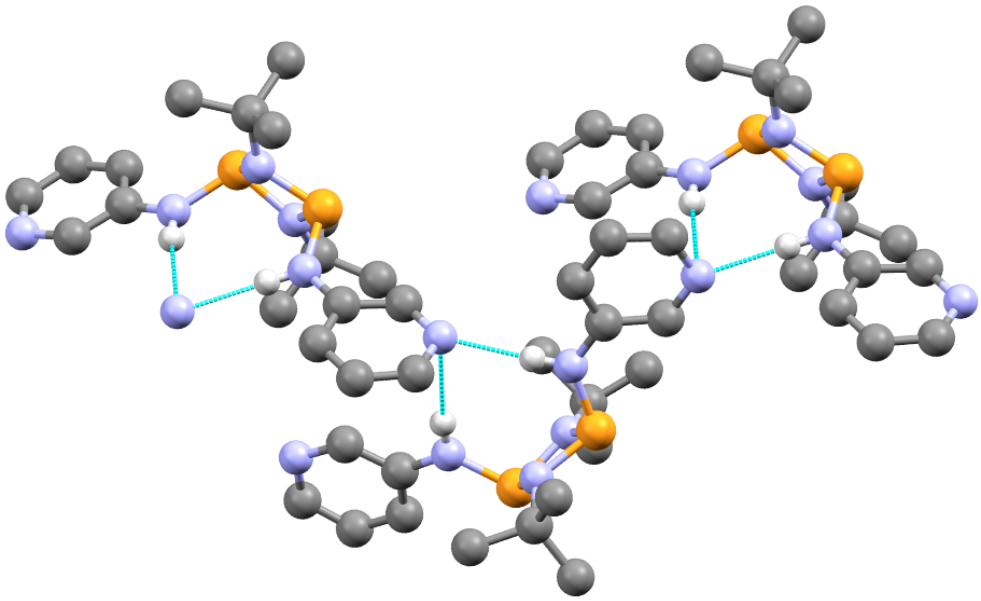

Figure 5.9: Extended X-ray crystal structure of **30**, with intermolecular H-bond shown in cyan. *tert*-butyl groups and non-relevant hydrogen atoms omitted for clarity. Selected H-bond lengths (Å): H(3)-N(33) 2.15(1).

Prolonged storage of solutions of **30** also resulted in partial hydrolysis, with one of the 3-aminopyridine substituents hydrolysing to yield the mixed P(III)/P(V) cyclodiphosphazane [(3-py)NHP(μ-N^{t}Bu)$_2$PH(=O)] (**31**), which can often be observed as a minor contaminant in samples of **30** (Scheme 5.10). Crystals of sufficient quality were also isolated, and the solid-state structure is shown in Figure 5.10.

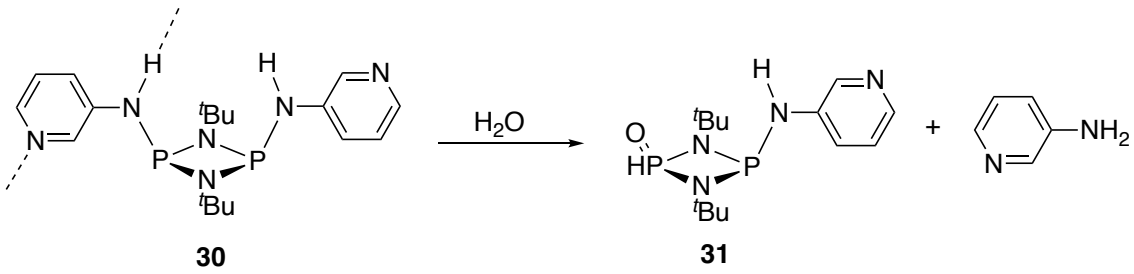

Scheme 5.10: Partial hydrolysis of **30** to form compound **31**.

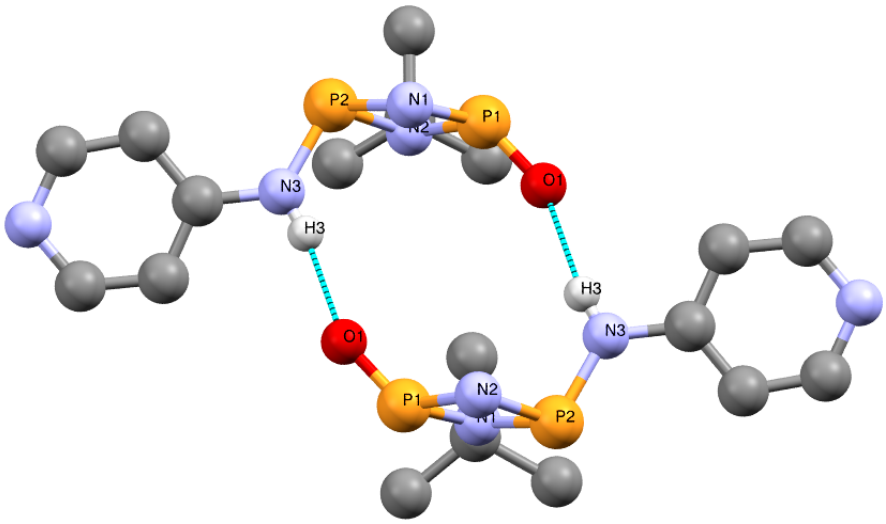

Figure 5.10: Solid-state structure of **31**, with intermolecular H-bonds shown in cyan. H-atoms omitted for clarity, except those on the N-H groups. Selected bond lengths (Å) and angles (°): P(1)-O(1) 1.464(2), P(1)-N(1) 1.651(3), P(1)-N(2) 1.657(2), P(2)-N(3) 1.678(2), P(2)-N(1) 1.718(2), P(2)-N(2) 1.741(2), N(3)-H(3) 0.81(3), O(1)-P(1)-N(1) 121.46(14), O(1)-P(1)-N(2) 121.73(14), P(2)-N(3)-H(3) 122(2). Intermolecular separation (Å) O(1)---H(3) 2.145.

While the X-ray data were of poor quality, they were sufficient to determine atomic connectivity. The presence of oxygen atoms introduced by the hydrolysis also leads to the formation of dimers through H-bonding. The H-bonds between O(1) and H(3) are both 2.14(1) Å.

5.2.4 Coordination Behaviour and Reactivity of 30

A range of transition metals, alkali metal salts and complexes were reacted with **30**. Inspired by the previously reported reactivity of **H**, **30** was reacted with two equivalents of ^{n}BuLi in THF, as well as with two equivalents of benzyl potassium (**K**) in THF in attempts to deprotonate **30** (Scheme 5.11).

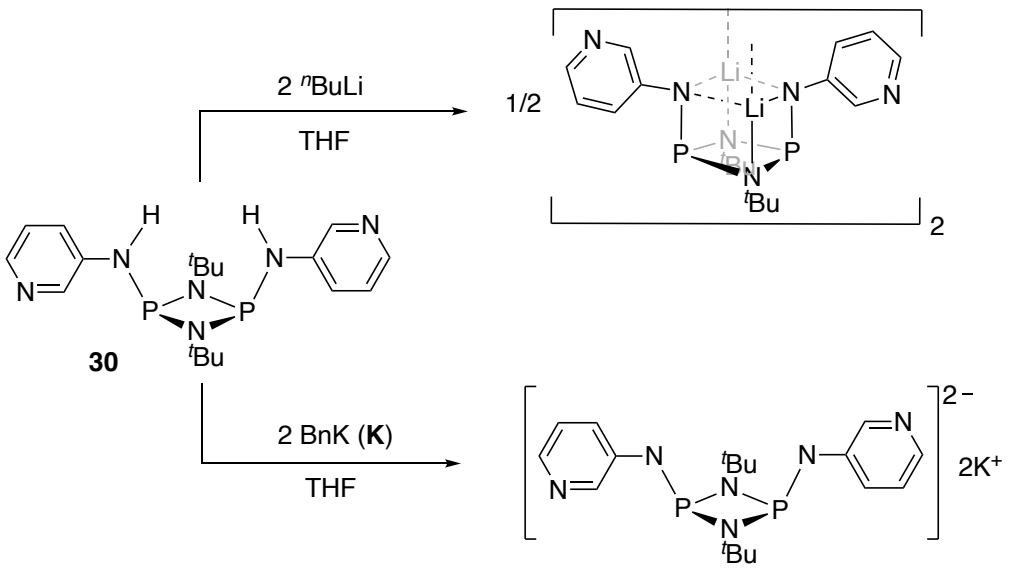

Scheme 5.11: Deprotonation of **30** using ^{n}BuLi or benzyl potassium.

Both reactions resulted in a colour change from colourless to amber with ^{n}BuLi, and from red to pale-green with BnK. Obtaining the solid-state structures of both compounds proved not to be possible, owing to the highly sensitive nature of the compounds and the inherent decomposition upon crystallisation attempts, with repeated attempts only producing precipitates. However, ^{1}H NMR spectroscopic studies were undertaken, shown in Figure 5.11.

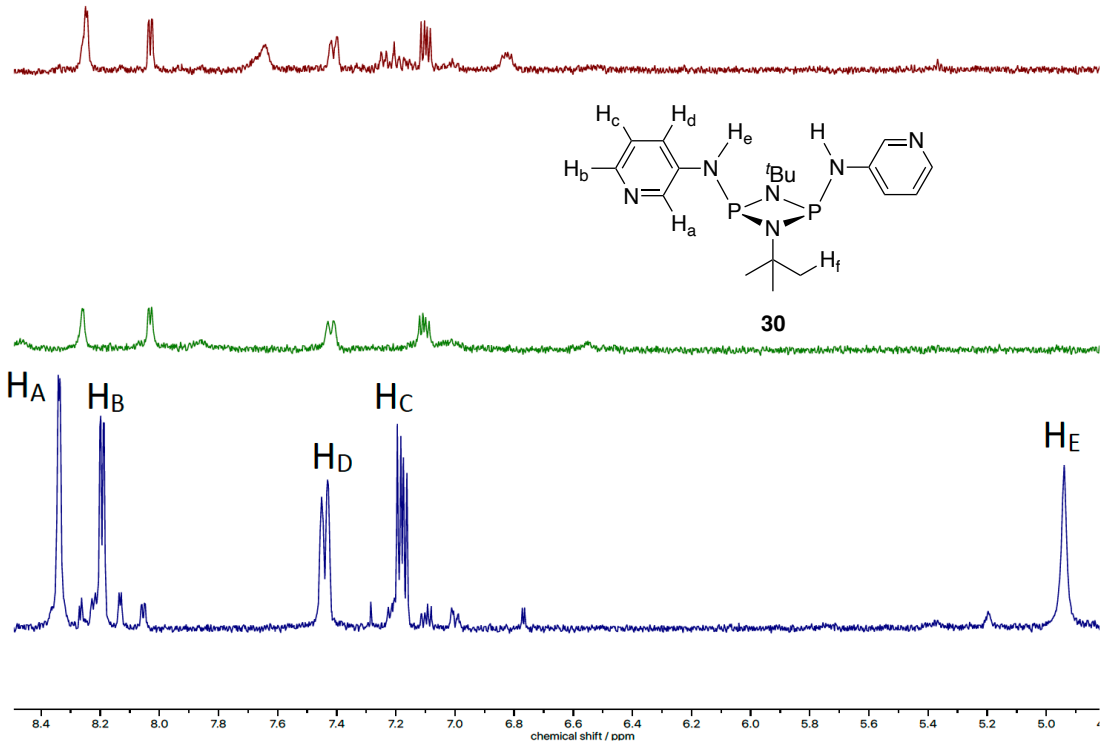

Figure 5.11: Labelled figure of **30** for ^{1}H NMR assignments and stacked spectra of **30** (blue) in $CDCl_3$ and the products of its reactions with ^{n}BuLi (green) and BnK (red), both in D_8-THF.

Assignment of the ^{1}H NMR spectra of the solid products from the reactions was not straightforward. However, it is clear in both cases from both a shift in pyridyl peaks and the loss of the N-H resonance of ligand **30** at δ = 4.98 ppm that deprotonation has occurred. Consistent with this, the shift of the pyridyl peaks upfield relative to the spectrum of **30** in both cases also suggests increased donation of the now-anionic exocyclic nitrogen lone pair into the pyridyl rings. The ^{31}P NMR spectra (Figure 5.12) show significant broadening and a similar downfield shift for the ^{n}BuLi product (3.6 ppm) and the benzyl potassium product (3.2 ppm) compared to the singlet present in **30**. Whilst this could indicate the formation of a dimetalate (lithiate/potassiate), the downfield shifts are not as significant as that observed upon the dilithiation of **H** (51.0 ppm).

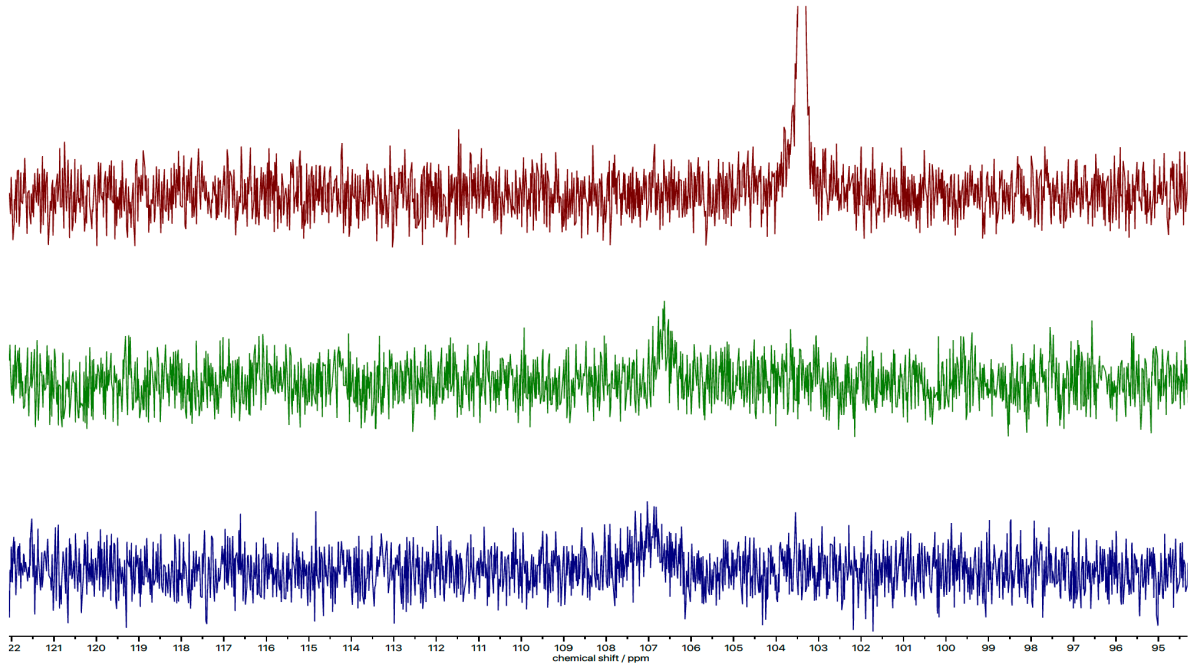

Figure 5.12: Stacked $^{31}P\{^{1}H\}$ NMR spectra of **30** (red) in $CDCl_3$ and the products of its reactions with ^{n}BuLi (green) and BnK (blue), both in D_8-THF.

Reactions of **30** with various transition metal salts and complexes were met with variable success. Coordination studies of **H** and **I** with molybdenum(0), ruthenium(II) and gold(I) have all previously been reported, along with the aforementioned silver(I) complex with **H** discussed earlier in this Chapter. The coordination behaviour of **30** was investigated using the same metal salts, as well as with copper(I) and cobalt(II) salts. Unfortunately, although colour changes were observed, no solid products could be isolated from reactions of **30** with CuBr, $AgPF_6$, AgOTf, AuCl(THT), $Mo(CO)_6$, $(C_7H_8)Mo(CO)_3$ and $CoCl_2$, preventing sufficient characterisation by X-ray crystallography and NMR spectroscopy. Similar problems were encountered in reactions of the dilithiate of [**27**·Li_2] with $MnCp_2$ and $Mo(CO)_6$, and although crystals were isolated in the case of the latter they were identified as unreacted $Mo(CO)_6$.

However, upon the reaction with one equivalent of [(*p*-cymene)$RuCl_2$]$_2$ (containing two equivalents of Ru(II)) with **30**, a colour change from red to orange was observed and the solid product was successfully isolated (Scheme 5.12). Whilst a solid-state structure was not obtainable despite repeated attempts to grow single crystals, the ^{31}P NMR spectrum suggests the formation of a single product.

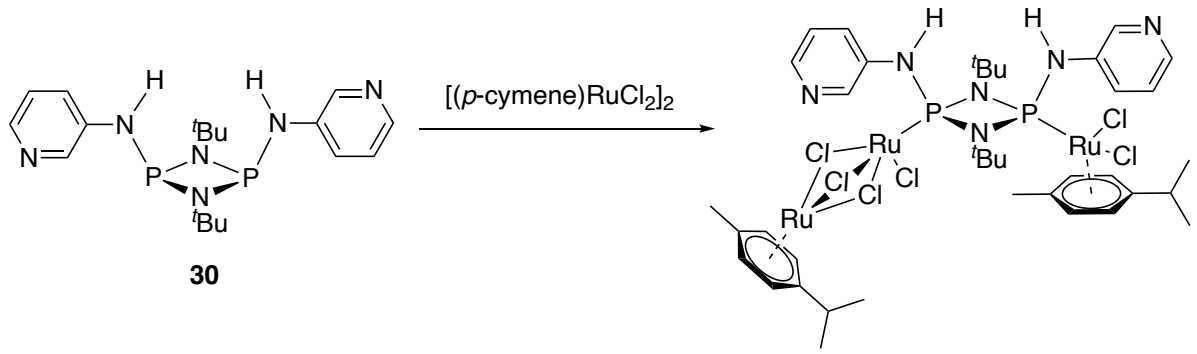

Scheme 5.12: Reaction of **30** with one equivalent of $[(p\text{-cymene})RuCl_2]_2$, along with predicted product formed.

The stacked spectra of **30** and its solid product from the Ru(II) dimer are show in Figure 5.13.

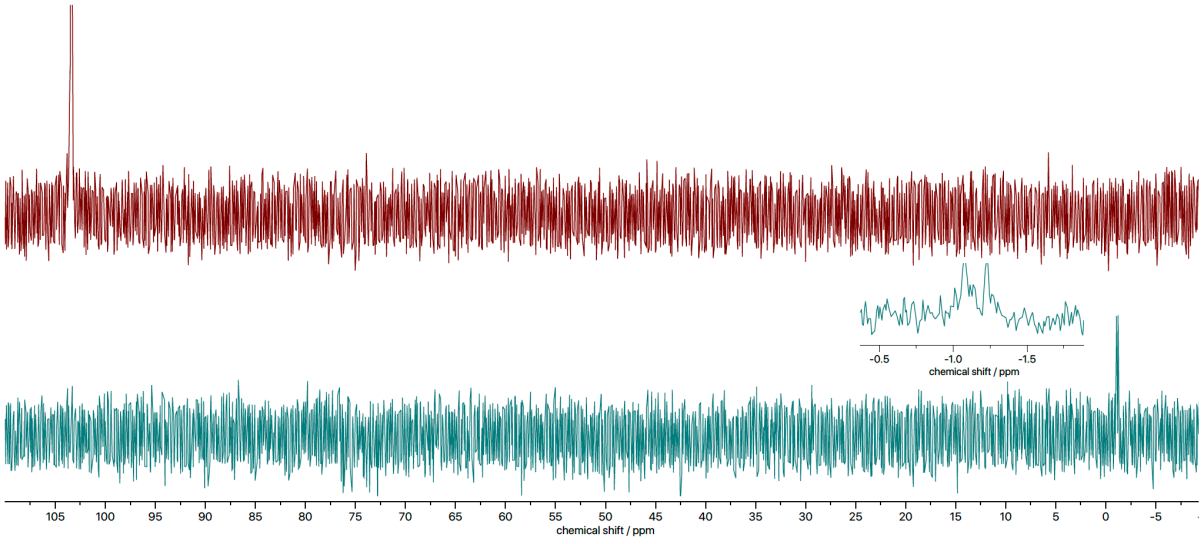

Figure 5.13: Stacked $^{31}P\{^{1}H\}$ NMR spectra of **30** (red) in $CDCl_3$ and the product of its reaction with $[(p\text{-cymene})RuCl_2]_2$ (blue) in $CDCl_3$.

The spectrum of the product contains two singlets with similar shifts ($\delta = -1.08$ ppm; $\delta = -1.23$ ppm), which are located upfield with respect to the single environment of **30**. Given that neither of these peaks are present in either the spectrum of **30**, or the spectrum of the hydrolysis product, this result suggests that a complex has formed in which both of the phosphorus atoms have coordinated to a Ru(II) centre (no coupling to ruthenium is expected). The slight difference in chemical shifts observed between the two environments may be attributed to

retention of chloride ligands by the two Ru(II) centres, as was seen previously with the analogous complex formed between **H** and [(*p*-cymene)$RuCl_2$]$_2$.[170] However, the ^{31}P NMR spectrum of this complex is rather different to that mentioned, above, with the complex from **H** forming two products. The chemical shifts of one of these compounds are cf. δ = 111.6 ppm; δ = 89.5 ppm),[170] both of which differ from the complex formed from **30** (δ = –1.08 ppm; δ = –1.23 ppm), whose peaks are shifted significantly upfield.

Given the very limited success of the coordination studies of **30** with transition metals and the observed tendency for this phosph(III)azane to hydrolyse, it was decided to oxidise **30** with Group 16 elements (E) in order to obtain a more stable ligand arrangement - oxidation has been shown previously to potentially improve air- and moisture-stability (P(III) → P(V)). A comparison between the coordination mode is shown in Figure 5.14.

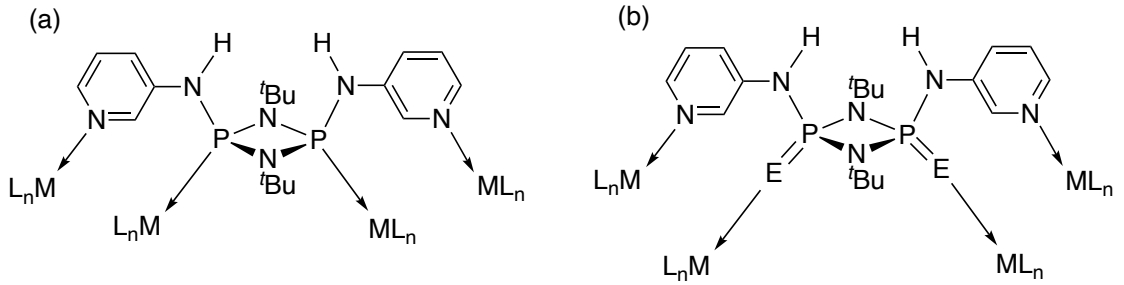

Figure 5.14: Figure depicting (a) compound **30**, in which bridging is less likely, and (b) Group 16-oxidised (E) equivalent, illustrating its potential as a bridging ligand.

The first attempt to oxidise **30** was made by reacting it with excess hydrogen peroxide (Scheme 5.13).

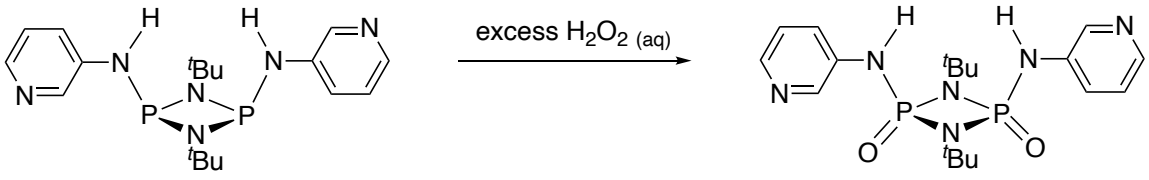

30

Scheme 5.13: Oxidation of **30** with H_2O_2.

Recrystallisation from acetonitrile led to the formation of a brown fibrous precipitate, which was too insoluble to permit further analyses by NMR spectroscopy. Additional attempts to oxidise **30** adopted the use of excess elemental sulfur (Scheme 5.14), leading to the formation of a crystalline product. However, this was unsuitable for X-ray studies as a large amount of unreacted sulfur present proved difficult to separate. Nonetheless, ^{1}H, ^{31}P and ^{1}H-^{1}H COSY NMR spectroscopic studies pointed towards the formation of the desired cyclodiphosph(V)azane as the only product of the reaction, [(3-py)(S=)P(μ-N^{t}Bu)]$_2$ (**32**).

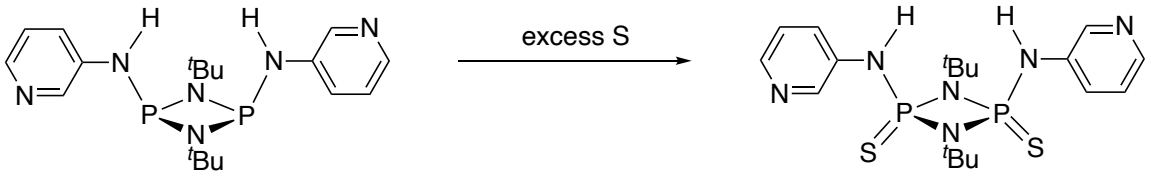

30 **32**

Scheme 5.14: Oxidation of **30** with sulfur to form **32**.

^{1}H NMR spectrum of **32** is shown in Figure 5.15. It is noticeable that all peaks are shifted downfield (particularly the N-H peak) compared to **30**.

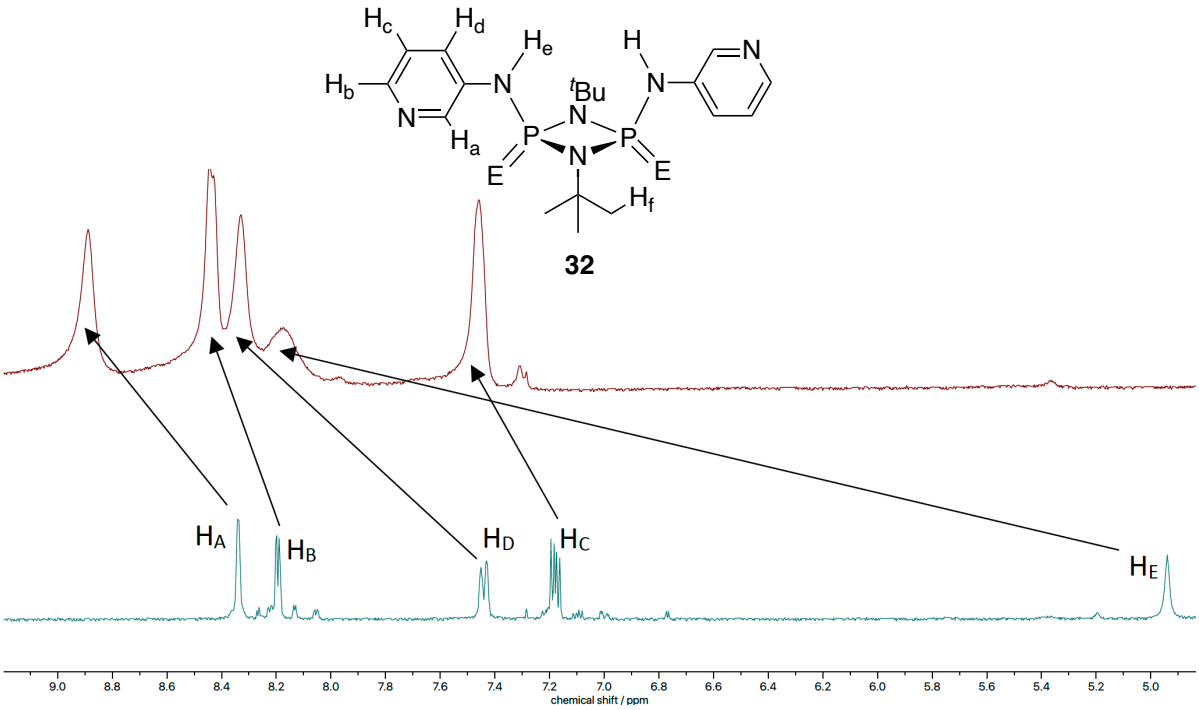

Figure 5.15: Labelled figure of **32**, stacked ^{1}H NMR spectra of **30** (blue) and [(3-pyNH)(S=)P(μ-N^{t}Bu)]$_2$ (E = S), (**32**) (red), both in $CDCl_3$.

In the case of the ^{31}P NMR spectra (Figure 5.16), a significant upfield shift is observed of the singlet in the product spectrum ($\Delta\delta$ = – 63.0(7) ppm), confirming the successful oxidation of both phosphorus centres from P(III) to P(V).

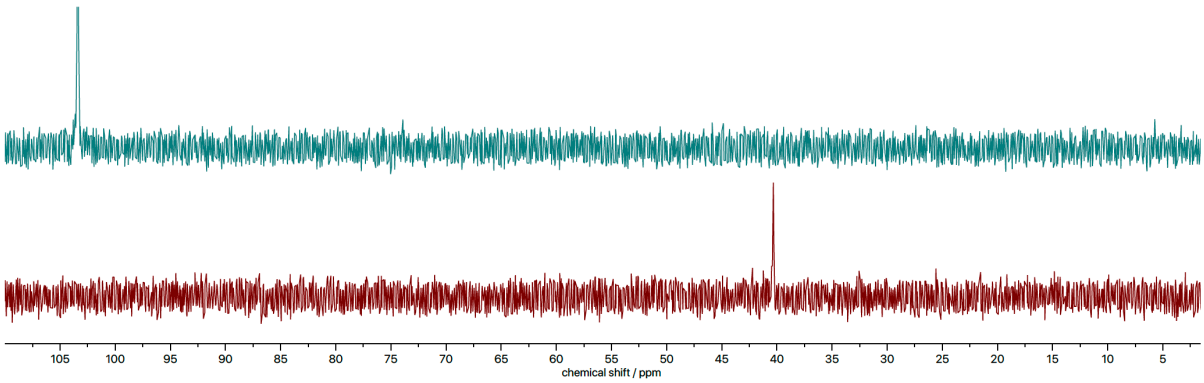

Figure 5.16: ^{31}P{^{1}H} NMR spectra of **30** (blue) and [(3-py)(S=)P(μ-N^{t}Bu)]$_2$ (**32**) (red), both in $CDCl_3$.

In the ^{1}H-^{1}H COSY (Figure 5.17), ^{3}J coupling is observed from H_c to both H_b and H_d, with weaker ^{4}J W-coupling also seen between H_a and H_b. The absence of any cross-peaks between the signal at δ = 8.15 ppm and any other signal confirms its identity as H_e.

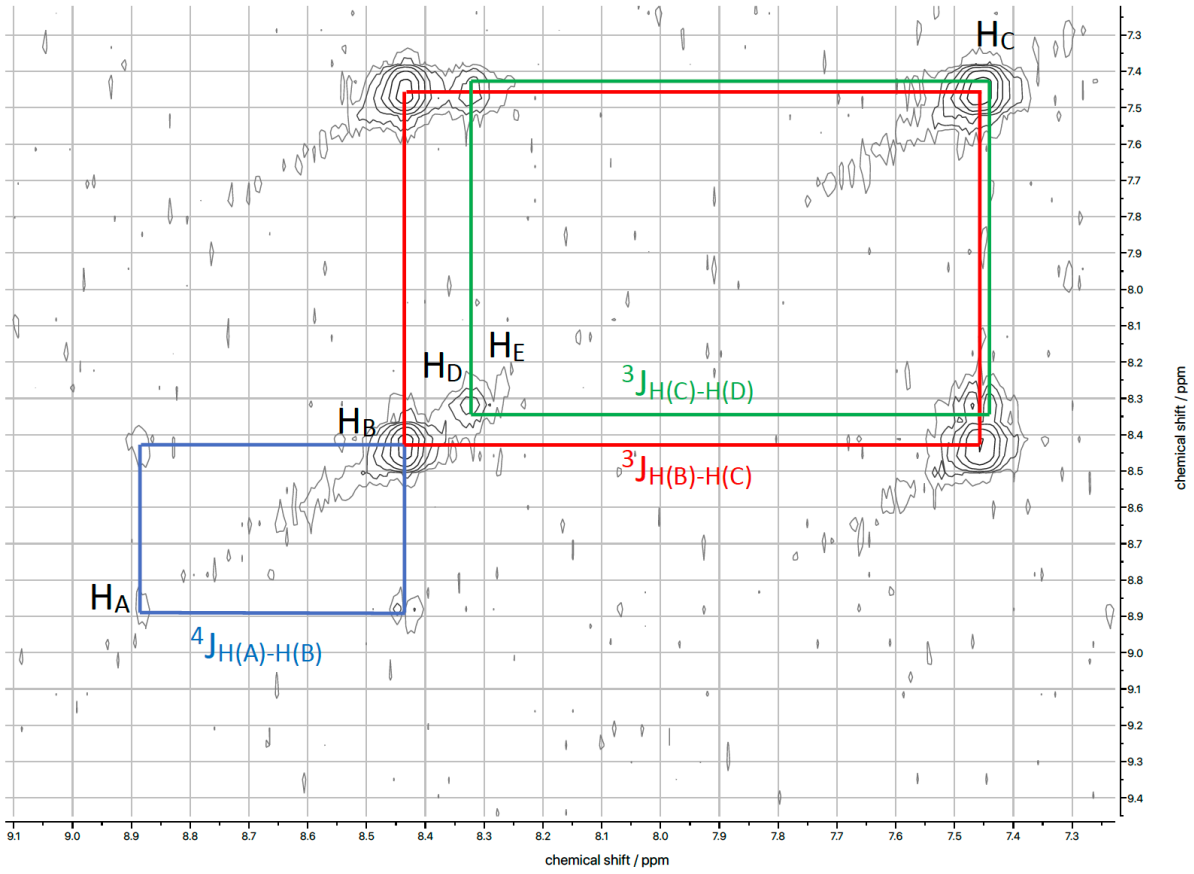

Figure 5.17: ^{1}H-^{1}H COSY NMR spectrum (25 °C, 400 MHz, $CDCl_3$) of [(3-pyNH)(S=)P(μ-N′Bu)]$_2$ (**32**).

The reaction of **30** with excess selenium afforded the doubly-oxidised product [(3-py)(Se=)P^{V}(μ-N′Bu)]$_2$] (**33**) (Scheme 5.15), in the absence of other by-products.

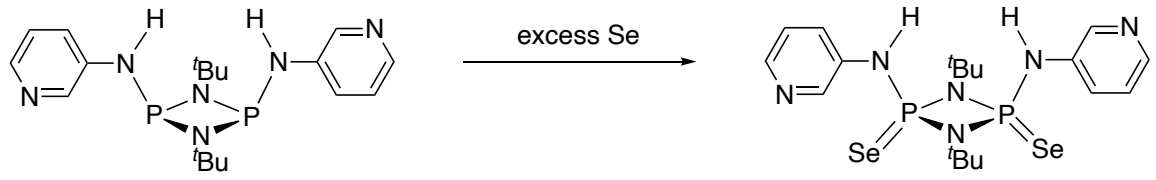

30 **33**

Scheme 5.15: Oxidation of **30** with selenium to form **33**.

Compound **33** was successfully obtained as a white crystalline product, through an extraction in acetonitrile, followed by filtration to remove any unreacted selenium. It was characterised by ^{1}H and ^{31}P NMR spectroscopy, and X-ray crystallography. Figure 5.18 shows the overlaid ^{1}H NMR spectra of **30** and product **33**, with added expansion in the aromatic (pyridyl) region – all signals are deshielded and are observed at values slightly downfield relative to their corresponding resonances in **30**.

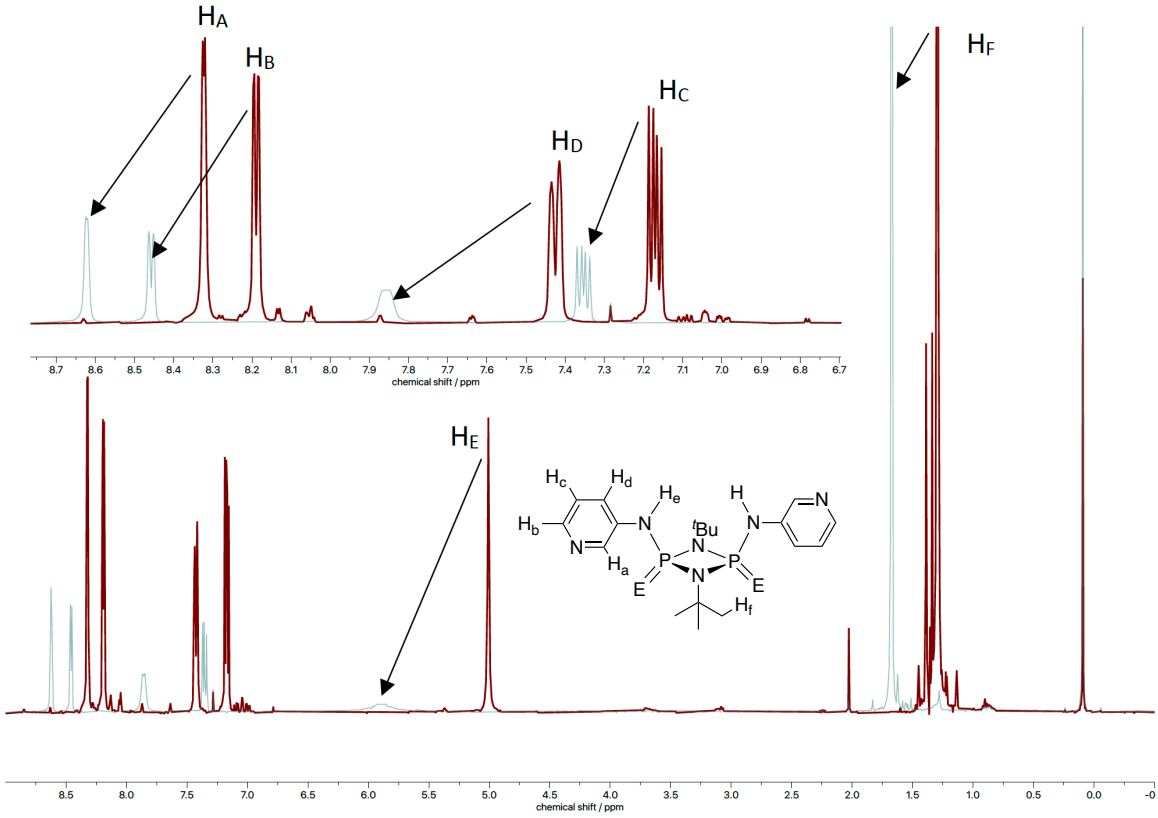

Figure 5.18: Labelled figure for **30** and **33** alongside the overlaid ^{1}H NMR spectra in $CDCl_3$: **30** (red) and **33** (blue), with expansion showing the pyridyl region. E = Se.

This upfield shift can be ascribed to greater electron donation from the 3-aminopyridyl groups to the now-more-electronegative P(V) centres, due to oxidative addition of Se. Complementary behaviour is observed in the ^{31}P NMR spectra (Figure 5.19), with the oxidative addition of Se to form more shielded P(V) centres being demonstrated by an upfield shift of δ = 71.2 ppm.

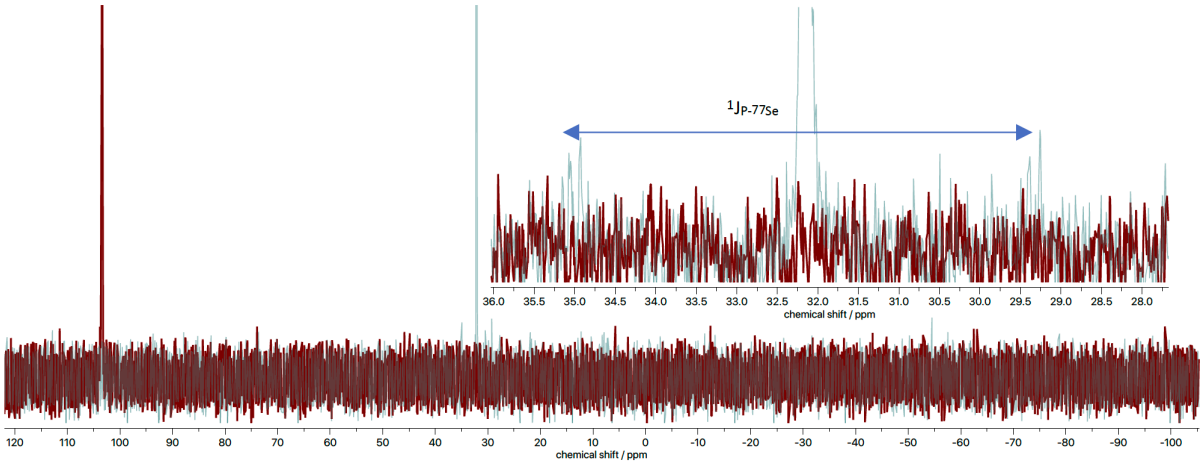

Figure 5.19: Overlaid ^{31}P{^{1}H} NMR spectra of **30** (red) and **33** (blue), both in $CDCl_3$.

Notably, ^{77}Se satellites are also observed ($^{1}J_{P\text{-}Se}$ = 916 Hz) which is further proof of the oxidation. Furthermore, the reduced electronegativity of Se relative to S is also consistent with the ^{31}P resonance for **33** being upfield of that seen in [(3-pyNH)(S=)P^{V}(μ-N^{t}Bu)]$_2$] (**32**) (described above). The solid-state structure of **33** shows both P atoms have been oxidised by selenium. Unlike **30** in which the pyridyl groups adopt an *exo-exo* conformation, the groups in **33** are found in an *endo-exo* arrangement (Figure 5.20a). This is probably due to the presence of multiple non-covalent interactions in the lattice, including π-π stacking from overlapping pyridyl rings, resulting in the formation of a supramolecular polymer (Figure 5.20b).[186] H-bonding is also present between dimers of **33** between the amino protons and pyridyl nitrogens. As a consequence of both the presence of π-π stacking and H-bonding interactions, a ladder-like structure is formed (Figure 5.20c). The π-π stacking interactions adopt a staggered conformation, with the centres of the stacked rings slightly offset from one another, maximising the electrostatic interactions between their aromatic quadrupoles.[186]

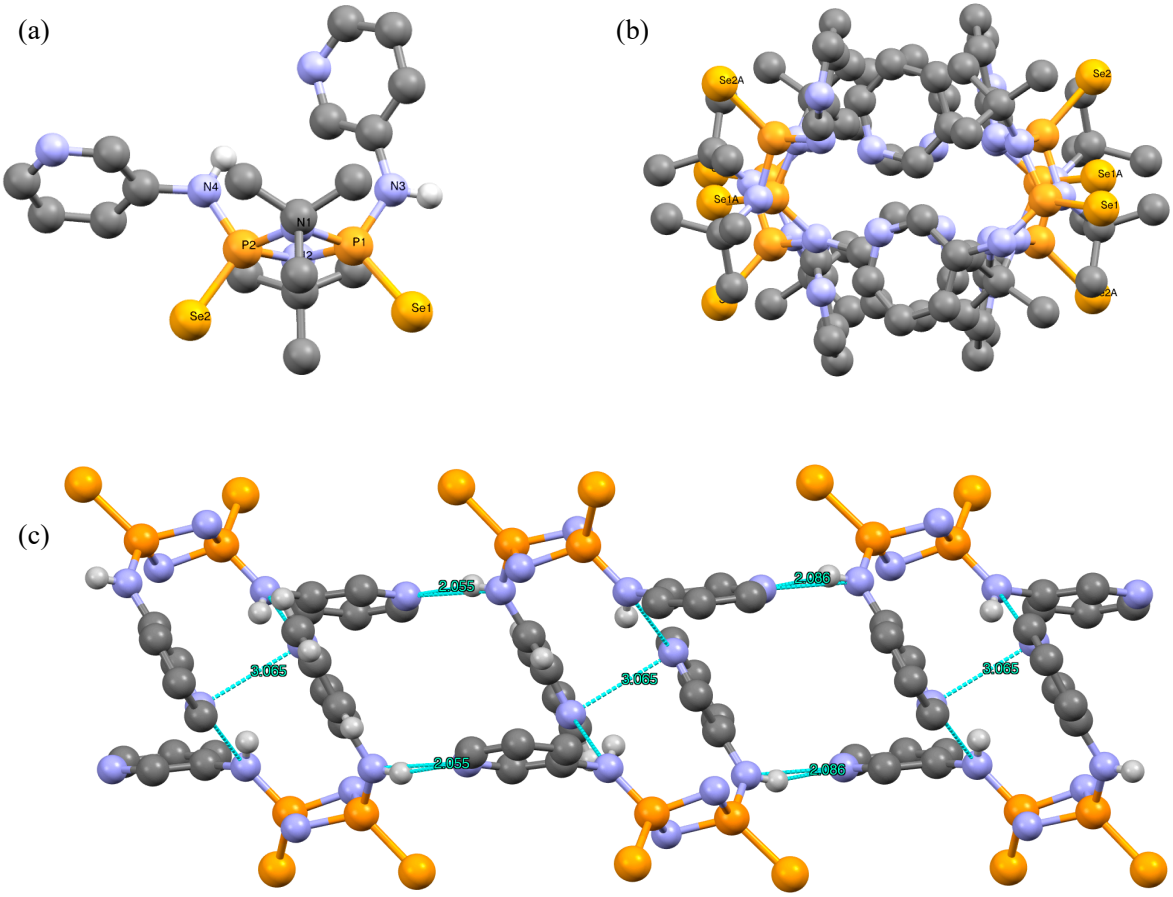

Figure 5.20: X-ray crystal structure of **33**. MeCN solvent of crystallisation, non-relevant H atoms and *tert*-butyl groups (except in (a)) omitted for clarity. Selected bond lengths (Å): P(1)-Se(1) 2.079(3); P(1)-N(3) 1.62(1); P(2)-Se(2) 2.075(4); P(2)-N(4) 1.637(9). (a) Shows monomer with both P atoms oxidised with selenium. Unlike **30**, the molecule is found in the *endo-exo* conformation, with this explained by the extended structure shown in b) and c). (b) Shows a view down the axis of a linear supramolecular polymer, with the overlapping pyridyl rings exhibiting π-π stacking interactions. (c) Shows the ladder-like structure formed as a consequence of the formation of both π-π stacking and H-bonding interactions. The π-π stacking interactions can be seen to be in the expected staggered conformation in this view, with the centres of stacked rings offset relative to one another in order to maximise the electrostatic interactions between their aromatic quadrupoles.

5.3 Conclusions

The work presented in this Chapter forms the foundation towards the incorporation of 3-pyridyl substituents into cyclophosphazanes. Initially, further reactions with previously-reported **H** were investigated, with the novel complex [OTf·**H**·{AgOTf(THF)}{Ag(THF)$_3$}] (**26**) being synthesised and its properties studied extensively. This is a rare example containing five-coordination silver(I) centres, as well as providing a model system for the anion-sensing

capabilities conferred to the cyclodiphosph(III)azane **H**. Further studies of **H** involved an attempt to deprotonate it with benzyl potassium, with the formation of an unexpected product of reaction with vacuum grease $[KLi\{(SiMe_2)_5O_4\}O_2]_4$ (**28**), containing units of $[\{(SiMe_2)_5O_4\}O_2]^{2-}$. One of the most important advances made was the successful synthesis of the cyclodiphosph(III)azane $[(3\text{-pyNH})P(\mu\text{-N}^t\text{Bu})]_2$ (**30**). Although initial reactivity studies of **30** towards alkali and transition metals was found to be largely inconclusive, oxidation by both sulfur and selenium led to the formation of the cyclodiphosph(V)azanes $[(3\text{-pyNH})(S{=})P(\mu\text{-N}^t\text{Bu})]_2$ (**32**) and $[(3\text{-pyNH})(Se{=})P(\mu\text{-N}^t\text{Bu})]_2$ (**33**). Lastly, the ability of both compounds **30** and **33** to form supramolecular polymers in the solid-state was also observed in supramolecular assemblies.

6

6. Conclusions

The investigation of main group-based pyridyl and quinolyl ligands presented in this thesis highlights their potential as highly-tuneable and previously inaccessible ligands from simple main group-containing starting materials.

The synthesis of a series of aluminium-based bis- and tris-quinolyl ligands and their various reactivities towards Li^+ cations illustrate the effect of relocating the N-donor atom to a more remote position with respect to the bridgehead atom/group. The impact of this is seen in the comparison between the coordination behaviour of **2a** and (**3**)Li with Li^+, comprising a pseudo-tetrahedral and trigonal planar geometry, respectively, owing to the remoteness of the N-donor atom relative to the central bridgehead. Further studies involve the direct comparison of these ligands to bis-quinolyl [**4a**(Li)] and pyridyl (**5** and **6**) counterparts. In the case of the former, DFT studies confirm the presence and nature of an agostic interaction in place of N-donor bonding present in the tris(2-Me-8-qy) aluminate. Unsurprisingly, both pyridyl-aluminate ligands are solvated by two THF molecules, providing a neat comparison to their tris-pyridyl aluminate counterparts, which coordinate one. Changing the source of aluminium from Me_2- to Et_2 results in the formation of a dianionic oxygen-bridged hydrolysis product, indicating a contrasting reactivity in the case of tris-2-pyridyl-aluminates $[RAl(2\text{-py})_3]^-$, in which the 2-py groups are more basic than the R-group. Modification of the bridgehead towards Sn(IV) and Sb(III) tris- and bis-quinolyl/pyridyl counterparts provided straightforward access to neutral ligand arrangements, as opposed to the anionic nature of the aluminates. In turn, two types of coordination behaviours may be observed: quinolyl ligand transfer to the transition metal centre, and (where lone pairs on the bridgehead are available), lone pair donation.

As a major part of this thesis it was shown that, not only have the first examples of tris-4-pyridyl ligands of heavier *p*-block elements of Groups 14 and 15 been reported, but that most crucially - ligands of this type illustrate how simple periodic trends may be used to explain/predict their coordination behaviour. The discovery of such ligands has paved the way for the systematic exploration of the structure-directing effects of the bridgehead and anion on the formation of MOFs. Preliminary studies show how both Ag(I) and Cu(I) can form giant 2D and 3D networks, showing rich topological complexity. Neat structural comparisons can be made between compounds **18**, **19** and **20** and the parent idealised NaCl-type structure based on the Group 15 and Ag atoms through the appropriate removal of edges in order to produce the desired coordination geometries. Taking previous studies of the nitrogen-bridged $N(4\text{-py})_3$ ligand into account, it is shown that the coordination mode can be modulated by descending

Group 15 (planar N,N,N-, to tetrahedral N,N,N/E-, to pyramidal N,N,N-) as a result of the dual periodic effects of the decrease in *s*/*p* mixing and Lewis basicity. At nitrogen, planar networks are formed, owing to *s*/*p* hybridisation resulting in a planar arrangement of $N(4\text{-py})_2$. Upon descending the Group, the decrease in *s*/*p*-separation leads to decreased *s*/*p*-mixing (at P, As and Sb), until finally at Bi, relativistic stabilisation results in poor availability of the 6*s* orbital as a donor atom. The coordination modes of these ligands reflect the extent of involvement of the lone pair of the bridgehead atom, i.e. the lack of involvement of the Bi lone pair of **16** in any of the arrangements and the involvement of the lone pair of **15**.

Additional work in this thesis has shown that the behaviour of the pyridyl ligand set can be extensively elaborated upon through its application to well-established main group-based ligand systems, such as the cyclodiphosphazanes. Subsequential studies associated with the incorporation of 2-pyridyl substituents (**H**) were initially investigated, with a rare example of a structure containing five-coordinate silver(I) centres synthesised from AgOTf (**26**). This compound could also provide a model system for the anion-sensing capabilities attributed to cyclodiphosphazanes. The attempted deprotonation of **H** with benzyl potassium unexpectedly resulted in the interesting product from reaction with vacuum grease $[KLi\{(SiMe_2)_5O_4\}O_2]_4$ (**28**), containing $[\{(SiMe_2)_5O_4\}O_2]^{2-}$.

One important contribution to the field was the incorporation of 3-pyridyl substituents to form cyclodiphosph(III)azane $[(3\text{-pyNH})P(\mu\text{-N}^t\text{Bu})]_2$ (**30**), which follows on from previous studies and provides a neat comparison to the 2-pyridyl-substituted system. The hypothesis was that the use of 3-pyridyl substituents could encourage the formation of supramolecular assemblies. Whilst preliminary studies of the reactivity of **30** towards alkali and transition metals were largely unresolved, oxidation by both sulfur and selenium led to the successful isolation of the cyclodiphosph(V)azanes $[(3\text{-pyNH})(S{=})P(\mu\text{-N}^t\text{Bu})]_2$ (**32**) and $[(3\text{-pyNH})(Se{=})P(\mu\text{-N}^t\text{Bu})]_2$ (**33**). The latter, along with compound **30** provided confirmation of the initial hypothesis, through their ability to form supramolecular polymers in the solid state.

7

7. Future Work

The work discussed in this thesis has laid some foundations for further development of tris-pyridyl ligands, along with further potential deviations from these frameworks in the area of phosphazane chemistry. This progress in several new areas of research should serve as a basis for future studies in the group. In this Chapter, several future research directions are discussed.

7.1 Studies Following on Directly From the Ph.D. Work

Considering the advancements made in the areas of tris-3- and 4-pyridyl ligands (Chapter 4), there is clearly a large prospect of expanding structural studies to other cages and 3D networks. Ultimately, there may be the potential to exploit any porous MOF materials in applications such as gas exchange/storage, solid-state host-guest chemistry, and also catalysis. Moreover, the elegant ability to modulate the coordination mode of the tris-4-pyridyl ligands by taking advantage of simple periodic trends provides a tool with which to fine-tune/manipulate the assembly of both molecular and extended lattice arrangements. A particular area of interest in future studies is the potential for tris-4-pyridyl ligands to build three-connected polyhedral cages (e.g., tetrahedra) containing molecular voids.

There is still a great deal of work to do in the development of 3-aminopyridine and 4-aminopyridine substituted cyclodiphosphazane ligands (Chapter 5). Nonetheless significant progress has been made in this thesis so far in opening up this area. The applications of these types of ligands in coordination chemistry is an obvious area which should be studied in the future, and their potential for the construction of supramolecular cages and lattices. As part of these studies, the anion binding properties of the new tris-3-pyridyl cyclodiphosphazane ligands **32** and **33** would be of interest. A further brief study could investigate the variable-temperature ^{1}H NMR spectroscopy of **26**, to study the extent of fluxionality of the Ag(I) coordination within the complex and perhaps obtain an activation energy of the process. Finally, further investigations of the synthesis of $[KLiO(SiMe_2O)_5]_4$ (**28**) should be undertaken. If the cyclodiphosphazane dianion is genuinely involved in the abstraction of an Me_2Si^{2+} unit this would present a very interesting way forward in the siloxane area (e.g., using more well-defined precursors like $[Me_2SiO]_6$). The investigation of the coordination chemistry and synthetic utility of larger chains would be an exciting area for future studies.

7.2 Further Studies and Developments of Main Group N-donor-based Ligands

There are a number of ideas that the author had during this Ph.D. research but did not have enough time to pursue owing to time limitations. In particular, there is a very large scope for using other N-donor groups to develop new families of main group bridgehead ligands.

7.2.1 Tris-Diazyl Ligands

Moving on from the use of 2-, 3- and 4-pyridyl units, an obvious direction is to increase the complexity and number of N-donor sites present in the organic substituents in main group-based ligands. The incorporation of multiple donor sites within one aromatic ring unit would be a potentially simple first step in this direction. Potential candidates include the use of diazines (pyrazine, pyrimidine, pyridazine, *etc*.) in place of pyridyl groups (Figure 7.1).

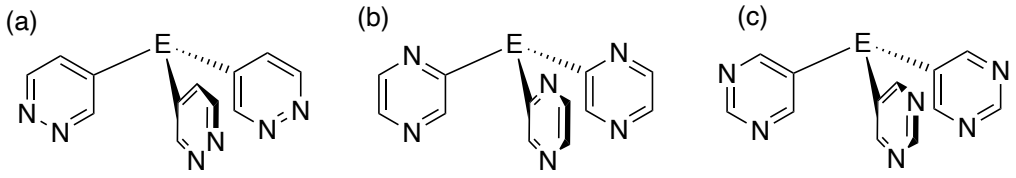

Figure 7.1: Tripodal ligands based on diazines, (a) tris-pyridazyl-, (b) tris-pyrazyl-, and (c) tris-pyrimidyl-ligands, E = bridgehead main group atom or group.

Initial synthetic attempts in this area during the Ph.D. research uncovered a number of challenges, with one difficultly being establishing a reliable method for diazine metalation, producing the key nucleophilic intermediates for reaction with the main group electrophiles. Complications normally arise due to nucleophilic addition of reagents such as ^{n}BuLi onto the ring units, stemming from the low-lying LUMO in the heteroatomic rings. In order to prevent this nucleophilic addition, various metalation techniques, along with temperature and quenching times should be carefully considered. Examples of successful metalation techniques in this area include the use of the more-bulky LiTMP (TMP = 2,2,6,6-tetramethylpiperidide), which is preferred to more basic alkyllithiums as the base for these π-deficient diazines. Other techniques which have previously been established include the use of 'synergic bases' such as LiTMP/$ZnCl_2$·TMEDA, a potassium base (i.e. benzyl potassium – especially if the intermediate can be stabilised through π -arene interactions), or KHMDS (potassium

bis(trimethylsilyl)amide), or even various trans-metal-trapping techniques ($^{i}Bu_3Al$ with LiTMP, Scheme 7.1).[8] Other examples could look to move away from simple N-donor atoms, and begin to consider heterocyclic rings with a variety of elements, i.e. sulfur and oxygen.

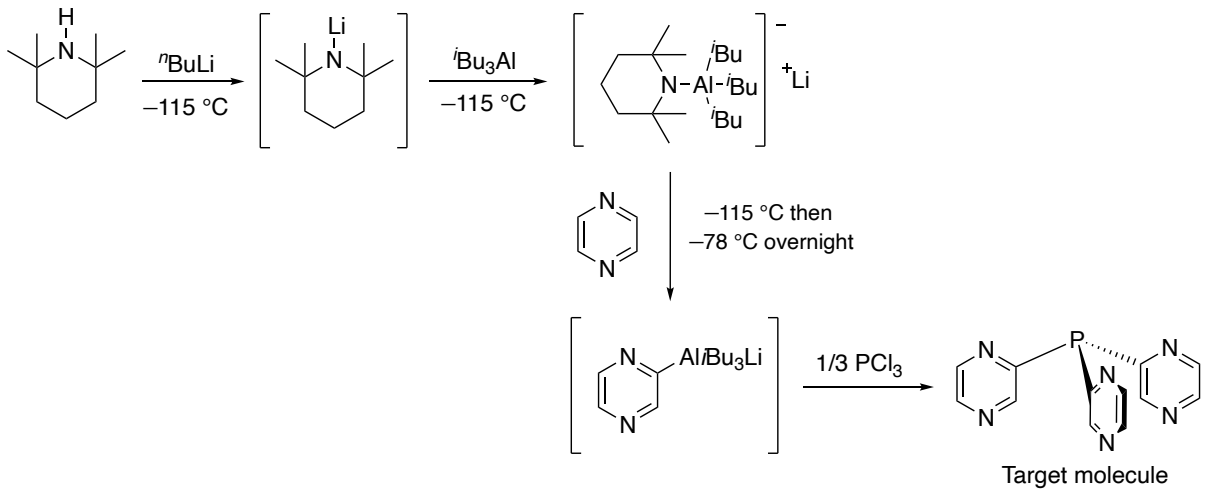

Scheme 7.1: Potential synthetic method towards tris-pyrazyl-phosphine, via $^{i}Bu_3Al$/LiTMP trans-metal-trapping (TMT) route.

7.2.2 Tris-Bipyridyl-Ligands

Following a similar direction to that established in the Ph.D. research in which pyridyl groups were replaced by quinolyl, the incorporation of multiple donor atoms within polycyclic aromatic systems is also an area which should be ripe for development. A good starting point would be 2,2′-bipyridyl ligand frameworks (Scheme 7.2), since metal-halogen exchange is easily accomplished using ^{n}BuLi, and the phosphine derivative $P(bipy)_3$ is already known.[66]

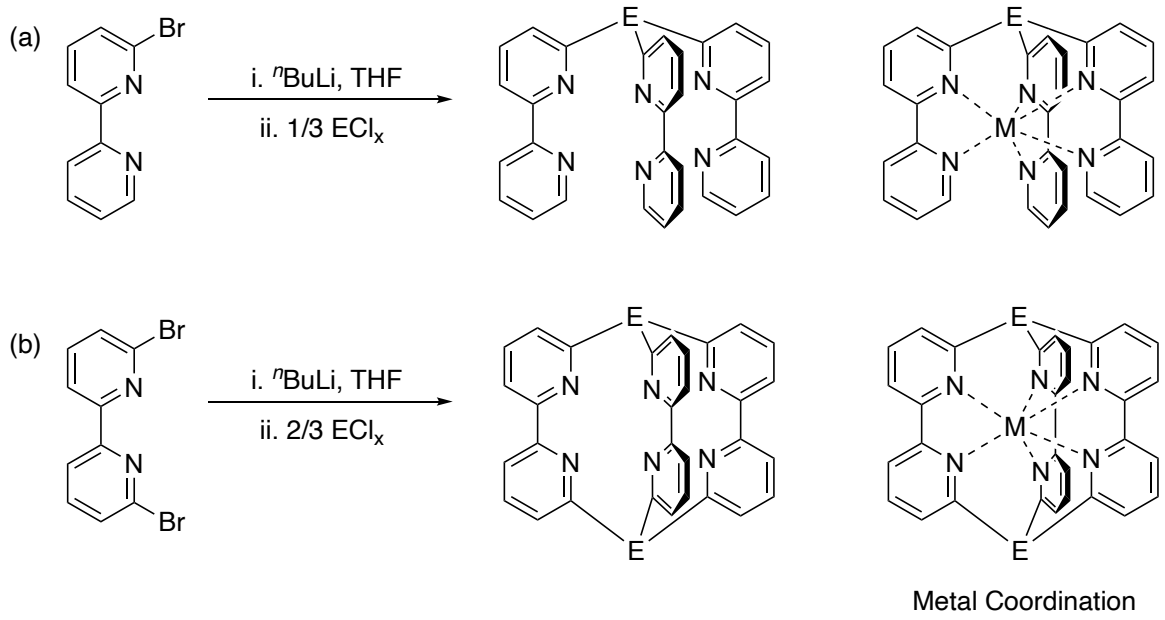

Scheme 7.2: Potential synthesis and coordination behaviour of tris-bipyridyl ligands, E = bridgehead atom/group.

Bis-bipyridyl systems may also be of interest (Scheme 7.3).

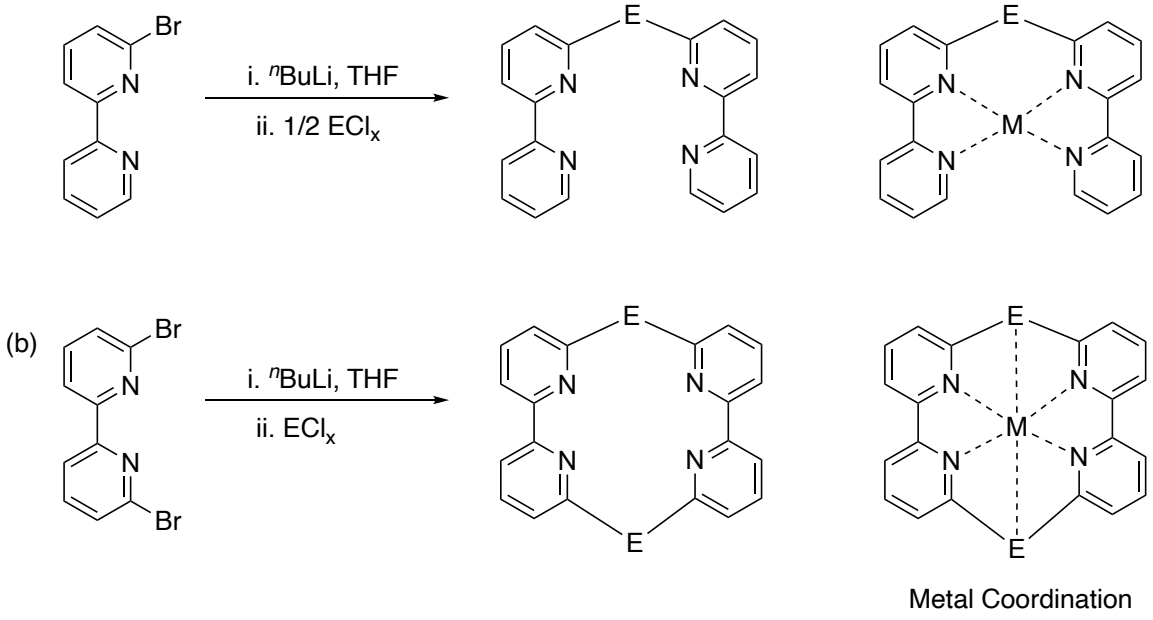

Scheme 7.3: Potential synthesis and coordination behaviour of tris-bipyridyl ligands, E = bridgehead atom/group.

Not only could these ligands be exploited for their interesting coordination behaviour, but it may also be possible to obtain chiral 2,2´-bipyridyl-ligands, through the introduction of chiral amino and alkoxy groups (R*, Figure 7.2a) or the formation of "E"-stereogenic ligands (Figure 7.2b).[187]

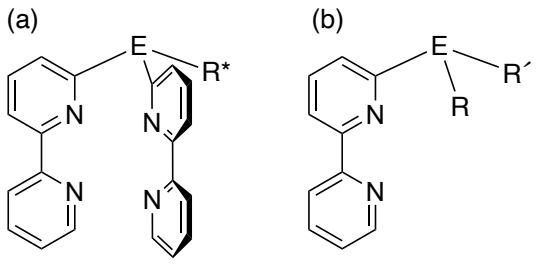

Figure 7.2: 2,2´-Bipyridine-based tripodal ligands and unsymmetrical 2,2´-bipyridyl-ligand derivatives (R =amino or alkoxy group, E = main group bridgehead atom/group).

8

8. Experimental

8.1 General Laboratory & Inert Atmosphere Techniques

All experiments were carried out a room temperature under dry, oxygen-free nitrogen with using standard Schlenk techniques. Reaction vessels were oven-dried (80 °C) and cycled between high vacuum and dry nitrogen four times prior to use. For light sensitive materials, reaction flasks were wrapped in aluminium foil and stored in a dark place to keep out light. Reactions were conducted in Schlenk flasks and filtration was performed using a glass-sinter filter stick or using a 30 mm diameter 1.2 μm porosity syringe filter, unless otherwise stated. Solid reagents were added to the vessel prior to evacuation, whereas liquid reagents were added under a positive pressure of N_2. Dry ice/acetone or dry ice/ethanol mixtures were used as cooling baths to obtain temperatures of around –78 °C, whereas temperatures of –115 °C were achieved through the addition of liquid N_2 to a dry ice ethanol/diethyl ether bath. Solid products were isolated by either decanting the supernatant into another flask under positive flow of N_2 or by use of filter stick apparatus, with any residual solvent removed under vacuum. In order to obtain further analysis, samples were manipulated in a N_2-filled glovebox (Saffron Type α). Vessels were introduced to the glovebox through an antechamber connected to a vacuum pump and N_2 supply. The antechamber was cycled between high vacuum and dry N_2 three times over 30 minutes prior to introducing materials to the inside of the box. In extreme cases where the vessels in question were not air-tight/fully sealed in their own atmosphere of N_2, the antechamber was flushed with dry N_2 for a full 30 – 40 minutes prior to sample introduction to the glovebox interior.

8.2 Solvents and Starting Materials

All solvents were collected freshly distilled over sodium wire/benzophenone (THF, diethyl ether), sodium metal (toluene) or sodium wire, alone (*n*-pentane, *n*-hexane). TMEDA and all pyridine derivatives were distilled under nitrogen from calcium hydride and stored over 4 Å molecular sieves before use. Deuterated NMR solvents were degassed and dried over 4 Å molecular sieves. Phosphorus trichloride was distilled prior to use. All other reagents were purchased from the supplier and used without any further purification.

8.3 Analytical Techniques

8.3.1 Nuclear Magnetic Resonance Spectroscopy

NMR spectra were recorded on a 400 MHZ Avance III HD Smart Probe Spectrometer (^{1}H at 400.1 MHz, ^{31}P 162.0 MHz, ^{13}C 100.6 MHz) or a Bruker Avance HD 500 MHZ Smart Probe Spectrometer (^{1}H at 500.1 MHz, ^{31}P 202.5 MHz, ^{13}C 125.7 MHz) at 25 °C unless otherwise stated. Chemical shifts (δ) are reported in parts per million (ppm) to the nearest 0.01 ppm, with coupling constants (J) recorded in Hertz (Hz). Data are reported in the order: (i) chemical shift, (ii) multiplicity, abbreviated as s (singlet), d (doublet), t (triplet), q (quartet), m (multiplet) and combinations thereof for highly coupled systems, (iii) coupling constant(s), (iv) integration and (v) assignment. All spectra were recorded in dry $CDCl_3$, CD_2Cl_2, CD_3CN, C_6D_6, D_8-THF D_6-DMSO or D_8-toluene. ^{1}H and ^{13}C NMR spectra were referenced to the residual solvent peak, whereas all other heteronuclei were referenced to an external. Unambiguous assignments of the NMR resonances were made on the basis of 2D NMR experiments (^{1}H-^{1}H COSY, ^{1}H-^{13}C HSQC and ^{1}H-^{13}C HMBC experiments). For simplification, Figure 8.1, Figure 8.2 and Figure 8.3 below show the labelling scheme for the NMR spectroscopy assignments used for the quinolyl, pyridyl and substituted-diphosphazane ligand systems.

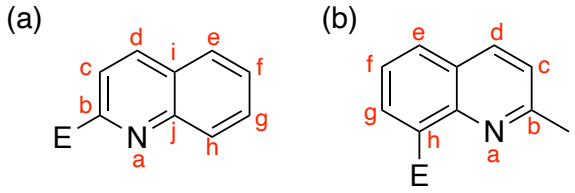

Figure 8.1: Labelling schemes for NMR spectroscopy assignments of quinolyl ligands.

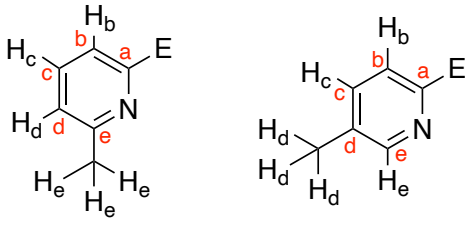

Figure 8.2: Labelling schemes for NMR spectroscopy assignments of bis-pyridyl ligands.

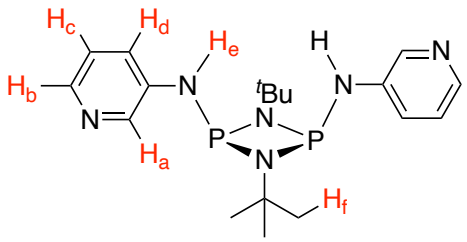

Figure 8.3: Labelling schemes for NMR assignments of pyridyl-disubstituted cyclodiphosphazane ligands.

8.3.2 Elemental Analysis

Elemental microanalytical data were obtained from the University of Cambridge, Department of Chemistry microanalytical service. In a glovebox, a few milligrams of material were placed into two, small pre-weighed aluminium capsules and then sealed using a press. The capsules were weighed accurately. Carbon, hydrogen and nitrogen contents of compounds was carried out using an Exeter Analytical CE-440 Elemental Analyser by combustion of the sample under a pure O_2 atmosphere at 975 °C.

8.3.3 Infrared Spectroscopy

A Thermo Fischer Scientific Nicolet Summit PRO FITR instrument was used for the IR measurements of all relevant solid compounds.

8.3.4 Single-crystal X-ray Diffraction

Single-crystal X-ray crystallography was carried out with a Bruker D8-Quest Photo-100 diffractometer using Incoatec IμS Cu microsource (Cu-Kα, λ = 1.5418 Å), a Nonius Kappa CCD diffractometer (Mo- Kα, λ = 0.71073 Å) or an Oxford Xcalibur S CCD diffractometer Mo-Kα, λ = 0.71073 Å). For the Bruker machine, data collection and reduction were carried out using the APEX2/APEX3 and SAINT packages,[188] whereas for the Nonius machine the HKL Denzo and Scalepack programs[189] were used. Structures were solved using SHELXS[190] or SHELXT[191] and refined using full-matrix least squares on F^2 (SHELXT-2014[192] and the graphical interface shelXle[193]). In general, carbon-bound hydrogen atoms were included in idealised positions and refined using a riding model. Multi-scan corrections were applied using SADABS.[194] Pictures were generated in Mercury. Crystallographic details are given at the end

of Chapter 8, and the colour code for the solid-state structures is depicted within the preliminary sections of this thesis.

8.3.5 Powder X-ray Diffraction

PXRD data were collected on a Panalytical Xpert Pro instrument in Bragg-Brentano geometry using non-monochromated Cu Kα radiation (λ_{ave} –1.5418 Å). The scan was run overnight (12 h) with the sample dispersed in a thin film of oil on a low-background Si holder.

8.3.6 Computational Studies

Calculations in Chapter 3 on compound [(**4a**)Li(THF)] were performed by Dr Schirin Hanf (Karlsruhe Institute of Technology, Germany). All calculations, except the NBO analyses, were carried out using the ORCA package (Version: 4.2.1) in the gas phase.[195,196] For all ORCA calculations, atom-pairwise dispersion corrections with the Becke-Johnson damping scheme (D3BJ) were utilised.[197,198] Density fitting techniques, also called resolution-of-identity approximation (RI), were used for GGA calculations, whereas the RIJCOSX[199] approximation was used for hybrid calculations. Geometry optimisation, frequency analysis and single point calculations of [(**4a**)Li(THF)] were carried out at the TPSS,[200] def2-TZVP[201,127] level of theory. This functional was selected since the Li–H and Li–C bond lengths were represented best in comparison with the X-ray crystal structure. Additionally, the computational results were confirmed using the BP86[131,202,203] and B3LYP[132,204] functionals. NBO analyses[205,206] were computed using Gaussian 09 (Revision D.01).[207] The atoms in molecules method (AIMS) by Bader [136] were performed using the program package Multiwfn.[208] The strength of bonds, based on the electron density of the bond critical point, was estimated using the following equation: BE/kcal/mol = –223.08 x ρBCP/a. u. + 0.7423.[137]

8.3.7 Mass Spectrometry

Mass spectra were obtained by positive ion electrospray ionisation using a Thermo Fisher Orbitrap mass spectrometer.

8.4 Synthetic Protocols

8.4.1 Synthesis of 4-bromopyridine (A)

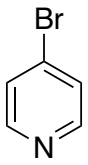

4-bromopyridine hydrochloride (4 g, mmol) was dissolved in water (10 mL) in a 250 mL conical flask. $NaHCO_3$ was added in small portions until no further gas formation was observed. A milky emulsion formed, which separated into two clear phases after stirring for 10 minutes. The mixture was extracted with Et_2O (2 x 25 mL) and the combined organic phases were washed with brine (2 x 25 mL) and dried over Na_2SO_4 (anhydrous) while stirring. After further stirring for 1 h, the suspension was placed in the freezer overnight. The mixture was filtered, and solids washed with dry Et_2O. The solvent of the filtrate was removed under vacuum, and the resulting oil was kept under high vacuum for 8 min while cooling in ice, and a further 5 min until it warmed to room temperature. The colourless oil was stored at –14 °C and used in further syntheses without further purification.

8.4.2 Synthesis of MeSi(4-py)$_3$ (B)

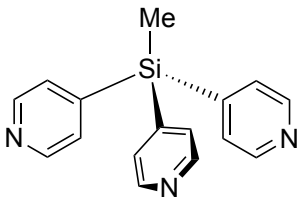

A solution of ^{n}BuLi (1.6M in hexanes, 3.3 mL, 5.15 mmol) and TMEDA (0.77 mL, 5.15 mmol) in Et_2O (20 mL) was prepared while cooling in a dry ice/Et_2O bath. Liquid N_2 was then added to the cooling bath until partially frozen (approximately –115 °C). A separate solution of 4-bromopyridine (0.814 g, 5.15 mmol) in diethyl ether (7 mL) was then added dropwise. After stirring for 15 min, $MeSiCl_3$ (0.18 mL, 1.53 mmol) was added dropwise, and the solution was left to stir at –115 °C for 5 h, after which, more dry ice was added to the cooling bath and the solution was left at –78 °C for 40 h. After warming up to room temperature overnight, the reaction was then quenched with distilled water (25 mL), the phases were separated, and the aqueous layer was extracted with Et_2O (3 x 50 mL). The combined organic extracts were dried over anhydrous $MgSO_4$ and filtered through Celite. Volatiles were removed under vacuum to yield a brown solid, which was washed with a small quantity of Et_2O and purified by evaporative recrystallisation in acetone under N_2 to yield colourless crystals of **B**, (70 mg, 0.252 mmol, 17%). ^{1}H NMR (25 °C, $CDCl_3$, 400 MHz), δ (ppm) = 8.7 (d, 6 H, J_{HH} = 2.9 Hz, H_a), 7.65 (d, 6 H, J_{HH} = 2.9 Hz, H_b), 2.28 (s, 3 H CH_3). ^{13}C{^{1}H} NMR (25 °C, $CDCl_3$, 100.5 MHz), δ (ppm) = 164.5 (C1), 151.4 (C1), 132.4 (C2). The compound was stored in a glovebox and used without further purification.

8.4.3 Synthesis of [(2-py)P(μ-N^{t}Bu)]$_2$ (H)

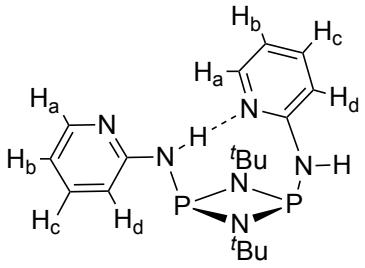

A Schlenk tube was charged with ClP(μ-N^{t}Bu)]$_2$ (2.75 g, 10 mmol) inside a nitrogen-filled glovebox, and transferred to a Schlenk line. The solid was dissolved in THF (30 mL) with triethylamine (30 mL) added slowly to the resulting solution. A solution of 2-aminopyridine (1.88 g, 20 mmol, 2 eq.) in THF (30 mL) was prepared under nitrogen and transferred via dropwise addition to the ClP(μ-N^{t}Bu)]$_2$ solution. The resulting mixture was stirred for 16 h at 40 °C to yield a cloudy white suspension. All solvents were removed *in vacuo* and the resulting pale-cream solid was extracted in hot hexane (60 mL) and filtered under nitrogen. The remaining solid was extracted in hot toluene (60 mL) and filtered once again. All solvents were removed *in vacuo* form both extracts to yield [(2-py)P(μ-N^{t}Bu)]$_2$ as a colourless crystalline powder (1.25 g, 3.23 mmol, 32%). ^{1}H NMR (25 °C, $CDCl_3$, 400 MHz): δ(ppm) = 8.19 (dd, 2 H, $^3J_{HH}$ = 5.1 Hz, H_a), 7.51-7.43 (m, 2 H, H_c), 6.97 (d, 2 H, $^3J_{HH}$ = 8.5 Hz, H_d), 6.77 (dd, $^3J_{HH}$ = 7.1 Hz, $^3J_{HH}$ = 5.0 Hz, H_b), 6.15 (bs, 2 H, NH), 1.27 (s, 18 H, ^{t}Bu). ^{31}P NMR (25 °C, $CDCl_3$, 162 MHz) δ(ppm) = 106.70 (s, 2P). Elemental analysis (%): calcd. for $C_{18}H_{38}N_6P_2$: C 55.7, H 7.4, N 21.5; found: N 55.7, H 7.4, N 21.3.

8.4.4 Synthesis of [ClP(μ-N^{t}Bu)$_2$] (J)

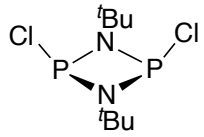

An oven-dried Schlenk (3 L) equipped with an overhead stirrer and a pressure-equalised dropping funnel connected to a Schlenk line was charged with NEt_3 (1 L) and THF (1.5 L) under a stream of N_2. The solution was degassed for 1 h with N_2. The solution was then cooled to –78 °C and distilled PCl_3 (60 mL, 94.2 g, 0.69 mol) was added dropwise via the dropping funnel, causing the formation of a fine white precipitate. Once all of the PCl_3 had been added, the funnel was flushed with THF (25 mL), followed by the dropwise addition of ^{t}BuNH$_2$ (72.2 mL, 50.5 g, 0.69 mol) through the dropping funnel over the course of 1 h. The resulting mixture was stirred overnight and allowed to warm slowly to room temperature. After 16 h, a thick faint yellow suspension formed. The mixture was then filtered under a N_2 atmosphere using a 2 L capacity filter stick and a 10 mM cannula, and the precipitate was washed with THF (200 mL). The combined yellow filtrate was connected to an external trap and all volatiles were removed *in vacuo*, yielding an orange residue. The residue was transferred to an oven-dried 250 mL Schlenk flask, which was connected to an external trap and heated to 80 °C for 1 h to remove any volatile by-products

and equilibrate the product mixture. The remaining residue was extracted in toluene (150 mL) yielding an orange suspension which was filtered to remove residual $^{t}BuNH_3Cl$. All solvent was removed *in vacuo*, yielding a thick orange solution which solidified upon heating. The product was then distilled to remove any remaining toluene, yielding [ClP(μ-N^{t}Bu)$_2$] as a white crystalline solid (72 g, 0.26 mol, 69%). The spectra data was in agreement with literature values: ^{1}H NMR (25 °C, C_6D_6, 400 MHz), δ(ppm) = 1.25 (s, 18 H, ^{t}BuN). ^{31}P NMR (25 °C, C_6D_6, 162 MHz), δ(ppm) = 207.6 (s, 2P).

8.4.5 Synthesis of benzyl potassium (K)

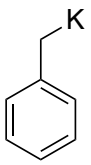

A Schlenk tube was charged with potassium *tert*-butoxide (1.05 g, 9.36 mmol) inside a nitrogen-filled glovebox, and transferred to a Schlenk line. Toluene (40 mL, excess) was then added, and the suspension heated until the white solid dissolved. The solution was then cooled to 0 °C and ^{n}BuLi (1.6 M in hexanes, 5.85 mL, 9.36 mmol, 1 eq.) was added dropwise. The resulting orange solution was stirred at 0 °C for 15 min, then allowed to warm to room temperature while stirring for another hour. The resulting red suspension was then filtered to isolate the product, a red powder which was washed with toluene (3 x 20 mL) and *n*-pentane (3 x 20 mL), and finally dried *in vacuo* for 1 h. Benzyl potassium was obtained as a free-flowing powder (1.15 g, 8.83 mmol, 94%), and was used without further purification.

8.4.6 Synthesis of [(1)Li(μ-Cl)Li(THF)$_3$], (2a) and [{1}$_2$(μ-Br)]$^-$Li(THF)$_4^+$, (2b)

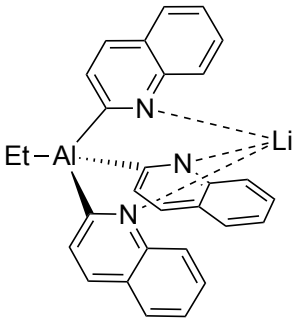

A solution of 2-bromoquinoline (900 mg, 4.32 mmol) in THF (30 mL) was cooled to −78 °C. ^{n}BuLi (1.6 M in hexanes, 2.7 mL, 4.32 mmol) was added dropwise and the red solution was stirred at −78 °C for 2.5 h. In a separate flask, ethylaluminium dichloride (1.0 M in hexanes, 1.43 mL, 1.43 mmol) was diluted in 10 mL THF and kept at −78 °C. This solution was transferred to the first flask (containing 2-lithioquinoline) dropwise with a cannula. The solution was allowed to warm to room temperature and stirred overnight. The volatiles were removed from the dark brown solution under vacuum, and toluene (20 mL) and THF (5 mL) were added to the residue. The mixture was gently heated, filtered, and concentrated under vacuum. Storage at –15 °C afforded colourless crystals of a mixture of **2a** and **2b**. ^{1}H NMR (25 °C, D_8-THF, 400 MHz), δ

(ppm) = 8.79 (d, 3 H, J_{HH} = 8.4 Hz, qy-H_g), 7.89 (d, 3 H, J_{HH} = 8.1 Hz, qy-H_c), 7.82 (d, 3 H, J_{HH} = 8.1 Hz, H_d), 7.65 (t, 3 H, J_{HH} = 7.7 Hz, H_j-qy), 7.56-7.52 (m, 3 H, H_h-qy), 7.32 (t, 3 H, J_{HH} = 7.6 Hz, H_h-qy), 1.56 (t, 3 H, J_{HH} = 7.2 Hz, CH_3), 0.78 (q, 2 H, J_{HH} = 8.1 Hz, $AlCH_2$) ppm. ^{13}C NMR (25 °C, D_8-THF, 126 MHz): δ = 194.4 (br, C(2), detected through ^{1}H-^{13}C HMBC experiment), 151.2 (C6 or C5), 149.8 (C5 or C6), 131.0 (C3), 130.9 (C4), 129.7 (C7), 128.6 (C10), 128.1 (C8), 124.9 (C9), 11.21 (CH3), -0.2 (br, $AlCH_2$, detected through ^{1}H-^{13}C HMQC). ^{27}Al-NMR (25 °C, D_8-THF, 130 MHz, ref. solution of $AlCl_3 \cdot 6H_2O/D_2O$): δ = 128 ppm (br, s). ^{7}Li-NMR (25 °C D_8-THF, 194.4 MHz, ref. solution of $LiCl/D_2O$): δ = 1.02 ppm.

8.4.7 Synthesis of [{EtAl(2-Me-8-qy)$_3$}Li] (1Li), [(3a)THF]

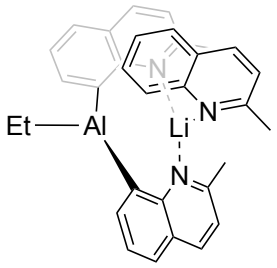

A solution of 8-bromo-6-methylquinoline (666 mg, 3.00 mmol) in THF (40 mL) was cooled to −78 °C. ^{n}BuLi (1.6 M in hexanes, 1.9 mL, 3.00 mmol) was added dropwise and the red solution was stirred at −78 °C for 1 h. Ethylaluminium dichloride (0.9 M in heptane, 1.5 mL, 1.5 mmol) was added. The solution was allowed to warm to room temperature and stirred overnight. The volatiles were removed from the orange solution under vacuum. The residue was extracted with toluene (40 mL) and filtered through Celite. The solution was concentrated under vacuum until a precipitate formed. The precipitate was dissolved by the addition of THF (ca. 5 mL), and the solution was stored in the freezer at −20 °C. Needle-like colourless crystals were collected by filtration and dried under vacuum. The solvent was removed from the filtrate and the residue was recrystallized from toluene to yield a second crop. Isolated yield 416 mg (0.850 mmol, 43%).^{1}H NMR (25 °C, CD_2Cl_2, 400 MHz), δ (ppm) = 8.22 (dd, 3 H, J_{HH} = 6.7, 1.4, H7), 8.11 (d, 3 H, J_{HH} = 8.3, H4), 7.63 (dd, 3 H, J_{HH} = 8.0, 1.4, H5), 7.42 (dd, 3 H, J_{HH} = 7.8, 6.7, H6), 7.16 (d, 3 H, J_{HH} = 8.3, H3), 2.18 (s, 9 H, Qy-CH_3), 1.40 (t, 3 H, J_{HH} = 7.9, Et-CH_3), 0.72 (q, 2 H, J_{HH} = 7.9, Et-CH_2). ^{13}C{^{1}H} NMR (25 °C, CD_2Cl_2, 100.5 MHz), δ (ppm) = 156.5 (C2), 154.7 (C10), 142.2 (C7), 139.6 (C4), 126.4 (C9), 126.3 (C6), 126.2 (C5), 120.8 (C3), 24.3 (qy-CH_3), 11.4 (Et-CH_3). C8 and Et-CH_2 not observed. ^{27}Al NMR (25 °C, CD_2Cl_2, 104.1 MHz), δ (ppm) = 137.2. ^{7}Li NMR (25 °C, CD_2Cl_2, 155.3 MHz), δ (ppm) = 4.9. Elemental analysis (%): calcd. for $C_{32}H_{29}AlLiN_3$ C 78.5, H 6.0, N 8.6; found C 77.6, H 5.8, N 8.6.

8.4.8 Synthesis of [{Me$_2$Al(2-Me-8-qy)$_2$}Li(THF)], [(4a)Li(THF)]

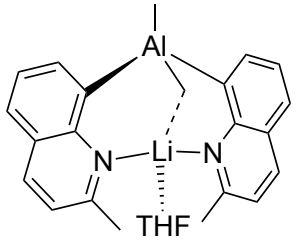

A solution of 8-bromo-6-methylquinoline (666 mg, 3.00 mmol) in THF (40 mL) was cooled to −78 °C. ^{n}BuLi (1.6 M in hexanes, 1.9 mL, 3.00 mmol) was added dropwise and the red solution was stirred at −78 °C for 1 h. Dimethylaluminium chloride (1.0 M in hexanes, 1.5 mL, 1.5 mmol) was added. The solution was allowed to warm to room temperature and stirred overnight. The volatiles were removed from the orange solution under vacuum. The residue was extracted with toluene (40 mL) and filtered through Celite. The solution was concentrated under vacuum until a precipitate formed. The precipitate was dissolved by the addition of THF (ca. 5 mL), and the solution was stored in the freezer at −20 °C. Needle-like colourless crystals were collected by filtration and dried under vacuum. The solvent was removed from the filtrate and the residue was recrystallized from toluene to yield a second crop. Isolated yield 320 mg (0.762 mmol, 50%). ^{1}H NMR (25 °C, C_6D_6, 400 MHz), δ (ppm) = 8.25 (dd, 2 H, J_{HH} = 6.7, 1.1, H7), 8.06 (d, 2 H, J_{HH} = 8.2, H4), 7.56 (dd, 2 H, J_{HH} = 8.1, 1.4, H5), 7.42 (dd, 2 H, J_{HH} = 8.1, 7.5, H6) 7.17 (d, 2 H, J_{HH} = 8.3, H3), 2.70 (s, 6 H, qy-CH_3), –0.34 (s, 6 H, Al-CH_3). ^{13}C{^{1}H} NMR (25 °C, D_8-THF, 100.5 MHz), δ (ppm) = 155.9 (C2), 154.6 (C9), 140.8 (C7), 138.7 (C4), 125.9 (C10), 125.3 (C3), 124.8 (C5), 120.0 (C3), 24.0 (qy-CH_3). C8 and Al-CH_3 not observed. ^{27}Al NMR (25 °C, D_8-THF, 104.1 MHz), δ (ppm) = 146.9. ^{7}Li NMR (25 °C, D_8-THF, 155.3 MHz), δ (ppm) = 3.5. Elemental analysis (%) calcd. for $C_{26}H_{29}AlLiN_2$ (THF molecule removed) C 75.8, H 6.4, N 8.0; found C 75.5, H 6.9, N 8.3.

8.4.9 Synthesis of [{Me$_2$Al(6-Me-2-py)$_2$}Li(THF)$_2$], [(5)Li(THF)$_2$]

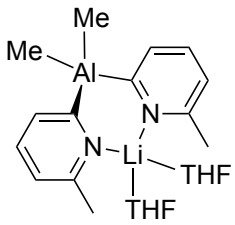

2-bromo-6-methylpyridine (0.5 mL, 4.4 mmol) was dissolved in THF (10 mL). ^{n}BuLi (1.6 M in hexanes, 2.75 mL, 4.4 mmol) was added dropwise to the solution at –78 °C, and the resulting dark red solution was stirred for 2 h at –78 °C. Me_2AlCl (1.0 M in hexanes, 2.2 mL, 2.2 mmol) was added to the solution in one portion and stirred for a further 16 h. After warming up to room temperature overnight, all volatiles were removed *in vacuo* and the resulting orange oil was extracted in toluene to yield an orange solution that was then filtered through Celite. The solvent was removed under vacuum to yield a light brown residue (529 mg, 1.35 mmol, 61%). Crystals suitable for X-ray crystallographic analysis were grown from a solution of [(**5**)Li(THF)$_2$] in toluene at –20 °C. ^{1}H NMR (25 °C, 400 MHz, C_6D_6), δ (ppm) = 7.95 (d, 2 H, J_{HH} = 7.2 Hz, H_b), 7.14 (t, 2 H, J_{HH} = 8.2 Hz, H_c), 6.60 (d, 2 H, J_{HH} = 7.7 Hz, H_d), 3.41 (m, 4

H, -CH_2-O, THF), 2.22 (s, 6 H, H_e-CH_3), 1.25 (m, 4 H, -CH_2-THF), 0.03 (s, 6 H, Al-CH_3). $^{13}C\{^1H\}$ NMR (25 °C, C_6D_6, 100.5 MHz), δ (ppm) = 154.9 (C6), 133.4 (C4), 130.9 (C3), 119.7 (C5), 68.7 (-CH_2-O, THF), 25.4 (-CH_2-, THF), 24.6 (C6). ^{27}Al NMR (25 °C, 104.2 MHz, D_8-THF), δ (ppm) = 142.0. ^{7}Li NMR (25 °C, 155.5 MHz, D_8-THF), δ (ppm) = 1.21.

8.4.10 Synthesis of [{$Me_2Al(5\text{-}Me\text{-}2\text{-}py)_2$}Li(THF)$_2$], [(6)Li(THF)$_2$]

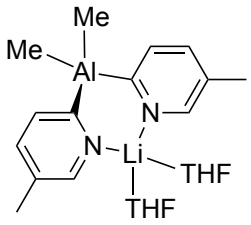

2-bromo-6-methylpyridine (0.5 mL, 4.4 mmol) was dissolved in THF (10 mL). ^{n}BuLi (1.6 M in hexanes, 2.75 mL, 4.4 mmol) was added dropwise to the solution at –78 °C, and the resulting dark red solution was stirred for 2 h at –78 °C. Me_2AlCl (1.8 M in hexanes, 2.2 mL, 2.2 mmol) was added to the solution in one portion and stirred for a further 16 h. After warming up to room temperature overnight, all volatiles were removed *in vacuo* and the resulting brown solid was extracted in toluene (15 mL) to give a cloudy orange solution that was then filtered through Celite. The solvent was removed under vacuum to yield a brown oil (311 mg, 0.79 mmol, 33%). Crystals suitable for X-ray crystallographic analysis were grown from a solution of [(**6**)Li(THF)$_2$] in toluene at –20 °C. ^{1}H NMR (25 °C, 400 MHz, C_6D_6), δ (ppm) = 8.22 (s, 2 H, H_b), 8.11 (d, 2 H, J_{HH} = 7.5 Hz, H_c), 7.07 (d, 2 H, J_{HH} = 7.5 Hz, H_e), 3.46 (m, 5 H, -CH_2-THF), 1.96 (s, 6 H, H_d-CH_3), 1.28 (m, 5 H, -CH_2-THF), 0.10 (s, 6 H, Al-CH_3). $^{13}C\{^1H\}$ NMR (25 °C, C_6D_6, 100.5 MHz), δ (ppm) = 148.3 (C6), 133.9 (C4), 133.7 (C3), 128.4 (toluene), 68.5 (-CH_2-O, THF), 25.4 (-CH_2-, THF), 18.4 (C5-CH_3). C2 and C5 not observed. ^{27}Al NMR (25 °C, 104.2 MHz, D_8-THF), δ (ppm) = 141.5. ^{7}Li NMR (25 °C, 155.5 MHz, D_8-THF), δ (ppm) = 1.40.

8.4.11 Synthesis of [{$EtAl(2\text{-}Me\text{-}8\text{-}qy)_2$}$_2$O}·($Li_2$THF)] (7)

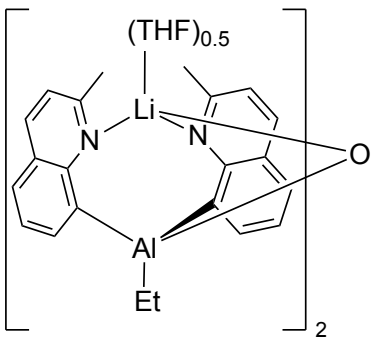

A solution of 8-bromo-6-methylquinoline (666 mg, 3.00 mmol) in THF (40 mL) was cooled to −78 °C. ^{n}BuLi (1.6 M in hexanes, 1.9 mL, 3.00 mmol) was added dropwise and the red solution was stirred at −78 °C for 1 h. Diethylaluminium chloride (1.0 M in hexanes, 1.5 mL, 1.5 mmol) was added. The solution was allowed to warm to room temperature and stirred overnight. The volatiles were removed from the orange solution under vacuum. The residue was extracted with toluene (40 mL) and filtered through Celite.

The solution was concentrated under vacuum until a precipitate formed. The precipitate was dissolved by the addition of THF (ca. 5mL), and the solution was stored in the freezer at −20 °C. Needle-like colourless crystals were collected by filtration and dried under vacuum. The solvent was removed from the filtrate and the residue was recrystallised from THF to yield a second crop. Isolated yield 0.246 mg (0.346 mmol, 23%). Elemental analysis (%) calcd. for $C_{28}H_{33}AlLiN_2$ C 74.3, H 6.0, N 7.9; found C 73.8, H 5.9, N7 .6. Further analysis was not possible owing to the highly moisture-sensitive nature of the compound.

8.4.12 Synthesis of PhSn(2-Me-8-qy)$_3$ (8)

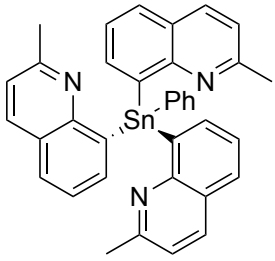

A solution of 8-bromo-6-methylquinoline (666 mg, 3.00 mmol) in THF (20 mL) was cooled to −78 °C. ^{n}BuLi (1.6 M in hexane, 1.9 mL, 3.0 mmol) was added dropwise and the red solution was stirred at −78 °C for 1 hour. Phenyltin trichloride (0.16 mL, 0.97 mmol) was added, resulting in a yellow solution. The solution was allowed to warm to room temperature and stirred for 3 hours. The volatiles were removed under vacuum. The work-up was performed in air. DCM (40 mL) and water (20 mL) were added, and the phases separated. The aqueous layer was extracted with Et_2O (3 × 20 mL). The solvent was removed from the DCM layer, and Et_2O (20 mL) and water (20 mL) were added. The aqueous phase was extracted with Et_2O (2 × 20 mL). The organic extracts were combined, and the solvent removed to give a white solid. Crystallisation from DCM/hexane gave PhSn(2-Me-8-qy)$_3$ as colourless crystals that were collected by filtration and washed with hexane (3 × 3 mL). Isolated yield 348 mg (0.560 mmol, 57%). ^{1}H NMR (25 °C, C_6D_6, 400 MHz), δ (ppm) = 8.37 (dd, 2 H, H_b-Ph, J_{HH} = 7.8, 1.5), 8.15 (dd, 3 H, H_g-qy', J_{HH} = 6.7, 1.3), 7.51 (d (coincident), 6 H, H_d-qy', H_e-qy', J_{HH} = 8.3), 7.30-7.20 (m, 6 H, H_c-Ph, H_d-Ph and H_f-qy'), 6.60 (d, 3 H, H_c-qy', J_{HH} = 8.3), 2.19 (s, 9 H, Me). ^{13}C{^{1}H} NMR (25 °C, C_6D_6, 100.5 MHz), δ (ppm) = 157.6 (C2-qy′), 153.1 (C10-qy′), 148.8 (C8-qy′), 145.1 (C1-Ph), 139.5 (C7-qy′), 138.6 (C2-Ph), 136.0 (C4-qy′), 127.9 (C3-Ph, C4-Ph), 127.8 (C3-Ph, C4-Ph), 127.5 (C5-qy′), 126.4 (C9-qy′), 126.3 (C6-qy′), 121.5 (C3-qy′), 24.4 (Me). ESI-MS(+) (m/z): Found: 646.1260. Calc. for $C_{36}H_{29}N_3NaSn$ $[M + Na]^+$: 646.1281. Elemental analysis (%): calcd. for $C_{36}H_{29}N_3Sn$ C 69.5, H 4.7, N 6.8; found C 69.1, H 4.6, N 6.6.

8.4.13 Synthesis of $Ph_2Sn(2\text{-Me-}8\text{-qy})_2$ (9)

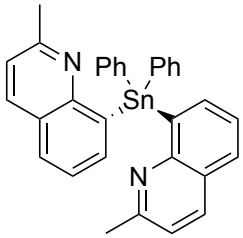

A solution of 8-bromo-6-methylquinoline (442 mg, 2.00 mmol) in THF (20 mL) was cooled to −78°C. ^{n}BuLi (1.6 M in hexane, 1.24 mL, 2.00 mmol) was added dropwise and the red solution was stirred at −78 °C for 1 hour. Diphenyltin dichloride (0.16 mL, 0.999 mmol) was added, resulting in a yellow solution. The solution was allowed to warm to room temperature and stirred for 3 hours. The volatiles were removed under vacuum. The work-up was performed in air. DCM (40 mL) and water (20 mL) were added, and the phases separated. The aqueous layer was extracted with Et_2O (3 × 20 mL). The solvent was removed from the DCM layer, and Et_2O (20 mL) and water (20 mL) were added. The aqueous phase was extracted with Et_2O (2 × 20 mL). The organic extracts were combined, and the solvent removed to give a white solid. Crystallisation from DCM/hexane gave $Ph_2Sn(2\text{-Me-}8\text{-qy})_2$ as colourless crystals that were collected by filtration and washed with hexane (3 × 3 mL). Isolated yield

8.4.14 Synthesis of $Ph_2Sn(3\text{-py})_2$ (10)

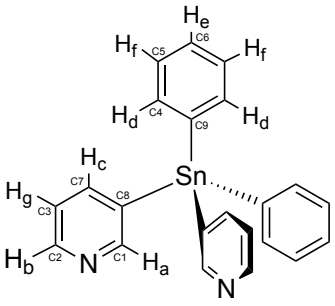

3-pyridylmagnesium chloride lithium chloride was prepared *in situ* using a previously reported procedure. 3-bromopyridine (0.96 mL, 10.0 mmol) was added in one portion to a stirred solution of 1.3 M isopropylmagnesium chloride lithium chloride complex in THF (8.08 mL, 10.5 mmol) at −15 °C under a nitrogen atmosphere. The resulting brown mixture was stirred for 15 min at −10 °C. Diphenyltin dichloride (1.72 g, 5.00 mmol) in THF (5 mL) was added dropwise to the reaction mixture, which was allowed to warm to room temperature and stirred overnight. The resulting white suspension was treated with water (20 mL), and the organic phase was extracted with DCM (3 x 15 mL). The extract was washed with brine (15 mL), dried over anhydrous $MgSO_4$, then filtered through Celite. The solvent was removed by evaporation under reduced pressure to give a pale-yellow-white solid, which was purified by recrystallisation (DCM/hexane) and washed with acetone to yield $Ph_2Sn(3\text{-py})_2$, (820 mg, 1.91 mmol, 38%) as needle-like crystals suitable for X-ray crystallography. ^{1}H NMR (25 °C, $CDCl_3$, 400 MHz), δ (ppm) = 8.75 (s, 2 H, H_a), 8.67 (dd, 2 H, J_{HH} = 2 Hz, 5 Hz, H_b), 7.88 (d, 2 H, J_{HH} = 8 Hz, H_c), 7.56 (m, 2 H, H_d), 7.43 (m, 6 H, $H_{e/f}$), 7.35 (dd, 2 H, J_{HH} = 5 Hz, 8 Hz, H_g). ^{13}C{^{1}H} NMR (25 °C, $CDCl_3$, 100.5 MHz), δ (ppm) = 149.4 (C1), 149.6 (C2), 137.0 (C3), 135.7 (C4), 128.6 (C5), 129.1 (C6), 123.8 (C7). C8 and C9 not observed.

8.4.15 Synthesis of $Au_4(2\text{-Me-8-qy})_4$ (11)

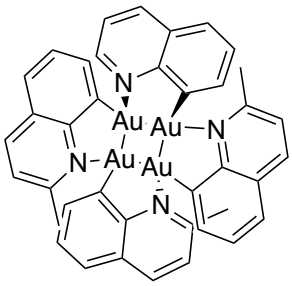

$PhSn(2\text{-Me-8-qy})_3$ (**8**, 20 mg, 0.032 mmol) and AuCl(THT) (10 mg, 0.032 mmol) were both added to a Schlenk tube and dissolved in THF to form a brown solution. After eventually dissolving compound **8**, elemental Au(0) began to precipitate out of solution in the form of black particles and a purple mirror. The mixture was filtered into a new Schlenk to yield a bright orange solution, which was reduced down to an orange residue. The solid was recrystallised from a mixture of DCM/hexane to afford **11** as red needle-like crystals (1 mg, 2.3%) in a yellow solution. Satisfactory NMR spectroscopy and elemental analysis were not obtained owing to the low yield of the material.

8.4.16 Synthesis of $Sb(2\text{-Me-8-qy})_3$ (12)

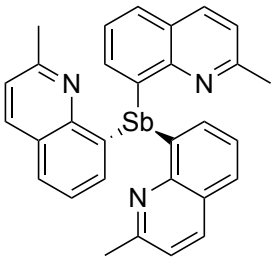

A solution of 8-bromo-6-methylquinoline (666 mg, 3.00 mmol) in THF (15 mL) was cooled to −78 °C. ^{n}BuLi (1.6 M in hexanes, 1.9 mL, 3.0 mmol) was added dropwise and the red solution was stirred at −78 °C for 1 hour. Antimony trichloride (228 mg, 0.999 mmol) in THF (3 mL) was added, resulting in a yellow solution. The solution was allowed to warm to room temperature and stirred for 2 hours. The volatiles were removed under vacuum. The residue was extracted with DCM (40 mL), filtered through Celite and washed through with an extra 20 mL DCM. The solution was concentrated under vacuum to 20 mL and hexane (30 mL) was added. The white precipitate collected by filtration, washed with hexane (2 × 10 mL) and dried under vacuum. A second crop was collected from the filtrate. Isolated yield 886 mg. 1.62 mmol, 49%. ^{1}H NMR (25 °C, C_6D_6, 400 MHz), δ (ppm) = 8.09 (d, 3 H, H4, J_{HH} = 8.3), 7.73 (dd, 3 H, H5, J_{HH} = 8.0, 1.3), 7.29 (d, 3 H, H3, J_{HH} = 8.4), 7.14 (dd, 3 H, H6, J_{HH} = 7.9, 7.0), 6.98 (dd, 3 H, H7, J_{HH} = 6.8, 1.4), 2.58 (s, 9 H, Me). $^{13}C\{^1H\}$ NMR (25 °C, C_6D_6, 100.5 MHz), δ (ppm) = 158.4 (C2), 152.2 (C10), 144.7 (C8), 138.0 (C7), 136.6 (C4), 127.7 (C5), 126.5 (C6), 126.4 (C9), 122.1 (C3), 25.3 (Me). ESI-MS(+) (m/z): Found: 548.1085. Calc. for $C_{30}H_{25}N_3Sb$ $[M + H]^+$: 548.1087. Elemental analysis (%): calcd. For $C_{30}H_{24}N_3Sb$ C 65.7, H 4.4, N 7.7; found: C 65.54, 4.48, 7.50.

8.4.17 Synthesis of Sb(2-Me-8-qy)$_2$Cl (13)

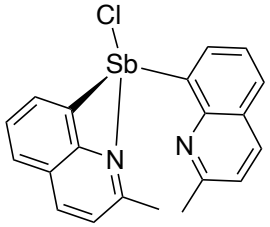

Sb(2-Me-8-qy)$_2$ (**12**, 110 mg, 0.20 mmol) and [RuCl$_2$(*p*-cymene)]$_2$ (61 mg, 0.10 mmol) were both added to a Schlenk, and fitted with a reflux condenser. MeCN (6 mL) was added to form a yellow suspension, and the mixture was heated to reflux for 3 h, after which a cream precipitate was formed within the brown solution. The solution was filtered off, after which a grey precipitate was left behind. The filtrate was left at ambient temperature for 2.5 h, after which colourless crystals began to form, which were isolated and identified as Sb(2-Me-8-qy)$_2$Cl, **13**. Isolated yield 57 mg, 0.129 mmol, 64%. Satisfactory NMR spectroscopy and elemental analysis were not obtained owing to time difficulties.

8.4.18 Synthesis of Sb(2-Me-8-qy)$_3$AuCl (14)

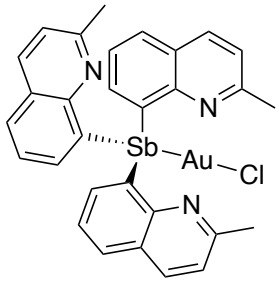

Sb(2-Me-8-qy)$_2$ (**12**, 100 mg, 0.182 mmol) and AuCl(THT) (58 mg, 0.181 mmol) were both added to a Schlenk and dissolved in THF (10 mL) and DCM (10 mL) to form a white suspension. After stirring for 45 min, the suspension was filtered, and all solvents removed *in vacuo*. After unsuccessful attempts to redissolve a white precipitate in 1:1 THF:DCM (found to be decomposed Sb(2-Me-8-qy)$_3$), the suspension was filtered again to form a pale-yellow solution, which formed a few colourless crystals successfully isolated as Sb(2-Me-8-qy)$_3$AuCl, **14**. Isolated yield 68 mg, 0.087 mmol, 48%. Satisfactory NMR spectroscopy and elemental analysis were not obtained owing to time difficulties.

8.4.19 Synthesis of Sb(4-py)$_3$ (15)

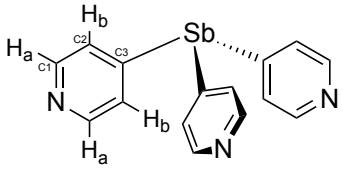

A solution of ^{n}BuLi (1.6 M in hexanes, 5.7 mL, 9.12 mmol) in THF (20 mL) was prepared while cooling in a dry ice/Et$_2$O bath. Liquid N$_2$ was then added to the cooling bath until partially frozen (approximately –115 °C). A separate solution of 4-bromopyridine (1.30 g, 8.23 mmol) in diethyl ether (7 mL) was then added dropwise. After stirring for 15 min, SbCl$_3$ (0.57 g, 2.5 mmol) was added in one portion, and the solution was left to stir at –115 °C for 5 h, after which, more dry ice was added to the cooling bath and the solution was left at –78 °C for 40 h. After warming up to room temperature overnight, the reaction was then

quenched with distilled water (25 mL), the phases were separated, and the aqueous layer was extracted with DCM (3 x 50 mL). The combined organic extracts were dried over anhydrous $MgSO_4$ and filtered through Celite. Volatiles were removed under vacuum to yield a brown solid, which was washed with a small quantity of Et_2O (15 mL) overnight to yield **15**, (175 mg, 0.49 mmol, 20%). ^1H NMR (25 °C, $CDCl_3$, 400 MHz), δ (ppm) = 8.6 (d, 6 H, J_{HH} = 3.0 Hz, H_a), 7.32 (d, 6 H, J_{HH} = 3.0 Hz, H_b). $^{13}C\{^1H\}$ NMR (25 °C, $CDCl_3$, 100.5 MHz), δ (ppm) = 150.0 (C1), 146.4 (C3), 130.9 (C2). Elemental analysis (%): calcd. for $C_{15}H_{12}N_3Sb$: C 50.6, H 3.4, N 11.8; found C 50.1, H 3.4, N 11.6.

8.4.20 Synthesis of Bi(4-py)$_3$ (16)

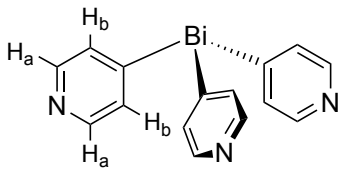

A solution of ^{n}BuLi (1.6M in hexanes, 5.5 mL, 8.8 mmol) in THF (20 mL) was prepared while cooling in a dry ice/Et_2O bath. Liquid N_2 was then added to the cooling bath until partially frozen (approximately –115 °C). A separate solution of 4-bromopyridine (1.38 g, 8.7 mmol) in diethyl ether (7 mL) was then added dropwise. After stirring for 15 min, $BiCl_3$ (0.84 g, 2.66 mmol) was added in one portion, and the solution was left to stir at –115 °C for 5 h, after which, more dry ice was added to the cooling bath and the solution was left at –78 °C for 40 h. After warming up to room temperature overnight, the reaction was then quenched with distilled water (25 mL), the phases were separated, and the aqueous layer was extracted with DCM (3 x 50 mL). The combined organic extracts were dried over anhydrous $MgSO_4$ and filtered through Celite. Volatiles were removed under vacuum to yield a brown solid, which was washed with a small quantity of DCM and purified by evaporative recrystallisation in DCM to yield **16**, (650 mg, 1.47 mmol, 55%). (Second attempt starting with 0.80 g $BiCl_3$: 530 mg, 1.2 mmol, 47%). ^1H NMR (25 °C, $CDCl_3$, 400 MHz), δ (ppm) = 8.7 (d, 6 H, J_{HH} = 2.9 Hz, H_b), 7.65 (d, 6 H, J_{HH} = 2.9 Hz, H_b). $^{13}C\{^1H\}$ NMR (25 °C, $CDCl_3$, 100.5 MHz), δ (ppm) = 164.5 (C1), 151.4 (C1), 132.4 (C2). Elemental analysis (%): calcd. for $C_{15}H_{12}BiN_3$: C 40.7, H 2.7, N 9.5; found C 40.4, H 2.8, N 9.5.

8.4.21 Synthesis of PhSn(4-py)$_3$ (17)

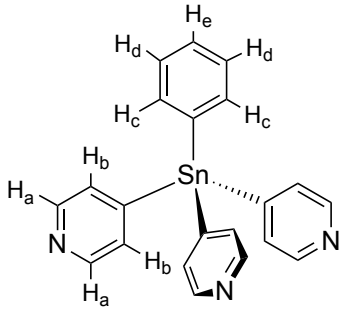

A solution of ^{n}BuLi (1.6M in hexanes, 7.0 mL, 11.1 mmol) in THF (20 mL) was prepared while cooling in a dry ice/Et_2O bath and stirred for 15 min. Liquid N_2 was then added to the cooling bath until partially frozen (approximately –115 °C). A separate solution of 4-bromopyridine (1.68 g, 10.6 mmol) in diethyl ether (20 mL) was then added dropwise. After stirring for 15 min, $PhSnCl_3$ (0.55 mL, 3.36 mmol) was added dropwise over 10 min, and the solution was left to stir at –115 °C for 5 h, after which, more dry ice was added to the cooling bath and the solution was left to warm to room temperature overnight. The reaction was then quenched with distilled water (30 mL), the phases were separated, and the aqueous layer was extracted with DCM (3 x 15 mL). The combined organic extracts were dried over anhydrous Na_2SO_4 and filtered through Celite. Volatiles were removed under vacuum to yield a brown solid, which was purified by recrystallisation. ^{1}H NMR (25 °C, $CDCl_3$, 400 MHz), δ (ppm) = 8.61 (d, H_a, J_{HH} = 4.6 Hz, 6H), 7.47 (d, H_b, J_{HH} = 2.9 Hz), 7.50 (m, H_c-Ph, H_d-Ph, H_e-Ph). ^{13}C{^{1}H} NMR (25 °C, $CDCl_3$, 100.5 MHz), δ (ppm) = 149.7 (C1), 145.9 (C3), 136.9 (C4), 133.6 (C5), 132.0 (C2), 130.5 (C7), 129.5 (C6). Elemental analysis (%): calcd. for $C_{21}H_{17}N_3Sn$: C 58.7, H 4.0, N 9.8; found C 58.5, H 4.0, N 9.8.

8.4.22 Synthesis of {Ag$^I_2$(16)$_3$}$_n$(CF$_3$SO$_3$)$_{2n}$ (18)

A solution of **16** (25 mg, 0.058 mmol) in dry DCM (3 mL) was prepared in a narrow Schlenk flask under N_2. A solution of silver(I) trifluoromethanesulfonate (22 mg, 0.085 mmol) in dry acetonitrile (1 mL) was then layered carefully on top of the ligand solution in DCM. The two layers were left to diffuse slowly at room temperature for three weeks, resulting in crystals of **18** (27.8 mg, 0.0144 mmol, 74%, based on (limiting) ligand supplied). Elemental analysis (%): calcd for **18**·CH_2Cl_2 (from crystal data): C 29.8, H 2.0, N 6.5; found C 31.0, H 2.1, N 6.5. The results suggest partial or complete loss of the lattice CH_2Cl_2, i.e., calcd. for **18** (no solvent in the lattice), C 30.6, H. 2.0, N 6.8.

8.4.23 Synthesis of {Ag$^I_2$(16)$_3$}$_n$(SbF$_6$)$_{2n}$ (19)

A solution of **16** (40 mg, 0.090 mmol) in dry DCM (3 mL) was prepared in a narrow Schlenk flask under N_2. A solution of silver(I) hexafluoroantimonate (20 mg, 0.058 mmol) in dry

acetonitrile (1 mL) was then layered carefully on top of the ligand solution in DCM. The two layers were left to diffuse slowly at room temperature for three weeks, resulting in crystals of **19** (34.4 mg, 0.0171 mmol, 59% based on (limiting) salt supplied). Elemental analysis (%): calcd. for **19** (no solvation in lattice): C 26.8, H 1.8, N 6.3; found C 26.0, H 1.8, N 6.5.

8.4.24 Synthesis of $\{Ag^{I}_{2}(16)_{3}\}_{n}(PF_{6})_{2n}$ (20)

A solution of **16** (25 mg, 0.058 mmol) in dry DCM (3 mL) was prepared in a narrow Schlenk flask under N_2. A solution of silver(I) hexafluorophosphate (14 mg, 0.055 mmol) in dry acetonitrile (1 mL) was then layered carefully on top of the ligand solution in DCM. The two layers were left to diffuse slowly at room temperature for three weeks, resulting in crystals of 20 (40.2 mg, 0.0219 mmol, 80% based on (limiting) salt supplied). Elemental Analysis (%): calcd. for **20** (no solvent in the lattice): C 29.9, H 2.1, N 6.8; found C 29.1, H 2.2, N 5.8.

8.4.25 Synthesis of $\{Ag^{I}(15)\}_{n}(SbF_{6})_{n}$ (21)

A solution of **15** (25 mg, 0.070 mmol) in dry DCM (3 mL) was prepared in a narrow Schlenk flask under N_2. A solution of silver(I) hexafluoroantimonate (24 mg, 0.070 mmol) in dry acetonitrile (1 mL) was then layered carefully on top of the ligand solution in DCM. The two layers were left to diffuse slowly at room temperature for three weeks, resulting in crystals of **21** (22.0 mg, 0.0314 mmol, 45% based on ligand and metal supplied). Elemental analysis (%): calcd. for **21** (no solvent in lattice) 25.3, H 1.8, N 6.7; found C 25.8, H 1.7, N 6.0.

8.4.26 Synthesis of $\{Ag^{I}(17)\}_{n}(CF_{3}SO_{3})_{n}$ (22)

A solution of **17** (25 mg, 0.070 mmol) in dry DCM (3 mL) was prepared in a narrow Schlenk flask under N_2. A solution of silver(I) trifluoromethanesulfonate (24 mg, 0.070 mmol) in dry acetonitrile (1 mL) was then layered carefully on top of the ligand solution in DCM. The two layers were left to diffuse slowly at room temperature for three weeks, resulting in crystals of **22** (31.7 mg, 0.0461 mmol, 30% based on ligand or metal supplied). Satisfactory elemental analysis was not obtained.

8.4.27 Synthesis of $\{Ag^{I}(B)\}_n(CF_3SO_3)_n$ (23)

A solution of **B** (30 mg, 0.108 mmol) in dry DCM (3 mL) was prepared in a narrow Schlenk flask under N_2. A solution of silver(I) trifluoromethanesulfonate (42 mg, 0.163 mmol) in dry acetonitrile (1 mL) was then layered carefully on top of the ligand solution in DCM. The two layers were left to diffuse slowly at room temperature for three weeks, resulting in crystals of **23** (34.7 mg, 0.0649 mmol, 60% based on ligand or metal supplied). Satisfactory elemental analysis was not obtained owing to time difficulties.

8.4.28 Synthesis of $\{Cu(16)(MeCN)\}_n(PF_6)_n$ (24)

A solution of **16** (25 mg, 0.056 mmol) in dry DCM (3 mL) was prepared in a narrow Schlenk flask under N_2. A solution of tetrakis(acetonitrile)copper(I) hexafluorophosphate (20 mg, 0.054 mmol) in dry acetonitrile (1 mL) was then layered carefully on top of the ligand solution in DCM. The two layers were left to diffuse slowly at room temperature for three weeks, resulting in crystals of **24** (24.5 mg, 0.0354 mmol, 63% based on ligand or metal supplied). Satisfactory elemental analysis was not obtained owing to time difficulties.

8.4.29 Synthesis of $(\{Cu(16)_2\}\{Cu(16\text{-}SiF_5)\})_n(PF_6)_n$ (25)

A solution of **16** (25 mg, 0.056 mmol) in dry DCM (3 mL) was prepared in a narrow Schlenk flask under N_2. This solution was carefully layered on top of a solution of a solution of copper(I) hexafluorophosphate (24 mg, 0.0464 mmol) in dry acetonitrile (3 mL) was layered carefully on top of the silver(I) hexafluorophosphate solution. The two layers were left to diffuse slowly at room temperature for three weeks, resulting in crystals of **25** (31.7 mg, 0.0461 mmol, 30% based on ligand or metal supplied). Satisfactory elemental analysis was not obtained owing to time difficulties.

8.4.30 Synthesis of [TfO.S.{AgOTf(THF)}{Ag(THF)$_3$}] (26)

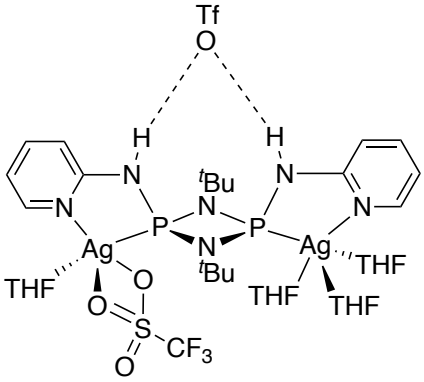

Inside a nitrogen filled glovebox a Schlenk tube wrapped in aluminium foil was charged with silver(I) triflate (134 mg, 0.52 mmol) and transferred to a Schlenk line, and the solid dissolved in dry THF (5 mL). To this a solution of **H** (100 mg, 0.26 mmol) in dry THF (5 mL) was added dropwise via syringe then stirred for 16 h at room temperature. The resulting dark brown solution was then filtered under nitrogen using magnesium sulfate to remove metal impurities. The resulting pale-grey filtrate was concentrated and stored at –20 °C to yield [TfO.**H**.{AgOTf(THF)}{Ag(THF)$_3$}], **26**, as grey crystals suitable for X-ray diffraction. Photodegradation prevented the elemental analysis of the product and the recording of a yield. ^{1}H NMR (25 °C , D$_8$-THF, 400 MHz): δ (ppm) = 9.01 (s, br, 2H, H$_e$), 7.59 (2 x dd, $J_{H\text{-}H}$ = 8 Hz, $^3J_{109Ag\text{-}H}$ =/= $^3J_{109Ag\text{-}H}$, 2H, H$_a$), 7.32 (dd, $J_{H\text{-}H}$ = 5 Hz, 2 Hz, 2H, H$_d$), 7.26 (t, $J_{H\text{-}H}$ = 8 Hz, 2H, H$_c$), 6.68 (dd, $J_{H\text{-}H}$ = 8 Hz, 6 Hz, 2H, H$_b$), 1.42 (s, 18H, H$_f$). ^{31}P NMR (25 °C, THF, 162 MHz): d (ppm) = 86.85 (2 x d, $^1J_{P\text{-}109Ag}$ = 656 Hz, $^1J_{P\text{-}107Ag}$ = 570 Hz, 2P).

8.4.31 Reaction of H with benzyl potassium (28)

Inside a nitrogen filled glovebox a Schlenk tube was charged with **H** (100 mg, 0.26 mmol) and benzyl potassium (70 mg, 0.52 mmol, 2 eq.) and transferred to a Schlenk line. The solids were dissolved in THF (10 mL) and the reaction mixture stirred at room temperature for 5 min, producing a yellow solution. The solution was concentrated to ca. 3 mL and stored at –14 °C. This yielded small yellow crystals suitable for X-ray diffraction. These were identified as [KLiO((SiMe$_2$O)$_5$)]$_4$ (**28**), the result of a side reaction with vacuum grease (along with an unknown by-product, **29**). ^{1}H NMR (25 °C, CDCl$_3$, 400 MHz): δ (ppm) = 0.094 (s, 24 H), 0.077 (s, 48 H), 0.071 (s, 48 H). No yield could be recorded due to the small amount of product obtained, which was all used in analysis.

8.4.32 Synthesis of [(3-py)P(μ-N^{t}Bu)]$_2$ (30)

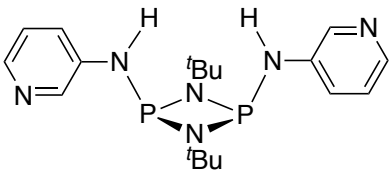

Inside a nitrogen filled glovebox a Schlenk tube was charged with [ClP(μ-N^{t}Bu)]$_2$ (2.0 g, 7.2 mmol) and transferred to a Schlenk line. The solid was dissolved in THF (60ml). A solution of 3-aminopyridine (1.38 g, 14.5 mmol, 2 eq.) in

THF (20 mL) and triethylamine (80 mL) was prepared under nitrogen and transferred by dropwise addition to the $[ClP(\mu\text{-}N^tBu)]_2$ solution. The resulting mixture was stirred for 16 h at 40 °C to yield a cloudy white suspension. All solvents were removed in vacuo and the resulting precipitate dissolved in hot toluene (100 mL). The yellow suspension was filtered through Celite. All solvents were removed *in vacuo* with the impure product then dissolved in boiling MeCN (80 mL) to form a green suspension which was similarly filtered. This yielded a concentrated green solution which was left to cool to room temperature, yielding a pale-yellow crystalline solid after being left to stand for 72 h. The solvent was syringed off and the crystals then dried *in vacuo*. $[(3\text{-py})P(\mu\text{-}N^tBu)]_2$ was obtained as a pale-yellow crystalline solid (1.60 g, 4.10 mmol, 57%). ^{1}H NMR (25 °C, $CDCl_3$, 400 MHz): δ (ppm) = 8.30 (d, $J_{H\text{-}H}$ = 3 Hz, 2H, H_a), 8.17 (dd, $J_{H\text{-}H}$ = 5 Hz, 1Hz, 2H, H_b), 7.40 (dt, 8 Hz, 2 Hz, 2H, H_d), 7.15 (dd, $J_{H\text{-}H}$ = 8 Hz, 5 Hz, 2H, H_c), 4.98 (s, br, 2H, H_e), 1.26 (s, 18H, H_f). ^{31}P NMR (25 °C, $CDCl_3$, 162 MHz): d (ppm) = 103.39 (s, br, 2P). Elemental analysis (%) calcd. for $C_{18}H_{28}N_6P_2$: C, 55.38; H, 7.23; N, 21.53; P 15.87; found: C, 55.58; H, 7.26; N, 21.32. N.B: Prolonged storage of **30** led to the partially-oxidised mixed P(III)/P(V) product $[(3\text{-py})NHP(\mu\text{-}N^tBu)_2PH(=O)]$, **31**.

8.4.33 Synthesis of $[(3\text{-py})(S)P^V(\mu\text{-}N^tBu)]_2$ (32)

A Schlenk tube was charged with elemental sulfur (43 mg, 1.32 mmol, excess) and transferred to a Schlenk line where the solid was dried in vacuo for 1 h. Inside a nitrogen filled glovebox a second Schlenk tube was charged with **28** (80 mg, 0.205 mmol), transferred to a Schlenk line and dissolved in THF (12 mL). The solution of **28** was added dropwise to the dried sulfur and stirred at room temperature for 72 h. All solvents were removed in vacuo and the resulting solid extracted in ether (20 mL) and filtered through Celite. All solvents were removed in vacuo to yield a white solid. This was extracted in toluene (20 mL) and filtered again to remove insoluble impurities. All solvents were removed in vacuo to yield $[(3\text{-py})(S)P^V(\mu\text{-}N^tBu)]_2$ as a white amorphous solid (82 mg, 0.180 mmol, 88%). ^{1}H NMR (25 °C, $CDCl_3$, 400 MHz): δ (ppm) = 8.86 (br, 2H, H_a), 8.41 (br, 2H, H_b), 8.30 (br, 2H, H_d), 8.15 (br, 2H, H_e), 7.44 (br, 2H, H_c), 1.57 (s, 18H, H_f). ^{31}P NMR (25 °C, $CDCl_3$, 162 MHz): δ (ppm) = 40.32 (s).

8.4.34 Attempted Oxidation of 30 with selenium (33)

Inside a nitrogen filled glovebox a Schlenk tube was charged with **30** (100 mg, 0.26 mmol) and elemental selenium (130 mg, 1.65 mmol, excess), transferred to a Schlenk line and dissolved in THF (15 mL). The resulting black suspension was stirred for 16 h at room temperature. All

solvents were removed in vacuo and the resulting black solid extracted in MeCN. The resulting black suspension was filtered through Celite to remove excess selenium, yielding a colourless solution. Concentration of the solution to ca. 5 mL resulted in the precipitation of a white solid, which was heated back into solution. Cooling to room temperature resulted in the formation of a white crystalline solid suitable for X-ray diffraction. $[(3\text{-py})(S)P^{V}(\mu\text{-}N^{t}Bu)]_2$ was obtained as white needle-like crystals, but was not characterised fully, owing to the decomposed nature of the compound.

8.4.35 Synthesis of $[(3\text{-py})(Se)P^{V}(\mu\text{-}N^{t}Bu)]_2$ (34)

Inside a nitrogen filled glovebox a Schlenk tube was charged with **30** (100 mg, 0.26 mmol) and elemental selenium (130 mg, 1.65 mmol, excess), transferred to a Schlenk line and dissolved in THF (15 mL). The resulting black suspension was stirred for 16 h at room temperature. All solvents were removed in vacuo and the resulting black solid extracted in MeCN. The resulting black suspension was filtered through Celite to remove excess selenium, yielding a colourless solution. Concentration of the solution to ca. 5 mL resulted in the precipitation of a white solid, which was heated back into solution. Cooling to room temperature resulted in the formation of a white crystalline solid suitable for X-ray diffraction. $[(3\text{-py})(S)P^{V}(\mu\text{-}N^{t}Bu)]_2$ (**34**) was obtained as white needle-like crystals (127 mg, 0.23 mmol, 88%). ^{1}H NMR (25 °C , $CDCl_3$, 400 MHz): δ (ppm) = 8.43 (br, 2H, H_a), 8.41 (d, $J_{H\text{-}H}$ = 5 Hz, 2H, H_b), 7.84 (br, 2H, H_d), 7.33 (dd, $J_{H\text{-}H}$ = 8 Hz, 5 Hz, 2H, H_c), 5.89 (s, br, 2H, H_e), 1.65 (s, 18H, H_f). ^{31}P NMR (25 °C, $CDCl_3$, 162 MHz): δ (ppm) = 32.16 (s, ^{77}Se satellites, $^{1}J_{P\text{-}Se}$ = 916 Hz).

8.4.36 Reaction of 30 with *n*-butyllithium

Inside a nitrogen filled glovebox a Schlenk tube was charged with **30** (100 mg, 0.26 mmol) and transferred to a Schlenk line, and the solid dissolved in THF (10 mL). To this ^{n}BuLi (1.6 M in hexane, 0.325 mL, 0.52 mmol, 2 eq.) was added dropwise at room temperature. The resulting orange solution was stirred for 10 min at room temperature. All solvents were removed in vacuo to yield an amber precipitate. Recrystallisation did not yield satisfactory crystals for X-ray diffraction. ^{1}H NMR (25 °C, D_8-THF, 400 MHz): δ (ppm) = 8.23 (s, 2H, H_a), 8.00 (d, $J_{H\text{-}H}$ = 5 Hz, 2H, H_b), 7.39 (d, $J_{H\text{-}H}$ = 9 Hz, 2H, H_d), 7.07 (dd, $J_{H\text{-}H}$ = 5 Hz, 2H, H_c), 1.27 (s, 9H, H_f). ^{31}P NMR (25 °C, D_8-THF, 162 MHz): d (ppm) = 107.04 (br).

8.4.37 Reaction of 30 with benzyl potassium

Inside a nitrogen filled glovebox a Schlenk tube was charged with **30** (100 mg, 0.26 mmol) and benzyl potassium (70 mg, 0.52 mmol, 2 eq.) and transferred to a Schlenk line. The solids were dissolved in THF (10 mL) and the reaction mixture stirred at room temperature for 5 min, producing a green solution. All solvents were removed in vacuo to yield a green solid. Recrystallisation did not yield satisfactory crystals for X-ray diffraction. ^{1}H NMR (25 °C, D_8-THF, 400 MHz): δ (ppm) = 8.21 (s, 2H), 7.99 (dd, J_{H-H} = 5 Hz, 1 Hz, 1H), 7.62 (br, 2H), 7.37 (d, J_{H-H} = 8 Hz, 1H), 7.06 (dd, J_{H-H} = 8 Hz, 5 Hz, 1H), 6.79 (br, 1H), 1.27 (s, 9H). ^{31}P NMR (25 °C, D_8-THF, 162 MHz): δ (ppm) = 106.73 (br).

8.4.38 Reaction of 30 with methyl iodide

Inside a nitrogen filled glovebox a Schlenk tube was charged with **30** (180 mg, 0.46 mmol), transferred to a Schlenk line and dissolved in THF (20 mL). Methyl iodide (0.2 mL, 3.2 mmol, excess) was added dropwise to the stirred solution of **30**. The reaction mixture was stirred for 16 hr at 60 °C to produce a yellow suspension. All solvents were removed in vacuo and the resulting yellow precipitate suspended in *n*-hexane (10 ml) and isolated by filtration. The precipitate was then washed with *n*-pentane (20 mL) and dried *in vacuo* for 30 min to yield a yellow amorphous solid. Recrystallisation did not yield satisfactory crystals for X-ray diffraction, with a low signal to noise ratio resulting from the solid's poor solubility preventing successful analysis by NMR spectroscopy.

8.4.39 Reaction of 30 with [(*p*-cymene)$RuCl_2$]$_2$

Inside a nitrogen filled glovebox a Schlenk tube was charged with **30** (15 mg, 0.04 mmol) and (*p*-cymene)ruthenium(II)dichloride dimer (25 mg, 0.05 mmol, 1 eq.) and transferred to a Schlenk line. The solids were dissolved in DCM (2 mL) with the resulting red solution stirred for 10 min at room temperature, resulting in an orange solution. All solvents were removed *in vacuo* to yield an orange solid. Recrystallisation did not yield satisfactory crystals for X-ray diffraction. ^{1}H NMR – poor signal to noise ratio prevented full assignment. ^{31}P NMR (25 °C), $CDCl_3$, 162 MHz): δ (ppm) = –1.08 (s, 1P), –1.23 (s, 1P).

8.4.40 Reaction of 30 with hydrogen peroxide

Inside a nitrogen filled glovebox a Schlenk tube was charged with **30** (80 mg, 0.205 mmol), transferred to a Schlenk line and dissolved in THF (10 mL). Hydrogen peroxide (0.2 mL, >30% w/v aqueous solution, excess) was added dropwise and the reaction mixture stirred for 16 hr at

room temperature. All solvents were removed in vacuo and the resulting white solid dissolved in MeCN. Recrystallisation yielded a brown fibrous material not suitable for X-ray diffraction. Time constraints prevented analysis by NMR spectroscopy.

8.5 Infrared Spectroscopy (Chapter 4)

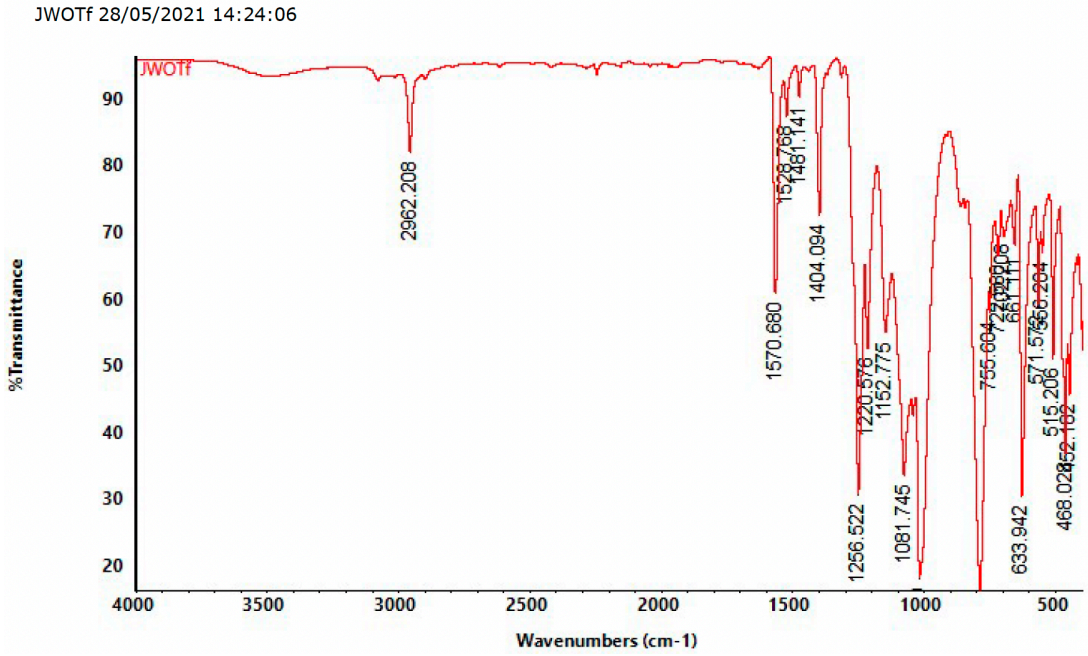

Figure 8.4: IR spectrum of **18**.

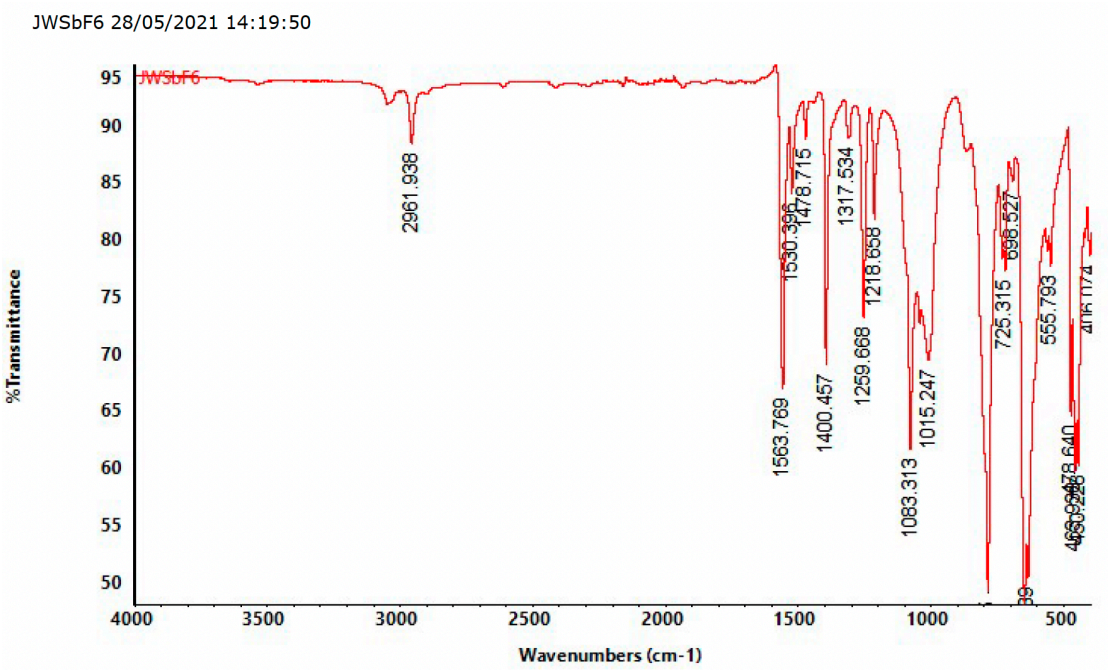

Figure 8.5: IR spectrum of **19**.

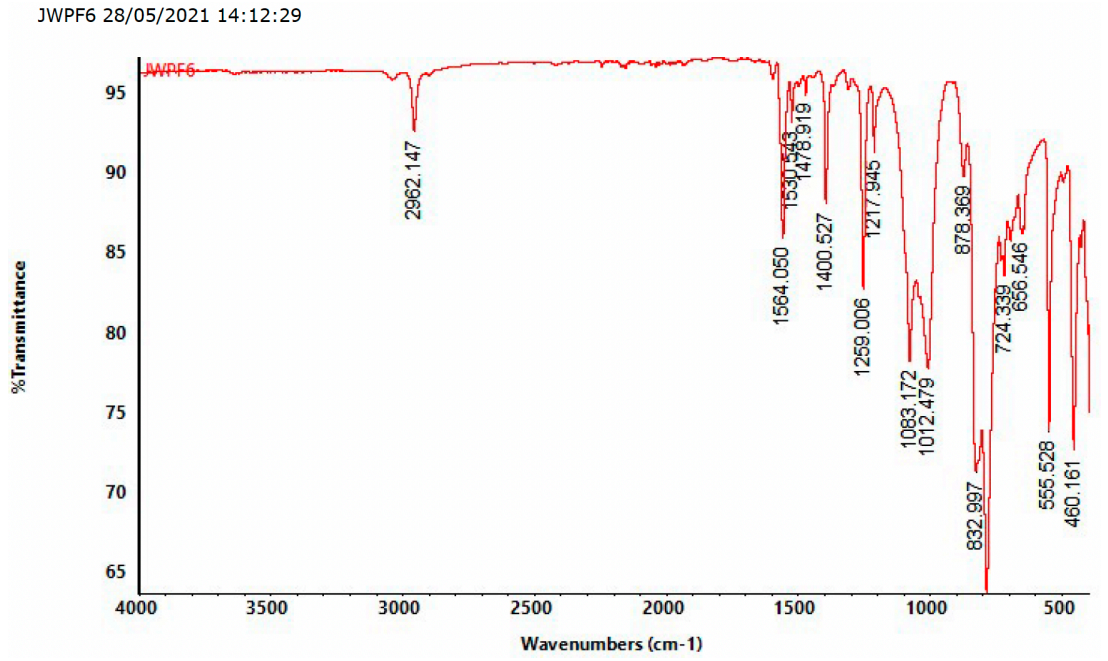

Figure 8.6: IR spectrum of **20**.

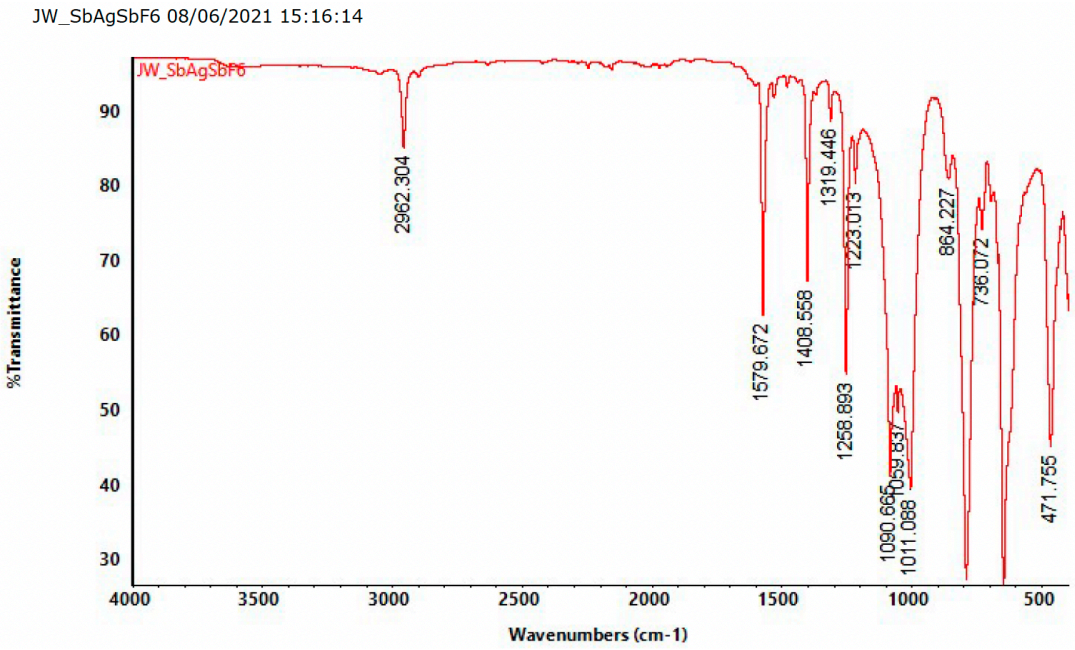

Figure 8.7: IR spectrum of **21.**

8.6 Crystal Data and Refinements for Single-Crystal X-ray Structures

Compound	**2a**	**2b**	[(**3**)Li]	[(**4a**)Li(THF)]	[(**5**)Li(THF)$_2$]
CCDC Number	2096428	2096426	2096425	2096424	2097862
Chemical Formula	$C_{48}H_{55}AlBr_{0.38}Cl_{0.62}Li_2N_2O_3$	$C_{81}H_{86}Al_2BrLi_3N_6O_4$*	$C_{32}H_{29}AlLiN_3$	$C_{29.5}H_{34}AlLiN_2O$	$C_{22}H_{34}AlLiN_2O_2$
Formula Mass	814.93	1362.24	489.50	466.50	392.43
Crystal System	monoclinic	orthorhombic	monoclinic	triclinic	monoclinic
a/Å	13.2730(3)	21.0518(6)	12.2250(9)	9.8424(3)	10.9054(4)
b/Å	17/3309(5)	21.3454(6)	13.9726(10)	10.1963(3)	15.1908(6)
c/Å	20.3751(4)	16.3309(5)	15.8078(12)	13.6820(5)	14.5647(5)
α/°	90	90	90	76.7685(10)	90
β/°	90.3302(13)	90	91.136(5)	81.8527(11)	99.935(2)
γ/°	90	90	90	89.3717(10)	90
Unit Cell Volume/Å^3	4686.87(19)	7338.4(4)	2699.7(3)	1322.81(7)	2376.63(15)
Temperature/K	180(2)	180(2)	180(2)	180(2)	180(2)
Space Group	$P2_1/n$	$P2_12_12$	$P2_1/n$	P -1	$P2_1/n$
Z	4	4	4	2	4
Radiation Type	MoKα	CuKα	CuKα	MoKα	CuKα
Absorption Coefficient, μ/mm^{-1}	0.440	1.409	0.836	0.100	0.872
No. of Reflections Measured	20738	84666	29543	11615	34188
No. of Independent Reflections	4800	12996	4757	4751	4185
R_{int}	0.0327	0.0647	0.1394	0.0465	0.0487
Final R1 Values (I>2σ(I))	0.0819	0.0682	0.0562	0.0582	0.0486
Final R(F^2) Values (all data)	0.0947	0.0848	0.1138	0.0957	0.0581
Goodness-of-Fit on F^2	1.034	1.041	1.021	1.034	1.071
Flack x Determined using Quotients [(I+)-(I-)]/[(I+)+(I-)]	-	0.003(7)	-	-	-

Compound	[**6**]Li(THF)$_2$]	**7**	**8**	**9**	**10**
CCDC Number	-	2096427	-	-	-
Chemical Formula	$C_{22}H_{34}AlLiN_2O_2$	$C_{52}H_{48}Al_2Li_2N_4O_3$	$C_{36}H_{29}N_3Sn1$	$C_{32}H_{26}N_2Sn$	$C_{22}H_{18}N_2Sn$
Formula Mass	392.43	854.86	622.34	557.24	429.07
Crystal System	orthorhombic	triclinic	monoclinic	triclinic	tetragonal
a/Å	28.3782(15)	10.8075(2)	10.289499(17)	9.5276(4)	11.7833(4)
b/Å	37.293(2)	13.5483(3)	15.01290(2)	10.9194(4)	11.7833(4)
c/Å	9.0129(5)	16.8949(4)	19.84580(2)	14.4665(5)	6.5376(2)
α/°	90	88.7384(10)	90	68.494(2)	90
β/°	90	80.4185(11)	104.777(3)	75.879(2)	90
γ/°	90	70.9850(9)	90	69.0670(10)	90
Unit Cell Volume/Å^3	9538.3(9)	2304.82(9)	2964.29(4)	1296.73(9)	907.72(7)
Temperature/K	180(2)	180(2)	180(2)	180(2)	180(2)
Space Group	Fdd2	P -1	P21/c	P -1	P -4 2n
Z	16	2	4	2	2
Radiation Type	CuKα	MoKα	CuKα	CuKα	CuKα
Absorption Coefficient, μ/mm^{-1}	0.869	0.110	7.067	7.995	11.223
No. of Reflections Measured	33616	21216	17154	14429	5222
No. of Independent Reflections	4198	8324	5240	4577	801
R_{int}	0.0373	0.0501	0.044	0.0327	0.0288
Final R1 Values (I>2σ(I))	0.0425	0.0555	0.0318	0.0206	0.0165
Final R(F^2) Values (all data)	0.1202	0.0924	0.0490	0.0231	0.0197
Goodness-of-Fit on F^2	1.055	1.018	1.0066	1.077	1.159
Flack x Determined using Quotients [(I+)-(I-)]/[(I+)+(I-)]	-	-	-	-	– 0.005(10)

Compound	**11**	**12**	**13**	**14**	**16**
CCDC Number	-	-		-	2058021
Chemical Formula	$C_{80}H_{64}Au_8N_8$	$C_{34}H_{32}N_3Sb_1$	$C_{20}H_{16}ClN_2Sb$	$C_{31}H_{26}AuCl_3N_3Sb$	$C_{15}H_{12}BiN_3$
Formula Mass	2713.18	620.40	441.55	865.61	443.26
Crystal System	monoclinic	triclinic	monoclinic	triclinic	monoclinic
a/Å	17.10010(2)	9.21060(2)	7.6299(2)	9.4666(3)	8.1322(3)
b/Å	11.431999(17)	12.20920(2)	18.9997(6)	12.4594(4)	16.4755(5)
c/Å	35.22970(3)	13.79120(2)	12.3437(4)	13.8988(5)	10.2394(3)
α/°	90	98.378(2)	90	82.363(2)	90
β/°	97.1060(18)	94.620(2)	94.7730(10)	81.239(2)	92.1815(13)
γ/°	90	108.074(2)	90	70.840(2)	90
Unit Cell Volume/Å^3	6834.10(3)	1445.52(3)	1783.21(9)	1524.41(9)	1370.90(8)
Temperature/K	180(2)	180(2)	180(2)	180(2)	180(2)
Space Group	P 1 21/n 1	P -1	P 21/c	P -1	P 21/c
Z	4	2	4	2	4
Radiation Type	CuKα	CuKα	CuKα	CuKα	CuKα
Absorption Coefficient, μ/mm^{-1}	31.830	7.803	13.660	18.557	25.144
No. of Reflections Measured	41202	13246	21348	15109	11396
No. of Independent Reflections	12004	5063	3167	5388	2435
R_{int}	0.037	0.028	0.0402	0.0680	0.0505
Final R1 Values (I>2σ(I))	0.0558	0.0296	0.0193	0.0408	0.0269
Final R(F^2) Values (all data)	0.0601	0.0328	0.0225	0.0639	0.0715
Goodness-of-Fit on F^2	1.0641	1.1177	1.079	1.053	1.084
Flack x Determined using Quotients [(I+)-(I-)]/[(I+)+(I-)]	-	-	-	-	-

Compound	**17**	**18**	**19**	**20**	**21**
CCDC Number	2058019	2058025	2058022	2058023	2058024
Chemical Formula	$C_{21}H_{17}N_3Sn$	$C_{48}H_{38}Ag_2Bi_3Cl_3F_6N_9O_6S_2$	$C_45H_{36}Ag_2Bi_3F_{12}N_9Sb_2$	$C_{45}H_{36}Ag_2Bi_3F_{12}N_9P_2$	$C_{15}H_{12}AgF_6N_3Sb_2$
Formula Mass	430.07	1928.57	2017.01	1835.45	699.65
Crystal System	tetragonal	triclinic	triclinic	trigonal	orthorhombic
a/Å	11.6521(5)	10.80190(10)	10.9376(3)	14.6602(2)	13.3033(3)
b/Å	11.6521(5)	16.8490(2)	14.1125(3)	14.6602(2)	18.2923(6)
c/Å	6.6128(3)	19.2471(2)	18.8227(5)	105.129(3)	11.1208(3)
α/°	90	64.8809(5)	88.8818(9)	90	90
β/°	90	88.5160(5)	88.2960(9)	90	90
γ/°	90	75.0663(7)	82.7109(15)	120	90
Unit Cell Volume/$Å^3$	897.83(9)	3050.57(6)	2880.30(13)	19567.4(8)	2706.22(13)
Temperature/K	180(2)	180(2)	180(2)	180(2)	180(2)
Space Group	P -4 21 c	P -1	P -1	R -3 c :H	P n n m
Z	2	2	2	4	4
Radiation Type	CuKα	MoKα	MoKα	MoKα	MoKα
Absorption Coefficient, μ/mm^{-1}	11.365	9.480	10.797	8.774	2.742
No. of Reflections Measured	5012	30915	24768	11919	16016
No. of Independent Reflections	783	13604	10110	3815	3233
R_{int}	0.0303	0.0712	0.0730	0.0499	0.0458
Final R1 Values (I>2σ(I))	0.0159	0.0542	0.0417	0.0292	0.0537
Final R(F^2) Values (all data)	0.0352	0.1576	0.0874	0.0652	0.1980
Goodness-of-Fit on F^2	1.092	1.039	0.866	0.946	1.036
Flack x Determined using Quotients [(I+)-(I-)]/[(I+)+(I-)]	–0.032(9)	-	-	-	-

Compound	**22**	**23**	**24**	**25**	**26**
CCDC Number	2058020	-	-	-	
Chemical Formula	$C_{22}H_{17}AgF_3N_3O_3SSn$	$C_{17}H_{15}AgF_3N_3O_3SSi$	$C_{17}H_{15}BiCuF_6N_4P$	$C_{45}H_{36}Bi_3Cu_2F_{11}N_9PS$	$C_{48}H_{84}Ag_2F_6N_6O_{13}P_2S_2$
Formula Mass	687.01	534.34	692.82	1724.91	1409.01
Crystal System	monoclinic	monoclinic	monoclinic	monoclinic	triclinic
a/Å	10.9205(4)	18.6973(3)	11.0962(3)	11.3520(3)	8.8662(5)
b/Å	20.8833(6)	11.9967(2)	21.2515(5)	25.4329(7)	13.0623(6)
c/Å	14.5849(5)	37.2133(8)	12.0940(4)	12.9806(4)	14.4437(7)
α/°	90	90	90	90	79.606(4)
β/°	96.016(2)	103.8478(8)	94.7498(10)	112.0546(11)	89.825(4)
γ/°	90	90	90	90	75.203(3)
Unit Cell Volume/Å^3	3307.86(19)	8104.5(3)	2842.10(14)	3473.44(17)	1589.13(14)
Temperature/K	180(2)	180(2)	180(2)	180(2)	180(2)
Space Group	P 21/c	C -2yc	P 21/n	P 21/m	P1
Z	4	16	4	2	1
Radiation Type	MoKα	MoKα	MoKα	MoKα	CuKα
Absorption Coefficient, μ/mm^{-1}	1.448	1.208	7.035	8.278	6.699
No. of Reflections Measured	21093	11017	22740	19738	16359
No. of Independent Reflections	4267	11017	4959	6336	8734
R_{int}	0.1323	-	0.0787	0.0801	0.0881
Final R1 Values (I>2σ(I))	0.05060	0.0789	0.0457	0.0466	0.0730
Final R(F^2) Values (all data)	0.1532	0.1282	0.0660	0.0852	0.2018
Goodness-of-Fit on F^2	0.996	0.906	1.011	0.959	1.042
Flack x Determined using Quotients [(I+)-(I-)]/[(I+)+(I-)]	-	-	-	-	-

Compound	**28**	**30**	**33**
CCDC Number	-	-	-
Chemical Formula	$C_{40}H_{120}K_4Li_4O_{24}Si_{20}$	$C_{18}H_{28}N_5P_2$	$C_{22}H_{34}N_8P_2Se_2$
Formula Mass	1731.31	390.4	630.43
Crystal System	tetragonal	orthorhombic	triclinic
a/Å	14.2421(3)	11.8909(2)	11.8183(5)
b/Å	14.2421(3)	16.9886(3)	15.7480(6)
c/Å	28.5686(8)	21.0029(5)	18.0121(9)
α/°	90	90	66.279(2)
β/°	90	90	74.164(2)
γ/°	90	90	84.812(3)
Unit Cell Volume/Å^3	5794.8(3)	4242.79(14)	2951.9(2)
Temperature/K	180(2)	180(2)	180(2)
Space Group	I – 4	Pbca	P -1
Z	2	8	4
Radiation Type	MoKα	MoKα	MoKα
Absorption Coefficient, μ/mm^{-1}	0.405	0.219	2.638
No. of Reflections Measured	12093	24939	20307
No. of Independent Reflections	6296	3751	7193
R_{int}	0.0343	0.0607	0.1041
Final R1 Values (I>2σ(I))	0.0370	0.0499	0.0876
Final R(F^2) Values (all data)	0.0757	0.1564	0.1950
Goodness-of-Fit on F^2	0.852	1.084	1.124
Flack x Determined using Quotients [(I+)-(I-)]/[(I+)+(I-)]	-	-	-

9. References

1 W. B. Tolman, A. L. Balch, S. Bart, B. Cossairt, S. Dehnen, P. S. Halasyamani, H. Kageyama, F. Meyer, J. Morrow, P. S. Mukherjee, F. Neese, P. P. Power, R. Sessoli, V. W. W. Yam and H.-C. Zhou, *Inorg. Chem.*, 2019, **58**, 9515–9516.

2 S. Dehnen, *Angew. Chem. Int. Ed.*, 2018, **57**, 10386–10387.

3 P. P. Power, *Nature*, 2010, **463**, 171.

4 G. C. Welch, R. R. San Juan, J. D. Masuda and D. W. Stephan, *Science*, 2006, **314**, 1124–1126.

5 A. S. S. Wilson, M. S. Hill, M. F. Mahon, C. Dinoi and L. Maron, *Science*, 2017, **358**, 1168–1171.

6 M. J. Rodríguez-Álvarez, J. García-Álvarez, M. Uzelac, M. Fairley, C. T. O'Hara and E. Hevia, *Chem. Eur. J.*, 2018, **24**, 1720–1725.

7 C. Vidal, J. García-Álvarez, A. Hernán-Gómez, A. R. Kennedy and E. Hevia, *Angew. Chem. Int. Ed.*, 2016, **55**, 16145–16148.

8 M. Uzelac, A. R. Kennedy, E. Hevia and R. E. Mulvey, *Angew. Chem. Int. Ed.*, 2016, **55**, 13147–13150.

9 B. Rösch, T. X. Gentner, J. Langer, C. Färber, J. Eyselein, L. Zhao, C. Ding, G. Frenking and S. Harder, *Science*, 2021, **371**, 1125–1128.

10 L. Gade and P. Hoffman, *Molecular Catalysts: Structure and Functional Design*, Wiley-VCH Weinheim, Heidelberg, 2014.

11 C. Moberg, *Angew. Chem. Int. Ed.*, 1998, **37**, 248–268.

12 C. Vogel, F. W. Heinemann, J. Sutter, C. Anthon and K. Meyer, *Angew. Chem. Int. Ed.*, 2008, **47**, 2681–2684.

13 N. L. Lampland, M. Hovey, D. Mukherjee and A. D. Sadow, *ACS Catal.*, 2015, **5**, 4219–4226.

14 A. G. Walden and A. J. M. Miller, *Chem. Sci.*, 2015, **6**, 2405–2410.

15 M. S. Deshmukh, A. Yadav, R. Pant and R. Boomishankar, *Inorg. Chem.*, 2015, **54**, 1337–1345.

16 E. Yang, A. J. Plajer, Á. García-Romero, A. D. Bond, T. K. Ronson, C. M. Álvarez, R. García-Rodríguez, A. L. Colebatch and D. S. Wright, *Chem. Eur. J.*, 2019, **25**, 14003–14009.

17 M. Cernerud, H. Adolfsson and C. Moberg, *Tetrahedron Asymmetry*, 1997, **8**, 2655–2662.

18 G. Parkin, *Chem. Commun.*, 2000, 1971–1985.

19 I. Kuzu, I. Krummenacher, J. Meyer, F. Armbruster and F. Breher, *Dalton Trans.*, 2008, 5836–5865.

20 J. Lloret Fillol, A. Kruckenberg, P. Scherl, H. Wadepohl and L. H. Gade, *Chem. Eur. J.*, 2011, **17**, 14047–14062.

21 A. Petuker, K. Merz, C. Merten and U. P. Apfel, *Inorg. Chem.*, 2016, **55**, 1183–1191.

22 S. Trofimenko, *Chem. Rev.*, 1972, **72**, 497–509.

23 S. Trofimenko, *Chem. Rev*, 1993, **93**, 943–980.

24 S. Trofimenko, in *Progress in Inorganic Chemistry*, eds. K. M. Kadish and S. J. Lippard, John Wiley & Sons, Ltd, 1986, p. 435.

25 N. Kitajimaj and W. B. Tolman, in *Progress in Inorganic Chemistry*, ed. K. D. Karlin, John Wiley & Sons, Ltd, 1995.

26 L. F. Szczepura, L. M. Witham and K. J. Takeuchi, *Coord. Chem. Rev.*, 1998, **174**, 5–32.

27 A. G. Blackman, *Polyhedron*, 2005, **24**, 1–39.

28 C. Bianchini, A. Meli, M. Peruzzini, F. Vizza, P. Frediani and J. A. Ramirez, *Organometallics*, 1990, **9**, 226–240.

29 W. H. Hohman, D. J. Kountz and D. W. Meek, *Inorg. Chem.*, 1986, **25**, 616–623.

30 R. B. Siedschlag, V. Bernales, K. D. Vogiatzis, N. Planas, L. J. Clouston, E. Bill, L. Gagliardi and C. C. Lu, *J. Am. Chem. Soc.*, 2015, **137**, 4638–4641.

31 T. J. Del Castillo, N. B. Thompson and J. C. Peters, *J. Am. Chem. Soc.*, 2016, **138**, 5341–5350.

32 L. D. Field, R. W. Guest, K. Q. Vuong, S. J. Dalgarno and P. Jensen, *Inorg. Chem.*, 2009, **48**, 2246–2253.

33 W. H. Wang, Y. Himeda, J. T. Muckerman, G. F. Manbeck and E. Fujita, *Chem. Rev.*, 2015, **115**, 12936–12973.

34 M. J. Burk, *J. Am. Chem. Soc.*, 1991, **113**, 8519–8521.

35 M. J. Burk, *Acc. Chem. Res.*, 2000, **33**, 363–372.

36 M. J. Burk and R. L. Harlow, *Angew. Chem. Int. Ed. English*, 1990, **29**, 1462–1464.

37 M. J. Burk, J. E. Feaster and R. L. Harlow, *Organometallics*, 1990, **9**, 2653–2655.

38 C. Dro, S. Bellemin-Laponnaz, R. Welter and L. H. Gade, *Angew. Chem. Int. Ed.*, 2004, **43**, 4479–4482.

39 D. L. Jameson, J. K. Blaho, K. T. Kruger and K. A. Goldsby, *Inorg. Chem.*, 1989, **28**, 4312–4314.

40 C. Cui, R. A. Lalancette and F. Jäkle, *Chem. Commun.*, 2012, **48**, 6930.

41 S. Y. Jeong, R. A. Lalancette, H. Lin, P. Lupinska, P. O. Shipman, A. John, J. B. Sheridan and F. Jäkle, *Inorg. Chem.*, 2016, **55**, 3605–3615.

42 F. García, A. D. Hopkins, R. A. Kowenicki, M. McPartlin, M. C. Rogers and D. S. Wright, *Organometallics*, 2004, **23**, 3884–3890.

43 H. R. Simmonds and D. S. Wright, *Chem. Commun.*, 2012, **48**, 8617–8624.

44 R. García-Rodríguez and D. S. Wright, *Chem. Eur. J.*, 2015, **21**, 14949–14957.

45 R. García-Rodríguez, T. H. Bullock, M. McPartlin and D. S. Wright, *Dalt. Trans.*, 2014, **43**, 14045–14053.

46 R. García-Rodríguez, S. Kopf and D. S. Wright, *Dalton Trans.*, 2018, **47**, 2232–2239.

47 C. S. Alvarez, F. García, S. M. Humphrey, A. D. Hopkins, R. A. Kowenicki, M. McPartlin, R. A. Layfield, R. Raja, M. C. Rogers, A. D. Woods and D. S. Wright, *Chem. Commun.*, 2005, 198–200.

48 R. García-Rodríguez, S. Hanf, A. D. Bond and D. S. Wright, *Chem. Commun.*, 2017, **53**, 1225–1228.

49 R. García-Rodríguez, H. R. Simmonds and D. S. Wright, *Organometallics*, 2014, **33**, 7113–7117.

50 F. García, A. D. Hopkins, R. A. Kowenicki, M. McPartlin, M. C. Rogers, J. S. Silvia and D. S. Wright, *Organometallics*, 2006, **25**, 2561–2568.

51 T. H. Bullock, W. T. K. Chan, D. J. Eisler, M. Streib and D. S. Wright, *Dalt. Trans.*, 2009, 1046–1054.

52 R. García-Rodríguez and D. S. Wright, *Dalton Trans.*, 2014, **43**, 14529–14532.

53 R. García-Rodríguez, S. Hanf, A. D. Bond and D. S. Wright, *Chem. Commun.*, 2017, **53**, 1225–1228.

54 Á. García-Romero, A. J. Plajer, L. Álvarez-Miguel, A. D. Bond, D. S. Wright and R. García-Rodríguez, *Chem. Eur. J.*, 2018, **24**, 17019–17026.

55 A. J. Plajer, S. Kopf, A. L. Colebatch, A. D. Bond, D. S. Wright and R. García-Rodríguez, *Dalton Trans.*, 2019, **48**, 5692–5697.

56 K. Zeckert, *Dalt. Trans.*, 2012, **41**, 14101.

57 K. Zeckert and D. Fuhrmann, *Inorg. Chem.*, 2019, **58**, 16736–16742.

58 J. P. Wibaut, A. P. de Jonge, H. G. P. van der Voort and P. P. H. L. Otto, *Recl. des Trav. Chim. des Pays-Bas*, 1951, **70**, 1054–1066.

59 D. L. White and J. W. Faller, *Inorg. Chem.*, 1982, **21**, 3119–3122.

60 H. Adolfsson, K. Wärnmark and C. Moberg, *J. Chem. Soc. Chem. Commun.*, 1992, 1054–1055.

61 R. García-Rodríguez and D. S. Wright, *Dalt. Trans.*, 2014, **43**, 14529–14532.

62 M. A. Beswick, C. J. Belle, M. K. Davies, M. A. Halcrow, P. R. Raithby, A. Steiner and D. S. Wright, *Chem. Commun.*, 1996, 2619–2620.

63 S. Hanf, R. García-Rodríguez, A. D. Bond, E. Hey-Hawkins and D. S. Wright, *Dalton Trans.*, 2016, **45**, 276–283.

64 D. Morales, J. Pérez, L. Riera, V. Riera and D. Miguel, *Organometallics*, 2001, **20**, 4517–4523.

65 F. García, A. D. Hopkins, S. M. Humphrey, M. McPartlin, M. C. Rogers and D. S. Wright, *J. Chem. Soc. Dalt. Trans.*, 2004, **40**, 361361–362362.

66 J. E. Parks, B. E. Wagner and R. H. Holm, *J. Organomet. Chem.*, 1973, **56**, 53–66.

67 A. J. Plajer, A. L. Colebatch, M. Enders, Á. García-Romero, A. D. Bond, R. García-Rodríguez and D. S. Wright, *Dalton Trans.*, 2018, **47**, 7036–7043.

68 F. Reichart, M. Kischel and K. Zeckert, *Chem. Eur. J*, 2009, **15**, 10018–10020.

69 K. Zeckert, S. Zahn and B. Kirchner, *Chem. Commun.*, 2010, **46**, 2638–2640.

70 K. Zeckert, *Organometallics*, 2013, **32**, 1387–1393.

71 J. P. Wibaut and G. L. C. la Bastide, *Recl. des Trav. Chim. des Pays-Bas*, 2010, **52**, 493–498.

72 A. V. Artem'ev, N. K. Gusarova, S. F. Malysheva, N. A. Belogorlova, O. N. Kazheva, G. G. Alexandrov, O. A. Dyachenko and B. A. Trofimov, *Mendeleev Commun.*, 2015, **25**, 196–198.

73 B. A. Trofimov, A. V. Artem'Ev, S. F. Malysheva, N. K. Gusarova, N. A. Belogorlova, A. O. Korocheva, Y. V. Gatilov and V. I. Mamatyuk, *Tetrahedron Lett.*, 2012, **53**, 2424–2427.

74 A. V. Artem'ev, E. P. Doronina, M. I. Rakhmanova, A. O. Sutyrina, I. Y. Bagryanskaya, P. M. Tolstoy, A. L. Gushchin, A. S. Mazur, N. K. Gusarova and B. A. Trofimov, *New J. Chem.*, 2016, **40**, 10028–10040.

75 A. V. Artem'Ev, N. K. Gusarova, S. F. Malysheva, O. N. Kazheva, G. G. Alexandrov, O. A. Dyachenko and B. A. Trofimov, *Mendeleev Commun.*, 2012, **22**, 294–296.

76 W. C. Davies and F. G. Mann, *J. Chem. Soc.*, 1944, 276–283.

77 X. Hu, T. Sun and C. Zheng, *Phosphorus, Sulfur Silicon Relat. Elem.*, 2018, **193**, 300–305.

78 F. Richard Keene and P. J. Stephenson, *Inorganica Chim. Acta*, 1991, **187**, 217.

79 T. Gneuß, M. J. Leitl, L. H. Finger, N. Rau, H. Yersin and J. Sundermeyer, *Dalton*

Trans., 2015, **44**, 8506–8520.

80 A. N. Kharat, A. Bakhoda, T. Hajiashrafi and A. Abbasi, *Phosphorus, Sulfur Silicon Relat. Elem.*, 2010, **185**, 2341–2347.

81 A. V. Artem'Ev, I. Y. Bagryanskaya, E. P. Doronina, P. M. Tolstoy, A. L. Gushchin, M. I. Rakhmanova, A. Y. Ivanov and A. O. Suturina, *Dalton Trans.*, 2017, **46**, 12425–12429.

82 A. V. Artem'Ev, N. K. Gusarova, V. A. Shagun, S. F. Malysheva, V. I. Smirnov, T. N. Borodina and B. A. Trofimov, *Polyhedron*, 2015, **90**, 1–6.

83 L. Dubován, A. Pöllnitz and C. Silvestru, *Eur. J. Inorg. Chem.*, 2016, **2016**, 1521–1527.

84 S. Solyntjes, B. Neumann, H.-G. Stammler, N. Ignat'ev and B. Hoge, *Eur. J. Inorg. Chem.*, 2016, **2016**, 3999–4010.

85 S. Hanf, R. García-Rodríguez, S. Feldmann, A. D. Bond, E. Hey-Hawkins and D. S. Wright, *Dalton Trans.*, 2017, **46**, 814–824.

86 A. V. Artem'Ev, A. V. Kashevskii, A. S. Bogomyakov, A. Y. Safronov, A. O. Sutyrina, A. A. Telezhkin and I. V. Sterkhova, *Dalton Trans.*, 2017, **46**, 5965–5975.

87 R. Suter, H. Sinclair, N. Burford, R. McDonald, M. J. Ferguson and E. Schrader, *Dalton Trans.*, 2017, **46**, 7681–7685.

88 X. Wang, S. S. Nurttila, W. I. Dzik, R. Becker, J. Rodgers and J. N. H. Reek, *Chem. Eur. J.*, 2017, **23**, 14769–14777.

89 C. Zheng, X. Hu and Q. Tao, *Mendeleev Commun.*, 2018, **28**, 208–210.

90 A. V. Artem'ev and D. G. Samsonenko, *Inorg. Chem. Commun.*, 2018, **93**, 47–51.

91 A. V. Artem'ev, E. A. Pritchina, M. I. Rakhmanova, N. P. Gritsan, I. Y. Bagryanskaya, S. F. Malysheva and N. A. Belogorlova, *Dalton Trans.*, 2019, **48**, 2328–2337.

92 A. V. Artem'ev, M. Z. Shafikov, A. Schinabeck, O. V. Antonova, A. S. Berezin, I. Y. Bagryanskaya, P. E. Plusnin and H. Yersin, *Inorg. Chem. Front.*, 2019, **6**, 3168–3176.

93 R. Zaffaroni, W. I. Dzik, R. J. Detz, J. I. van der Vlugt and J. N. H. Reek, *Eur. J. Inorg. Chem.*, 2019, **2019**, 2498–2509.

94 A. Y. Baranov, A. S. Berezin, D. G. Samsonenko, A. S. Mazur, P. M. Tolstoy, V. F. Plyusnin, I. E. Kolesnikov and A. V. Artem'Ev, *Dalton Trans.*, 2020, **49**, 3155–3163.

95 W. Huber, R. Linder, J. Niesel, U. Schatzschneider, B. Spingler and P. C. Kunz, *Eur. J. Inorg. Chem.*, 2012, **2012**, 3140–3146.

96 H. Qi, L. Chen, B. Liu, X. Wang, L. Long and D. Liu, *Bioorganic Med. Chem. Lett.*, 2014, **24**, 1108–1110.

97 S. Hanf, A. L. Colebatch, P. Stehr, R. García-Rodríguez, E. Hey-Hawkins and D. S. Wright, *Dalton Trans.*, 2020, **49**, 5312–5322.

98 L. J. Jongkind and J. N. H. Reek, *Chem. - An Asian J.*, 2020, **15**, 1–10.

99 A. V. Artem'Ev, S. F. Malysheva, B. G. Sukhov, N. A. Belogorlova, Y. V. Gatilov, V. I. Mamatyuk and N. K. Gusarova, *Mendeleev Commun.*, 2012, **22**, 18–20.

100 V. Bocokić, A. Kalkan, M. Lutz, A. L. Spek, D. T. Gryko and J. N. H. Reek, *Nat. Commun.*, 2013, **4**, 1–9.

101 A. N. Kharat, B. T. Jahromi and A. Bakhoda, *Transit. Met. Chem.*, 2012, **37**, 63–69.

102 A. J. Plajer, A. L. Colebatch, F. J. Rizzuto, P. Pröhm, A. D. Bond, R. García-Rodríguez and D. S. Wright, *Angew. Chem. Int. Ed.*, 2018, **57**, 6648–6652.

103 A. García-Romero, A. J. Plajer, D. Miguel, D. S. Wright, A. D. Bond, C. M. Alvarez and R. García-Rodríguez, 2020, **59**, 7103–7116.

104 K. Urgin, C. Aubé, C. Pichon, M. Pipelier, V. Blot, C. Thobie-Gautier, E. Léonel, D. Dubreuil and S. Condon, *Tetrahedron Lett.*, 2012, **53**, 1894–1896.

105 K. Urgin, C. Aubé, M. Pipelier, V. Blot, C. Thobie-Gautier, S. Sengmany, J. Lebreton, E. Léonel, D. Dubreuil and S. Condon, *European J. Org. Chem.*, 2013, 117–124.

106 W. Tyrra, S. Aboulkacem, B. Hoge, W. Wiebe and I. Pantenburg, *J. Fluor. Chem.*, 2006, **127**, 213–217.

107 Á. García-Romero, A. J. Plajer, D. Miguel, D. S. Wright, A. D. Bond, C. M. Álvarez and R. García-Rodríguez, *Inorg. Chem.*, 2020, **59**, 7103–7116.

108 V. F. Slagt, P. C. J. Kamer, P. W. N. M. Van Leeuwen and J. N. H. Reek, *J. Am. Chem. Soc.*, 2004, **126**, 1526–1536.

109 J. P. Wibaut and P. P. H. L. Otto, *Recl. des Trav. Chim. des Pays-Bas*, 1958, 1048–1063.

110 M. S. Deshmukh, V. S. Mane, A. S. Kumbhar and R. Boomishankar, *Inorg. Chem.*, 2017, **56**, 13286–13292.

111 K. Sravan Kumar, V. S. Mane, A. Yadav, A. S. Kumbhar, R. Boomishankar and chemcomm ChemComm COMMUNICATION, *13156 | Chem. Commun*, 2019, **55**, 13156.

112 A. Krasovskiy and P. Knochel, *Angew. Chem. Int. Ed.*, 2004, **43**, 3333–3336.

113 L. J. Jongkind, X. Caumes, A. P. T. Hartendorp and J. N. H. Reek, *Acc. Chem. Res.*, 2018, **51**, 2115–2128.

114 S. S. Nurttila, W. Brenner, J. Mosquera, K. M. van Vliet, J. R. Nitschke and J. N. H. Reek, *Chem. Eur. J.*, 2018, **25**, 609–620.

115 L. J. Jongkind, J. A. A. W. Elemans and J. N. H. Reek, *Angew. Chem. Int. Ed.*, 2019, **58**, 2696–2699.

116 C. Miao and T. E. Su, *Inorg. Chem. Commun.*, 2020, **112**, 107733.

117 S. Kitagawa, S. Noro, J. A. Mecleverty, T. J. Meyer, K. Uemura, S. R. Batten, R. Robson, J. Zhang, W. Lin, Z.-F. Chen, R.-G. Xiong, B. F. Abrahams, H.-K. Fun, S. Ferlay, S. Koenig, M. W. Hosseini, J. Pansanel, A. Cian, N. Kyritsakas, L. Carlucci, G. Ciani, D. M. Proserpio, S. Rizzato, Y. K.-L. Liu, A. Westcott, N. Whitford, M. J. Hardie, R. Natarajan, O. R. Evans, K. Matsumoto, M. Kannami, M. Oda, A. Okazawa, T. Ishida and T. Nogami, *Angew. Chem., Int. Ed*, 2003, **7**, 2903–2906.

118 S. Ghosh, S. R. Batten, D. R. Turner and P. S. Mukherjee, *Organometallics*, 2007, **26**, 3252–3255.

119 A. W. Kleij, M. Kuil, D. M. Tooke, A. L. Spek and J. N. H. Reek, *Inorg. Chem.*, 2005, **44**, 7696–7698.

120 F. A. Cotton, E. V. Dikarev, M. A. Petrukhina, M. Schmitz and P. J. Stang, *Inorg. Chem.*, 2002, **41**, 2903–2908.

121 N. Wei, N. N. Murthy and K. D. Karlin, *Chemistry of Pentacoordinate [LCun-Cl]+ Complexes with Quinolyl Containing Tripodal Tetradentate Ligands L*, 1994, vol. 33.

122 A. J. Peel, J. E. Waters, R. García-Rodríguez and D. S. Wright, in *Advanced Organometallic Chemistry*, 2021, pp. 193–244.

123 T. H. Bullock, W. T. K. Chan, D. J. Eisler, M. Streib and D. S. Wright, *Dalton Trans.*, 2009, 1046–1054.

124 T. H. Bullock, W. T. K. Chan and D. S. Wright, *Dalton Trans.*, 2009, 6709–6711.

125 J. M. Cole, P. G. Waddell, A. E. H. Wheatley, G. J. McIntyre, A. J. Peel, C. W. Tate and D. J. Linton, *Organometallics*, 2014, **33**, 3919–3923.

126 J. O. Bauer and C. Strohmann, *Organometallics*, 2020, **40**, 11–15.

127 F. Weigend, *Phys. Chem. Chem. Phys.*, 2006, **8**, 1057–1065.

128 F. Weigend and R. Ahlrichs, *Phys. Chem. Chem. Phys.*, 2005, **7**, 3297–3305.

129 A. D. Becke, *Phys. Rev. A*, 1988, **38**, 3098–3100.

130 J. P. Perdew, *Phys. Rev. B*, 1986, **33**, 8822–8824.

131 J. P. Perdew, *Phys. Rev. B*, 1986, **34**, 7406.

132 A. D. Becke, *J. Chem. Phys.*, 1993, **98**, 5648–5652.

133 P. J. Stephens, F. J. Devlin, C. F. Chabalowski and M. J. Frisch, *J. Phys. Chem.*, 1994, **98**, 11623–11627.

134 E. D. Glendening, A. E. Reed, J. E. Carpenter and F. Weinhold, 1998.

135 A. E. Reed, L. A. Curtiss and F. Weinhold, *Chem. Rev.*, 1988, **88**, 899–926.

136 R. F. W. Bader, *Atoms in Molecules - A Quantum Theory*, Clarendon Press, 1994.

137 S. Emamian, T. Lu, H. Kruse and H. Emamian, *J. Comput. Chem.*, 2019, **40**, 2868–2881.

138 T. S. Thakur and G. R. Desiraju, *Chem. Commun.*, 2006, 552–554.

139 Dario Braga, A. Fabrizia Grepioni, E. Tedesco, K. B. And and G. R. Desiraju, *Organometallics*, 1997, **16**, 1846–1856.

140 T. S. Thakur and G. R. Desiraju, *J. Mol. Struct. THEOCHEM*, 2007, **810**, 143–154.

141 A. J. Plajer, A. L. Colebatch, M. Enders, Á. García-Romero, A. D. Bond, R. García-

Rodríguez and D. S. Wright, *Dalton Trans.*, 2018, **47**, 7036–7043.

142 A.-H. Li, D. J. Beard, H. Coate, A. Honda, M. Kadalbajoo, A. Kleinberg, R. Laufer, K. M. Mulvihill, A. Nigro, P. Rastogi, D. Sherman, K. W. Siu, A. G. Steinig, T. Wang, D. Werner, A. P. Crew and M. J. Mulvihill, *Chem. Pharm. Bull.*, 1982, **10**, 1678–1686.

143 J. K. Stille, *Angew. Chem. Int. Ed. English*, 1986, **25**, 508–524.

144 Y. Zhou and W. Chen, , DOI:10.1021/om070104j.

145 M. Scudder and I. Dance, *Chem. Eur. J*, 2002, **8**, 5456–5468.

146 C. J. Whiteoak, J. D. Nobbs, E. Kiryushchenkov, S. Pagano, A. J. P. White and G. J. P. Britovsek, *Inorg. Chem.*, 2013, **52**, 7000–7009.

147 L. Dostál, R. Jambor, A. Růžička, R. Jirásko, E. Černošková, L. Beneš and F. de Proft, *Organometallics*, 2010, **29**, 4486–4490.

148 V. R. Bojan, E. J. Fernández, A. Laguna, J. M. López-de-Luzuriaga, M. Monge, M. E. Olmos, R. C. Puelles and C. Silvestru, *Inorg. Chem.*, 2010, **49**, 5530–5541.

149 A. M. Kluwer, I. Ahmad and J. N. H. Reek, *Tetrahedron Lett.*, 2007, **48**, 2999–3001.

150 R. J. Bowen, A. C. Garner, S. J. Berners-Price, I. D. Jenkins and R. E. Sue, *J. Organomet. Chem.*, 1998, **554**, 181–184.

151 K. Matsumoto, M. Kannami, D. Inokuchi, H. Kurata, T. Kawase and M. Oda, *Org. Lett.*, 2007, **9**, 2903–2906.

152 C. J. Kuehl, Y. K. Kryschenko, U. Radhakrishnan, S. Russell Seidel, S. D. Huang and P. J. Stang, *Proc. Natl. Acad. Sci. U. S. A.*, 2002, **99**, 4932–4936.

153 S. Ghosh, D. R. Turner, S. R. Batten and P. S. Mukherjee, *Dalton Trans.*, 2007, 1869–1871.

154 M. Fujita, S. Yu, T. Kusukawa, H. Funaki, K. Ogura and K. Yamaguchi, *Angew. Chem. Int. Ed.*, 1998, **37**, 2082–2085.

155 W. W. Ellis, M. Schmitz, A. A. Arif and P. J. Stang, *Inorg. Chem.*, 2000, **39**, 2547–2557.

156 F. Bureš, D. Cvejn, K. Melánová, L. Beneš, J. Svoboda, V. Zima, O. Pytela, T. Mikysek, Z. Růžičková, I. V. Kityk, A. Wojciechowski and N. Alzayed, *J. Mater.*

Chem. C, 2016, **4**, 468–478.

157 L. Carlucci, G. Ciani, D. M. Proserpio and A. Sironi, *Angew. Chem. Int. Ed.*, 1995, **34**, 1895–1898.

158 N. S. Oxtoby, A. J. Blake, N. R. Champness and C. Wilson, *Proc. Natl. Acad. Sci. U. S. A.*, 2002, **99**, 4905–4910.

159 K. M. Anderson, C. J. Baylies, A. H. M. M. Jahan, N. C. Norman, A. G. Orpen and J. Starbuck, *Dalton Trans.*, 2003, **16**, 3270–3277.

160 J. P. H. Charmant, A. H. M. M. Jahan, N. C. Norman, A. G. Orpen and T. J. Podesta, *CrystEngComm*, 2004, **6**, 29–33.

161 A. Bondi, *J. Phys. Chem.*, 1964, **68**, 441–451.

162 R. Custelcean, *Chem. Soc. Rev.*, 2010, **39**, 3675–3685.

163 G. A. Bowmaker, Effendy, J. D. Kildea and A. H. White, *Aust. J. Chem.*, 1997, **50**, 577–586.

164 Angela M. Hill, * and William Levason and M. Webster, *Inorg. Chem.*, 1996, **35**, 3428–3430.

165 A. Phan, C. J. Doonan, F. J. Uribe-Romo, C. B. Knobler, M. O' Keeffe and O. M. Yaghi, *Acc. Chem. Res.*, 2010, **43**, 58–67.

166 A. J. Plajer, R. Garcia-Rodriguez, F. J. Rizzuto and D. S. Wright, *Chem. Eur. J*, 2018, **24**, 2013–2019.

167 L. Stahl, *Coord. Chem. Rev.*, 2000, **210**, 203–250.

168 Tristram Chivers, Mark Krahn, A. Masood Parvez and G. Schatte, *Inorg. Chem.*, 2001, **40**, 2547–2553.

169 Graham R. Lief, A. Christopher J. Carrow, L. Stahl and R. J. Staples, *Organometallics*, 2001, **20**, 1629–1635.

170 A. J. Plajer, A. D. Bond and D. S. Wright, *Chem. Eur. J.*, 2021, **27**, 289–297.

171 A. J. Plajer, J. Zhu, P. Pröhm, F. J. Rizzuto, U. F. Keyser and D. S. Wright, *J. Am. Chem. Soc.*, 2019, **142**, 1029–1037.

172 P. A. Gale, E. N. W. Howe, X. Wu and M. J. Spooner, *Coord. Chem. Rev.*, 2018, **375**, 333–372.

173 P. A. Gale, *Acc. Chem. Res.*, 2011, **44**, 216–226.

174 V. Amendola, G. Bergamaschi, M. Boiocchi, L. Fabbrizzi and M. Milani, *Chem. Eur. J.*, 2010, **16**, 4368–4380.

175 N. Busschaert, I. L. Kirby, S. Young, S. J. Coles, P. N. Horton, M. E. Light and P. A. Gale, *Angew. Chem., Int. Ed*, 2012, **124**, 4502–4506.

176 A. J. Plajer, F. J. Rizzuto, H.-C. Niu, S. Lee, J. M. Goodman and D. S. Wright, *Angew. Chem. Int. Ed.*, 2019, **58**, 10655–10659.

177 T. Roth, H. Wadepohl, D. S. Wright and L. H. Gade, *Chem. Eur. J.*, 2013, **19**, 13823–13837.

178 K. Zangger and L. M. Armitage, *Met. Based Drugs*, 1999, **6**, 239–245.

179 A. Del Zotto, P. Di Bernardo, M. Tolazzi, G. Tomat and P. Zanonatob, *J. Chem. Soc., Dalt. Trans.,* 1993, 3009.

180 A. Decken, F. A. LeBlanc, J. Passmore and X. Wang, *Eur. J. Inorg. Chem.*, 2006, 4033–4036.

181 Brigitte S. Fox, M. K. Beyer and V. E. Bondybey, *J. Am. Chem. Soc.*, 2002, **124**, 13613–13623.

182 R. Knorr, B. Schmidt, J. Mehlstäubl and T. von Roman, *J. Organomet. Chem.*, 2018, **871**, 185–196.

183 I. Schranz and L. Stahl, *Inorganica Chim. Acta*, 2010, **363**, 975–980.

184 I. Haiduc, *Organometallics*, 2003, **23**, 3–8.

185 F. Dankert, F. Weigend and C. von Hänisch, *Inorg. Chem.*, 2019, **58**, 15417–15422.

186 C. A. Hunter and J. K. M. Sanders, *J. Am. Chem. Soc.*, 1990, **112**, 5525–5534.

187 S. Hanf, 2019.

188 Bruker AXS Inc., 2012.

189 Z. Otwinowski and W. Minor, *Methods Enzymol.*, 1997, **276**, 307–326.

190 G. M. Sheldrick, *Acta Crystallogr. A*, 2008, **64**, 112–122.

191 G. M. Sheldrick, *Acta Crystallogr. A*, 2015, **71**, 3–8.

192 G. M. Sheldrick, *Acta Crystallogr. C*, 2015, **71**, 3–8.

193 C. B. Hübschle, G. M. Sheldrick, B. Dittrich and IUCr, *urn:issn:0021-8898*, 2011, **44**, 1281–1284.

194 Bruker, *SADABS*.

195 F. Neese, *WIREs Comput. Mol. Sci.*, 2018, **8**, e1327.

196 F. Neese, *WIREs Comput. Mol. Sci.*, 2012, **2**, 73–78.

197 S. Grimme, S. Ehrlich and L. Goerigk, *J. Comput. Chem.*, 2011, **32**, 1456–1465.

198 S. Grimme, J. Antony, S. Ehrlich and H. Krieg, *J. Chem. Phys.*, 2010, **132**, 154104.

199 F. Neese, F. Wennmohs, A. Hansen and U. Becker, *Chem. Phys.*, 2009, **356**, 98–109.

200 J. Tao, J. P. Perdew, S. V. N. and S. G. E., *Phys. Reivew Lett.*, 2003, **91**, 140601-1-14601–4.

201 F. Weigend and R. Ahlrichs, *Phys. Chem. Chem. Phys.*, 2005, **7**, 3297–3305.

202 A. D. Becke, *Phys. Rev. A*, 1988, **38**, 3098–3100.

203 J. Perdew, *Phys. Rev. B*, 1986, **33**, 8822–8824.

204 P. J. Stephens, F. J. Devlin, C. F. Chabalowski and M. J. Frisch, *J. Phys. Chem.*, 1994, **98**, 11623–11627.

205 E. D. Glendening and U. F. Weinhold, *J. Comput. Chem.*, 1998, **19**, 610627.

206 A. E. Reed, L. A. Curtiss and F. Weinhold, *Chem. Rev.*, 1988, **88**, 899–926.

207 M. J. Frisch, G. W. Trucks, H. B. Schlegel, G. E. Scuseria, M. A. Robb, G. R. Cheeseman, J. Scalmani, V. Barone, B. Mennucci, G. A. Petersson, H. Nakatsuji, M. Caricato, X. P. Li, H. Hratchian, A. F. Izmaylov, J. Bloino, G. Zheng and D. J. Sonnenb, .

208 T. Lu and F. Chen, *J. Comput. Chem.*, 2012, **33**, 580–592.